

**CHARACTERIZATION OF AEROSOL PHYSICAL  
PROPERTIES AND ITS IMPACT ON SOLAR  
RADIATION OVER NEPAL**



A THESIS SUBMITTED TO THE  
CENTRAL DEPARTMENT OF PHYSICS  
INSTITUTE OF SCIENCE AND TECHNOLOGY  
TRIBHUVAN UNIVERSITY  
NEPAL

FOR THE AWARD OF  
DOCTOR OF PHILOSOPHY  
IN PHYSICS

BY

**JEEVAN REGMI**

**DECEMBER, 2022**



**CHARACTERIZATION OF AEROSOL PHYSICAL  
PROPERTIES AND ITS IMPACT ON SOLAR  
RADIATION OVER NEPAL**



A THESIS SUBMITTED TO THE  
CENTRAL DEPARTMENT OF PHYSICS  
INSTITUTE OF SCIENCE AND TECHNOLOGY  
TRIBHUVAN UNIVERSITY  
NEPAL

FOR THE AWARD OF  
DOCTOR OF PHILOSOPHY  
IN PHYSICS

BY  
JEEVAN REGMI  
DECEMBER, 2022



TRIBHUVAN UNIVERSITY  
Institute of Science and Technology

**DEAN'S OFFICE**

Kirtipur, Kathmandu, Nepal  
Institute of Science & Technology  
Dean's Office  
July 12, 2023

Reference No.:

**EXTERNAL EXAMINERS**

**The Title of Ph.D. Thesis:** "Characterization of Aerosol Physical Properties and its Impact on Solar Radiation over Nepal "

**Name of Candidate:** Jeevan Regmi

**External Examiners:**

- (1) Prof. Dr. Narayan Prasad Chapagain  
Amrit Campus, Tribhuvan University  
Kathmandu, NEPAL
- (2) Prof. Dr. Shamima Chaudhary  
University of Dhaka  
Dhaka, BANGLADESH
- (3) Dr. Parashu Kharel  
South Dakota State University  
Brookings, USA

July 12, 2023

(Dr. Surendra Kumar Gautam)  
Asst. Dean

## DECLARATION

Thesis entitled “**Characterization of Aerosol Physical Properties and its Impact on Solar Radiation over Nepal**” is being submitted to the Central Department of Physics, Institute of Science and Technology (IoST), Tribhuvan University, Nepal for the award of the degree of Doctor of Philosophy (Ph.D.); is a research work carried out under the supervision of Prof. Khem Narayan Poudyal, Dept. of Applied Sciences, Institute of Engineering Tribhuvan University, Lalitpur, Nepal , and co-supervised by Dr. Rudra Aryal, Franklin Pierce University, 40 University Drive, Rindge, NH, USA.

I confirm that this research is original and has not been submitted for any other degree or form to any university or institute here or elsewhere.

..... 

Jeevan Regmi

December, 2022

## RECOMMENDATION

This is to recommend that **Mr. Jeevan Regmi** has carried out research entitled **“Characterization of Aerosol Physical Properties and its Impact on Solar Radiation over Nepal”** for the award of Doctor of Philosophy (Ph.D.) in **Physics** under our supervision. To our knowledge, this work has not been submitted for any other degree.

He has fulfilled all the requirements laid down by the Institute of Science and Technology (IoST), Tribhuvan University, Kirtipur, for the submission of the thesis for the award of Ph.D. degree.

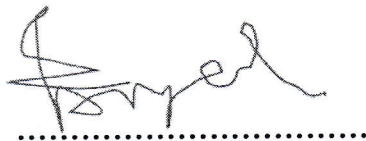


**Dr. Khem Narayan Poudyal**

**Supervisor**

**(Professor)**

Department of Applied Sciences and Chemical Engineering  
Tribhuvan University, Lalitpur, Nepal



**Dr. Rudra Aryal**

**Co-supervisor**

**(Associate Professor)**

Franklin Pierce University,  
40 University Drive, Rindge, NH, USA

**December, 2022**



# TRIBHUVAN UNIVERSITY

CENTRAL DEPARTMENT OF PHYSICS

Kirtipur, Kathmandu, Nepal

☎ 4331054

www.tucdp.edu.np



Date: 19 July 2023

.....) CDP .....

## LETTER OF APPROVAL

Date: .....

On the recommendation of **Prof. Khem Narayan Poudyal**, and **Dr. Rudra Aryal**, this **Ph.D.** thesis submitted by **Jeevan Regmi**, entitled “**Characterization of Aerosol Physical Properties and its Impact on Solar Radiation over Nepal**” is forwarded by the Central Department of Research Committee (CDRC) to the Dean, Institute of Science and Technology (IoST), Tribhuvan University.

*OP Niraula*

**Dr. Om Prakash Niraula**

**(Professor)**

Head

Central Department of Physics,

Tribhuvan University, Kirtipur,

Kathmandu, Nepal

## ACKNOWLEDGMENTS

I am deeply grateful to my supervisor, Prof. Dr. Khem Narayan Poudyal, for his guidance, positive feedback, and encouragement during my research. It was through his inspiration and his ever-present willingness to help nature that I was able to overcome my difficult times. I am equally thankful for the constant support, motivation, and guidance from my supervisor Dr. Rudra Aryal. His day/night presence was my strength. He provided me complete liberty to explore on my own while always being very observant of my diligence.

I like to sincerely acknowledge Prof. Dr. Om Prakash Niraula, Head, Central Department of Physics for his support, encouragement and facilities provided from the department during my research work.

I would like to acknowledge Prof. Dr. Binil Aryal, Dean, IOST, TU for his encouragement and positive feedback throughout the work.

I want to thank Prof. Dr. Narayan Prasad Adhikari for his constant support, suggestions and inspiration throughout my Ph.D. studies. I also greatly appreciate the valuable suggestions and guidance from Dr. Amod Pokhrel. The valuable suggestions and help provided by Nabin Malakar, Madhu Gyawali, Lekhendra Tripathy, and Mukesh Rai are also greatly appreciated.

I take this opportunity to remember my late father Mr. Bohari Prasad Regmi, whom I lost during my PhD work. His inspiration and dream to see his son as a PhD graduate with flourishing academic career always provided strength for me to keep going. I am deeply indebted to him for everything he did for my education. Similarly, I thank my mother Bhawani Devi Regmi for making sure of keeping me hassle free during my PhD work, especially in mourning period. The love and care I got from my sisters Anita, Sunita, Binita and brother Naba Raj is always appreciable.

I thank my wife Sabitri Gautam, for always being available in my thick and thin. My children Shashwat and Jia for adjusting with their fathers' prolonged absence in their valuable growing years.

Finally, I like to thank all my friends and well-wishers for their support, encouragement and appreciation to complete my research work.

.....  
Jeevan Regmi  
December, 2022



## ABSTRACT

This thesis focuses on characterizing the physical and optical properties of aerosols over Nepal by including the Himalayan region (Jomsom, Kyanjin Gompa, and EVK2\_CNR), the Hilly region (Pokhara, and KTM-Bode), and the Terai region (Lumbini). NASA's (National Aeronautics and Space Administration) AERONET (Aerosol Robotic Network) provides a significant amount of aerosol data for analysis for these locations, covering the country's largest and most strategic areas. PurpleAir, a low-cost instrument installed in Pokhara and Kathmandu, provides continuous one-minute average data. These data were analyzed and compared with satellite data from MODIS (Moderate Resolution Imaging Spectroradiometer). An analysis of HYSPLIT back trajectory, such as cluster analysis, was used to identify aerosol particle sources. Pyranometer data were used to observe global solar radiation (GSR).

Different statistical tools, such as Root Mean Square Error (RMSE), standard deviation, and correlation coefficient, were used to analyze aerosol optical properties over multiple years.

Based on AERONET data, the four metrics aerosol optical depth (AOD), precipitable water (PW), angstrom exponent (AE), and single scattering albedo (SSA) are presented in this study. There was a maximum PW of  $5.87 \pm 0.12$  cm in Lumbini in July and an average of  $3.25 \pm 0.21$  cm, whereas the minimum was observed in EVK2\_CNR with an average of  $0.23 \pm 0.02$  cm. An analysis of the AE can provide crucial information on the size distribution of aerosols based on their dependence on a wavelength. Except for EVK2\_CNR, all observed stations have an average AE value greater than one. Jomsom has the highest average ( $1.52 \pm 0.18$ ), and EVK2\_CNR has the lowest ( $0.77 \pm 0.34$ ). A clear domination of fine-mode aerosols can be seen between 440 and 870 nm in the wavelength range. There is a tendency for AOD to decrease with the altitude of the geographical locations. Monthly average values of AOD 500 nm decrease with altitude from Lumbini ( $0.71 \pm 0.19$ ) to EVK2\_CNR ( $0.04 \pm 0.01$ ). Accordingly, Lumbini has the highest pollution level, and EVK2\_CNR has the lowest pollution level. SSA varied between 0.79 and 0.96 for all observation periods except for EVK2\_CNR, with an average of  $0.68 \pm 0.17$  and varies between 0.27 to 0.98. Monsoon and post-monsoon seasons have higher values, while winter and pre-monsoon seasons have lower values.

SSA shows different monthly variations showing the variability of aerosol optical characteristics.

The maps plotted based on MODIS data for AOD from 2015 to 2020 show that AOD is highest in the southern part of the country, relatively low in the middle hills, and lowest in the high mountains. Additionally, AOD is relatively lower in 2020, indicating a reduction in anthropogenic aerosols due to the COVID-19 lockdown.

Pokhara's aerosol product time-series analysis from 2010-2018 shows lower aerosol loading during the morning and evening compared to mid-day. As demonstrated by the correlation between AOD at 500 nm and Precipitable Water level (PW) from December to April (0.96), aerosol and water vapor accumulation in the atmosphere significantly increases during the winter and pre-monsoon seasons and varies inversely from May to November, with a correlation coefficient of -0.61. A five-day back trajectory cluster analysis reveals that air masses reaching Pokhara valley comes from the Indo Gangetic Plains (IGP) region during winter and West Indian plains (West India, Pakistan) during the pre-monsoon when strong western disturbances prevail. During monsoon, most air mass arrives east of the IGP region and the Bay of Bengal.

Analysis of daily average data for Global Solar Radiation (GSR) in Pokhara shows that maximum GSR values gradually increased from January to March, then decreased in April, then increased again in June. It gradually decreases from July to December. Almost all months had mean values that were lower than their median values. March has the highest average [ $19.19 \pm 4.61$  MJ/m<sup>2</sup>], and January has the lowest average [ $9.31 \pm 4.39$  MJ/m<sup>2</sup>] with yearly average [ $14.48 \pm 4.31$  MJ/m<sup>2</sup>]. Comparison of GSR data with AOD data shows, the amount of solar radiation reaching the ground decreased with an increase in aerosol loading in the vertical column.

While investigating the reliability of PurpleAir measurements, this study compares column-integrated aerosol data from MODIS with surface-level aerosol concentration. PurpleAir Hourly averaged PM<sub>2.5</sub> levels fluctuate bimodally in all seasons, with the peak values in the rush hours of morning and evening. In Pokhara, PM<sub>2.5</sub> values range from a minimum of  $22.78 \pm 3.23$   $\mu\text{g m}^{-3}$  in the summer to a maximum of  $101 \pm 26.31$   $\mu\text{g m}^{-3}$  in the winter. During pre-monsoon and post-monsoon, it was observed to be  $55.58 \pm 11.42$   $\mu\text{g m}^{-3}$  and  $45.46 \pm 12.16$   $\mu\text{g m}^{-3}$  respectively. During the summer, PM<sub>2.5</sub> levels are lowest due to rain and diffusion in the vertical atmosphere.

## LIST OF ACRONYMS AND ABBREVIATIONS

AERONET	: Aerosol Robotic Network
AOD	: Aerosol optical depth
AO	: Auto Optimization
API	: Application Programming Interface
ASCII	: American Standard Code for Information Interchange
cf	: Cloud Transmittance Factor
CARD	: Centre for Applied Research and Development
CBS	: Central Bureau of Statistics
DAAC	: Distributed Active Archive Center
DAI	: Deep-Blue Aerosol Index
DHM	: Department of Hydrology and Meteorology
DOY	: Day of the Year
EOSDIS	: Earth Observing System Data and Information System
ESA	: European Space Agency
FIRMS	: Fire Information for Resource Management System
GES	: Goddard Earth Sciences
HYSPLIT	: Hybrid Single-Particle Lagrangian Integrated Trajectory
IGP	: Indo-Gangetic Plane
IOE	: Institute of Engineering
IPCC	: Inter-governmental Panel on Climate Change
GEF	: Global Environment Facility
GJ	: Giga Joule
GoN	: Government of Nepal
GOES	: Geostationary Operational Environmental Satellite

GSR	: Global Solar Radiation or Solar Radiation (UK)
kWh	: Kilo Watt hour
KTM	: Kathmandu
MeV	: Mega electron Volts
MJ	: Mega Joules
MLE	: Maximum Likelihood Estimation
MODIS	: Moderate Resolution Imaging Spectroradiometer
MOEST	: Ministry of Environment, Science & Technology
NASA	: National Aeronautics and Space Administration
NOAA	: National Oceanic and Atmospheric Administration
PM	: Particulate Matter
PKR	: Pokhara
RH	: Relative Humidity
SZA	: Solar Zenith Angle
TSR	: Total Solar Radiation
TOMS	: Total Ozone Mapping Spectrometer
WMO	: World Meteorological Organization

## LIST OF SYMBOLS

$\gamma$	Surface azimuth angle
$^{\circ}\text{C}$	Degree Celsius
$c$	Velocity of light in vacuum
$\varepsilon$	Emissivity of surface
$h$	Planck's Constant
$k$	Boltzmann Constant
$\text{K}$	Kelvin
$\sigma$	Stefan-Boltzmann Constant
$\text{W}$	Watt
$\Omega$	Solid angle
$\tau$	Optical depth
$\rho$	Density of attenuator
$\sigma$	Mass extinction
$\varphi$	Latitude
$\omega$	Hour angle
$\omega_s$	Hour angle at sunrise or sunset
$\alpha$	Solar altitude angle
$\theta$	Angle of incident
$\theta_z$	Zenith angle
$\delta$	Declination
$\Gamma$	Surface azimuth angle
$\gamma$	Gamma function
$r^2$	Coefficient of determination

$H_c$	Average daily GSR at clear sky day on horizontal surface
$H_g$	Global Solar Radiation on horizontal surface
$H_0$	Extraterrestrial Radiation above the atmosphere
$H_{sc}$	Solar Constant above the atmosphere
$g$	Assymetry Parameter
$\omega$	Single Scattering Albedo (SSA)
$\lambda$	Wavelength
$m$	Optical Air mass
$F_0$	Incident flux density
$Q_s$	Scattering Efficiency
$Q_a$	Absorption Efficiency
$Q_e$	Extinction Efficiency
$\sigma_s$	Scattering Cross-Section
$\sigma_a$	Absorption Cross-Section
$\sigma_e$	Extinction Cross-Section

# LIST OF TABLES

	Page No.
<b>Table 1:</b> Refractive indices of some of the selected atmospheric aerosol substances at $\lambda = 0.5 \mu\text{m}$ (Liou, 2002) .....	48
<b>Table 2:</b> Monthly mean maximum and minimum values for PW(cm), AE (nm) and $\tau$ (nm) for different stations Lumbini (2013, 2014, 2017 and 2018 (110m)), Pokhara (2011 to 2015 (800m)), Kathmandu-Bode (2012 to 2014 (1362m)), Jomsom (2011to 2013 (2825m)), Kyanjin-Gompa .....	59
<b>Table 3:</b> Seasonal and spectral variation of monthly mean SSA at different AERONET sites Lumbini (2013, 2014, 2017 and 2018 (110m)), Pokhara (2011 to 2015 (800m)), Kathmandu-Bode (2012 to 2014 (1362m)), Jomsom (2011to 2013 (2825m)), and EVK2-CNR (2011 to 2013).....	62
<b>Table 4:</b> Monthly average of Aerosol optical depth (AOD), Angstrom exponent (AE) and Precipitable water (PW) with standard deviation during 2017 at Pokhara station. A large variation in daily data gives significant standard deviation. ....	81
<b>Table 5:</b> Variation of Radiative Forcing during Pre- Monsoon Period of Pokhara, 2017 .....	86
<b>Table 6:</b> Monthly Variation of Diffuse Radiation and AOD _500 nm at Pokhara, 2017. ....	88
<b>Table 7:</b> Seasonal Meterological Parameters for the year 2020 January to 2020 November .....	90
<b>Table 8:</b> Seasonal average concentrations of PM <sub>2.5</sub> and PM <sub>10</sub> in Pokhara and Pulchowk along with the ratio of PM <sub>2.5</sub> to PM <sub>10</sub> . ....	92
<b>Table 9:</b> The average, maximum and minimum mass concentration (PM <sub>2.5</sub> ) hourly averaged data of each season at Pulchowk in 2020.....	99

**Table 10:** Comparison of PM<sub>2.5</sub> data from two different devices (Beta Attenuation Monitor; BAMs and PurpleAir) in two different locations: Phora Durbar(PH) and Pulchowk (PK) (Near to each other) ..... 103



# LIST OF FIGURES

	<b>Page No.</b>
<b>Figure 1:</b> Atmospheric aerosol number, and volume distribution versus particle size (Seinfeld & Pandis, 2006).....	4
<b>Figure 2:</b> Size range of aerosol particles in the atmosphere and their role in atmospheric physics and chemistry (Tomasi & Lupi, 2017).....	5
<b>Figure 3:</b> Schematic diagram to show total flux density along z, $\rho$ and u coordinates (Liou, 2002). ....	11
<b>Figure 4:</b> CIMEL Sun Photometer Deployed in AERONET Stations (Gregory, 2011). ....	21
<b>Figure 5:</b> <i>CMP6 - Pyranometer (Kipp and Zonen)</i> , 2019.....	26
<b>Figure 6:</b> (a) Zenith angle, slope, surface azimuth angle, and solar azimuth angle for a titled surface and (b) Plane view showing solar azimuth angle (Duffie & Beckman, 2013). ....	27
<b>Figure 7:</b> External (left) and bottom view (right) showing the inlet air flow and outlet air flow along with a fan in two sensors of a Purple-air monitor (Regmi et al., 2022). ....	30
<b>Figure 8:</b> Functional Block Diagram of Purple Air II-AP/SD sensor and an overview of the PMS5003 (( <a href="http://www.Aqmd.Gov/Docs/Default-Source/Aq-Spec/Resources-Page/Plantower-Pms5003-Manual_v2-3.Pdf">Http://Www.Aqmd.Gov/Docs/Default-Source/Aq-Spec/Resources-Page/Plantower-Pms5003-Manual_v2-3.Pdf</a> ), 2021)....	31
<b>Figure 9:</b> Terra Satellite carrying MODIS and showing a coverage area.....	31
<b>Figure 10:</b> Transformation of rectangular to spherical coordinates. S is the Poynting vector; a is an arbitrary unit vector; $\theta$ and $\phi$ are zenith and azimuthal angles; and E and H are electric and magnetic vectors (Liou, 2002).....	38

<b>Figure 11:</b> Decomposition of the incident (i) and scattered (s) electric vectors into perpendicular (r) and parallel (l) components in Cartesian and spherical coordinates (Liou, 2002).....	43
<b>Figure 12:</b> The scattering efficiency factor $Q_s$ as a function of the size parameter $x$ for a real index of refraction of $n = 1.45$ and several values of the imaginary part .....	47
<b>Figure 13:</b> The variation of scattering efficiency with size parameter corresponding to different wavelength and at $n = 1.4500$ and $k = 0.0078$ .....	48
<b>Figure 14:</b> The variation of different efficiency factors corresponding to different size parameter at $n = 1.4500$ and $k = 0.0078$ during pre-monsoon period 2019 in Pokhara. ....	49
<b>Figure 15:</b> The variation of different efficiency factors corresponding to different size parameter at $n = 1.3300$ and $k = 0.0171$ during post-monsoon period 2019 in Pokhara. ....	50
<b>Figure 16:</b> The variation of different efficiency factors corresponding to different size parameter at $n = 1.5645$ and $k = 0.0183$ during winter period 2019 in Pokhara. ....	50
<b>Figure 17:</b> Different AERONET stations in the study area (Source: Map generated by the author using Arc GIS 10.4 Software).....	51
<b>Figure 18:</b> The Moderate Resolution Imaging Spectroradiometer (on NASA's Terra satellite) image shows an evident accumulation of haze is visible along the Himalayan foothills on 9th February 2020. A PurpleAir monitor is also shown on the top right corner of the figure, which was installed on the IOE Pulchowk Campus, Lalitpur, Kathmandu, Nepal, as located on the map of Nepal. ....	53
<b>Figure 19:</b> Comparitive analysis of seasonal variation of monthly mean $\tau_{500nm}$ , AE (440nm-870nm) and PW (cm) in different AERONET stations; Lumbini, Pokhara, KTM-Bode, Jomsom, Kyanjin-Gompa and EVK2-CNR in the order of increasing altitude. ....	60

<b>Figure 20:</b> Seasonal spectral variation of monthly mean SSA at EVK2-CNR AERONET Station for the years 2011-2013 .....	63
<b>Figure 21:</b> Seasonal spectral variation of monthly mean SSA at Jomsom for the years 2011-2013. ....	64
<b>Figure 22:</b> Seasonal spectral variation of monthly mean SSA at Pokhara AERONET Station for the years 2011-2015.....	65
<b>Figure 23:</b> Seasonal spectral variation of monthly mean SSA at Kathmandu-Bode (KTM-BODE) AERONET Station for the years 2012-2014. ....	66
<b>Figure 24:</b> Seasonal spectral variation of monthly mean SSA at Lumbini AERONET Station for the years 2013-2014, 2017 and 2018. ....	67
<b>Figure 25:</b> Distribution of annually averaged $\tau$ at 550nm over Nepal for the period of 2015 to 2020 as observed by MODIS AQUA and TERRA satellite.....	68
<b>Figure 26:</b> Spectral variation of monthly mean, over 9 years period between 2010-2018, aerosol optical depth representing different seasons at Pokhara (Regmi et al., 2020). ....	70
<b>Figure 27:</b> Seasonal variation (2010-2018) of monthly mean AOD 500 nm and precipitable water at Pokhara (Regmi et al., 2020).....	71
<b>Figure 28:</b> Seasonal variation (2010-2018) of Ångström parameters ( $\alpha$ , $\beta$ ) at Pokhara using the linear regression (solid line), and $\alpha_2$ from second-order polynomial fit (dotted curve) of monthly mean spectral AOD (in $\mu\text{m}$ ) , in the logarithmic scale.....	73
<b>Figure 29:</b> Monthly variation (2010-2018) of $\tau$ 0.50 $\mu\text{m}$ , Turbidity Parameter ( $\beta$ ) and curvature ( $\alpha'$ ).....	74
<b>Figure 30:</b> The seasonal variation of monthly averaged volume size distribution in logarithmic scale. ....	75
<b>Figure 31:</b> The seasonal volume size distribution $dV(r)/d\ln r$ ( $\mu\text{m}^3/\mu\text{m}^2$ ) in the size range 0.05 $\mu\text{m}$ -15 $\mu\text{m}$ at Pokhara (2010-2018) (Regmi et al., 2020). ....	75

<b>Figure 32:</b> Monthly mean spectral SSA (top two), averaged within the months of years 2010-2018 at Pokhara, for January, February, March, April, and May and AAOD (bottom two) in the logarithmic scale with the linear fit in same scale.....	77
<b>Figure 33:</b> Clusters of five days air mass back trajectories computed with HYSPLIT model during four seasons of 2017 reaching Pokhara at altitude 500m. The active fire spots are symbolized with red dots at different seasons obtained from FIRMS. The percentage contribution of each cluster is given on the bottom right corners (Regmi et al., 2020).....	78
<b>Figure 34:</b> (a) The true-color image of the 27th of October, 2017 from the MODIS satellite, displays significant air pollution in the form of plumes over the IGP. (b)) NOAA HYSPLIT MODEL Back Trajectories ending at Pokhara at 0600UTC on 27 October 2017 (Regmi et al.; 2020).....	78
<b>Figure 35:</b> Time series of daily averaged columnar (a) AOD values at a wavelength 0.50 $\mu\text{m}$ , AOD <sub>0.50</sub> (b) AE values with in the wavelength range 0.44 $\mu\text{m}$ - 0.87 $\mu\text{m}$ and (c) PW in cm, at Pokhara during the year 2017. The bottom scale represents Julian days. ....	80
<b>Figure 36:</b> Seasonal variation of the mean AOD at Pokhara, 2017 (a) at various wavelengths ( $\lambda$ ) and (b) linear fit in logarithmic wavelength scale. ....	83
<b>Figure 37:</b> Monthly Percentage contribution of fine mode particles on total AOD over Pokhara, 2017. ....	84
<b>Figure 38:</b> Monthly average total AOD and AODs due to fine and Coarse Mode particles in Pokhara in the year 2017.....	85
<b>Figure 39:</b> Variation of Radiative Forcing (a-e) in Pokhara during Pre-monsoon period of 2017. ....	86
<b>Figure 40:</b> Daily variation of flux down at the top of atmosphere (TOA) and bottom of atmosphere (BOA) at Pokhara, 2017. ....	87

<b>Figure 41:</b> Daily variation of flux up at the top of atmosphere (TOA) and bottom of atmosphere (BOA) at Pokhara, 2017. ....	87
<b>Figure 42:</b> Daily Variation of Radiative forcing at the top of atmosphere (TOA) and bottom of atmosphere (BOA) during the year 2017 at Pokhara. ....	88
<b>Figure 43:</b> Monthly averaged Aerosol Optical Depth at 500 nm with the months of 2017.....	89
<b>Figure 44:</b> Box plot for monthly variation of GSR for the year 2020 at Pokhara .....	89
<b>Figure 45:</b> Comparative analysis of GSR data obtained from Pyranometer with aeronet AOD data for the year 2020 at Pokhara.....	90
<b>Figure 46:</b> Daily mean concentrations of (a) PM <sub>10</sub> and (b) PM <sub>2.5</sub> in Pokhara and Pulchowk from January 15, 2020 to November 27, 2020. ....	91
<b>Figure 47:</b> Comparison of Concentration of PM <sub>1</sub> µg/m <sup>3</sup> , PM <sub>2.5</sub> µg/m <sup>3</sup> and PM <sub>10</sub> µg/m <sup>3</sup> in Pokhara observation site during winter, pre-monsoon and monsoon season 2020. ....	93
<b>Figure 48:</b> Comparison of Concentration of PM <sub>1</sub> µg/m <sup>3</sup> , PM <sub>2.5</sub> µg/m <sup>3</sup> and PM <sub>10</sub> µg/m <sup>3</sup> in Pulchowk observation site during winter, pre-monsoon, monsoon and post-monsoon season 2020. ....	94
<b>Figure 49:</b> Seasonal scatter plot for PM <sub>2.5</sub> in Pulchowk and Pokhara for the year 2020 .....	95
<b>Figure 50:</b> (A to K) Hourly averaged (at local time 0:45 – 23:45 hrs, shown in the bottom scale) particle concentration (PM <sub>2.5</sub> ), Relative Humidity (RH%), and temperature (°C) by using entire months' data at Pulchowk in 2020.....	97
<b>Figure 51:</b> Hourly averaged (at local time) particle concentration (PM <sub>2.5</sub> ), relative Humidity (RH%), and temperature (°F) for seasonally averaged data by using the corresponding months' data for each season at Pulchowk in 2020. The scales for all graphs are shown .....	98

<b>Figure 52:</b> Scatter plot of a) MODIS AOD (Terra) vs MODIS AOD (Aqua) using the same day data observed from two satellites in Kathmandu, 2020 with 3km × 3km resolution. In the figure, some of the data also show the very nominal standard deviation. ....	100
<b>Figure 53:</b> Scatter plot of MODIS AOD 500 nm observed by Aqua and Terra satellites vs. PM <sub>2.5</sub> (PA) observed by PurpleAir monitor at Pulchowk in 2020 (Regmi et al., 2023). ....	101
<b>Figure 54:</b> Seasonal Comparison of Hourly averaged (at local time) particle concentration (PM <sub>2.5</sub> ), for two locations Pulchowk and Phora Durbar ...	102
<b>Figure 55:</b> Monthly variation of Scatter plot of PM <sub>2.5</sub> (US) at Phora Durbar vs. PM <sub>2.5</sub> (PA) observed by purple air monitor at Pulchowk to establish correlation between them .....	104
<b>Figure 56:</b> NOAA HYSPLIT Track showing the trans-boundary air pollution track showing the possible trajectories of the air parcels. The tracks are shown at 500 m asl ending at Kathmandu in 2020 (Regmi et al., 2023). ....	105
<b>Figure 57:</b> Cluster of five days air mass back trajectories computed with Analysis NOAA HYSPLIT with HYSPLIT model reaching Kathmandu valley at 1000 m asl at different seasons. The percentage contribution of each cluster is shown in different colors.....	106
<b>Figure 58:</b> Cluster of five days air mass back trajectories computed with Analysis NOAA HYSPLIT with HYSPLIT model reaching Kathmandu valley at 1500 m asl at different seasons. The percentage contribution of each cluster is shown in different colors.....	107

# TABLE OF CONTENTS

	<b>Page No.</b>
<b>Declaration.....</b>	<b>ii</b>
<b>Recommendation.....</b>	<b>iii</b>
<b>Letter of Approval .....</b>	<b>iv</b>
<b>Acknowledgments .....</b>	<b>v</b>
<b>Abstract.....</b>	<b>vi</b>
<b>List of Acronyms and Abbreviations .....</b>	<b>viii</b>
<b>List of Symbols .....</b>	<b>x</b>
<b>List of Tables .....</b>	<b>xii</b>
<b>List of Figures.....</b>	<b>xiv</b>
<b>Table of Contents .....</b>	<b>xx</b>
<b>CHAPTER 1 .....</b>	<b>1</b>
<b>INTRODUCTION.....</b>	<b>1</b>
1.1 Aerosols .....	1
1.1.1 Types of Aerosols .....	2
1.1.1.1 Primary and secondary Aerosols .....	2
1.1.1.2 Aerosols based on location .....	3
1.1.1.3 Natural and Anthropogenic aerosols.....	3
1.1.2 Physical Properties of Aerosols .....	3
1.1.2.1 Aerosol Size Distribution.....	3
1.1.2.2 Effective Radius:.....	8
1.1.3 Aerosol Optical Properties:.....	8
1.1.3.1 Phase Function:.....	9

1.1.3.2 Asymmetry Parameter .....	9
1.1.3.3 Refractive Index.....	10
1.1.3.4 Single Scattering Albedo .....	10
1.1.4 Atmospheric Solar Heating Rate .....	10
1.2 Fundamentals of Solar Radiation.....	12
1.2.1 Solar Zenith Angle (SZA).....	12
1.2.2 Atmospheric Ozone .....	13
1.2.3 Cloud.....	13
1.2.4 Albedo.....	13
1.2.5 Altitude .....	14
1.3 Objectives of the Study.....	14
1.4 Outline of Thesis.....	15
<b>CHAPTER 2.....</b>	<b>16</b>
<b>LITERATURE REVIEW .....</b>	<b>16</b>
2.1 Review of Articles .....	16
2.2 Statement of Problem.....	18
2.3 Research Gap .....	19
<b>CHAPTER 3.....</b>	<b>20</b>
<b>MATERIALS AND METHODS .....</b>	<b>20</b>
3.1 Aerosol Robotic Network (AERONET).....	20
3.1.1 Cimel Sun Photometer .....	21
3.1.2 Attenuation of Direct Solar Radiation: .....	22
3.1.3 Aerosol Optical Depth (AOD).....	23
3.2 CMP6 Pyranometer.....	25



3.2.1 Solar Geophysical parameters.....	26
3.3 PurpleAir sensor.....	29
3.3.1 Working principle .....	30
3.4 MODIS Satellite Measurement.....	31
3.4.1 Column MODIS AOD and ground-level PM <sub>2.5</sub> and Relative humidity factor .....	34
3.5 Mie theory and scattering of solar radiation .....	36
3.5.1 Formulation of Lorentz-Mie Theory from Maxwell’s Equations.....	37
3.5.2 Scattering of a plane wave by a homogeneous sphere.....	37
3.5.3 Influence of particle refractive index on scattering light intensity .....	47
3.5.4 Seasonal variation of efficiency factors with size parameter .....	49
3.6 Research Sites .....	51
3.7 Interpretation of data.....	54
3.7.1 HYSPLIT Back Trajectory .....	55
3.7.2 Cluster Analysis .....	55
3.7.3 Statistics .....	55
<b>CHAPTER 4.....</b>	<b>57</b>
<b>RESULTS AND DISCUSSION .....</b>	<b>57</b>
4.1 Variability of spectral columnar AOD, AE and PW in different AERONET stations of Nepal .....	57
4.2 Seasonal variation of monthly mean Single Scattering Albedo (SSA) at different AERONET Sites of Nepal .....	61
4.3 Monthly variation of columnar AOD 550nm over Nepal for the time period of 2015-2020; as analyzed from MODIS satellite data.....	68

4.4 Variability of Spectral Columnar AOD and Precipitable water of Pokhara AERONET site. (Analysis based on 10 years data-Pokhara station). .....	69
4.5 Time Series (2010-2018) Analysis of Aerosol Inversion Products (AE, Curvature of AOD Spectra, SSA, AAOB and AAE) .....	72
4.6 Investigation of Aerosol Sources and Types over Pokhara .....	77
4.7 Diurnal Variation of AOD <sub>0.50</sub> , AE coefficients and Precipitable Water during 2017 in Pokhara .....	79
4.8 Spectral dependence of AOD.....	81
4.9 Contribution of Fine and coarse mode particles on AOD.....	83
4.10 Variation of Radiative Forcing .....	85
4.11 Relationship between AOD and Radiative Forcing.....	88
4.12 Monthly Variation of Global Solar Radiation (GSR) in Pokhara in the year 2020 .....	89
4.13 Daily Variation of PM <sub>1</sub> , PM <sub>2.5</sub> and PM <sub>10</sub> in different Seasons .....	93
4.14 Seasonal Scatter Plot for PM <sub>2.5</sub> in Pulchowk and Pokhara.....	94
4.15 Monthly Variation of Hourly Averaged PM <sub>2.5</sub> Concentration.....	95
4.16 Morning and afternoon MODIS AOD and Comparison with PM <sub>2.5</sub> .....	99
4.17 Comparison of hourly averaged seasonal PM <sub>2.5</sub> data from two different types of Sensors installed at Pulchowk (Lalitpur) and Phora-Durbar (Kathmandu)..	102
4.18 Correlation between PM <sub>2.5</sub> at Pulchowk and PM <sub>2.5</sub> at Phora Durbar.....	104
4.19 Seasonal Cluster Analysis.....	105
<b>CHAPTER 5 .....</b>	<b>108</b>
<b>CONCLUSIONS .....</b>	<b>108</b>
1. Conclusions based on AERONET Data .....	108
2. Conclusions based on Pyranometer data.....	109
3. Conclusions based on PurpleAir data .....	110

Recommendations and Future Works .....	110
<b>CHAPTER 6</b> .....	<b>112</b>
<b>SUMMARY</b> .....	<b>112</b>
<b>REFERENCES</b> .....	<b>114</b>
<b>APPENDIX</b> .....	<b>133</b>

# CHAPTER 1

## INTRODUCTION

Nepal is situated in the Himalayan region, which is renowned for its unique topography and complex atmospheric conditions. As a result of the country's high mountains and a variety of land use patterns, including forests, farms, and urban areas, Nepal has extremely variable aerosol properties and distribution, making it a crucial place for researching how aerosols behave and affect solar radiation. The population and economy of Nepal are rapidly growing, with increasing industrialization, urbanization, and energy use. It is critical to comprehend how these changes will affect the nation's energy balance and climate as a result of the possibility for large changes in the atmospheric aerosol distribution and attributes. Not only this, the effect of aerosols on solar radiation and the Earth's energy balance is a worldwide issue, and a greater understanding of their characteristics and behavior in various places can offer important insights into their overall effect. The findings of this study can assist Nepal establish climate and energy policies and reduce the negative effects of aerosols on solar radiation. The study can help us understand the function of aerosols in the Earth's climate system and provide crucial information for decision-making by describing the physical characteristics of aerosols in Nepal and evaluating their effect on solar radiation. So that it is essential to precisely characterize aerosol physical characteristics in order to assess how they affect solar radiation and the climate of the Earth.

### 1.1 Aerosols

Aerosols are fine solids or liquids suspended in a gaseous medium. In the atmosphere, aerosols, which are embedded naturally and artificially, influence solar radiative forcing (Aryal et al., 2014). The most common natural aerosols are fog, dust, sea salt, forest exudates, and geyser steam, and the most common anthropogenic aerosols are haze, particulate air pollutants, and smoke (Hinds, 1999).

Particles with dimensions ranging from a few nanometers to about 100 micrometers are highly concentrated in urban areas (Seinfeld & Pandis, 2006). Primary particulate emissions from traffic, industry, power generation, natural sources, and gas-to-particle conversion are some of the origins of these aerosols (Salby, 1995). Aerosol particles

from combustion sources, like vehicles, burning wood, and power generated, can be very small that measures up to 1 micrometer ( $\mu\text{m}$ ). However, windblown dust, plant fragments, and pollen are usually greater than 1  $\mu\text{m}$  in size. It is possible to mathematically represent atmospheric particulate size distribution by describing aerosol size distributions, such as the lognormal aerosol distribution (Seinfeld & Pandis, 2006). According to Jaenicke, (1993), urban, rural, desert, and marine aerosols have different model aerosol size distribution characteristics. Distribution parameters varied due to the transportation or injection of different aerosol compositions over these areas.

### **1.1.1 Types of Aerosols**

The characteristics of aerosol populations, such as their size distribution, chemical composition, and shape, vary significantly with space and time (Boucher, 2015). Human activity contributes significantly to aerosols globally, resulting in severe health issues in highly populated areas. Anthropogenic aerosols can also cause local or regional climate change. Aerosols reflect sunlight into the atmosphere and lower the earth's surface temperature. As far as the visible range is concerned, light scattering processes predominate over light absorption; however, for the total radiation balance, light absorption must be considered. As wavelength decreases, aerosol absorption generally increases (Aryal et al., 2014). Aerosols can be classified in several ways according to their properties.

#### **1.1.1.1 Primary and secondary Aerosols**

Primary aerosols are generated directly in the atmosphere by natural and anthropogenic processes. Examples are wind-borne dust, sea spray, biogenic aerosols, industrial aerosols, wind-driven particles from agriculture, fossil fuel combustion, waste, and biomass burning. The secondary aerosol formation process involves the transformation of atmospheric pollutants into condensed phases (liquid or solid). Secondary aerosols mainly consist of sulfates and nitrates formed due to the condensation of sulfur- and nitrogen-containing gases (Tomasi & Lupi, 2017) as shown in Figure 2.

### **1.1.1.2 Aerosols based on location**

Environmental factors significantly affect the spatial distribution of aerosols. There are many types of aerosols, including urban aerosols, semi-urban aerosols, continental aerosols, aerosols from desert, marine, volcano, and stratosphere are some examples. However, they may mix with long-range particulate transport, so they may not accurately represent the aerosols of the place. Local effects are only significant if they dominate regional aerosols.

### **1.1.1.3 Natural and Anthropogenic aerosols**

Aerosols can also be classified as natural or anthropogenic based on their origin. The ocean, soils, vegetation, fires, and volcanoes are all natural sources of emissions. Aerosols produced by the combustion of fossil fuels (e.g., coal and oil), biofuels (including wood, vegetable oils, and animal waste), other fuels (e.g., peat), or vegetation fires are anthropogenic aerosols. There are many sources of aerosols, including industrial processes, transportation, heating, and even domestic activities such as cooking in developing countries.

## **1.1.2 Physical Properties of Aerosols**

### **1.1.2.1 Aerosol Size Distribution**

The determination of aerosol optical properties requires accurate knowledge of aerosol size distribution. The aerosol size distribution is usually represented by the number, area, volume, and mass of aerosol particles per unit volume of atmospheric air (Seinfeld & Pandis, 2006). The oversimplified consideration assumes the aerosol particles to be spherical. But in practice, they are found to have a wide variety of shapes and sizes. So, to describe the wide range in magnitude of particle sizes and visualize the aerosol particles conveniently, the size of aerosol particles is often described with a logarithmic scale.

The number size distribution of atmospheric aerosols can be represented by a continuous function that expresses the number  $n(D)$  of particles per unit volume per unit interval of diameter, expressed in logarithmic scale is given by Seinfeld & Pandis, (2006).

$$n(D) = \frac{dn(D)}{dD} = \frac{1}{D} \frac{dn(D)}{d \ln D} \quad (1.1)$$

The unit of  $n(D)$  in modeling is  $\text{cm}^{-3}\mu\text{m}^{-1}$  with dimension  $L^{-4}$ .

It is used to calculate the attenuation per unit path length of light (aerosol extinction coefficient) in the atmosphere.

The total aerosol concentration can be obtained by integrating over the size distribution:

$$N = \int n(D)dD \quad (1.2)$$

The Figure 1 shows the logarithmic distributions of aerosol particle sizes based on numbers and volume distribution per unit volume of space per unit aerosol diameter based on their sizes. It shows almost all the volume or mass contribution of aerosol particles are due to the particles with diameters larger than  $0.1 \mu\text{m}$  but their number are negligible whereas almost all the numbers of particles is of diameter less than  $0.1 \mu\text{m}$ .

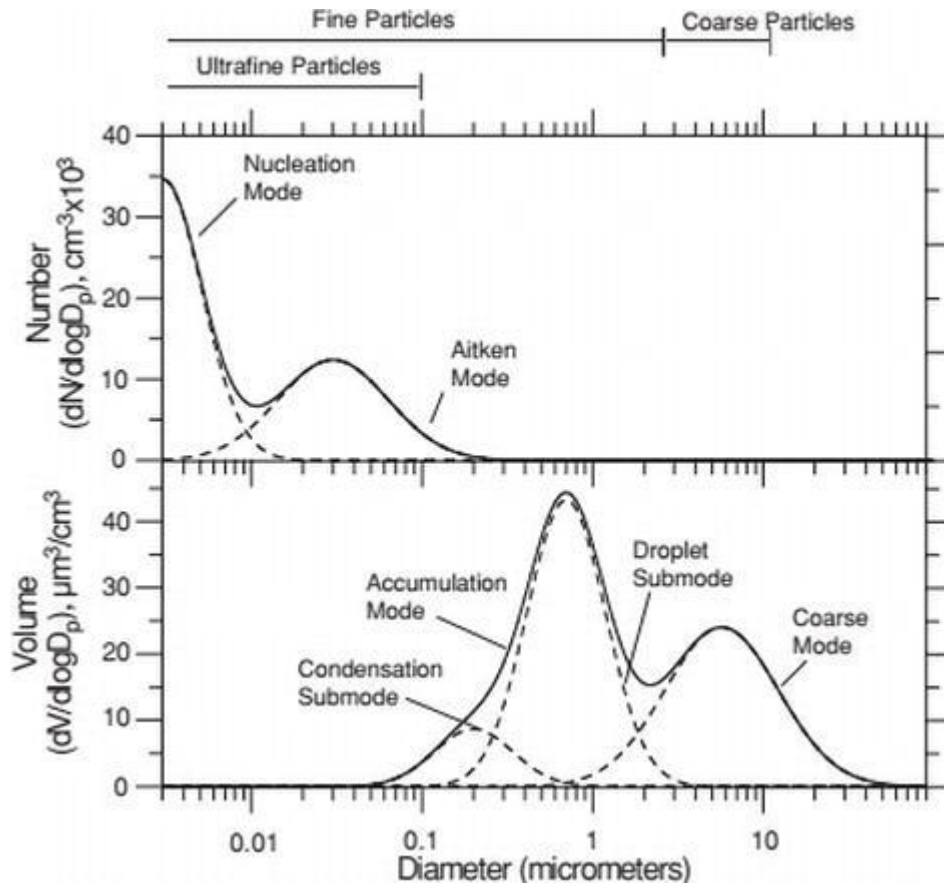


**Figure 1:** Atmospheric aerosol number, and volume distribution versus particle size (Seinfeld & Pandis, 2006)

Aerosol size ranges play a significant role in atmospheric physics and chemistry. It is vital to know the source and size of aerosols to study their properties and impacts on

the atmosphere. As shown in Figure 2, water and ice aerosols can play an important role in cloud and precipitation physics since they form cloud droplets and ice crystals. By incorporating particulate matter into cloud droplets, these processes contribute to removing aerosols from the atmosphere through the wet deposition. Figure 2 also illustrates the gas-to-particle conversion process leading to secondary aerosols.

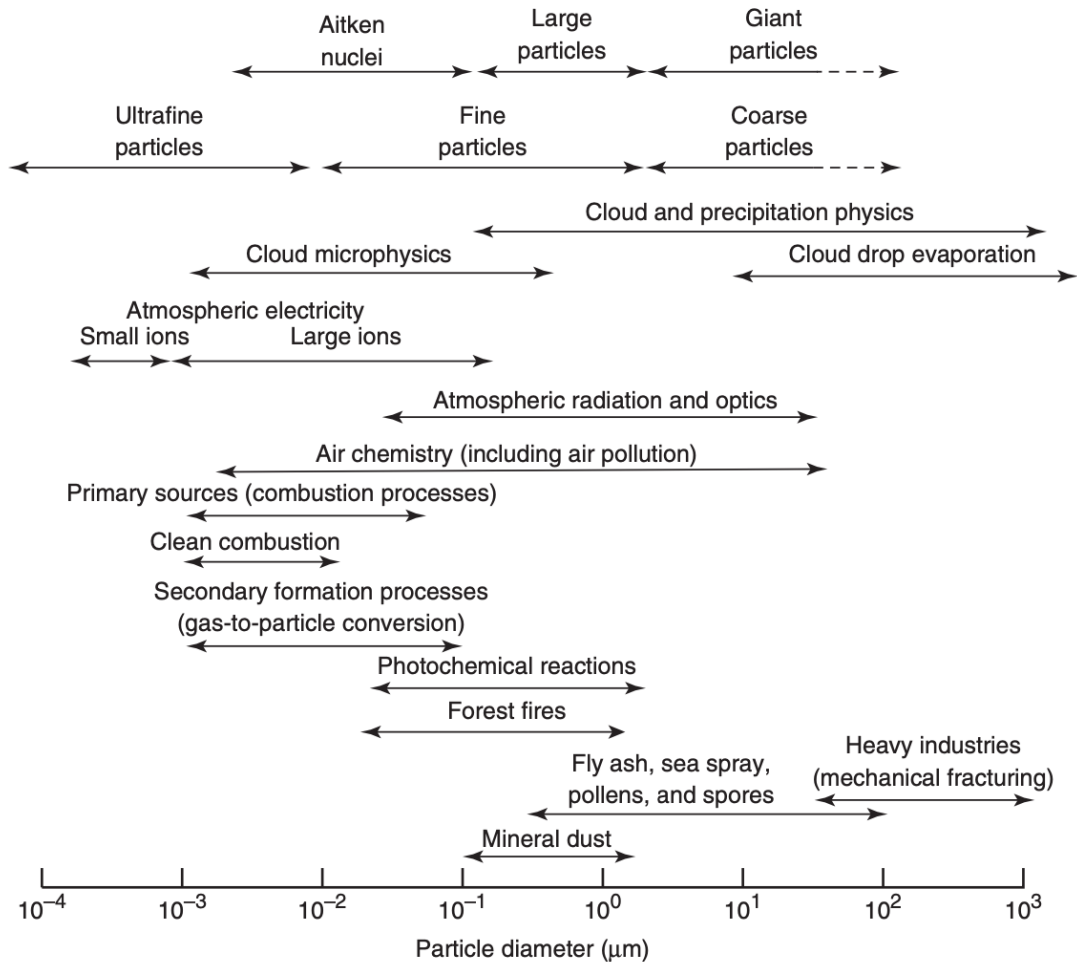


**Figure 2:** Size range of aerosol particles in the atmosphere and their role in atmospheric physics and chemistry (Tomasi & Lupi, 2017).

When describing aerosol optical properties and aerosol size distributions in the atmosphere, the following size distribution functions are typically used:

**Junge Power Law** describes the aerosol size distribution ( $n^*(D)$ ) by a simple dependence in  $D^{-\alpha}$ , where Angstrom exponent ( $\alpha$ ) is generally between 2 and 3 and  $D$  is limited to vary between two radii  $D_1$  and  $D_2$  (Boucher, 2015).

If  $N$  is the total aerosol concentration the Junge law can be expressed as:



$$n * (D) = N \frac{\alpha D_1^\alpha D_2^\alpha}{D_2^\alpha - D_1^\alpha} D^{-\alpha} \quad (1.3)$$

It can explain the spectral dependence of aerosol light scattering properly but can't explain for the size distribution to small sizes ( $r < 0.1 \mu\text{m}$ ) and describe a multimodal size distribution.

A modified Gamma law can describe a large number of actual size distributions through a rather large number of fitting parameters (Boucher, 2015).

$$n(D) = \frac{N \beta^{\alpha+1}}{\Gamma(\alpha+1)} D^\alpha \exp(-\beta D) \quad (1.4)$$

where  $\alpha$  and  $\beta$  are Angstrom exponents and,  $\gamma$  is the mathematical Gamma function that generalizes the factorial operator to real numbers.

The Log-normal distribution function is one of the most popular mathematical functions for describing the distribution of atmospheric aerosol which gives a more precise match to experimental data that can be applied in atmospheric particles. For this, common form of unimodal distribution expressed in log base 10 is given by, Seinfeld & Pandis, (2006).

$$n(\log D) = \frac{N}{\sqrt{2\pi} \log \sigma} \exp\left(-\frac{\log^2(D/\bar{D})}{2\log^2 \sigma}\right) \quad (1.5)$$

where  $N$  is the particle number concentration with a maximum at mean diameter  $\bar{D}$ , and  $\sigma$  quantifies the width of distribution.

Hobbs, (1993) explained the sum of  $j$  log-normal size distributions as poly-modal distribution given by ;

$$n(\log D) = \sum_{i=1}^j \frac{N_i}{\sqrt{2\pi} \log \sigma_i} \exp\left(-\frac{\log^2(D/\bar{D}_i)}{2\log^2 \sigma_i}\right) \quad (1.6)$$

Here  $\bar{D}_i$  is the median diameter and  $\sigma_i$  is the standard deviation of  $i$ th log-normal mode.

Due to the dependence of aerosol optical properties on particle surface area and volume distributions, it is necessary to express the size distribution in terms of surface area and volume.

When the aerosol surface area density is  $n_s(D)$ , the  $n_s(D) dD$  is the average size of the aerosol particles per cubic meter of air that have diameters between  $D$  and  $D + dD$ .

Assuming that all particles are spherical with surface area  $\pi D^2$  and have the same diameter  $D$  in this infinitesimally narrow size range, then we can write,

$$n_S(D) = \pi D^2 n_N(D) \quad (1.7)$$

Here  $n_S(D)$  is in  $\mu\text{m cm}^{-3}$

Hence the total surface area  $S$  of the aerosol particles per  $\text{cm}^3$  of air is given by,

$$S = \pi \int D^2 n_N(D) dD = n_S(D) dD \quad (1.8)$$

Here  $S$  is in  $\mu\text{m}^2 \text{cm}^{-3}$ .

In a similar manner volume distribution  $n_V(D)$  can be expressed as,

$$n_V(D) = \pi D^3 n_N(D)/6 \quad (1.9)$$

Here  $n_V(D)$  is in  $\mu\text{m}^3 \text{cm}^{-3}$ .

And the total aerosol volume  $V$  per  $\text{cm}^3$  of the air is given by,

$$V = \pi/6 \int D^3 n_N(D) dD = n_V(D) dD \quad (1.10)$$

Here  $V$  is in  $\mu\text{m}^3 \text{cm}^{-3}$ .

Additionally, the Volume Size Distribution has a significant role in the radiation budget by directly interacting with it (Pillai & Moorthy, 2004).

In terms of log-normal function volume size distribution can be expressed as,

$$n_V(\ln(D)) = dV/d \ln(D) = \frac{C_V}{\sqrt{2\pi} \ln \sigma_g} \exp\left(-\frac{\ln^2(D/D_V)}{2 \ln^2(\sigma_g)}\right)$$

Here  $D_V$  is the volume median diameter and  $\sigma_g$  is geometric standard deviation.

$$\ln D_V = \frac{\int \ln D \frac{dV}{d(\ln D)} d(\ln D)}{\int \frac{dV}{d(\ln D)} d(\ln D)} \quad (1.11)$$

$\sigma_V$  is the standard deviation from volume median diameter.

$$\sigma_V = \sqrt{\frac{\int (\ln D - \ln D_V)^2 \frac{dV}{d(\ln D)} d(\ln D)}{\int \frac{dV}{d(\ln D)} d(\ln D)}} \quad (1.12)$$

$C_V$  is the volume concentration.

$$C_V = \int \frac{dV}{d(\ln D)} d(\ln D) \quad (1.13)$$

For j modes volume size distribution is given by,

$$n_V(\ln(D)) = dV/d(\ln D) = \sum_{i=1}^j \frac{c_V^i}{\sqrt{2\pi} \ln \sigma_g^i} \exp\left(-\frac{\ln^2(D/D_g^i)}{2 \ln^2(\sigma_g^i)}\right) \quad (1.14)$$

### 1.1.2.2 Effective Radius

Effective radius of aerosol particles is one of the very important parameters in the study of radiative transfer and microphysical properties. Since the scattering and absorbing of the solar radiation depends upon the particle size, the knowledge of its dependence gives a better idea to understand the earth's climate system.

$$r_{eff} = \frac{\int_{r_{min}}^{r_{max}} r^3 \frac{dN(r)}{d \ln r} d \ln r}{\int_{r_{min}}^{r_{max}} r^2 \frac{dN(r)}{d \ln r} d \ln r} \quad (1.15)$$

### 1.1.3 Aerosol Optical Properties

When particles are exposed to radiation, their electric charges are excited and set into an oscillatory motion. As the electric charges are excited, they reradiate energy in all directions, resulting in a process called scattering and absorption, which increases the thermal energy of the system. The aerosol optical properties are determined by how light is scattered and absorbed when incident on aerosols. Aerosol extinction ( $Q_{ext}$ ) is the amount of radiation that is scattered ( $Q_{sca}$ ) and absorbed ( $Q_{abs}$ ) by aerosols and is given as,

$$Q_{ext} = Q_{sca} + Q_{abs} \quad (1.16)$$

Aerosol optical properties can be represented using several parameters. The most basic parameter is aerosol optical depth  $\tau(\lambda)$  at a wavelength  $\lambda$ , which is given by,

$$\tau = \int \sigma \rho dx \quad (1.17)$$

where  $\sigma$  is the mass extinction cross-section of the matter contained within the path length  $dx$ , and  $\rho$  is the density of the attenuator present along  $dx$ . In general, optical depth decreases exponentially with radiation intensity. If initial intensity of radiation is

$I_0(\lambda)$  that travels a thickness  $dx$  with an optical depth ( $\tau$ ), then final intensity ( $I$ ) is given by Beer-Lambert law,

$$I(\lambda) = I_0(\lambda) e^{-\tau} \quad (1.18)$$

Since  $\tau$  depends upon wavelength and number density of the attenuator, total attenuation of radiation is obtained by taking into account all types of attenuators. Hence

$$\tau(\lambda) = \tau_{\text{Rayleigh}}(\lambda) + \tau_{\text{Ozone}}(\lambda) + \tau_{\text{aerosol}}(\lambda) + \tau_{\text{cloud}}(\lambda)$$

where  $\tau_{\text{Rayleigh}}(\lambda)$ ,  $\tau_{\text{Ozone}}(\lambda)$ ,  $\tau_{\text{aerosol}}(\lambda)$  and  $\tau_{\text{cloud}}(\lambda)$  are the optical depths due to fine particles, ozone, aerosols and clouds present in the medium respectively (Bhattacharai et al., 2006; Holben et al., 1998b).

### 1.1.3.1 Phase Function:

The angular distribution due to scattered radiation is described by the phase function. It is a dimensionless quantity and described as normalized scattering function. In the case of a spherical particle, it depends only on the scattering angle. The phase function  $P(\theta)$  is normalized to 2 by the relation (Boucher, 2015).

$$\int_0^\pi P(\theta) \sin\theta d\theta = 2. \quad (1.19)$$

Where  $\theta$  is scattering angle between the directions of propagation of the incident and scattered beams.

If phase function is defined as the function of cosine of scattering angle,  $\mu = \cos \theta$  then, above equation can be written as,

$$\int_{-1}^1 P(\mu) d\mu = 2 \quad (1.20)$$

### 1.1.3.2 Asymmetry Parameter

Asymmetry parameter ( $g$ ) measures the degree of symmetry between forward and backward hemispheres of the first order moment of phase function ( $P$ )

$$g = \int_{-1}^1 P(\mu) \mu d\mu \quad (1.21)$$

- i) For  $g = 1$ , all the scattered radiation in the forward direction;

ii) For  $g = -1$ , all the scattered radiation in the backward direction;

iii) For  $g = 0$ , forward scattering is equal to backward scattering.

### 1.1.3.3 Refractive Index

The interaction of aerosols with light is governed by their refractive index which is defined by the ratio of the speed of light in vacuum to its speed in medium. The refractive index affects the scattering and absorption of light by aerosols, which in turn affects visibility and climate. For instance, the refractive index of dust particles in the atmosphere affects the way sunlight is scattered, which can lead to changes in temperature and precipitation patterns (Kokhanovsky et al., 2017). The complex refractive index is expressed as:

$$m = n + i k \quad (1.22)$$

where  $n$  is the real part of the refractive index, which represents the speed of light in the medium, and  $k$  is the imaginary part of the refractive index, which represents the absorption of light by the medium. Different aerosol particles have varied complex refractive indices depending upon the chemical makeup of the aerosol and wavelength of the light.

### 1.1.3.4 Single Scattering Albedo

The ratio of scattering to the extinction of light radiation is defined as single scattering albedo ( $\omega_0$ ). It is a dimensionless quantity that explains the probability of scattering a photon after interaction with an aerosol particle, which is given by:

$$\omega_0 = \frac{Q_{sca}}{Q_{ext}} = \frac{\tau_{sca}}{\tau_{sca} + \tau_{abs}} \quad (1.23)$$

where,  $\tau_{sca}$  and  $\tau_{abs}$  are the aerosol scattering and absorption optical depths.

From equation (1.23) if,  $\omega_0 = 1$ , the probability of scattering is 100% and absorption is zero. And if,  $\omega_0 = 0.5$ , then both the scattering and absorption have equal probabilities.

### 1.1.4 Atmospheric Solar Heating Rate

Atmospheric gases absorb solar radiation causing heating in the atmosphere that suffers multiple scattering. To understand this, let us consider a plane parallel absorbing and

scattering atmosphere. When spectral radiation of intensity  $F_{\odot}$  is incident on the top of the atmosphere, then the downward flux density normal to it is given by  $\mu_0 F_{\odot}$ . Let the spectral downward and upward flux densities centered at wavelength  $\lambda$  be denoted by  $F_{\downarrow}$  and  $F_{\uparrow}$  respectively as shown in Figure 3, then the net downward flux density at a given height  $z$  is defined by (Liou, 2002).

$$F(z) = F_{\downarrow}(z) - F_{\uparrow}(z). \quad (1.24)$$

The loss of flux density from upper layers to lower layers is given by the net flux density divergence for the differential layer,

$$\Delta F(z) = F(z) - F(z + \Delta z). \quad (1.25)$$

Here  $\Delta z$  is the differential thickness within the atmosphere.

According to the energy conservation principle, the energy absorbed must be equivalent to the rise in layer heat. As a result, the rate of temperature change can be used to express how much an air layer is heated as a result of radiation transfer.

$$\Delta F(z) = -\rho C_p \Delta z \frac{\partial T}{\partial t} \quad (1.26)$$

Here  $\rho$  is the density of air in the layer,  $C_p$  is specific heat at constant pressure, and  $t$  is the time.

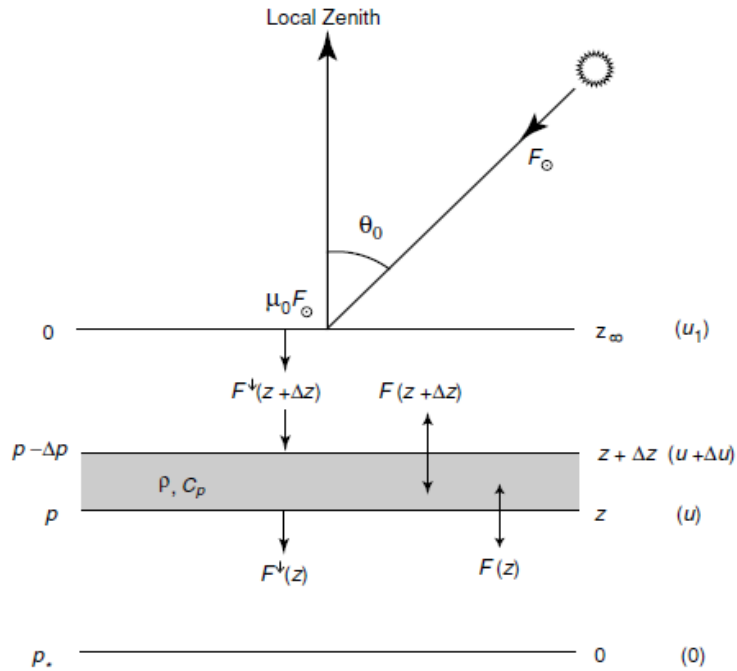


**Figure 3:** Schematic diagram to show total flux density along  $z$ ,  $\rho$  and  $u$  coordinates (Liou, 2002).

The heating rate for a differential layer  $\Delta z$  is given by,

$$\frac{\partial T}{\partial t} = - \frac{1}{\rho C_p} \frac{\Delta F(z)}{\Delta z} \quad (1.27)$$

Aerosol particles can, directly and indirectly, affect the ground level UV irradiances. The direct impact of blocking UV radiation is absorption and scattering. The aerosol also contributes indirectly by acting as cloud condensation nuclei and forming clouds, blocking the transmission of UV radiation to Earth. Liou et al., (1991), have estimated the variation of solar irradiance in the UV range (280 nm-315 nm) based on aerosol concentration.

This study of solar UV radiation is dramatically increased after the discovery of declines in global concentration of the thin ozone layer over the Antarctic. Despite this, much effort has been made to study the effects of increased UV on the surface of the earth (Bhattarai et al., 2007).

## **1.2 Fundamentals of Solar Radiation**

Global solar radiation consists of diffuse and direct solar radiation. The atmosphere diffuses solar radiation through aerosols, water vapor, molecules of air, and clouds. Moreover, direct beam solar radiation reaches the Earth's surface without being diffused. Our study focuses on the impact of aerosols on solar radiation. The significant factors that affect solar radiation and the methods used to measure it are outlined below:

### **1.2.1 Solar Zenith Angle (SZA)**

Solar Zenith Angle (SZA) is the sun's angle with the zenith at the observation point, which indicates where the sun is at any given time. The amount of solar radiation reaching the earth's surface varies with time. Besides this, many other factors affect radiation levels on the ground (Dahlback, 1996; Duffie & Beckman, 2013; Madronich, 1993). With an increasing SZA, a horizontal surface on earth experiences a decrease in radiation intensity. It occurs because incident radiation is proportional to the cosine of the angle between the beam radiations and normal to the surface, resulting in the cosine effect, and the relative path length of the beam increases as the sun descends in the sky (Kerr, 2005).

### **1.2.2 Atmospheric Ozone**

Although having a very low atmospheric concentration, ozone is essential to human survival. Around 90% of the ozone in the atmosphere is present in the stratosphere. This layer is located between 16 and 48 km in altitude (Barnes & Mauersberger, 1987). Below than the stratospheric layer, in the troposphere, is where the remaining ozone is located. The term "good ozone" refers to stratospheric ozone, which filters out some of the sun's physiologically hazardous UV rays.

On the other hand, ozone that is close to the surface is a dangerous air contaminant. Hence, it harms all living things. Ozone molecules significantly reduce the UVB wavelengths of sun light by several orders of magnitude (290-315 nm). Molina & Molina, (1986) claim that the scattering cross-section is temperature dependent.

### **1.2.3 Cloud**

The attenuation of solar radiation by clouds depends on the wavelength (Seckmeyer et al., 1996). Cumulonimbus clouds reduce solar radiation received at the surface. Solar radiation changes nonlinearly with cloud cover. The effectiveness of scattering from the sides of the cloud can increase by up to 25 percent, however, when the sun is not obscured by the cloud (Kylling et al., 2000; Sabburg & Wong, 2000). In addition, a broken cloud complicates the comparison of ground-based and satellite measurements of surface irradiance estimation.

### **1.2.4 Albedo**

The surface albedo is the amount of solar radiation that is reflected into the atmosphere when it falls on the earth's surface. In some cases, reflected radiation is re-reflected to the surface of the earth due to aerosols in the atmosphere, causing multiple reflections between the earth's surface and the atmosphere. As a result, the earth's surface receives more radiation. In quantitative terms, surface albedo coefficient is the ratio of upward spectral irradiance to downward global irradiance. Its coefficient ranges from 0 to 1, and a value of 1 indicates that all downward global radiation is reflected. According to Blumthaler et al., (1994), only spectral albedo is affected by wavelength and surface type for the visible range. Most rough soils have a smaller albedo coefficient in the UV range than in the visible range, whereas grassland behaves differently (McKenzie et al., 1996). Snow's effect on UV radiation has been demonstrated by Fioletov et al., (2002)



based on satellite measurements. The study shows that the albedo coefficient for fresh snow is 0.8 in the visible region and 0.9 in the UV region.

### **1.2.5 Altitude**

Global solar radiation is significantly affected by altitude (Blumthaler et al., 1997; Poudyal et al., 2010). In the atmosphere and on snow-covered surfaces, solar radiation increases with altitude due to the reduction in air molecules, ozone, aerosols, and clouds. Therefore, there are several factors that determine dependence. WMO, (2002) suggests that solar radiation at higher altitudes is dependent on SZA and wavelength changes. Also, a large portion of the population lives at altitudes of up to a few kilometers above the sea level and cause the different atmospheric pollutions at different altitudes. Altitude effect refers to the increase in solar radiation flux with height. Accordingly, the higher altitudes also have a greater altitude effect relative to valley sites because more turbidity per km increases as altitude increases.

### **1.3 Objectives of the Study**

In this thesis, we present results from comparing various aerosol optical and physical properties obtained at various places in Nepal, such as Kathmandu, Lumbini, Pokhara, Langtang, and the Himalayan site EVK2-CNR Pyramid at 5079 m asl (above sea level) which are part of National Aeronautics and Space Administration (NASA) based Aerosol Robotic Network (AERONET) (<http://aeronet.org>). Additionally, we examine aerosol characteristics at the surface level and the column-integrated satellite-based MODIS aerosol optical depth. Aerosol optical depth, Angstrom Exponents, and aerosol inversion product single scattering albedo are used for comparing and analyzing to represent the aerosol characteristics over Nepal. Mie scattering theory is applied to calculate the aerosol optical depth of size-segregated aerosols. The Mie scattering calculation was conducted using Fortran-95 code and input parameters obtained from aerosol inversion products from the AERONET website, which included aerosol size distribution and refractive indices values. PurpleAir monitors, which contain two Plan-tower PMS 5003 sensors, monitor particulate matters of less than 1 micron ( $PM_1$ ), 2.5 microns ( $PM_{2.5}$ ), and 10 microns ( $PM_{10}$ ). We installed PurpleAir monitors in Pulchowk and Pokhara for 2020-2021 and obtained particle concentrations and meteorological data from its website. As part of this thesis, we also present the global solar radiation

(GSR) measurement at the horizontal surface. This thesis's methodology (chapter 3) and results section (chapter 4) discuss detailed measurement techniques and results. In summary, the main objective of this research is to analyze fundamental physical and optical properties of aerosols and investigate their trend of impact on global solar radiation in Nepal by using various instruments and mathematical techniques and mainly we list them as,

### **Specific Objectives**

- To compare the ground-based aerosol concentrations with satellite-based aerosol optical data.
- To analyze the variation trend and impact of aerosols on global solar radiation
- To study the seasonal and altitude variation of Aerosols in different parts of Nepal.

### **1.4 Outline of Thesis**

The thesis is focused in the study of aerosol physical and optical properties over Nepal. Various direct and indirect impacts of aerosols on solar radiation and finally to atmosphere is studied and presented. It is organized in different chapters as follows,

Chapter 1: This chapter discusses the basics of aerosols, their types, sources, size, physical and optical properties to study the impact on solar radiation and hence on atmospheric variations.

Chapter 2: It is focused to review the literature on impact of aerosols in local, regional and global scale to identify their pattern and to identify the research gap.

Chapter 3: It describes the various devices for the measurement of aerosol properties, particulate matter concentration and theory involved to explain them.

Chapter 4: The results obtained from the research work has been interpreted and discussed with necessary validation from previous works is presented in this chapter.

Chapter 5: This chapter describes the conclusion and future recommendations of the research work.

Chapter 6: It gives a brief summary of the results obtained from the research work.

## CHAPTER 2

### LITERATURE REVIEW

#### 2.1 Review of Articles

We know aerosols significantly influence the Earth's climate directly by scattering and absorbing the solar and terrestrial radiations and indirectly by modifying the cloud macro- and micro-physical properties. Even though aerosols make up less than one billionth of the total mass of the atmosphere, they have a significant impact on how radiation is transmitted through the atmosphere. Urban aerosols have a significant impact on the extinction of solar radiation on a local scale, but they also have an impact on atmospheric long-wave radiation, which is crucial for the local energy balance. Because of this, understanding aerosols is crucial for understanding both the current climate and potential future climate change. The volume, nature, characteristics, and effects of aerosols vary significantly depending on location and time of day, which is a very intriguing fact. Therefore, there is still a great deal of uncertainty in the identification and forecasting of aerosol features and effects.

Several researches have studied the microphysical properties and aerosol optical depth (AOD) of different background aerosols (Boucher, 2015; Holben et al., 2001; Moody et al., 2014; Poudyal et al., 2012). The review paper by Liu et al., (2014), presents that aerosol optical properties are crucial for understanding aerosols' impact on climate since aerosol radiative effects can be positive (warming effect) or negative (cooling effect). It has been reported by Myhre & Shindell, (2013) and other investigators that atmospheric aerosols influence Earth's atmospheric radiation budget due to their direct scattering and absorption properties (Papadimas et al., 2012). Tripathi et al., (2007) examine the aerosol effect on the climate over the Indo-Gangetic plain, a northern India region, including the southern Terai region of Nepal. Xu et al., (2014) presented aerosols' physical, chemical, and optical properties in Himalayan sites of China and Nepal. This study shows that the aerosol optical properties in the Himalayan Mountains fluctuate over the seasons and are associated with air pollution over south Asia, indicating long-range transport of air pollution.

Similarly, some studies have examined the chemical composition of Himalayan aerosols (Bonasoni et al., 2008; Guo et al., 2017; Mahapatra et al., 2019; Sellegri et al., 2010; S. Shrestha et al., 2017; Tripathee et al., 2016; Wan et al., 2017). Cho et al., (2017) reported a cluster of high aerosol concentrations which occurred during the pre-monsoon season, a period in which distinct seasonal variations are closely related to regional-scale monsoon circulations over South Asia and emissions in the Kathmandu Valley. Based on our review of previous publications on aerosol dynamics in Nepal, we see that long-term aerosol datasets at the surface level and in the atmospheric-column is still needed to understand Nepal's air pollution and aerosol characteristics. Through a detailed analysis of the seasonal variations in aerosol transport across Nepal, we can comprehensively understand aerosols at multiple spatial and temporal scales over the atmosphere of Nepal. Over the different locations in Nepal, studying the temporal variations of aerosol concentration and aerosol optical properties will provide more accurate information about the overall air pollution sources. A long-term aerosol research from various locations will provide insight into regional aerosols reaching the foothills of the Himalayas and remote locations in the high Himalayas of Nepal. A few studies have examined the air quality and aerosol loading trends previously in Kathmandu indicate that mountains often block local emissions generated by horizontal winds in cities surrounded by mountains (Aryal et al., 2009; Islam et al., 2020; Mahapatra et al., 2019; Panday & Prinn, 2009). Therefore, various studies of the optical properties of aerosols at different stations support learning how they are affected by air pollution and the impact of transboundary air pollution over Nepal.

Aerosol optical measurements, such as the Sun Photometer within AERONET, have been used in many studies to analyze the characteristics of aerosols in different parts of the country (Adhikari & Mejia, 2022; Bhattarai et al., 2019; Bonasoni et al., 2008, 2010; Dhungel et al., 2018; Dumka et al., 2014; Gautam et al., 2011; Putero et al., 2018; Rai et al., 2019; Ramachandran et al., 2020; Ramachandran & Rupakheti, 2020; Regmi et al., 2020, 2021; Regmi, Poudyal, Pokhrel, Barinelli, & Aryal, 2019; Rupakheti et al., 2017; Rupakheti, Kang, Cong, et al., 2018a; Sellegri et al., 2010; Shrestha et al., 2020; Singh et al., 2019; Wan et al., 2017; C. Xu et al., 2014). Some studies have also examined atmospheric compounds and pollution levels in the Kathmandu valley (Aryal et al., 2009; Cho et al., 2017; Islam et al., 2020; Kim et al., 2015; Mahapatra et al., 2019; Panday & Prinn, 2009; Sarkar et al., 2017). Despite this, there have not been any

studies or publications comparing aerosol optical properties with the microphysical characteristics of the atmosphere over the different locations in Nepal.

Satellites provide information on the spatiotemporal characteristics of aerosols, and study reveals that the instruments cannot provide an in-depth picture of aerosol properties at a regional scale and are subject to significant uncertainties compared to ground-based instruments (El-Metwally et al., 2011). A comparison of Satellite-based aerosol optical data and ground-based aerosol measurement can provide information about the reliability of remote sensing data. As a result of all the above observations, observing aerosols over Nepal's various locations and comparing surface level and column integrated aerosol characteristics is very important to determine the effect of temporal variations of aerosols on total solar radiation at a regional scale. Comparing surface level and column-integrated aerosol characteristics will give a clear picture while studying the climatology of Nepal.

## **2.2 Statement of Problem**

The northern Himalayan location and dense population of the southern Indo-Gangetic plain of Nepal make it important to study aerosol characteristics in Nepal to determine the source of air pollution. Variations in topography and atmospheric conditions affect solar radiation reaching the ground. There is a significant difference in altitude between 60.0 and 8848.86 meters, along with differential temperatures of 45° Celsius. Kathmandu city is a bowl-shaped valley surrounded by mountains in Nepal's capital. Several other cities with large populations, such as Pokhara, are pollution pathways to the Himalayas. Located on the Indo-Gangetic Plain and with severe air pollution, Lumbini is also an important place to study mixed atmospheric pollution in Nepal and compare it to other cities (Chen et al., 2016; Rupakheti et al., 2017; Rupakheti, Kang, Rupakheti, et al., 2018; Wan et al., 2017). In larger cities, low visibility is becoming a challenging problem of urban atmospheric pollution. Besides scattering and absorbing solar radiation, particle, and gaseous pollutants also negatively affect visibility (Gautam et al., 2013; Gautam et al., 2011; Han et al., 2012; Latha & Badarinath, 2004; Saikawa et al., 2019). In addition to direct measurements of solar radiation at multiple locations in Nepal, long-term analyses of aerosol optical properties and long-range transport of aerosols will significantly impact Nepal's climate. Previous studies report the significant impacts of transportation of dust aerosols on the cloud microphysical

properties. Basically, biomass burning and dust storms in IGP region gets transported to the southern slopes of Himalayas to contribute aerosol loading which on mixing with local pollution sources increases the pollution to a high level (Adhikari & Mejia, 2022; Becker et al., 2021b; Dumka et al., 2014; Jethva et al., 2019; Ng et al., 2017)(Khanal et al., 2022; Das et al. 2020). The impact of transboundary aerosols on Himalayas is of rising concern to study the pattern of climate change(Adhikari & Mejia, 2022; Bonasoni et al., 2010; Chatterjee et al., 2012; Gautam et al., 2013; Gautam et al., 2011; Lüthi et al., 2015; Putero et al., 2018; Rupakheti, Kang, Cong, et al., 2018a; C. Xu et al., 2014). Thus, it is necessary to examine temporal and spatial aerosol properties, surface and column aerosol properties, long-term aerosol optical data, and transboundary aerosols.

### **2.3 Research Gap**

Investigation of temporal and spatial aerosol properties, surface and column aerosol properties, long-term aerosol optical data, and transboundary aerosols is essential for understanding atmospheric behavior, radiation budget, climate pattern, and pollution level of a region.

- long-term data are not available
- study is focused only in limited places.
- comparison and validation of different levels of data (surface, ground level and satellite) is lacking in this region.
- source of origin of Transboundary aerosol analysis is missing.

## CHAPTER 3

### MATERIALS AND METHODS

This section will discuss various techniques we have implemented to study the overall characteristics of aerosols in the atmosphere in Nepal. The main observation techniques, the mathematical techniques for analyzing the aerosol optical properties, and the various observation sites of Nepal covering the regional and geographical areas are mainly presented in this section. As part of this study, we used aerosol direct and inversion products from the Aerosol Robotic Network, a NASA-based observation that studies aerosol optical and microphysical properties. Our surface-level and column-integrated aerosol data analysis includes MODIS satellite measurements, CMP6 Pyranometer, and PurpleAir sensors. As a result of using NASA's remote sensing data, we have analyzed the surface-to-column integrated observations to determine the optical and microphysical characteristics of aerosols. This methodology uses the Mie theory to calculate the atmospheric extinction of solar radiation, and we used cluster analysis to study long-range aerosol transport analyzed based on air mass back trajectories.

#### 3.1 Aerosol Robotic Network (AERONET)

The Aerosol Robotic Network (AERONET) is a ground based-observation network established by NASA (National Aeronautics and Space Administration). It aims to monitor the global characteristics of atmospheric aerosols. Through a robotic Cimel Sun Photometer, the program collects data from more than 800 stations across the globe. The system is widely used for aerosol research and characterization, satellite product verification, and data synchronization (<https://aeronet.gfsc.nasa.gov>). AERONET measures in different spectral bands between 340 nm and 1020 nm every 15 minutes. In our calculations, level 2 and version 3 data have been used except for the Jomsom inversion, which uses level 1.5 (cloud-screened) data. The inversion product includes single scattering albedo, size distribution, phase functions, and complex index of refraction. In version 3, sphericity, radiative forcing, and spectral flux are also included.

### 3.1.1 Cimel Sun Photometer

The CIMEL Sun photometer is a multi-channel, automatic sun-and-sky scanning radiometer that measures the direct solar irradiance and diffuse-sky radiance at the Earth's surface. It works on the principle of Beer-Lambert-Bouguer law and calculates the total aerosol load in the atmosphere. It has a 1.2-degree field of view and two detectors for measuring sun and sky radiances. It is an active sun-tracking device in which the position of the sensor head is adjusted by internal calculation based on time, latitude, and longitude. It can be powered by solar panels in remote areas for full automation. The data recorded is possible to send via satellite. It points directly at the Sun during day time in every 15 minutes. The spectral data recorded undergoes cloud-screening algorithm to limit the variability within the triplet data (Smirnov et al., 2000). Spectral de-convolution algorithm is used to compute AE, coarse-mode, and fine-mode contributions (O'Neill et al., 2001).



**Figure 4:** CIMEL Sun Photometer Deployed in AERONET Stations (Gregory, 2011).

During the day, the sun photometer records direct solar radiances at wavelengths of 0.34  $\mu\text{m}$ , 0.38  $\mu\text{m}$ , 0.44  $\mu\text{m}$ , 0.50  $\mu\text{m}$ , 0.675  $\mu\text{m}$ , 0.87  $\mu\text{m}$ , 1.02  $\mu\text{m}$ , and 1.64  $\mu\text{m}$ . Direct spectral data are corrected for Rayleigh scattering, ozone absorption, and gaseous



components to determine the aerosol optical depth ( $\tau_{\text{AOD}}$ ) (Holben et al., 1998a, 2006). It also measures diffuse sky radiance at four different wavelengths 0.44  $\mu\text{m}$ , 0.675  $\mu\text{m}$ , 0.87  $\mu\text{m}$ , and 1.02  $\mu\text{m}$  (Dubovik & King, 2000; Holben et al., 2001, 2006). These measurements are used to retrieve aerosol inversion products, like single scattering albedo, size parameters, volume size distribution. It gives three different types of data quality levels, Level 1.0 (unscreened), Level 1.5 (cloud screened), and Level 2.0 (cloud-screened and quality-assured) (Dubovik & King, 2000; Holben et al., 2006). Level 2.0 data is made available after the instrument is returned to NASA during annual swap outs. All the AERONET products are automatically computed and uploaded on the AERONET website (<http://aeronet.gsfc.nasa.gov/>). For the calculation of direct normal solar irradiance ( $E$ ) at the surface at a given wavelength is given by Bouguer's law,

$$E = \left(\frac{E_0}{R^2}\right) \exp(-m \tau_\lambda) \quad (3.1)$$

where  $E_0$  is the extra-terrestrial solar irradiance at a distance of one astronomical Unit (AU),  $R$  is the sun-earth distance in AU at the time of measurement,  $m$  is the optical air mass, and  $\tau_\lambda$  is the total vertical optical thickness (Gregory, 2011).

If the instrument voltage is  $V$  for irradiance  $E$ , the above equation can be written as,

$$V = \left(\frac{V_0}{R^2}\right) \exp(-m \tau_\lambda) \quad (3.2)$$

Where,  $V_0$  is the calibration coefficient

The uncertainty in computed AOD is found to be wavelength dependent and is larger in the UV zone and is estimated to vary from  $\pm 0.01$  to  $\pm 0.02$  (Dubovik & King, 2000; Holben et al., 1998a; S. Kim et al., 2007).

### 3.1.2 Attenuation of Direct Solar Radiation:

The simple formulations describe attenuation of direct radiation by various atmospheric constituents. An algorithm is presented by which direct and diffuse spectral radiation arriving on the ground can be easily measured or computed. The equations are designed to permit the atmospheric parameters such as ozone layer thickness, aerosols, turbidity, and ground-level albedo to be varied independently.

When solar radiation enters the earth's atmosphere, a few portions of the incident light energy is removed by scattering and by absorption. The scattered radiation is called

diffuse radiation. A portion of this diffuse radiation goes back to space, and a portion reaches the ground. Both influence the extra-terrestrial spectrum by significantly modifying the spectral energy passing through the atmosphere. The radiation arriving on the ground directly in the line from the solar disk is called direct or beam radiation. The spectral irradiance (direct and diffuse) arriving at the earth's surface is very important designing solar energy applications (Iqbal, 1983).

Attenuation is the difference between the radiation's energy before and after the encounter. Attenuation includes two processes that involve the absorption and scattering of light. The interaction between radiation and matter is influenced by both the radiation's wavelength and the physical characteristics of the particle involved. It is well recognized that a location with many of these attenuators has the potential for greater attenuation.

### 3.1.3 Aerosol Optical Depth (AOD)

The quantitative measurement of extinction of solar radiation due to scattering and absorption of aerosol particles is defined as aerosol optical depth. Angstrom's parameters,  $\alpha$  and  $\beta$  (Ångström, 1961), are related to AOD as,

$$\tau_{\text{AOD}}(\lambda) = \beta \lambda^{-\alpha} \quad (3.3)$$

$\alpha$  in Eq. (3.3) is the wavelength exponent which represents aerosol size distribution in the atmosphere. And  $\beta$  is the turbidity coefficient that gives the aerosol number concentration in vertical column of the atmosphere. Normally value of  $\alpha$  is 1.3 but may vary from 0 to 4. The larger value indicates higher ratio of small to coarse particles and smaller value means just opposite.

At a wavelength,  $\lambda = 1 \mu\text{m}$ , we have

$$\tau_{\text{AOD}}(\lambda) = \beta. \quad (3.4)$$

On taking log of equation (3.3), we get,

$$\ln \tau_{\text{AOD}}(\lambda) = \ln \beta - \alpha \ln \lambda \quad (3.5)$$

It gives the values of Angstrom's parameters  $\alpha$  and  $\beta$ , with uncertainty, from least square analysis. The turbidity parameter,  $\beta$ , depends on the concentration of aerosols over the atmosphere. The value of  $\beta$  may vary from 0.0 to 0.5. Clean atmosphere is indicated by

the value of  $\beta$  less than 0.1 and is hazy if the value of  $\beta$  is greater than this. The higher values of  $\beta$  means the higher amount of aerosol present in the atmosphere (Iqbal, 1983). From Eq. (3.5), the negative of the slope of  $\tau_{\text{AOD}}$  with wavelength in logarithmic scale is the angstrom exponent ( $\alpha$ ).

From Eq. (3.5), we can write (also known as Volz method),

$$\alpha = -\frac{d \ln(\tau_{\text{AOD}}(\lambda))}{d(\ln \lambda)} = -\frac{\ln(\tau_{\text{AOD}}(\lambda_2)) / \tau_{\text{AOD}}(\lambda_1)}{\ln(\lambda_2) / \ln(\lambda_1)} \quad (3.6)$$

Where  $\tau_{\text{AOD}}(\lambda_1)$  and  $\tau_{\text{AOD}}(\lambda_2)$  are AODs at wavelengths  $\lambda_1$  and  $\lambda_2$ . The deviation of observed data from linear fit line (Eq. 3.5) will be verified by second order polynomial fit for  $\tau_{\text{AOD}}$  spectra with coefficients of polynomial fit  $\alpha_2$ ,  $\alpha_1$ , and  $\alpha_0$ , which can be utilized to account for the curvature on spectral variation of  $\tau_{\text{AOD}}$  in logarithmic scale (Eck et al., 1999; King & Byrne, 1976). Prior studies have reported that same  $\alpha$  can be obtained from different aerosol size distribution, however, by using second order polynomial fit we can detect the differences (Schuster et al., 2006).

$$\ln \tau_{\text{AOD}}(\lambda) = \alpha_2 (\ln \lambda)^2 + \alpha_1 (\ln \lambda) + \alpha_0 \quad (3.7)$$

Here, we are presenting coefficient  $\alpha_2$  to display the curvature of  $\tau_{\text{AOD}}$  spectra in the logarithmic scale. The second derivative of log of  $\tau_{\text{AOD}}$  with respect to log of wavelength gives the measure of the rate of change of the slope with wavelength. It is obtained by using second order polynomial (Eq.3.7),

$$\alpha' = \frac{d\alpha}{d(\ln \lambda)} = -\frac{d}{d(\ln \lambda)} \left[ \frac{d(\ln \tau_{\text{AOD}}(\lambda))}{d(\ln \lambda)} \right] = -2\alpha_2 \quad (3.8)$$

Curve with  $\alpha_2 < 0$  and  $\alpha' > 0$  will be representing aerosol size distribution dominated by fine mode and with  $\alpha_2 > 0$  and  $\alpha' < 0$  will indicate size distribution dominated by the coarse mode (Eck et al., 2001; Reid et al., 1999).

Along with the analysis of spectral  $\tau_{\text{AOD}}$ , computation of Angstrom Exponent Parameter, the Spectral Single Scattering Albedo (SSA), Absorption Aerosol Optical Depth (AAOD), and Absorption Angstrom Exponent (AAE) are also presented in this study for analyzing aerosol types over the atmosphere (Aryal et al., 2014; Kaufman, 1993). The aerosol Single Scattering Albedo is the fraction of the aerosol light scattering over the extinction;

$$SSA(\omega) = \frac{\sigma_s}{\sigma_s + \sigma_a} \quad (3.9)$$

Where  $\sigma_s$  is aerosol scattering coefficient and  $\sigma_a$  is aerosol absorption coefficient.

Previously it has been illustrated that the significant presence of urban-industrial aerosols and biomass burning will develop a graph of a negative slope of SSA. i.e., the curve decreases with increasing wavelength, while the dust type of aerosols gives positive slope SSA increases with increasing wavelength (Mallet et al., 2013). Another important parameter, AAOD is also considered for detecting the absorbing type of aerosol, which contributing to the total attenuation of light. The dominant effect of scattering effect of aerosol on total aerosol optical depth can be linked with the absorption effect of aerosols by,

$$AAOD(\lambda) = AOD(\lambda) \times (1 - SSA(\lambda)) \quad (3.10)$$

This mathematical equation conveys the understanding of overall aerosol loading over the observation site with spectral SSA and AAOD.

Another striking feature of aerosol composition is exhibited by tapping spectral AAOD data and implementing power law,

$$AAOD = K\lambda^{-AAE} \quad (3.11)$$

In this study, we have implemented seasonal variability of AAE by using monthly mean AAOD spectra. There are various studies in aerosol climatology for identifying aerosol characteristics by using AAE values obtained from linear fit in log-log scale between AAOD and  $\lambda$  (Bergstrom et al., 2003).

### 3.2 CMP6 Pyranometer

The total solar radiation on a horizontal surface is measured using CMP6 first class Pyranometer. It is designed by Kipp and Zonen, The Netherlands. It is ISO 9060 certified device that consists of sixty-four thermocouple junction sensing elements. Quality of absorption and long-term stability is ensured by coating the sensing element with highly stable carbon based non-organic coating (<https://www.kippzonen.com/Product/12/CMP6-Pyranometer#>). It consists of double glass dome attached on a metal body along with sensor, sun shield and bubble level as shown in Figure 5. Whenever sunlight is incident on the Pyranometer sensors, thermoelectric

current is generated. The strength of the sunlight decides the strength of the current, which is used to measure the electromagnetic radiation of various wavelengths.

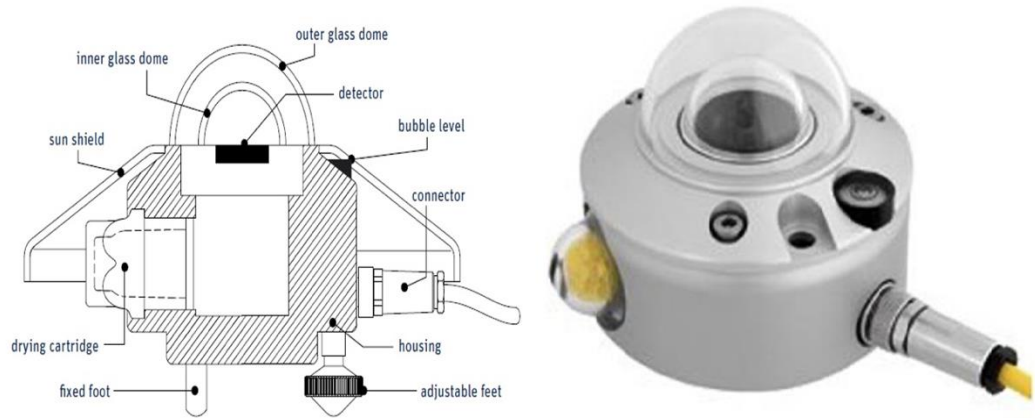


**Figure 5:** CMP6 - Pyranometer (Kipp and Zonen), 2019

The CMP6 first class Pyranometer has the operating temperature from  $-40^{\circ}\text{C}$  to  $80^{\circ}\text{C}$ . It has wide spectral range of measurement from 285 nm to 2800 nm. The sensitivity of instrument and field of view are  $5$  to  $20\ \mu\text{V}/\text{W}/\text{m}^2$  and  $180^{\circ}$  respectively. The response time of device is 18 seconds. In this instrument, the measuring data is recorded by LOGBOX SD data logger within a minute resolution for 24 hours. Its special features are low noise, high resolution and low power consumption. It works in all weather conditions. It collects the data at real time for the needs of meteorology and slow signal analysis. We can insert the SD memory card for long term data storage. For the communication LOGBOX uses either RS232 or RS485 communication port. According to Manual Enviro-data, (1982), the level of accuracy of the device is  $\pm 5\%$ .

### 3.2.1 Solar Geophysical parameters

In any location on the earth, the sun moves in a predictable trajectory. The geometric relationships between a plane of any particular orientation relative to the earth at any time, whether that plane is fixed or moving relative to the earth and the sun's position relative to that plane is shown in Figure 6.

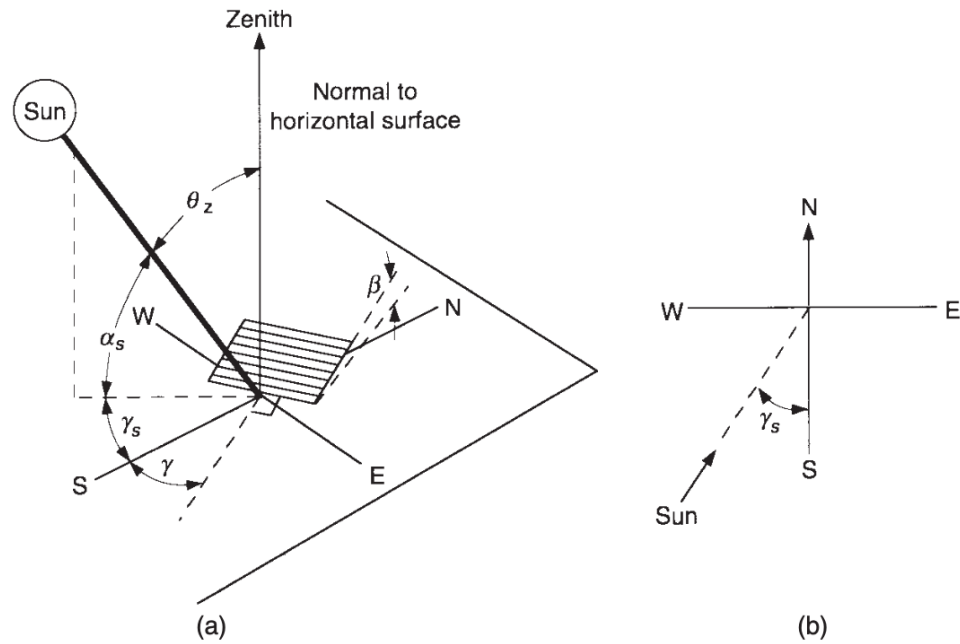


**Figure 6:** (a) Zenith angle, slope, surface azimuth angle, and solar azimuth angle for a titled surface and (b) Plane view showing solar azimuth angle (Duffie & Beckman, 2013).

**(a) Latitude ( $\phi$ )**

The angular location is the angle made by the radial line joining the given place to the center with the equator plane. It can vary from  $-90^\circ$  to  $+90^\circ$ . By convention, the latitude is positive for the northern hemisphere and negative for southern hemisphere.

**(b) Slope ( $\beta$ )**

It is an angle made by the plane surface with the horizontal. It varies from  $0^\circ$  to  $180^\circ$  surface.

**(c) The hour angle ( $\omega_z$ )**

It is the angular measure of time, is equivalent to  $15^\circ$  per hour. It varies from  $-180^\circ$  to  $180^\circ$ . The measuring time is adopted from noon based on the local solar time, being positive in the morning and negative in the afternoon.

**(d) Zenith Angle ( $\theta_z$ )**

It is the angle between the sun's ray and the perpendicular line to the horizontal plane. By convention, the displacement for east of south is negative, and west of south is positive.

**(e) Solar altitude angle ( $\alpha_s$ )**

It is an angle between the horizon and the line to the sun. This angle is the complement of the zenith angle.

**(f) Surface Azimuth Angle ( $\gamma$ )**

It is the angle in the horizontal plane, between the line due south and the horizontal projection of the sun's ray on the horizontal plane. It is taken as positive when measured from the south towards west. The ranges of angles are from  $-90^\circ$  to  $90^\circ$ .

**(g) Solar azimuth angle ( $\gamma_s$ )**

The angular displacement from south of the projection of beam radiation on the horizontal plane is shown in Figure 4. Displacements east of south are negative and west of south is positive.

**(h) Angle of Incidence ( $\theta$ )**

It is an angle formed between the incident sun's ray on a surface and the normal to that surface.

**(i) Declination ( $\delta$ )**

It is defined as the angular displacement of the sun from the plane of the earth's equator. It is positive when measured above the equatorial plane in the northern hemisphere. The declination can be determined from the equation (Duffie & Beckman, 2013).

$$\delta = 23.45 \sin\left(\frac{360}{365}(284 + n)\right) \quad (3.12)$$

Where n is the day of the year. The earth rotates about an axis which makes an angle of approximately  $66.5^\circ$  with the plane of its rotation around the sun. The declination angle varies from maximum value of  $+23.5^\circ$  on June 21 to a minimum value of  $-23.5^\circ$  on December 22.

Equations relating the angle of incidence of beam radiation on a surface ( $\theta$ ) to other parameters are

$$\begin{aligned} \cos\theta = \sin\delta \sin\phi \cos\beta - \sin\delta \cos\phi \sin\beta \cos\gamma + \cos\delta \cos\phi \cos\beta \cos\omega + \\ \cos\delta \sin\phi \sin\beta \cos\gamma \cos\omega + \cos\delta \sin\beta \sin\gamma \sin\omega \end{aligned} \quad (3.13)$$

And

$$\cos\theta = \cos\theta_z \cos\beta + \sin\theta_z \sin\beta \cos(\gamma_s - \gamma) \quad (3.14)$$

There are several commonly occurring cases for which equation (3.13) is simplified. For the fixed surfaces sloped toward the south or north that is with a surface azimuth angle, the surface azimuth angle  $\gamma$  of  $0^\circ$  or  $180^\circ$ , the last term drops out from equation (3.13). For vertical surfaces,  $\beta=90^\circ$ , the above equation becomes

$$\cos\theta = -\sin\delta \cos\phi \cos\gamma + \cos\delta \sin\phi \cos\gamma \cos\omega + \cos\delta \sin\gamma \sin\omega \quad (3.15)$$

For horizontal surfaces,  $\theta_z$  is zenith angle of sun. Its value must be between  $0^\circ$  and  $90^\circ$  when the sun is above the horizon. In this case  $\beta = 0$  and  $\theta$  tends to  $\theta_z$ , then the equation (3.13) becomes

$$\cos\theta_z = \cos\phi \cos\delta \cos\omega + \sin\phi \sin\delta \quad (3.16)$$

For a vertical surface facing due south,  $\gamma=0$  and  $\beta=90^\circ$ , then

$$\cos\theta = -\sin\delta \cos\phi + \cos\delta \cos\omega \sin\phi \quad (3.17)$$

Then, equation (3.16) can be solved for the sunset hour angle  $\omega = \omega_s$ , and  $\theta_z = 90^\circ$

Then,  $\cos 90^\circ = 0 = \cos\phi \cos\delta \cos\omega_s + \sin\phi \sin\delta$

$$\text{or} \quad \cos\omega_s = -\frac{\sin\phi \sin\delta}{\cos\phi \cos\delta} = -\tan\phi \tan\delta$$

$$\text{Finally, } \omega_s = \cos^{-1}(-\tan\phi \tan\delta) \quad (3.18)$$

The number of day light (sunshine) hours is given by (Duffie & Beckman, 2013).

$$N = \frac{2}{15} \cos^{-1}(-\tan\phi \tan\delta) \quad (3.19)$$

The variation of daylight hours for different days of the year is due to the variation of latitude.

### 3.3 PurpleAir Sensor

We used a PurpleAir sensor to take real-time measurements of  $PM_{1.0}$ ,  $PM_{2.5}$ , and  $PM_{10}$  concentrations. It is a small and handy device that can detect the particle sizes 0.3 micrometers to 10.0 micrometers of six different sizes. The six sides shielding of the device gives high anti interference performance and optional direction for air inlet and outlet.



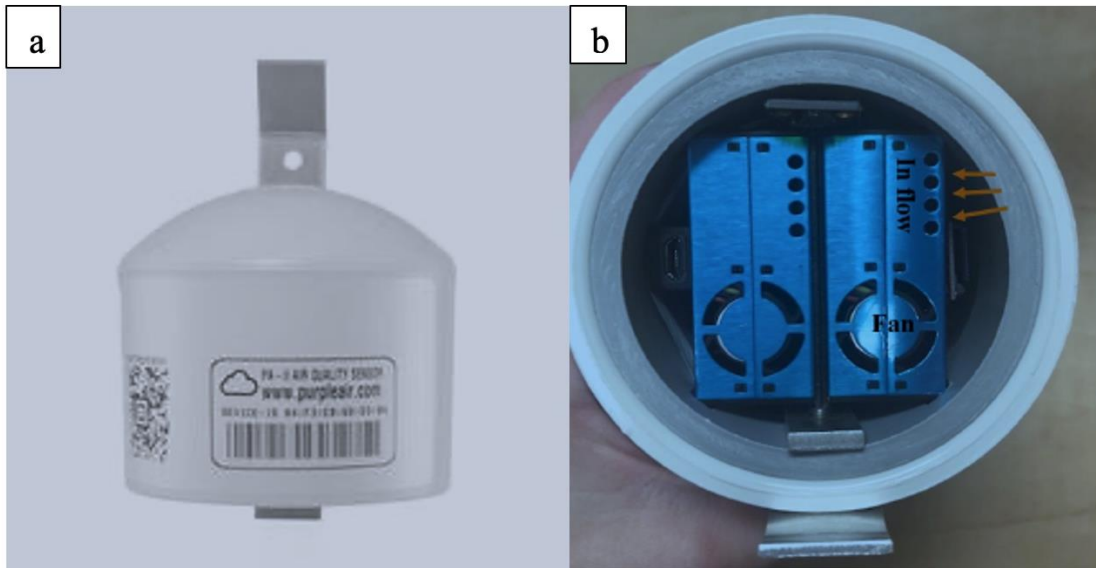


**Figure 7:** External (left) and bottom view (right) showing the inlet air flow and outlet air flow along with a fan in two sensors of a Purple-air monitor (Regmi et al., 2022).

It possesses two PMS 5003 sensors to detect and count the number of suspended particles in the air. One is BME 280 environmental sensor, and the other is ESP 8226 microcontroller. The BME 280 sensor monitors the units' inner pressure, temperature, and humidity. It can measure the temperature in a range of  $-40^{\circ}\text{F}$  to  $185^{\circ}\text{F}$  ( $-40^{\circ}\text{C}$  to  $85^{\circ}\text{C}$ ) and pressure in the range of 300 to 1100 hPa. Each PMS 5003 sensor has an effective measurement range for  $\text{PM}_{2.5}$  concentration of  $0\text{--}500\ \mu\text{g}\text{m}^{-3}$  with a resolution of  $1\ \mu\text{g}\text{m}^{-3}$ , and the maximum standard  $\text{PM}_{2.5}$  concentration is above  $1000\ \mu\text{g}\text{m}^{-3}$ . In contrast, the ESP 8266 microcontroller communicates with both the PMS 5003 sensors and with the Purple Air server over Wi-Fi, thereby allowing the PM concentration data through an application programming interface (API) to view and download live on the Purple Air map (<https://www.purpleair.com/map>).

### 3.3.1 Working principle

It works on the principle of laser scattering. When the laser passes through air, the air particle reflects some light from the laser beam onto a detection plate. It measures the reflection as a pulse, and its length determines the particle's size. The number of pulses measure the number of particles. Based on the Mie theory, the microprocessor calculates the equivalent particle diameter and the number of particles with different diameters per unit volume (<https://www.purpleair.com/map>).

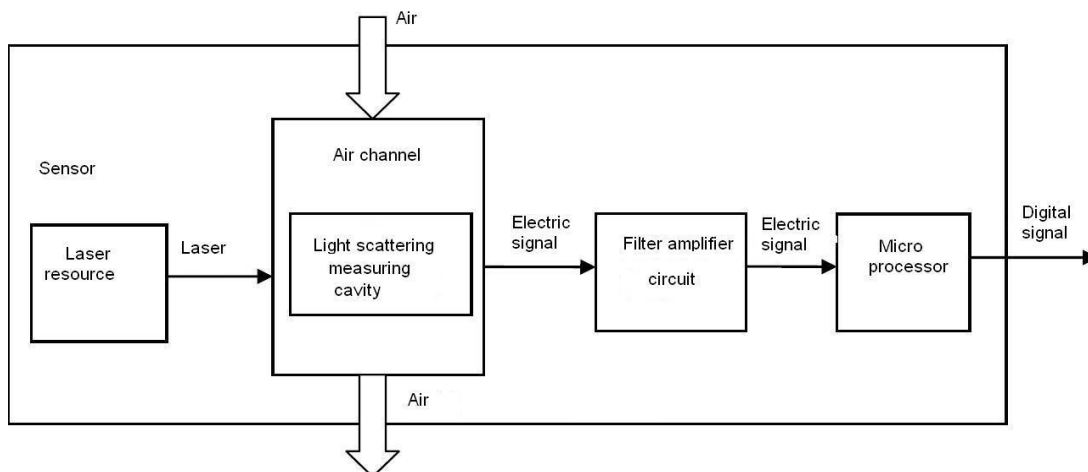
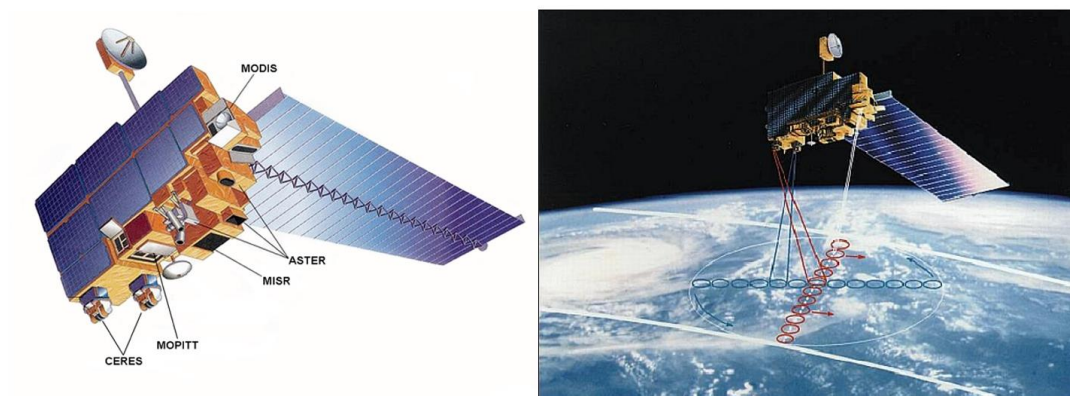


**Figure 8:** Functional Block Diagram of Purple Air II-AP/SD sensor and an overview of the PMS5003 ([http://www.aqmd.gov/docs/default-source/aq-spec/resources-page/plantower-pms5003-manual\\_v2-3.pdf](http://www.aqmd.gov/docs/default-source/aq-spec/resources-page/plantower-pms5003-manual_v2-3.pdf)), 2021)

It is an advanced real-time dust monitor (aerosol monitor) accurately measuring dust concentrations using proven light scatter technology. This portable instrument accurately measures and records dust from 1-10,000  $\mu\text{g}/\text{m}^3$  with resolution of 1  $\mu\text{g}/\text{m}^3$ . Sample modes are selectable between 60 second, 15-minute STEL, or continuous sampling.

### 3.4 MODIS Satellite Measurement



(Source: ESA Earth Online Terra - eoPortal Directory - Satellite Missions)

**Figure 9:** Terra Satellite carrying MODIS and showing a coverage area

NASA launched the Moderate Resolution Imaging Spectro-radiometer (MODIS) instrument on the Terra and Aqua satellites in 1999 and 2002, respectively. The Aqua

satellite crosses the equator from south to north in the afternoon (around 1:30 PM), whereas the Terra satellite orbits the earth from north to south in the morning (about 10:30 AM). With a daily swath of 2330 km, the Terra and Aqua MODIS see the whole surface of the world while collecting data in 36 spectral bands between 415 nm and 14235 nm. The MODIS aerosol products offer attributes for both land (Kaufman et al., 1997) and ocean (Tanre et al., 1997). The MODIS sensors take one to two days to picture the cloud-free surface views after collecting imagery of the same spot on the Earth three hours apart.

The level 1 radiance data and the higher levels of all ocean and atmospheric products are distributed by the NASA Goddard Earth Sciences Distributed Active Archive Center (Savtchenko et al., 2004). Aerosol attributes, atmospheric water vapor, cloud properties, atmospheric profiles, and cloud mask are used to categorize the MODIS atmosphere products (Dubovik et al., 2002). Level 2 data contains 5 different data types in HDF file format for Terra and Aqua. They are described as follows:

- The aerosol attributes for optical thickness, aerosol type, particle size distribution, mass concentration, asymmetry factor, cloud condensation nuclei, angstrom exponent, and backscattering are provided by MOD04\_L2 for Terra and MYD04\_L2 for Aqua.
- The data for atmospheric water vapor over clear land areas of the earth, are provided by MOD05\_L2 and MYD05\_L2 over clear oceanic areas, and above clouds over land.
- Cloud optical and physical parameters, including cloud temperature, cloud pressure, height, phase, brightness, temperature, forcing, and surface temperature, are provided by MOD06 L2 and MYD06 L2. Additionally, it has an effective radius, cloud reflectance, cloud optical thickness, and cloud water path.
- The data for atmospheric profiles and stability indices provided by MOD07 L2 and MYD07 L2 include temperature, moisture, total ozone, and stability indices. The estimated sum of the total tropospheric and stratospheric ozone columns is known as total ozone.

- The data for cloud masks provided by MOD35 L2 and MYD35 L2 include global cloud masks, clear sky confidence levels (high confident clear, probably clear, undecided, and cloudy), and identification for cirrus cloud.

The complexity of the Earth's land surfaces makes it difficult for satellites to retrieve the aerosol optical thickness over the land. Since the surface reflectance is variable with place and wavelength, different algorithms are used to satellite datasets to separate the surface and atmospheric scattering impacts.

According to Kaufman et al., (2002), MODIS aerosol retrievals over land are based on the correlation of reflectance in visible light wavelengths. Dark surfaces offer high contrast for observing aerosol because they reflect very little light at visible wavelengths (Hansen et al. 1992). Two distinct methods are used by MODIS to perform the aerosol retrievals, one for retrievals over land and the other for retrievals over ocean (Remer et al., 2005). The Deep Blue algorithm was created specifically for retrieving aerosols from bright surfaces like deserts and cities. The method was created to address the issue of retrieving aerosol properties using the fact that desert surfaces seem substantially darker in the blue channels (412 and 470 nm) than in the red (660 nm) channel. The intensity at the top of the atmosphere is determined for a given surface albedo by the Deep Blue algorithm using the measured radiances from each channel and a radiative transfer model. The 412, 470, and 660 nm channels' surface reflectance is calculated from a database using their geolocation (Hsu et al., 2004). The cloud screening process is used to stop retrievals of pixels that have been tainted by the cloud. Additionally, the TOMS aerosol index and the Deep Blue aerosol index (DAI), which is a related measurement, are used to separate heavy dust layers from the cloud (Hsu et al., 2004). To determine the best fit of the modeled radiance as a function of  $\tau$  and single-scattering albedo, a Maximum Likelihood Estimation (MLE) is applied. Based on the geographic location and time of the year, assumptions are made regarding the prevailing aerosol model that is used for the retrieval. The Deep Blue algorithm generates results with the spatial resolution of the satellite data (250-meter resolution). With the added benefit of working over bright surfaces, the MODIS channels 8 (412 nm), 10 (470 nm), and 13 (660 nm) offer Deep Blue retrievals with a higher resolution than the typical MODIS aerosol retrieval. The dry, semiarid, urban, and desert environments are among the bright surfaces to which the Deep Blue algorithm can be used. In order to reduce errors and improve the AOD ( $\tau$ ) quality, MODIS aerosol products are routinely updated based on

surface reflectance calculations, cloud mask, gas, and Rayleigh adjustments, and aerosol model schemes. The C6 MODIS DT algorithm has been built with improved retrieval capacity (Levy et al., 2015; Zhang et al., 2016).

### 3.4.1 Column MODIS AOD ( $\tau$ ) and ground-level PM<sub>2.5</sub> and Relative humidity factor

The atmospheric column is more affected vertically than horizontal atmospheric layers by various atmospheric physical parameters such as temperature, atmospheric humidity, atmospheric pressure, and transportation of aerosols from different sources (Aryal et al., 2014; Xu & Zhang, 2020b). In this study, the vertical aerosol optical depth obtained from satellite data is retrieved under the ambient conditions while, at the surface level, the aerosol particle mass concentration is obtained from the purple air monitor under dry conditions. The particle concentration observed in the ground level (PM) with the dry sample can be expressed quantitatively (Xu & Zhang, 2020a).

$$PM = \frac{4}{3} \pi \rho \int_0^{\infty} r^3 n_{dry}(r) dr \quad (3.20)$$

Where  $n(r)$  is the dry aerosol size distribution function with the dimension of  $[L]^{-4}$ , denotes the number of particles per unit volume in atmospheric space per unit particle radius under dry conditions, and  $\rho$  is the aerosol mass density

The aerosol optical component aerosol optical depth ( $\tau$ ) can be obtained from the particle size distribution by using the scattering Mie theory under the hypothesis of spherical particles with the equation.

Therefore, the AOD ( $\tau$ ) of the layer with height H is given by Koelemeijer et al., (2006)

$$AOD = \int_0^{\alpha} dh \int_0^{\alpha} \pi r^2 Q_{ext,amb}(r) n_{amb}(r, h) dr \quad (3.21)$$

Applying the same hypothesis as in equation (3.20), the aerosol extinction coefficient can be written as:

$$\sigma_{ext,amb} = \frac{1}{\Delta h} \int_{h_1}^{h_2} dh \int_0^{\alpha} \pi r^2 Q_{ext,amb}(r) n_{amb}(r, h) dr \quad (3.22)$$

Here  $r$  is the radius of the assumed spherical particles,  $Q_{ext}$  is the extinction coefficient factor (van de Hulst H.C., 1981), and  $n(r, h)$  is the aerosol size distribution giving a concentration of particles per unit volume per particle radius at height  $h$ , which can be factorized in two parts with height dependence

$$(n(r, h)) = n(r)n(h) = n_0 n(r) \exp(-h/H).$$

Where  $n_0$  is the particle concentration at the surface level and  $H$  is the aerosol scale height (Pesava et al., 2001). Then the equation (3.21) becomes as

$$AOD = n_0 H \int_0^\alpha \pi r^2 Q_{ext,amb}(r) n(r) dr \quad (3.23)$$

While considering the dry conditions, we have to introduce the hygroscopic growth factor  $f(RH)$ . Several models have been developed to explain the relationship between  $f(RH)$  and Relative humidity (RH). However, in this work, we have adopted the kappa equation to investigate the hygroscopic growth for aerosol light extinction (Brock et al., 2016, 2021; Chen et al., 2016; Kotchenruther & Hobbs, 1998; Zheng et al., 2018).

$$f(RH) \equiv \frac{AOD}{AOD_{dry}} \cong a \left( 1 + \frac{RH}{100 - RH} \right) \quad (3.24)$$

Where  $\tau_{dry}$  represents the aerosol optical depth with dehydration adjustment. ' $a$ ' is a fitting parameter and is not affected by RH (Zhao et al., 2018). A different range of  $a$  was reported previously. However, in this study, we have investigated by setting three different values, 0.5, 1, and 1.5, of this fitting parameter ( $a$ ) and have used the hygroscopic growth factor by assuming the ratio of aerosol extinction coefficient in ambient to dry condition. Then, equation (3.23) can be written as;

$$AOD = n_0 H f(RH) \int_0^\alpha \pi r^2 Q_{ext,dry}(r) n(r) dr \quad (3.25)$$

To investigate the AOD ( $\tau$ ) vs  $PM_{2.5}$  the size distribution and extinction efficiency  $\langle Q_{ext} \rangle$  and effective radius  $r_{eff}$  are expressed as (Xu & Zhang, 2020b, 2020a).

$$\langle Q_{ext} \rangle = \frac{\int_0^\alpha Q_{ext}(r) n(r) r^2 dr}{\int_0^\alpha n(r) r^2 dr} \quad (3.26)$$

$$\text{And, } r_{eff} = \frac{\int_0^\alpha n(r) r^3 dr}{\int_0^\alpha n(r) r^2 dr} \quad (3.27)$$

A relation between  $\tau / f(RH)$  and  $PM_{2.5}$  can be obtained based on the above equations (3.21), (3.23), (3.26), and (3.27) as

$$AOD = \frac{3}{4} n_0 \cdot H \cdot f(RH) \cdot PM \frac{\langle Q_{ext,dry}(r) \rangle}{\rho r_{eff}} \quad (3.28)$$

In this study, we have studied the relative humidity as the correcting factor to study the correlation between  $\frac{AOD}{f(RH)}$  vs  $PM_{2.5}$  and have not included the scale height variation due to the data unavailability.

### 3.5 Mie theory and scattering of solar radiation

The interaction of aerosol particles with electromagnetic radiation significantly affects Earth's radiative budget. The absorption and scattering of radiation due to aerosol particles strongly depend upon the size parameter  $x$ ; which is given by,

$$x = 2\pi r / \lambda \quad (3.29)$$

Where  $r$  is the particle radius and  $\lambda$  is the wavelength.

The degree of interaction is measured by the particle's extinction cross-section, which is the sum of absorption and the scattering cross-section. Rayleigh scattering assumes particles much smaller than the wavelength. For particles much larger than the wavelength, geometrical optics can be applied, and the extinction cross-section converges towards twice the geometric particle cross-section  $\sigma_g = \pi r^2$ .

Mie theory considers spherical particles in size range comparable to that of the wavelength. It bridges the gap between Rayleigh scattering and geometric optics. Based on wave optics, Mie theory precisely predict light's interaction with small spherical particles. The Mie theory depends on decomposing of the electromagnetic waves into spherical harmonics both within and outside the particle. The scattered wave equation is obtained from the boundary conditions at the particle's surface (Boucher, 2015).

Mie theory is an important tool to solve light scattering by a homogeneous sphere using Maxwell's equation with appropriate boundary conditions. Maxwell's equations are used to calculate the scattered electromagnetic field at all points within the particle and at all points of the homogeneous medium. These equations can be used in the entire field of atmospheric optics, and from one end of the electromagnetic spectrum to the other-from UV solar radiation backscattered by stratospheric aerosols to satellites, through visible and IR radiation scattered by clouds and aerosols, to microwaves and radar scattered from large hydrometeors.

### 3.5.1 Formulation of Lorentz-Mie Theory from Maxwell's Equations

Mie theory is a general solution for scattering an electromagnetic wave from a spherical particle having a uniform complex index of refraction. The complex part is responsible for absorption, and real portion is for scattering.

It is a solution to Maxwell's electromagnetic equations, asymptotic to plane waves at large distances from the particle. Since Maxwell's equations are linear, the solution can be built up from more elementary solutions to the equations. It furnishes the solution with an infinite sum over spherical Bessel functions.

The presence of electric charges in space constitutes an electromagnetic field. We can define  $\mathbf{E}$  and  $\mathbf{B}$  as the electric vector and magnetic induction, respectively (Liou, 2002). Based on the Mie scattering theory explained in section 3.5.2, we used Fortran 95 Code to calculate scattering, extinction, and single scattering albedos with complex refractive indices and volume size distributions from the AERONET website (Aryal et al., 2014).

### 3.5.2 Scattering of a plane wave by a homogeneous sphere

The light radiation gets linearly polarized if the medium outside a sphere is a vacuum. (Liou, 2002). Taking origin of a rectangular system of coordinates at the center of the sphere, with the positive  $z$  axis along the direction of propagation of the incident wave, then we can write, the incident electric and magnetic field vectors as given by van de Hulst (1981),

$$\mathbf{E}^i = \mathbf{a}_x e^{-ikz} \quad \mathbf{H}^i = \mathbf{a}_y e^{-ikz}, \quad (3.30)$$

Where  $\mathbf{a}_x$  and  $\mathbf{a}_y$  are unit vectors along the  $x$  and  $y$  axes, respectively.

We can change the components of any vector from the Cartesian system  $(x, y, z)$  into the spherical polar coordinates  $(r, \theta, \phi)$  as;

$$x = r \sin \theta \cos \phi, \quad y = r \sin \theta \sin \phi, \quad z = r \cos \theta. \quad (3.31)$$

So that, we can write,

$$\begin{aligned} \mathbf{a}_r &= \mathbf{a}_x \sin \theta \cos \phi + \mathbf{a}_y \sin \theta \sin \phi + \mathbf{a}_z \cos \theta, \\ \mathbf{a}_\theta &= \mathbf{a}_x \cos \theta \cos \phi + \mathbf{a}_y \cos \theta \sin \phi - \mathbf{a}_z \sin \theta, \\ \mathbf{a}_\phi &= -\mathbf{a}_x \sin \phi + \mathbf{a}_y \cos \phi, \end{aligned} \quad (3.32)$$



And, the electric and magnetic field vectors take the form,

$$\begin{aligned} \mathbf{E}_r^i &= e^{-ikr\cos\theta} \sin\theta \cos\phi \\ \mathbf{E}_\theta^i &= e^{-ikr\cos\theta} \cos\theta \cos\phi \\ \mathbf{E}_\phi^i &= -e^{-ikr\cos\theta} \sin\phi \end{aligned} \quad (3.33)$$

$$\begin{aligned} \mathbf{H}_r^i &= e^{-ikr\cos\theta} \sin\theta \sin\phi \\ \mathbf{H}_\theta^i &= e^{-ikr\cos\theta} \cos\theta \sin\phi \\ \mathbf{H}_\phi^i &= e^{-ikr\cos\theta} \cos\phi \end{aligned} \quad (3.34)$$

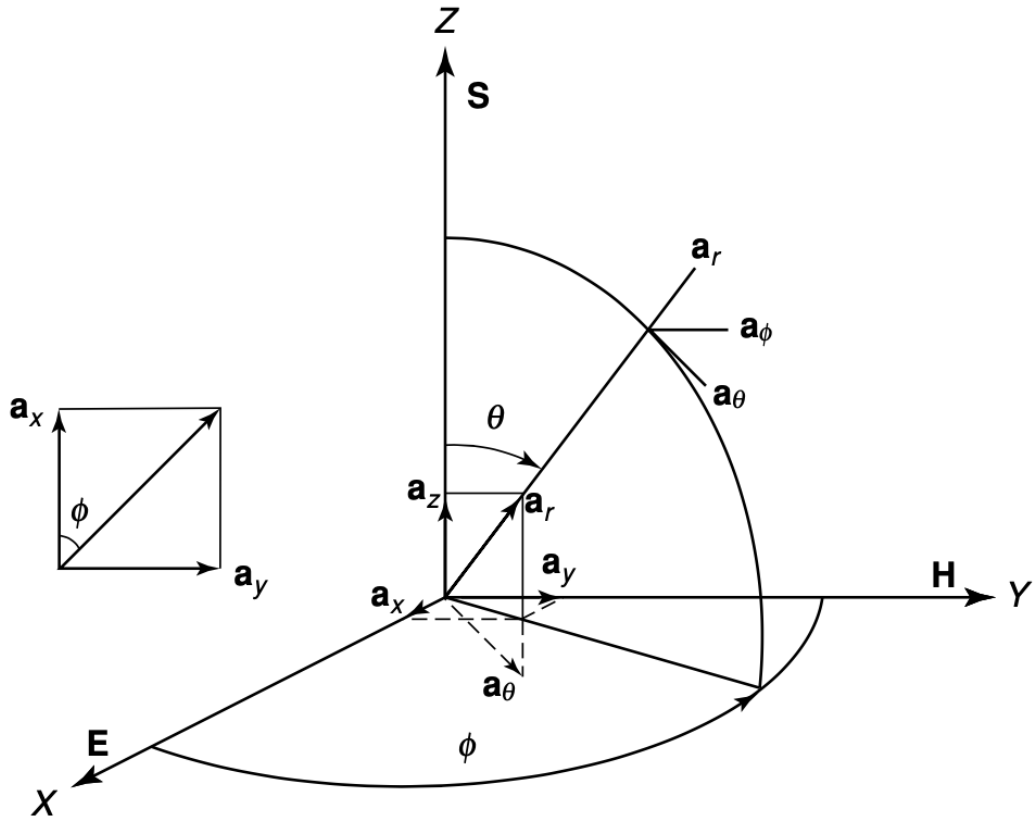


**Figure 10:** Transformation of rectangular to spherical coordinates.  $S$  is the Poynting vector;  $a$  is an arbitrary unit vector;  $\theta$  and  $\phi$  are zenith and azimuthal angles; and  $E$  and  $H$  are electric and magnetic vectors (Liou, 2002)

We can write,

$$e^{-ikr\cos\theta} = \sum_{n=0}^{\infty} (-i)^n (2n+1) \frac{\psi_n(kr)}{kr} P_n(\cos\theta) \quad (3.35)$$

We also have mathematical identities (Liou, 2002),

$$e^{-ikr \cos \theta} \sin \theta = \frac{1}{ikr} \frac{\partial}{\partial \theta} (e^{-ikr \cos \theta}) \quad (3.36)$$

$$\frac{\partial}{\partial \theta} P_n(\cos \theta) = -P_n^1(\cos \theta), \quad -P_0^1(\cos \theta) = 0 \quad (3.37)$$

Equation (3.37) relates Legendre polynomial  $P_n$  to associated Legendre polynomial  $P_n^1$ .

We have the relation for electric field from vector wave equation given by

$$\begin{aligned} \mathbf{E} = & \mathbf{a}_r \frac{i}{mk} \left[ \frac{\partial^2(ru)}{\partial r^2} + m^2 k^2 (ru) \right] + \mathbf{a}_\theta \left[ \frac{1}{r \sin \theta} \frac{\partial(rv)}{\partial \phi} + \frac{i}{mkr} \frac{\partial^2(ru)}{\partial r} \right] + \\ & \mathbf{a}_\phi \left[ -\frac{1}{r} \frac{\partial(rv)}{\partial \theta} + \frac{1}{mkr \sin \theta} \frac{\partial^2(ru)}{\partial r \partial \phi} \right] \end{aligned} \quad (3.38)$$

The potentials  $u$  and  $v$  are given by the first term of equation (3.38) at  $m = 1$ .

$$\mathbf{E}_r^i = e^{-ikr \cos \theta} \sin \theta \cos \phi = \frac{i}{k} \left[ \frac{\partial^2(ru^i)}{\partial r^2} + k^2 (ru^i) \right] \quad (3.39)$$

From equations (3.35), (3.36), and (3.37), we can write;

$$e^{-ikr \cos \theta} \sin \theta \cos \phi = \frac{1}{(kr)^2} \sum_{n=1}^{\infty} (-i)^{n-1} (2n+1) \psi_n(kr) P_n^1(\cos \theta) \cos \phi \quad (3.40)$$

Trial solution for equation (3.39) is,

$$ru^i = \frac{1}{k} \sum_{n=1}^{\infty} \alpha_n \psi_n(kr) P_n^1(\cos \theta) \cos \phi \quad (3.41)$$

Using equation (3.40) and (3.41) in (3.39) and comparing coefficients, we get,

$$\alpha_n \left[ k^2 \psi_n(kr) + \frac{\partial^2 \psi_n(kr)}{\partial r^2} \right] = (-i)^n (2n+1) \frac{\psi_n(kr)}{kr} \quad (3.42)$$

From equation,  $rR = c_n \psi_n(kmr) + d_n \chi_n(kmr)$  if we assume  $c_n=1$  and  $d_n=0$ , then

$$\psi_n(kr) = rR \quad (3.43)$$

For  $m=1$ , equation (3.43) is a solution of equation

$$\frac{d^2(rR)}{dr^2} + \left[ k^2 m^2 - \frac{n(n+1)}{r^2} \right] (rR) = 0 \quad (3.44)$$

So that we can write,

$$\frac{d^2 \psi_n}{dr^2} + \left[ k^2 - \frac{\alpha}{r^2} \right] \psi_n = 0 \quad (3.45)$$

Here  $\alpha_n = n(n+1)$ . Comparing equation (3.89) and (3.91), we get,

$$\alpha_n = (-i)^n \frac{2n+1}{n(n+1)} \quad (3.46)$$

So that for incident waves, equation (3.41) becomes,

$$ru^i = \frac{1}{k} \sum_{n=1}^{\infty} (-i)^n \frac{2n+1}{n(n+1)} \psi_n(kr) P_n^1(\cos\theta) \cos\phi$$

Similarly,

$$rv^i = \frac{1}{k} \sum_{n=1}^{\infty} (-i)^n \frac{2n+1}{n(n+1)} \psi_n(kr) P_n^1(\cos\theta) \sin\phi \quad (3.47)$$

We have general solution of scalar wave equation is,

$$r\psi(r, \theta, \phi) = \sum_{n=0}^{\infty} \sum_{l=-n}^n P_n^l(\cos\theta) [c_n \psi_n(kmr) + d_n \chi_n(kmr)] (a_l \cos l\phi + b_l \sin l\phi) \quad (3.48)$$

For internal waves the function in equation (3.48),  $\chi_n(kmr)$  becomes infinite at the origin, only the function  $\psi_n(kmr)$  may be used. Thus, for internal waves, we can write,

$$ru^t = \frac{1}{mk} \sum_{n=1}^{\infty} (-i)^n \frac{2n+1}{n(n+1)} c_n \psi_n(kmr) P_n^1(\cos\theta) \cos\phi$$

$$rv^t = \frac{1}{mk} \sum_{n=1}^{\infty} (-i)^n \frac{2n+1}{n(n+1)} d_n \psi_n(kmr) P_n^1(\cos\theta) \sin\phi \quad (3.49)$$

For scattered wave, these two functions vanish at infinity and Hankel function

$$\psi_n(p) + i \chi_n(p) = \sqrt{\frac{\pi p}{2}} H_{n+1/2}^{(2)}(p) = \xi_n(p) \quad (3.50)$$

comes into play.

$$\begin{aligned}
ru^s &= \frac{1}{k} \sum_{n=1}^{\infty} (-i)^n \frac{2n+1}{n(n+1)} a_n \xi_n(kr) P_n^1(\cos\theta) \cos\phi \\
rv^s &= \frac{1}{k} \sum_{n=1}^{\infty} (-i)^n \frac{2n+1}{n(n+1)} b_n \xi_n(kr) P_n^1(\cos\theta) \cos\phi
\end{aligned} \tag{3.51}$$

The Mie coefficients  $a_n$ ,  $b_n$ ,  $c_n$ , and  $d_n$  must be determined from the boundary conditions. Electromagnetic fields are required to satisfy Maxwell's equations in regions where the permittivity and the permeability are isotropic and constant. And the tangential components of  $\mathbf{E}$  and  $\mathbf{H}$  should be continuous across the spherical surface  $r = a$  such that,

$$\begin{aligned}
E_{\theta}^i + E_{\theta}^s &= E_{\theta}^t, & H_{\theta}^i + H_{\theta}^s &= H_{\theta}^t \\
E_{\phi}^i + E_{\phi}^s &= E_{\phi}^t, & H_{\phi}^i + H_{\phi}^s &= H_{\phi}^t
\end{aligned} \tag{3.52}$$

On applying the vector spherical harmonics, we get following equations,

$$\begin{aligned}
m[\psi_n'(ka) - a_n \xi_n'(ka)] &= c_n \psi_n'(kma), \\
[\psi_n'(ka) - b_n \xi_n'(ka)] &= d_n \psi_n'(kma), \\
[\psi_n(ka) - a_n \xi_n(ka)] &= c_n \psi_n(kma), \\
m[\psi_n(ka) - b_n \xi_n(ka)] &= d_n \psi_n(kma),
\end{aligned} \tag{3.53}$$

where the prime denotes differentiation with respect to the argument. When  $c_n$  and  $d_n$  are eliminated, the coefficients for the scattered waves are obtained.

$$\begin{aligned}
a_n &= \frac{\psi_n'(y)\psi_n(x) - m\psi_n(y)\psi_n'(x)}{\psi_n'(y)\xi_n(x) - m\psi_n(y)\xi_n'(x)} \\
b_n &= \frac{m\psi_n'(y)\psi_n(x) - \psi_n(y)\psi_n'(x)}{m\psi_n'(y)\xi_n(x) - \psi_n(y)\xi_n'(x)}
\end{aligned} \tag{3.54}$$

Where  $x=ka$  and  $y=mx$ . The solutions for  $c_n$ , and  $d_n$  contain the same respective denominator as those of  $a_n$  and  $b_n$  but with a common numerator

$$m[\psi_n'(x)\xi_n(x) - \psi_n(x)\xi_n'(x)].$$

Here, we have assumed the suspending medium is a vacuum.

For the far field solution, Hankel functions in equation (3.50) reduce to,

$$\xi_n(kr) \approx i^{n+r} e^{-ikr}, \quad kr \gg 1 \tag{3.55}$$

It makes equation (3.51) as,

$$ru^s \approx -\frac{ie^{-ikr} \cos \phi}{k} \sum_{n=1}^{\infty} \frac{2n+1}{n(n+1)} a_n P_n^1(\cos \theta)$$

$$rv^s \approx -\frac{ie^{-ikr} \sin \phi}{k} \sum_{n=1}^{\infty} \frac{2n+1}{n(n+1)} b_n P_n^1(\cos \theta)$$
(3.56)

The three components of electric and magnetic field vectors are given by,

$$E_r^s = H_r^s \approx 0$$

$$E_\theta^s = H_\phi^s \approx \frac{-i}{kr} e^{-ikr} \cos \phi \sum_{n=1}^{\infty} \frac{2n+1}{n(n+1)} \left[ a_n \frac{dP_n^1(\cos \theta)}{d\theta} + b_n \frac{P_n^1(\cos \theta)}{\sin \theta} \right],$$

$$E_\phi^s = H_\theta^s \approx \frac{i}{kr} e^{-ikr} \sin \phi \sum_{n=1}^{\infty} \frac{2n+1}{n(n+1)} \left[ a_n \frac{P_n^1(\cos \theta)}{\sin \theta} + b_n \frac{dP_n^1(\cos \theta)}{d\theta} \right].$$
(3.57)

For simplicity, we define two scattering functions,

$$S_1(\theta) = \sum_{n=1}^{\infty} \frac{(2n+1)}{n(n+1)} [a_n \pi_n(\cos \theta) + \mathbf{b}_n \tau_n(\cos \theta)],$$

$$S_2(\theta) = \sum_{n=1}^{\infty} \frac{(2n+1)}{n(n+1)} [a_n \tau_n(\cos \theta) + \mathbf{b}_n \pi_n(\cos \theta)],$$
(3.58)

Where

$$\pi_n(\cos \theta) = \frac{1}{\sin \theta} P_n^1 \cos \theta$$

$$\tau_n(\cos \theta) = \frac{d}{d\theta} P_n^1 \cos \theta$$
(3.59)

Where  $P_n^1$  is the associated Legendre function ( $m=1$ ).

Hence, we can write,

$$\begin{aligned} E_\theta^s &= \frac{i}{kr} e^{-ikr} \cos \phi S_2(\theta) \\ -E_\phi^s &= \frac{i}{kr} e^{-ikr} \sin \phi S_1(\theta). \end{aligned} \quad (3.60)$$

If we define  $E_r$  and  $E_l$  as perpendicular and parallel components of the electric field as shown in figure, then scattered field is given by,

$$E_r^s = -E_\phi^s, \quad E_l^s = E_\theta^s \quad (3.61)$$

And equation (3.30) can be decomposed as,

$$E_r^i = e^{-ikz} \sin \phi, \quad E_l^i = e^{-ikz} \cos \phi \quad (3.62)$$

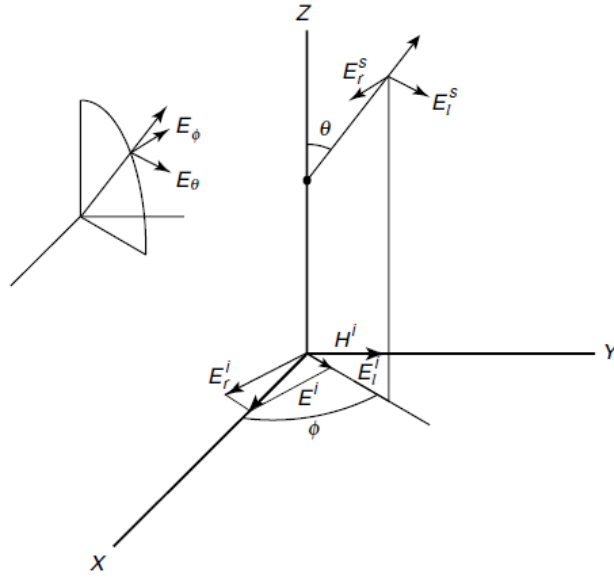


**Figure 11:** Decomposition of the incident (i) and scattered (s) electric vectors into perpendicular (r) and parallel (l) components in Cartesian and spherical coordinates (Liou, 2002)

The scattered intensity components in the far field zone in terms of incident components can be written as,

$$I_l^s = I_l^i \frac{i_2}{k^2 r^2} \quad I_r^s = I_r^i \frac{i_1}{k^2 r^2} \quad (3.63)$$

Where the intensity functions for perpendicular and parallel components are given by,

$$i_1(\theta) = |S_1(\theta)|^2 \quad i_2(\theta) = |S_2(\theta)|^2, \quad (3.64)$$

In the far-field zone, the reduction of the incident energy is due to the absorption and scattering of light by a sphere. So that we may consider incident light polarized linearly in the perpendicular direction. Hence, the scattered electric field is given by,

$$E_r^S = \frac{e^{-ikr+ikz}}{ikr} S_1(\theta) E_r^i \quad (3.65)$$

If we integrate the far-field  $\{x(y) \ll z\}$  combined flux density in the forward direction ( $\theta = 0$ ) of a sphere of radius  $a$  on its cross-sectional area to obtain the total power of the combined image as,

$$\frac{1}{|E_r^i|^2} \iint |E_r^i + E_r^S|^2 dx dy = \pi a^2 + \sigma_e \quad (3.66)$$

The physical meaning of  $\sigma_e$ , is the amount of light attenuated by a sphere out of total light received in the forward direction as if an area equivalent to  $\sigma_e$  of the object had been covered up. The double integral over  $dx dy$  extended to infinity from which  $\sigma_e$  is defined contains two Fresnel integrals and is given by;

$$\int_{-\infty}^{\infty} \int_{-\infty}^{\infty} e^{-ik(x^2+y^2)/2z} dx dy = \frac{2\pi z}{ik} \quad (3.67)$$

The extinction cross section is,

$$\sigma_e = (4\pi/k^2) \text{Re}[S(0)] \quad (3.68)$$

So, in forward direction, we can write,

$$S_1(0) = S_2(0) = S(0) = \frac{1}{2} \sum_{n=1}^{\infty} (2n + 1) \text{Re}(a_n + b_n), \quad (3.69)$$

The extinction efficiency of a sphere with radius  $a$  for Mie Scattering is given by,

$$Q_e = \frac{\sigma_e}{\pi a^2} = \frac{2}{x^2} \sum_{n=1}^{\infty} (2n + 1) \text{Re}(a_n + b_n), \quad (3.70)$$

where  $x=ka$  is the size parameter.

The amplitude functions  $S_1$ ,  $S_2$ ,  $S_3$  and  $S_4$  characterizes the scattering from any finite particle. These parameters are used to calculate total scattering cross section, extinction cross section, and absorption cross section can be obtained when the light is linearly polarized light.

In case of spherical particles  $S_3(\theta)$  and  $S_4(\theta)$  are zero. Here  $\theta$  is scattering angle. The scattering phase function  $F(\theta, \phi)$  defines the intensity of scattered light in an arbitrary direction.

$$F(\theta, \phi) = \frac{F_0}{k^2 r^2} [i_2(\theta) \cos^2 \phi + i_1(\theta) \sin^2 \phi], \quad (3.71)$$

where  $F_0$  is the incident flux density.

Similarly, scattering and absorption efficiencies are given by,

$$Q_s = \frac{2}{x^2} \sum_{n=1}^{\infty} (2n + 1) (|a_n|^2 + |b_n|^2)$$

$$Q_a = \frac{1}{x^2} \left| \sum_{n=1}^{\infty} (2n + 1) (-1)^n (a_n - b_n) \right|^2$$
(3.72)

The scattering behavior is influenced by the diameter of the sphere, incident wavelength, and the refractive index of the particle and medium. The extinction, scattering and absorption cross-section can be calculated as,

$$\sigma_e = \frac{2\pi}{k^2} \sum_{n=1}^{\infty} (2n + 1) \text{Re}(a_n + b_n),$$

$$\sigma_s = \frac{2\pi}{k^2} \sum_{n=1}^{\infty} (2n + 1) (|a_n|^2 + |b_n|^2),$$

$$\sigma_a = \sigma_e - \sigma_s \quad (3.73)$$

The single scattering albedo  $\omega$ , is defined as the ratio of scattering to extinction efficiency,

$$\omega = \frac{Q_s}{Q_e} \quad (3.74)$$



The asymmetry parameter  $g$ , is defined as,

$$g = \frac{4}{x^2 Q_{sca}} \sum_{n=1}^{\infty} \left( \frac{n(n+2)}{n+1} \text{Re}(a_n a_{n+1}^* + b_n b_{n+1}^*) + \frac{(2n+1)}{n(n+1)} \text{Re}(a_n b_n^*) \right) \quad (3.75)$$

The variation of scattering behavior of the particles at different values of imaginary part of refractive index was observed keeping the real part fixed at 1.45 as shown in Figure 12. It shows that for  $k = 0$ , i.e., a perfect reflector, there is no absorption. In this case, scattering efficiency ( $Q_s$ ) is equal to the extinction efficiency ( $Q_e$ ). We can see a series of major maxima and minima and ripples which are due to the interference of diffracted and transmitted light through the sphere. The value of  $Q_s$  is found to increase rapidly when the size parameter reaches to about 5 (like the size of wavelength) and on further increasing the value of size parameter ( $x$ ), it approaches an asymptotic value of 2. This apparent paradox results from the expectation that geometrical optics should have better approximation as a particle's size increases. However, because every particle has an edge, geometrical optics cannot fully explain the extinction caused by them. It means a larger particle can remove two times the light it has intercepted from the incident beam.

As the value of  $k$  increases, absorption due to the particle increases that causes to damp out both the ripples and the major maxima and minima. At a value of  $k = 0.01$ , absorption within the particle slightly increases and the value of maxima also decreases and approaches a value of approximately 1 at very large value of size parameter i.e., at geometric limit. But at a value of  $k=1$ , all the rays entering into the particle are absorbed inside and all the ripples, maxima and minima disappear and it quickly approaches a value 1. It indicates that smaller imaginary part of the refractive index requires larger particle to fully absorb internal rays but for larger value of imaginary part even a smaller particle can absorb all the internal rays.

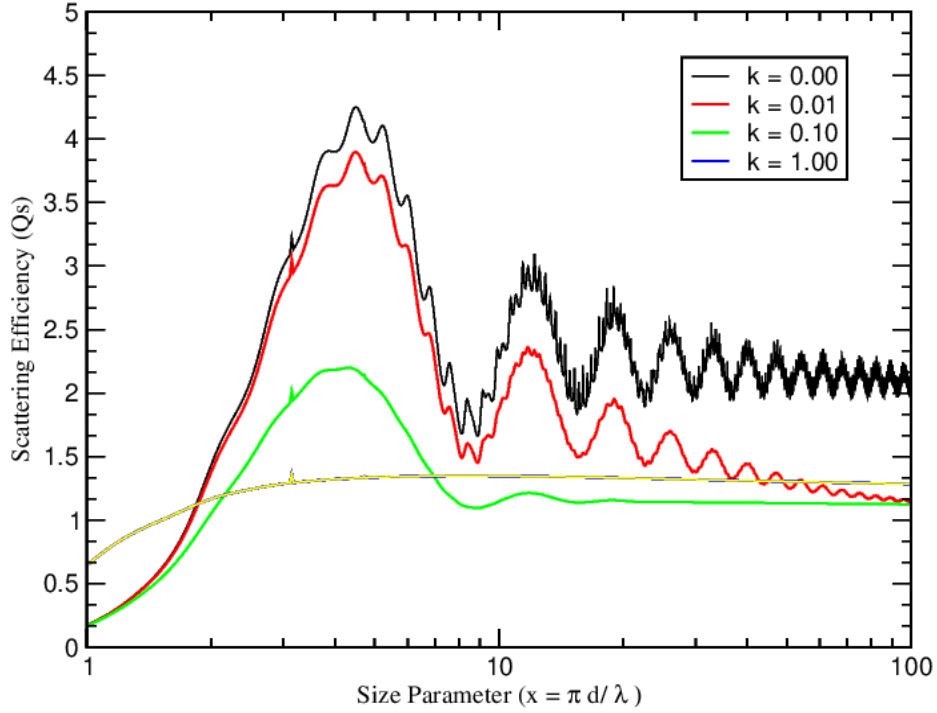


**Figure 12:** The scattering efficiency factor  $Q_s$  as a function of the size parameter  $x$  for a real index of refraction of  $n=1.45$  and several values of the imaginary part (Generated by author using Mie code with Fortran 95 programming for AERONET data of Pokhara station)

### 3.5.3 Influence of particle refractive index on scattering light intensity

The refractive index of the suspended particles is an important factor influencing the scattering light intensity. The complex-valued Mie coefficients  $a_n$  and  $b_n$  depend on  $x$  and on the complex refractive index, which is expressed as follows:

$$m = n + i k \quad (3.76)$$

Here,  $n$  refers to the real part of the refractive index, which is given by the ratio between the propagation velocity of light in a vacuum and the propagation velocity in the medium. This numerical value is related to the material's properties embodied as the scattering effect of incident light in the medium. And,  $k$  is the imaginary part, which indicates the degree of the light intensity attenuation in the medium and describes the performance as the absorption effect of the medium to the incident light. If  $k$  is equal to 0 at a given wavelength, then a particle does not absorb radiation at this wavelength.

Figure 13 shows a variation of scattering efficiency with size parameter corresponding to different wavelengths.

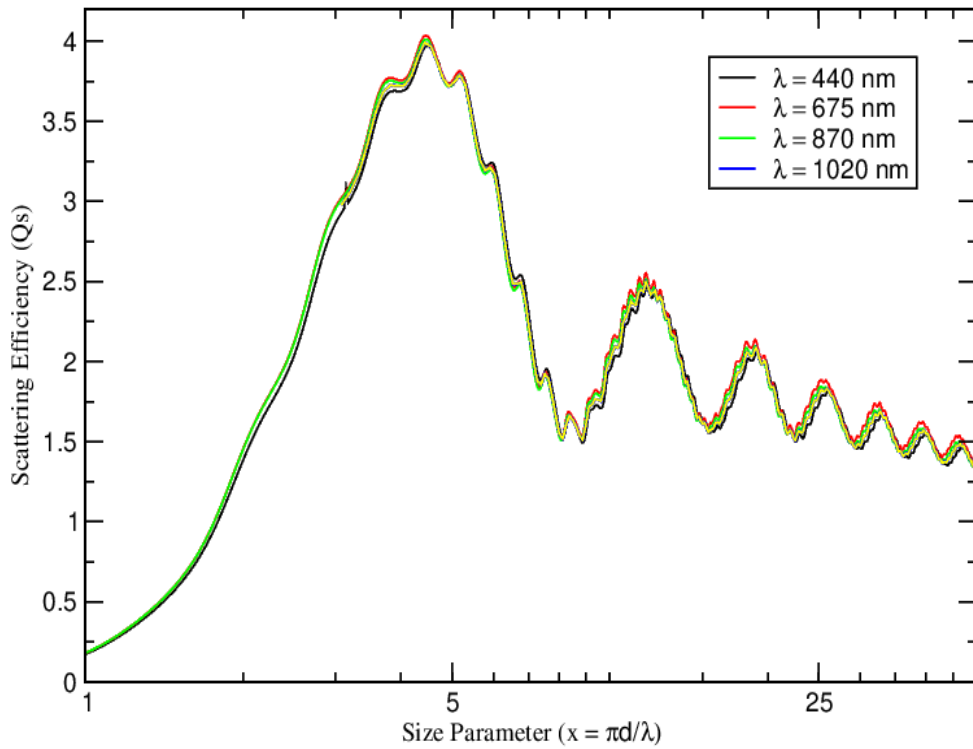


**Figure 13:** The variation of scattering efficiency with size parameter corresponding to different wavelength and at  $n = 1.4500$  and  $k = 0.0078$  (Generated by author using Mie code with Fortran 95 programming for AERONET data of Pokhara station)

The complex refractive index depends on its chemical composition and the wavelength, and is different for different particles. Few examples are shown in the table below.

**Table 1:** Refractive indices of some of the selected atmospheric aerosol substances at  $\lambda = 0.5 \mu\text{m}$  (Liou, 2002)

Substance	Real part (n)	Imaginary Part (k)
Water	1.33	0
Hematite	2.60	1.00
Elemental Carbon	1.75	0.44
Organic Carbon	1.53	0.05
NaCl (S)	1.54	0
H <sub>2</sub> SO <sub>4</sub> (aq)	1.53	0
(NH <sub>4</sub> ) <sub>2</sub> SO <sub>4</sub> (S)	1.52	0
SiO <sub>2</sub>	1.55	0

In the size parameter range (0-25  $\mu\text{m}$ ), which in the case of visible light corresponds to accumulation mode particle sizes, extinction generally acquires maximum value (Kleinschmitt, 2017). It enables the computation of the optical properties of aerosols

based on the particle size and the complex refractive index, whose imaginary portion describes the absorption inside the medium. For liquid atmospheric aerosols, the assumption that the particles are spherical is true, but not for all solid aerosols, such as dust and ice particles.

### 3.5.4 Seasonal variation of efficiency factors with size parameter

With the variation of season, there will be a variation in complex refractive index of aerosol particles. As complex refractive index is an effective parameter for the scattering and extinction of radiation by a particle, a significant seasonal variation in efficiency factors can be observed as shown in the figures (14, 15, and 16). During pre-monsoon period, the maximum values for extinction, scattering and absorption efficiency factors were observed to be 4.14, 3.97, and 0.92 respectively at  $n = 1.4500$  and  $k = 0.0078$  and a fixed wavelength of 440 nm. Peak values of efficiency factors were found to reduce during post monsoon season as refractive index also found to decrease during that period. Winter was found to have largest peak value of extinction efficiency factor ( $Q_e$ ) with a value 4.27.

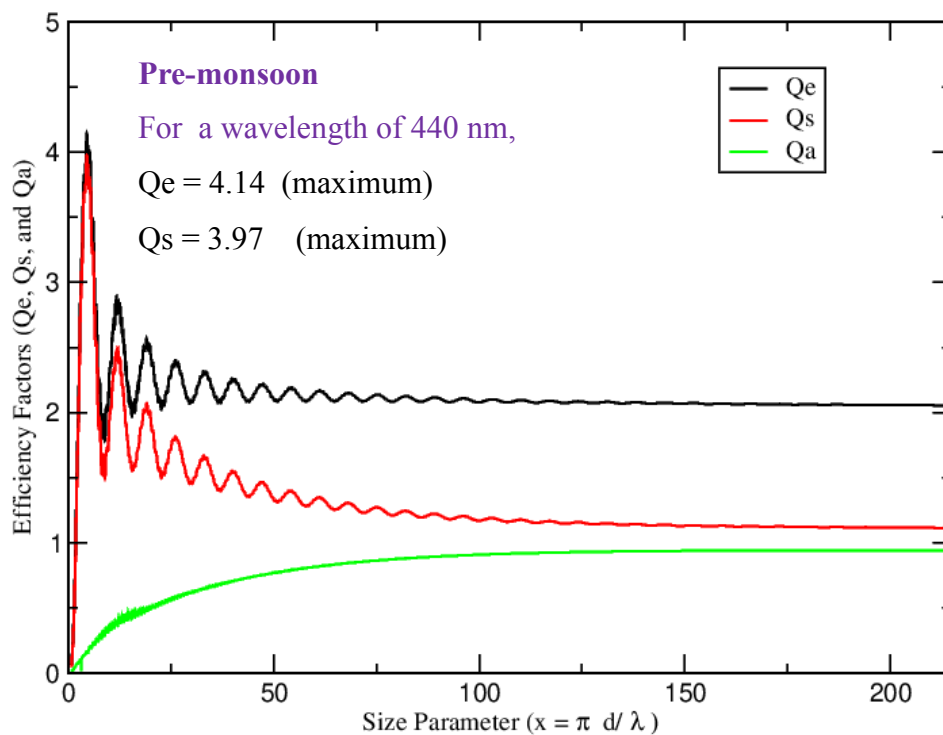


**Figure 14:** The variation of different efficiency factors corresponding to different size parameter at  $n = 1.4500$  and  $k = 0.0078$  during pre-monsoon period 2019 in Pokhara (Generated by author using Mie code with Fortran 95 programming for AERONET data of Pokhara station)

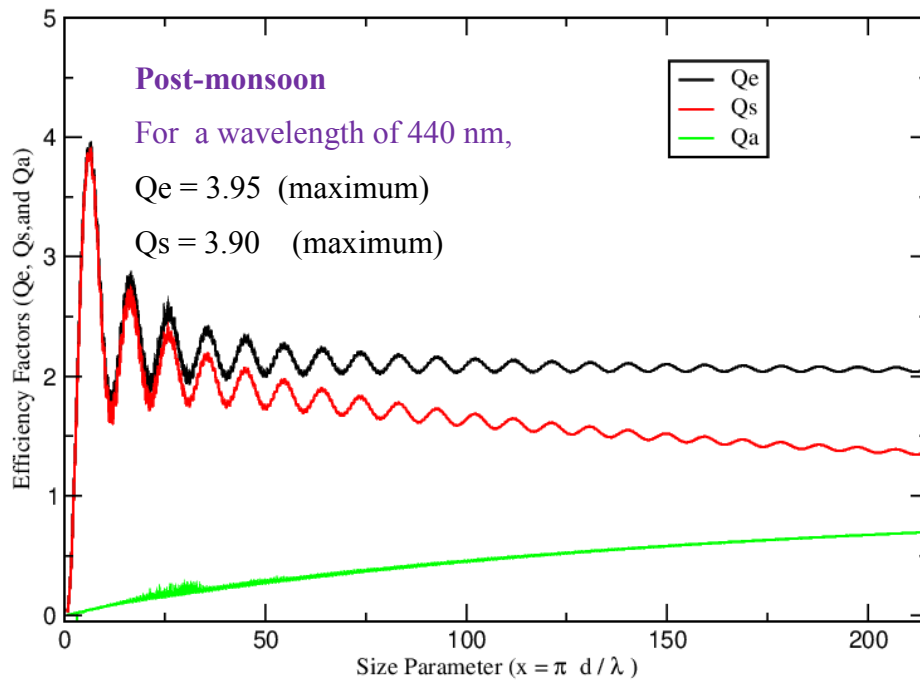


**Figure 15:** The variation of different efficiency factors corresponding to different size parameter at  $n = 1.3300$  and  $k = 0.0171$  during post-monsoon period 2019 in Pokhara (Generated by author using Mie code with Fortran 95 programming for AERONET data of Pokhara station).

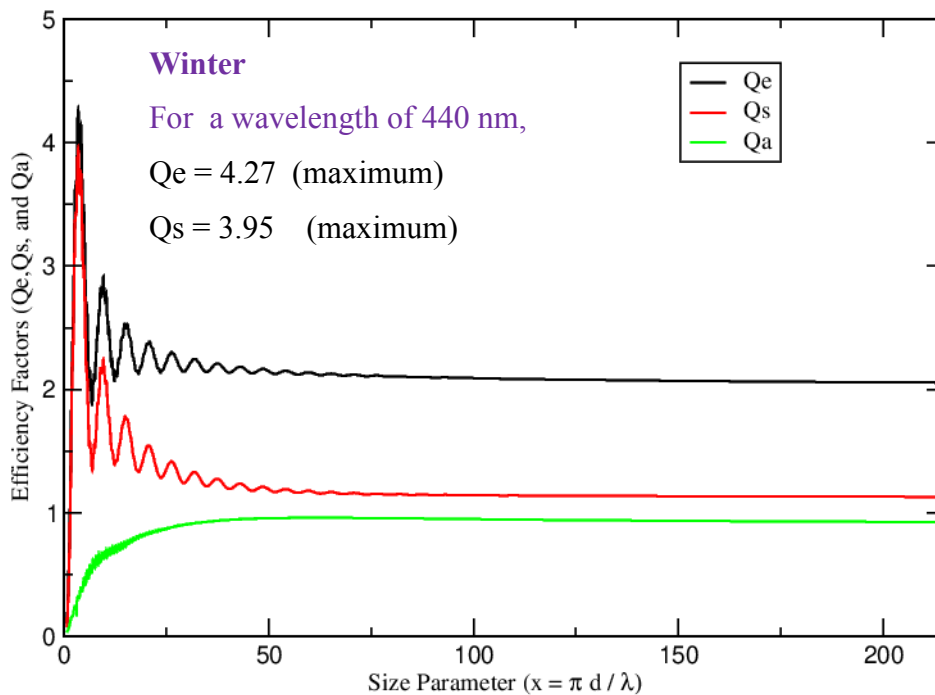


**Figure 16:** The variation of different efficiency factors corresponding to different size parameter at  $n = 1.5645$  and  $k = 0.0183$  during winter period 2019 in Pokhara (Generated by author using Mie code with Fortran 95 programming for AERONET data of Pokhara station).

### 3.6 Research Sites

The research work and data will be taken from various locations over Nepal, which are given below:

1. Institute of Engineering, Pulchowk, TU (Purple Air Monitor)
2. Department of Hydrology and Meteorology (DHM)/GON Field Offices, in various parts of Nepal).
3. Prithvi Narayan Campus, Pokhara (Purple Air Monitor)
4. Different Aerosol Robotic Network sites in Nepal: Pokhara, Jomsom, Lumbini, Kathmandu-Bode, Kyanjin Gompa, EVK2-CNR.

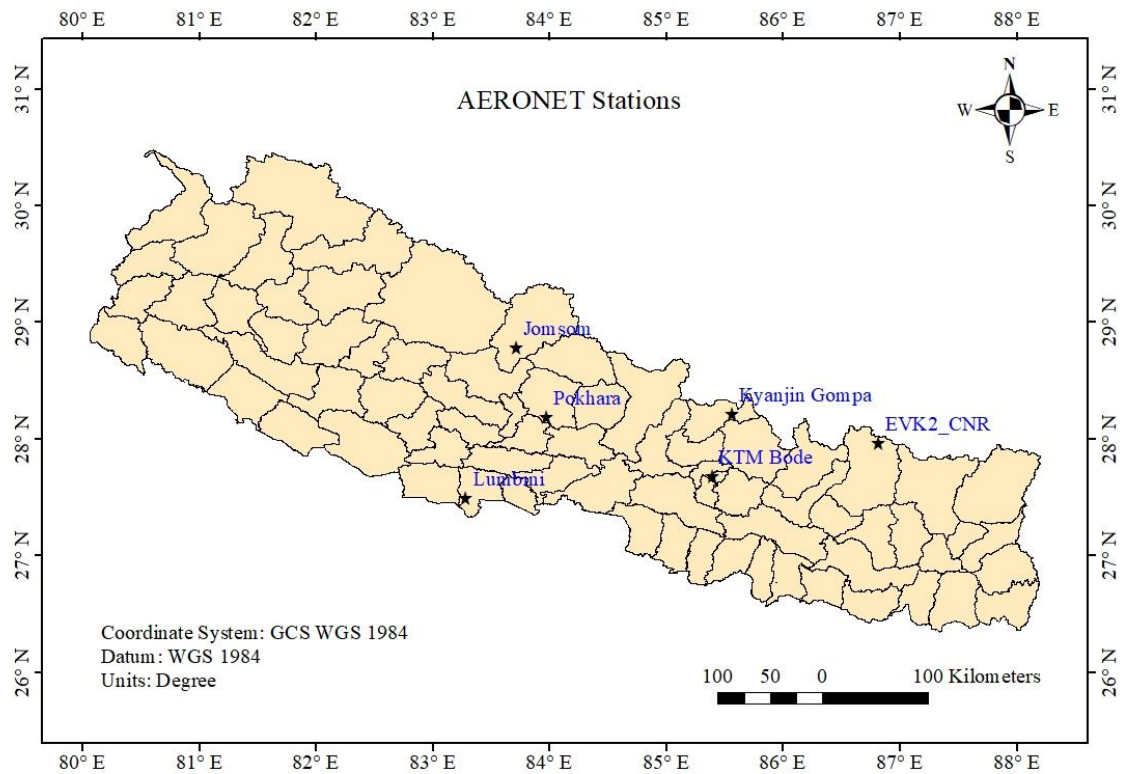


**Figure 17:** Different AERONET stations in the study area (Source: Map generated by the author using Arc GIS 10.4 Software).

The scope of study area for our work is different AERONET stations within Nepal (Latitude:  $26^{\circ} 22'$  North to  $30^{\circ} 27'$  North and Longitude:  $80^{\circ} 04'$  East to  $88^{\circ} 12'$  East). It is situated between two largely populated country of the world, China and India. It spans within an east-west length of 885km and a north-south average width of 193km

and a total area of 1,47,181 km<sup>2</sup> with a population of 29,192,480 (Source: National Population and Housing Census, CBS 2022). It has a unique topography and atmospheric conditions within this small range. The northern part is mountainous region (15%) that elevates up-to the highest peak of the world Sagarmatha 8848.86 m asl (above sea level) and the middle region is hilly region (68%) with diverse landscapes, vegetation and atmospheric conditions. The southern part is the Terai region (17%) with lowest elevation of 60m asl (above sea level) is most populated region connected to Indo-Gangetic Plain (IGP). Depending upon the meteorological conditions, seasons in Nepal are classified as winter (December, January and February: DJF), pre-monsoon (March, April, and May: MAM), monsoon (June, July, August, and September: JJAS) and post-monsoon (October, and November: ON).

In this study, we have presented the analysis of fine particulate matter PM<sub>2.5</sub> in the Kathmandu and Pokhara valleys. Two PurpleAir sensors (<https://www.purpleair.com>) are deployed in the Kathmandu valley (Pulchowk Engineering Campus, Lalitpur, (27.68° N, 85.31° E), at an Altitude of 1350 m asl and Prithvi Narayan Campus Pokhara (28.19°N, 83.97° E) at 810 m asl to take real-time measurements of PM<sub>1.0</sub>, PM<sub>2.5</sub>, and PM<sub>10</sub> concentrations. In this study, we have presented the analysis of fine particulate matter PM<sub>2.5</sub> in the Valley. The Kathmandu Valley is a fast-urbanizing city located between the Indo-Gangetic Plain in the south and the great Himalayas in the north (Sarkar et al., 2017). It is surrounded by tall mountains with an elevation ranging from 2000 m to 2800 m from all sides, giving a unique Bowl-shaped structure, which traps the pollutants within the valley (Kitada & Regmi, 2003). Moreover, the densely populated Valley with a population of 3 million is potentially affected by transboundary pollution and a gateway to high mountains and Himalaya.

Pokhara (28.19°N, 83.97°E) is the second largest city of Nepal which is a very famous tourist destination in Nepal. It is also known as city of lakes and surrounded by scenic mountains, flora and fauna. The valley is approximately at an altitude of 805 m asl and 200 km west of the capital city, Kathmandu. It is surrounded by 1000 to 2000 m hills and rises over 7000 m asl in the north within a span of 35 km. It is about 90 km northeast of the southern plains bordering the Indo-Gangetic Plain (IGP) (Dhungel et al., 2018; Singh et al., 2019; Tripathy et al., 2016). Pokhara receives the highest amount of precipitation during monsoon season with some different onset and departure dates of monsoon, which originates from the Bay of Bengal, for each year (Poudyal et al., 2014).

In monsoon season, the land becomes hot, and the ocean becomes cold in comparison to land, which creates more pressure over the ocean than on the land, causing the wind to blow mainly from the Bay of Bengal (BB) to the land side. High mountains on Pokhara's flank help to raise humid air masses, especially in the summer, causing a lot of precipitation that has a big impact on the amount of aerosols in the air. (Bhattarai et al., 2019; Ranabhat et al., 2015).

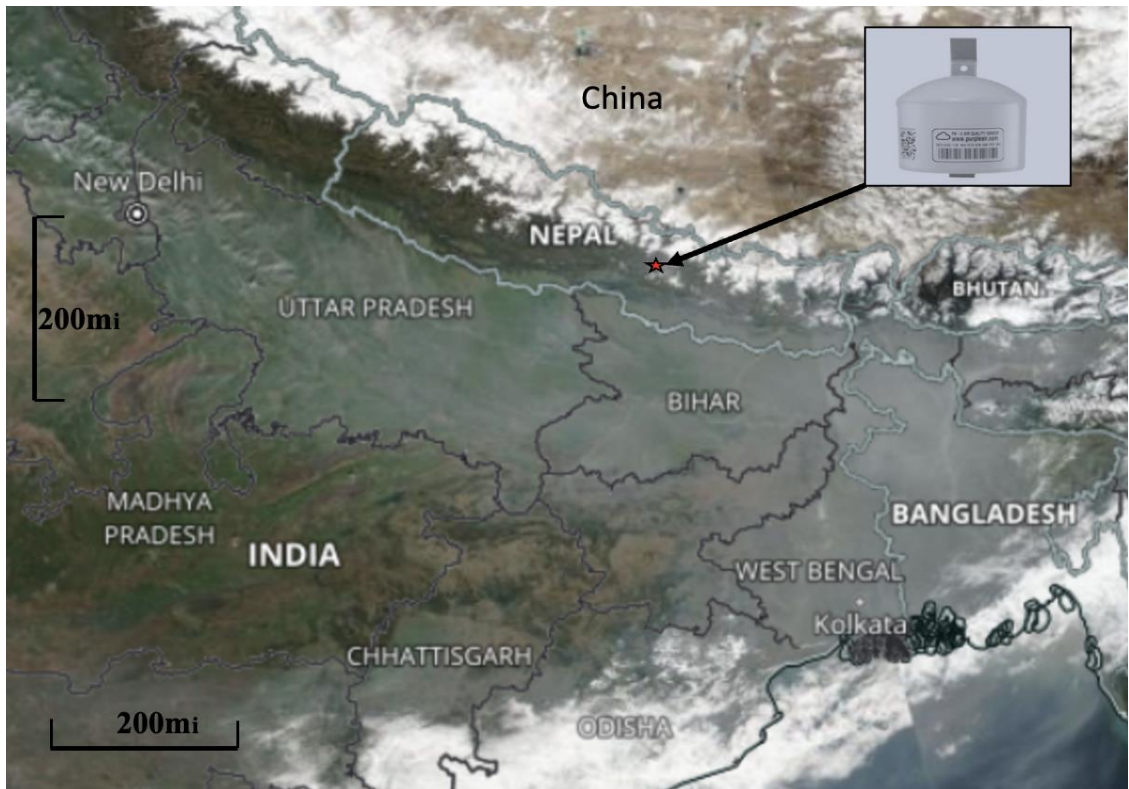


**Figure 18:** The Moderate Resolution Imaging Spectroradiometer (on NASA's Terra satellite) image shows an evident accumulation of haze which is visible along the Himalayan foothills on 9th February 2020. A PurpleAir monitor is also shown on the top right corner of the figure, which was installed on the IOE Pulchowk Campus, Lalitpur, Kathmandu, Nepal, as located on the map of Nepal.

EVK2-CNR (86.81 °E 27.96° N) is located at an elevation of 5079 m asl in the southwest valley of Mt. Everest in Nepal. It is surrounded by large moraines and high mountains. There is a clear mountain-valley circulation in the wind regime. All year long, the day time is dominated by surface wind from south direction whereas mountain winds dominate at night. Except in monsoon season, and north-western winds are observed as a result of the influence of the westerly winds (Bonasoni et al., 2008; Gobbi et al., 2010). This station is of special interest to observe the impact of climate change in the Himalayas.



Lumbini (27.67°N, 83.50°E, 110 m asl) is the southern part of Nepal in the Terai region and bordered to India. It also lies in the Indo-Gangetic Plain (IGP) which is one of the most polluted regions in Asia. Since it is the birthplace of Buddha, it attracts Buddhist pilgrims and enthusiast tourists. This makes Lumbini, one of the fast-growing economic centers with increasing number of industries, brick-kilns, a lot of construction work, all of which are the sources of air pollution in the region. Besides this, the transboundary pollution, biomass burning, fire like sources also enhances the pollution of the region. The study carried out in this location can give a small picture of aerosol properties in the terai. So Lumbini is also the area of interest of our study.

Jomsom (28.78°N, 83.71°E, 2825 m asl) is the district headquarter of Mustang district in Gandaki Province in northern part of Nepal that borders with China. It is situated in both the banks of Kali-Gandaki River with mount Dhaulagiri and mount Nilgiri in the backdrop. The trail passing through Jomsom follows Kali-Gandaki River, which forms deepest gorge in the world. The valley experiences the strong winds due the pressure difference between Tibetan plate and lower valleys. Past studies reveal that, it is the route of trans-boundary air pollution (Dhungel et al., 2018).

Kyanjin Gompa (28.21°N, 85.57°E, 3860 m asl) is a beautiful valley in the Langtang trekking zone of Rasuwa district in the Bagmati Province. Actually, it is the name of a Gumba (Monastery) around 700 years old (<https://english.onlinekhabar.com/kyanjin-valley-in-langtang-is-waiting-for-you-for-the-best-adventure-experience.html>, 6 March 2021) after which the valley is named. This is the highest human settlement region in the Langtang valley. It is surrounded by tall mountains like Lantang-Lirung, Changbu, Yubra, Yalla etc. As it is one of the major trekking routes in Nepal, the study of aerosol properties is important to observe climate pattern.

### **3.7 Interpretation of data**

Analysis of data is made using different clear sky and overcast conditions. Data interpretation and analysis of data are made by the use of FORTRAN 90 programming for Mie scattering. NOAA's HYSPLIT back trajectory and cluster analysis are applied to identify the source of aerosol particles. Graphical software Xm-grace, GNU plot, Igor-pro, and Origin pro 19 were used for graphical analysis.

### **3.7.1 HYSPLIT Back Trajectory**

The National Oceanic and Atmospheric Administration (NOAA) Air Resources Laboratory's (ARL) Hybrid Single-Particle Lagrangian Integrated Trajectory Model (HYSPLIT) is used to investigate the long-range transportation of air mass ending at the observation AERONET site. We have used satellite maps to present the aerosol sources that can affect the observation site due to the transportation of air masses. The satellite images are accessible in the HYSPLIT-WEB (<https://www.ready.noaa.gov/HYSPLIT.php>). Many researchers have already enjoyed this model for identifying air pollutants over the temporal and spatial ranges (Draxler & Hess, 1998; Stein et al., 2015). In our study, we have chosen seven days back trajectories with arrival heights of 1000 m, 500 m, and 100 m above the ground. The altitude for air mass trajectory is significant in classifying the aerosol types. Observation of air masses originating southerly, south-west, south-east, westerly, easterly, north easterly at a different layer of height will assist us identifying the aerosol types over the atmospheric column. Trajectory will be analyzed jointly with the satellite images of fire spots and dust images found on NASA Earth Observing System Data and Information System (EOSDIS). This will depict the possible air mass sources of aerosols due to forest fires, smoke, and dust activities that will add the aerosol components over the vertical column of the observation site.

### **3.7.2 Cluster Analysis**

Cluster analysis is a technique to group trajectories according to wind speed and direction to describe the main flows arriving at an observation site to identify the origin of the air masses affecting the region. It is a multivariate statistical technique designed to investigate structure within a dataset. According to the similarity principle, data sets with higher similarity are arranged in the same cluster and data sets with higher heterogeneity are arranged in different clusters. The calculations are made by the use of free software TrajStat (Wang et al., 2009).

### **3.7.3 Statistics**

Hourly averaged PurpleAir data  $PM_{2.5}$  ( $\mu g/m^3$ ) is compared with the corresponding MODIS AOD ( $\tau$ ) obtained from two satellite measurements, Aqua and Terra. These MODIS AOD ( $\tau$ ) data are corrected by dividing with  $f(RH)$ , where RH (Relative

Humidity) was obtained from the purple air sensor, installed at 15 meters above the ground, and are compared with the ground-based PM<sub>2.5</sub> data.

The MODIS AOD ( $\tau$ ) data from two satellites, Aqua and Terra, were co-located with the ground station location. The MOD/MYD04\_3K data, 3km x 3km AOD ( $\tau$ ) values at the 550 nm wavelength, were extracted by coinciding temporal variation of PM<sub>2.5</sub> obtained from the PurpleAir sensors in the ground level. The graphical analysis was conducted using the trust-region Levenberg-Marquardt least orthogonal distance method implemented in IGOR (<https://www.wavemetrics.com/>). Linear regression was then performed, and a coefficient of determination ( $R^2$ ) was presented to determine the regression representing the data. Values were presented for each combination coefficient of determination ( $R^2$ ) and two-tailed P to observe that the correlation is statistically significant. Data with less than 95% confidence intervals based on P values were disregarded.

## CHAPTER 4

### RESULTS AND DISCUSSION

#### 4.1 Variability of spectral columnar AOD ( $\tau$ ), AE and PW in different AERONET stations of Nepal

In this section, we have compared the variability of spectral columnar AOD ( $\tau$ ) alongwith the precipitable water (PW) and angstrom exponent (AE) for different seasons of different AERONET sites of Nepal. We have tried to match the data for maximum number of years as per their availability. For example, the data for the year 2015 and 2016 are not available in Lumbini station. We have presented the monthly mean data for different stations, Lumbini (2013, 2014, 2017 and 2018 (110 m)), Pokhara (2011 to 2015 (800 m)), Kathmandu-Bode (2012 to 2014 (1362 m)), Jomsom (2011 to 2013 (2825 m)), Kyanjin-Gompa (2017 to 2019 (3860 m)) and EVK2-CNR (2011 to 2013 (5079 m)). We know AOD ( $\tau$ ) is the attenuation of solar radiation due to vertical column of atmosphere at a place at a time and is significantly affected by atmospheric conditions and the wavelength of solar radiation. The hazy atmosphere shows the higher values of AOD ( $\tau$ ) whereas the clean and clear atmosphere shows the comparatively lower values of AOD ( $\tau$ ).

AE ( $\alpha$ ) is the measure of the ratio of fine to coarse mode aerosol particles that gives an idea about the average size of the particles. Actually, it is inversely related to the average size of the aerosol particles. In general,  $\alpha \leq 1$  indicates the aerosol size distribution dominated by coarse mode ( $r_{\text{eff}} > 0.5 \mu\text{m}$ ) and  $\alpha \geq 1$  indicates a domination of fine mode ( $r_{\text{eff}} < 0.5 \mu\text{m}$ ) showing a presence of urban pollution and biomass burning (Eck et al., 1999; Srivastava et al., 2012). When we analyzed the monthly mean AOD ( $\tau$ ) at 500 nm for above mentioned stations, the monthly average value shows a decreasing trend with increasing altitude from Lumbini (110 m) to EVK2-CNR (5079 m). In Lumbini, it was observed the maximum AOD ( $\tau$ ) ( $0.94 \pm 0.38$ ) in December and the minimum ( $0.29 \pm 0.03$ ) in July with a monthly average of  $0.71 \pm 0.19$  as shown in Table 2. In Pokhara (800 m) the maximum, minimum and monthly average were observed to be  $0.72 \pm 0.16$  (May),  $0.22 \pm 0.13$  (July) and  $0.45 \pm 0.16$  respectively. Though

the monthly maximum ( $0.78\pm 0.07$ ) in KTM-Bode (1362 m) is higher than that in Pokhara, the monthly average ( $0.39\pm 0.09$ ) is lower following the decreasing trend with altitude. The monthly average of AOD ( $\tau$ ) at 500 nm in Jomsom (2825 m), KG (3860 m) and EVK2-CNR (5079 m) are  $0.08\pm 0.03$ ,  $0.06\pm 0.02$  and  $0.04\pm 0.01$  respectively; which is significantly low and indicating the fairly clean atmosphere. These three stations at higher altitude shows a small increase in the value of AOD ( $\tau$ ) during the month of May that may be due to trans-boundary fine particles. In almost all stations under study for the above- mentioned period show a higher value of AOD ( $\tau$ ) during pre-monsoon season.

The analysis of AE in all the stations, except in EVK2-CNR shows the average value of  $\alpha > 1$ , indicating the domination of fine-mode aerosols in the wavelength range of 440 nm to 870 nm. The highest average is observed in Jomsom ( $1.52\pm 0.18$ ) and lowest in EVK2-CNR ( $0.77\pm 0.34$ ). AE shows a strong dependence on wavelength that can be analyzed to draw crucial information for aerosol size distribution ((Kaskaoutis & Kambezidis, 2006, 2008; Schuster et al., 2006). The higher values of  $\alpha$  in these locations suggest the abundance of fine-mode particles that originates from biomass burning, mineral fuel burning, industrial and vehicular emission as well as trans-boundary pollution (Giles et al., 2012; Kedia et al., 2014; Ramachandran & Rupakheti, 2021). But lower value of  $\alpha$  in EVK2-CNR indicates the presence of coarse-mode particles due to trans-boundary pollution as well as the dust due to very windy atmosphere (Bonasoni et al., 2008; Gobbi et al., 2010).

Precipitable water (PW) is the total water vapour content in the vertical column in the atmosphere that plays significant role in climate behaviour. From Table 2, it can be observed that the monsoon season is the prime season of rainfall in Nepal. The maximum amount of PW is observed during the month of July in Lumbini ( $5.87\pm 0.12$ ) cm, Pokhara ( $4.63\pm 0.18$ ) cm, KTM-Bode ( $3.69\pm 0.13$ ) cm and Jomsom ( $1.86\pm 0.08$ ) cm whereas KG ( $1.16\pm 0.11$ ) cm and EVK2-CNR ( $0.64\pm 0.03$ ) cm observed maximum PW during August. The minimum value of PW is observed in January in all the stations. Though Pokhara is considered as the place to observe larger amount of precipitation, our data in the given period of time shows that average value of PW is maximum in Lumbini ( $3.25\pm 0.21$ ) cm, Pokhara ( $2.63\pm 0.17$ ) cm, KTM-Bode ( $1.83\pm 0.13$ ) cm, Jomsom ( $0.85\pm 0.07$ ) cm, KG ( $0.49\pm 0.05$ ) cm and EVK2-CNR ( $0.23\pm 0.02$ ) cm. It indicates the decreasing trend of PW with increasing altitude (Wang et al., 2007).

**Table 2:** Monthly mean maximum and minimum values for PW(cm), AE (nm) and AOD ( $\tau$ ) (nm) for different stations Lumbini (2013, 2014, 2017 and 2018 (110 m)), Pokhara (2011 to 2015 (800 m)), Kathmandu-Bode (2012 to 2014 (1362 m)), Jomsom (2011to 2013 (2825 m)), Kyanjin-Gompa (2017 to 2019 (3860 m), EVK2-CNR (2011 to 2013) (5079 m)).

Aeronet Sites	PW (cm)		AE (440-870) nm		AOD ( $\tau$ ) 500 nm	
	Max	Min	Max	Min	Max	Min
Lumbini (110 m)	(5.87±0.12) July	(1.24±0.00) Jan	(1.37±0.01) Nov	(1.05±0.02) May	(0.94±0.38) Dec	(0.29±0.03) July
	Average (3.25±0.21)		Average (1.23±0.06)		Average (0.71±0.19)	
Pokhara (800 m)	(4.63±0.18) July	(1.18±0.10) Jan	(1.41±0.07) Jan	(1.08±0.31) Aug	(0.72±0.16) May	(0.22±0.13) July
	Average (2.63±0.17)		Average (1.28±0.18)		Average (0.45±0.16)	
KTM-Bode (1362 m)	(3.69±0.00) July	(0.66±0.08) Jan	(1.53±0.00) July	(1.17±0.02) May	(0.78±0.07) Apr	(0.14±0.00) July
	Average (1.83±0.13)		Average (1.31±0.09)		Average (0.39±0.09)	
Jomsom (2825 m)	(1.86±0.08) July	(0.20±0.00) Jan	(2.02±0.12) Sept	(1.27±0.34) Mar	(0.22±0.07) May	(0.04±0.01) Sept
	Average (0.85±0.07)		Average (1.52±0.18)		Average (0.08±0.03)	
Kyanjin– Gompa (KG) (3860 m)	(1.16±0.11) Aug	(0.10±0.02) Jan, Dec	(1.60±0.79) Aug	(1.08±0.16) Dec	(0.12±0.03) May	(0.02±0.01) Dec
	Average (0.49±0.05)		Average (1.21±0.21)		Average (0.06±0.02)	
EVK2-CNR (5079 m)	(0.64±0.03) Aug	(0.05±0.00) Jan	(1.16±0.01) Jan	(0.44±0.23) Aug	(0.05±0.02) May, Jun	(0.02±0.00) Jan, Oct
	Average (0.23±0.02)		Average (0.77±0.34)		Average (0.04±0.01)	

Figure 19 shows the monthly variation of PW which shows nearly similar trend. In almost all the stations, PW increases with smaller values from January and reaches to peak value in July/ August and then decreases gradually and reaches to minimum around December. On comparing PW trend with  $\tau$  values, it seems they correlate inversely with each other. Previous studies in the southeast Asia region indicates that there might be both positive or negative correlation between precipitation and AOD ( $\tau$ )

(Ng et al., 2017). But we cannot observe any significant correlation between PW and AE. From one station to another, there are different types of variation of AE with PW.

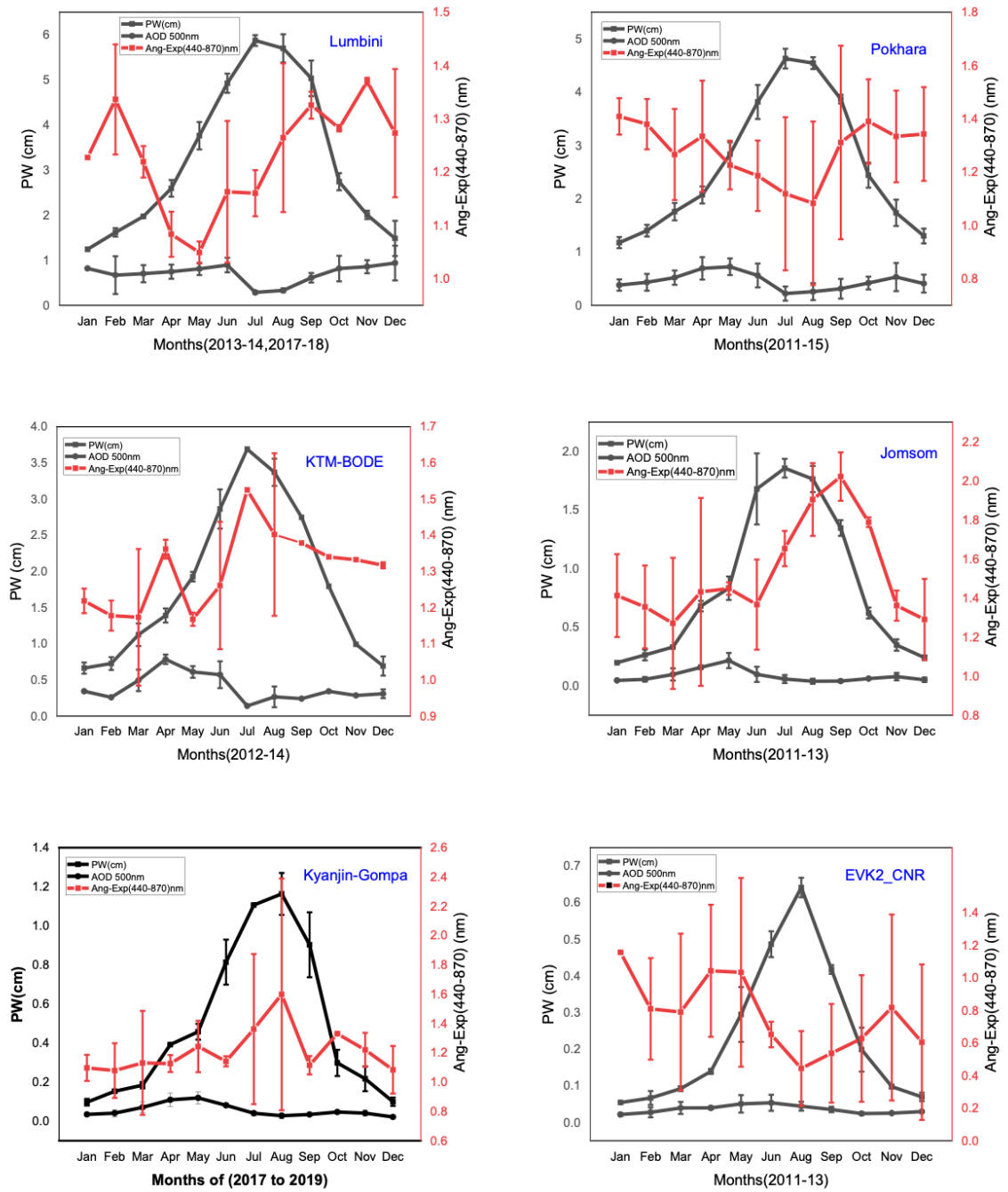


**Figure 19:** Comparative analysis of seasonal variation of monthly mean AOD at 500 nm, AE (440 nm-870 nm) and PW (cm) in different AERONET stations; Lumbini, Pokhara, KTM-Bode, Jomsom, Kyanjin-Gompa and EVK2-CNR in the order of increasing altitude.

## **4.2 Seasonal variation of monthly mean Single Scattering Albedo (SSA) at different AERONET Sites of Nepal**

Single Scattering Albedo (SSA) is one of the crucial optical property to explain the different types of chemical species present in atmospheric aerosols. It gives an idea of scattering and absorbing properties of aerosols. The mixing of same type of particles and different types of particles in the atmosphere possesses little effect on scattering but larger impact on absorption efficiency(Liu et al., 2014). Since it contains the combined effect of absorption and scattering properties, determining SSA values are very important. For purely scattering aerosols like sulphates, SSA value is nearly equal to 1 and for absorbing aerosol particles like black carbon and mineral dust, it has lower values and for purely absorbing its value is zero (Dubovik et al., 2002; Kedia et al., 2014). According to Dubovik et al., (2002), different values for SSA for different types of aerosols are reported as 0.78-0.94 for biomass burning, 0.83-0.98 for urban/ industrial and mixed aerosols, and 0.92-0.99 for desert dust and marine aerosols.

The average value of SSA in all the locations except in EVK2-CNR is found to vary in the range of 0.79 to 0.96 in the observed period of time. The general trend of SSA seems to be maximum at a wavelength of 675 nm and the higher values are observed in monsoon and post monsoon season with winter and pre-monsoon lower values. When monthly variation is observed, the SSA value decreases from January to April and increases from May to December.



**Table 3:** Seasonal and spectral variation of monthly mean SSA at different AERONET sites Lumbini (2013, 2014, 2017 and 2018 (110 m)), Pokhara (2011 to 2015 (800 m)), Kathmandu-Bode (2012 to 2014 (1362 m)), Jomsom (2011 to 2013 (2825 m)), and EVK2-CNR (2011 to 2013) (5079 m).

AERONET Sites	SSA	Wavelengths			
		440 nm	675 nm	870 nm	1020 nm
Lumbini (110 m)	Max	(0.96±0.00) Sept	(0.96±0.00) Sept	(0.95±0.00) Sept	(0.95±0.00) Sept
	Min	0.88±0.00 Dec	0.89±0.00 Dec	(0.87±0.00) Dec	(0.85±0.00) Dec
	Average	0.91±0.02	0.92±0.01	0.91±0.02	0.90±0.03
Pokhara (800 m)	Max	(0.89±0.02) Jan	(0.91±0.02) Jan	(0.89±0.03) Jan	0.88±0.03 May
	Min	(0.87±0.03) Jun	(0.87±0.07) Jun	(0.85±0.08) Jun	(0.83±0.12) Jun
	Average	0.88±0.03	0.89±0.04	0.87±0.05	0.86±0.06
KTM-Bode (1362 m)	Max	(0.93±0.00) Oct	(0.93±0.00) Oct	(0.91±0.00) Oct	(0.90±0.00) Oct
	Min	(0.83±0.00) Apr	(0.83±0.00) Apr	(0.81±0.00) Apr	(0.79±0.00) Apr
	Average	0.87±0.00	0.87±0.00	0.85±0.00	0.84±0.00
Jomsom (2825 m)	Max	(0.99±0.00) Jan	(0.98±0.00) Jan	(0.98±0.00) Jan	(0.98±0.00) Jan
	Min	0.89±0.00 Mar	(0.92±0.00) May	(0.92±0.00) May	(0.91±0.00) May
	Average	0.95±0.00	0.96±0.00	0.96±0.00	0.96±0.00
EVK2-CNR (5079 m)	Max	(0.98±0.01) Jan	(0.98±0.01) Jan	(0.97±0.01) Jan	(0.97±0.01) Jan
	Min	(0.40±0.01) Sept	(0.33±0.01) Sept	(0.29±0.02) Sept	(0.27±0.02) Sept
	Average	0.74±0.14	0.70±0.16	0.68±0.17	0.68±0.17

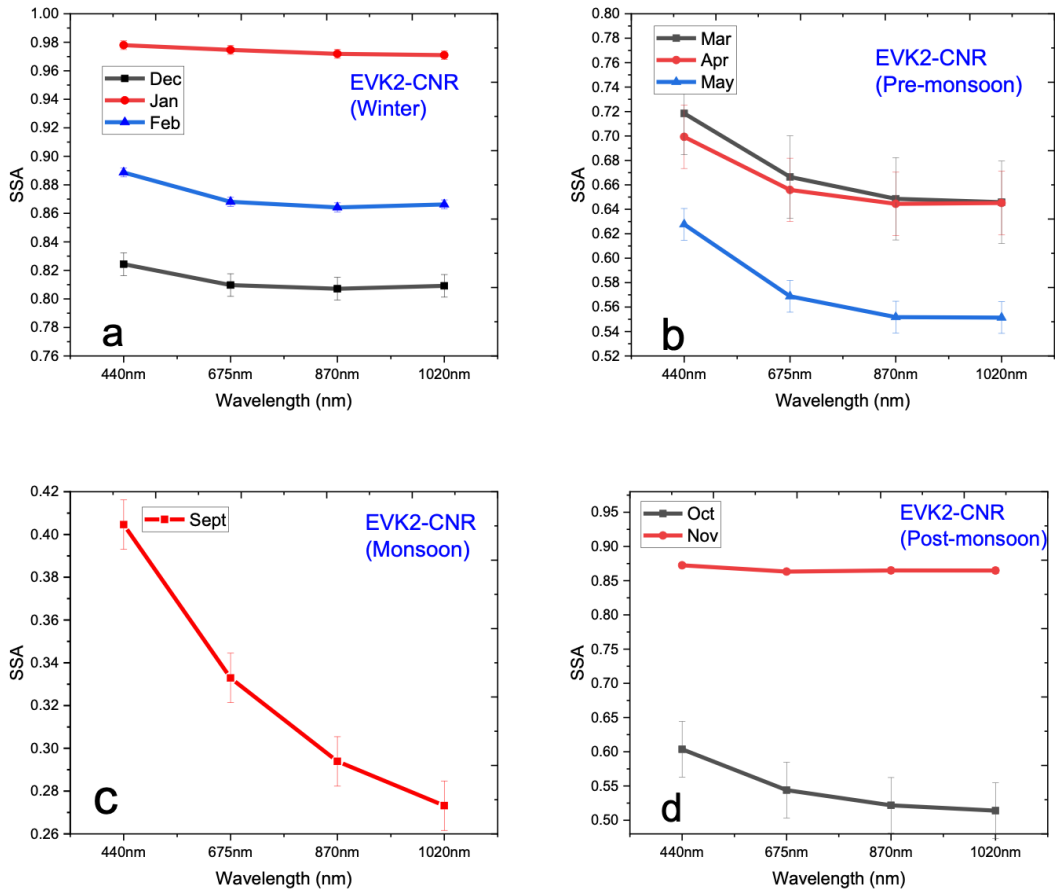


**Figure 20:** Seasonal spectral variation of monthly mean SSA at EVK2-CNR AERONET Station for the years 2011-2013

The observation of SSA values on EVK2- CNR shows extreme results. In the month of September SSA values are found to be very low  $0.27 \pm 0.02$  (1020 nm),  $0.29 \pm 0.02$  (870 nm),  $0.33 \pm 0.01$  (675 nm) and  $0.40 \pm 0.01$  (440 nm) in all four wavelengths. The SSA measurements are found to be very few in the monsoon-period. This is due to the lack of  $360^\circ$  clear sky conditions needed to perform almucantar observations. When the available data are less in number for a large period of a year, then it makes the SSA statistics weaker. Previous studies performed in EVK2\_CNR and Tibetan side of the Everest suggested the presence of such low values may be due to the presence of very large particles ( $>20 \mu\text{m}$ ). The inversion algorithm could not reproduce the data for such large sized particles (Gobbi et al., 2010; C. Xu et al., 2014).

The average value of SSA in Jomsom is 0.96 with a maximum of 0.99 in January and a minimum of 0.89 in March. Though it ranges from 0.89 to 0.99, most of the time of a year the SSA value is in the range of 0.92 – 0.99 indicating the presence of scattering type of particles, that may be dust particles of local origin. As it can be seen in the

Figure 21, winter, monsoon and post-monsoon are the seasons with higher values of SSA and pre-monsoon is the only season of lower SSA values. Previous studies carried out in different parts of the world revealed that the SSA values found to decrease for biomass burning and continental aerosol particles with increasing wavelength from 440 nm to 1020 nm, whereas it is found to increase with increasing wavelength for the larger aerosol particles dominated by dust (Giles et al., 2012; Russell et al., 2010).

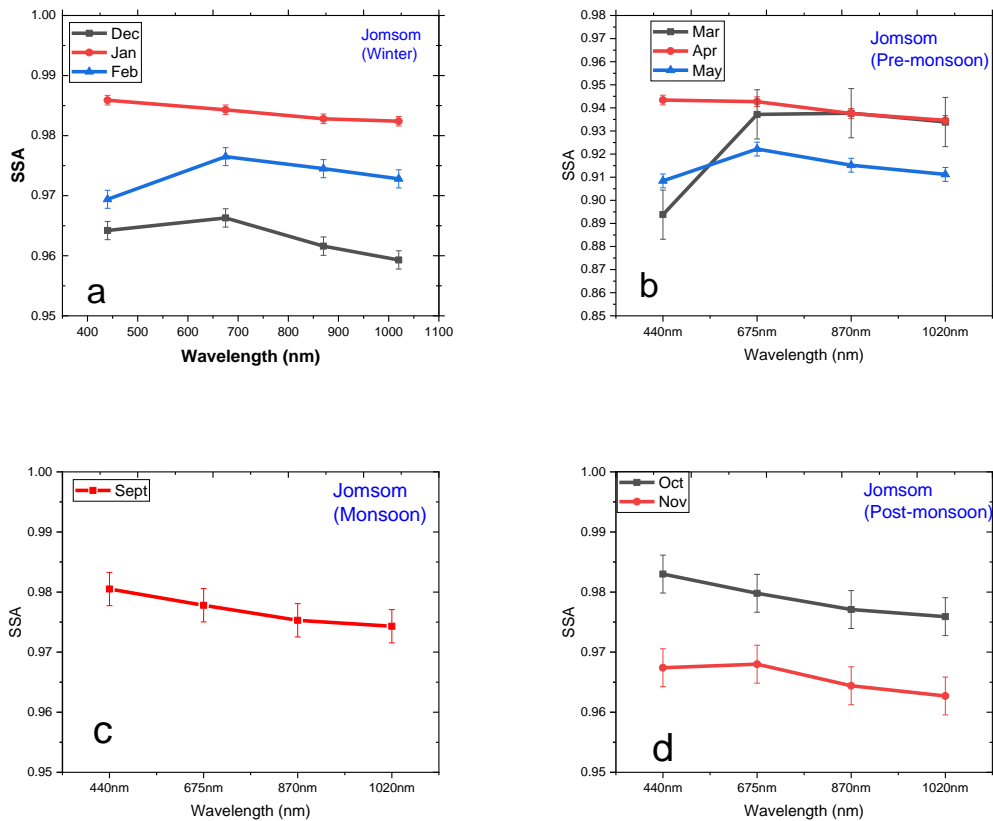


**Figure 21:** Seasonal spectral variation of monthly mean SSA at Jomsom for the years 2011-2013.

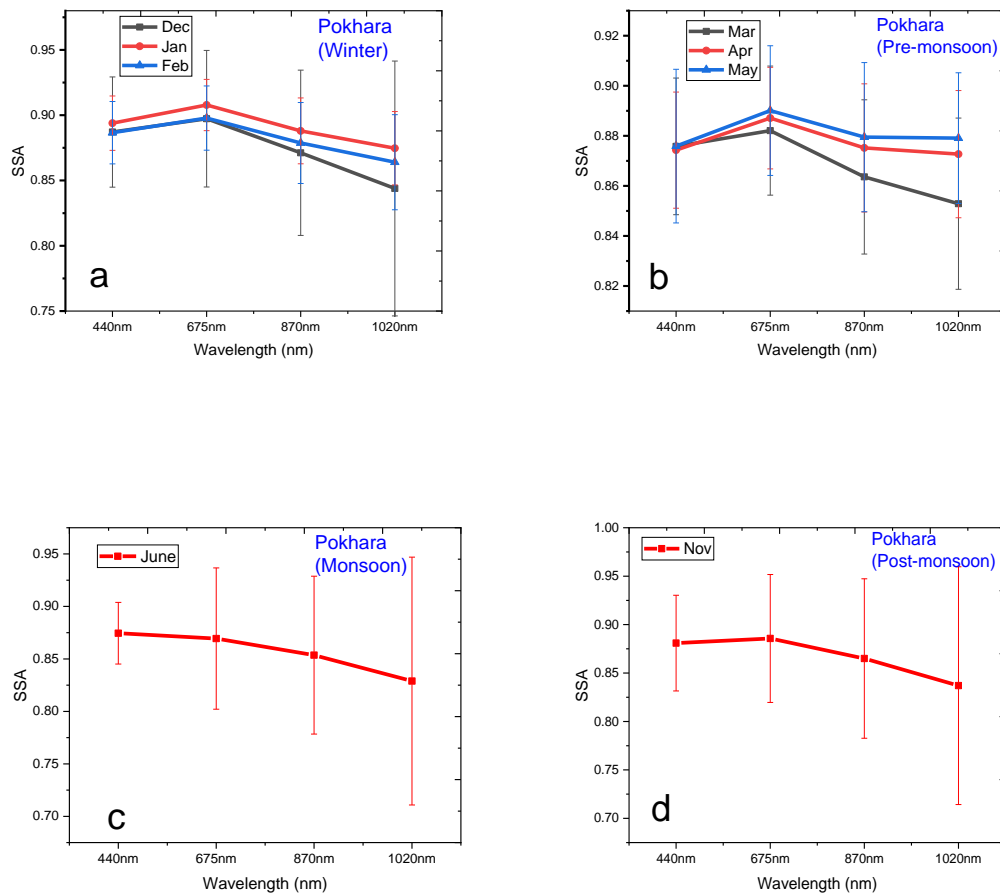


**Figure 22:** Seasonal spectral variation of monthly mean SSA at Pokhara AERONET Station for the years 2011-2015.

The SSA in the month of September, October, November, and December shows similar trend of decreasing value with the increasing wavelength, indicating the presence of biomass burning and continental aerosol in Jomsom whereas other months contain mixed type of dust along-with transboundary aerosol due to updraft of particles due to convection (Dhungel et al., 2018; Singh et al., 2018).

Pokhara observes minimum value of SSA ( $0.83 \pm 0.12$ ) in the month of June at 1020 nm and maximum value in the month of January ( $0.91 \pm 0.02$ ) at 675 nm with an annual average of ( $0.89 \pm 0.04$ ). Previous studies analyzed over Pokhara reported similar results (Ramachandran & Rupakheti, 2020; A. Singh et al., 2019). Since pre-monsoon season in the IGP region experiences strong convective activity, the near-surface pollution gets lifted to higher altitudes and transported towards northern high hills and mountains (Rupakheti et al., 2017; Singh et al., 2019). The vertical uplift of airmasses from IGP region is affected by westerly circulation that transports it towards mountain regions

(R. Gautam et al., 2011; Lawrence & Lelieveld, 2010; Lüthi et al., 2015; Putero et al., 2018). The accumulation and regional transport of fine mode aerosols from south Asia during post monsoon and winter season might have contributed to lower the value of SSA with flat spectra (Ramachandran & Rupakheti, 2021). During monsoon, the heavy precipitation in the region suppresses the regional transportation of aerosol particles and even the local factors like biomass burning and dust of local origin, resulting higher value of SSA. During pre-monsoon season, a mix characteristic of aerosol particles can be observed in Pokhara valley. Relatively lower values of SSA during pre-monsoon may be due to the domination of dust particles of local origin along-with trans-boundary pollution from IGP region.

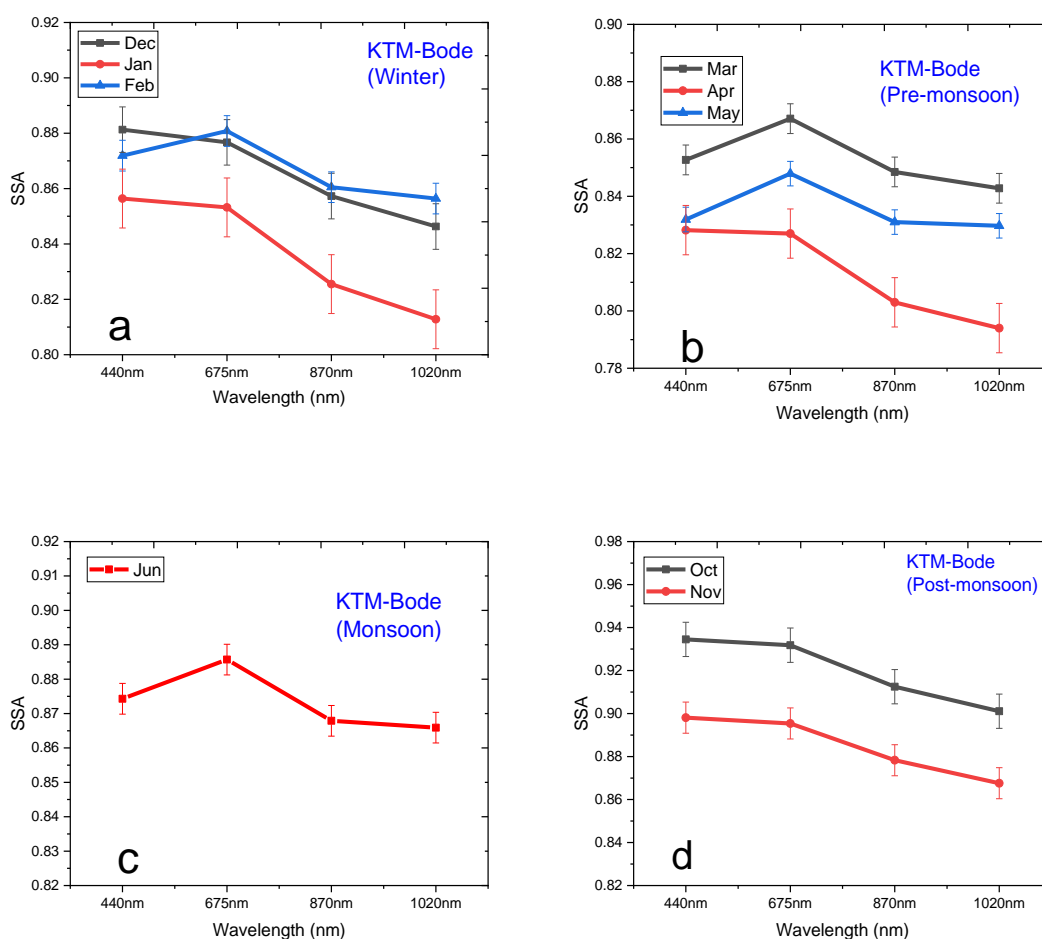


**Figure 23:** Seasonal spectral variation of monthly mean SSA at Kathmandu-Bode (KTM-BODE) AERONET Station for the years 2012-2014.

The average SSA of KTM-Bode is lowest (0.84 at 1020 nm) of all the stations except EVK2-CNR. The lowest value of SSA is in the month of April in all the spectral range which is less than 0.87, which indicates the domination of light-absorbing carbonaceous

particles which is similar to the previous results (Ramachandran et al., 2020). The maximum value of SSA is observed during post-monsoon (October 0.93). The emission of such particles is of anthropogenic nature, basically biomass burning and the vehicular emissions.

The SSA values in Lumbini shows the presence of absorbing type of aerosols as the average value of SSA is greater than 0.90 at all wavelengths. But it doesnot indicate any significant spectral dependence which is consistent with previous results (Rupakheti, Kang, Rupakheti, et al., 2018; Wan et al., 2017).

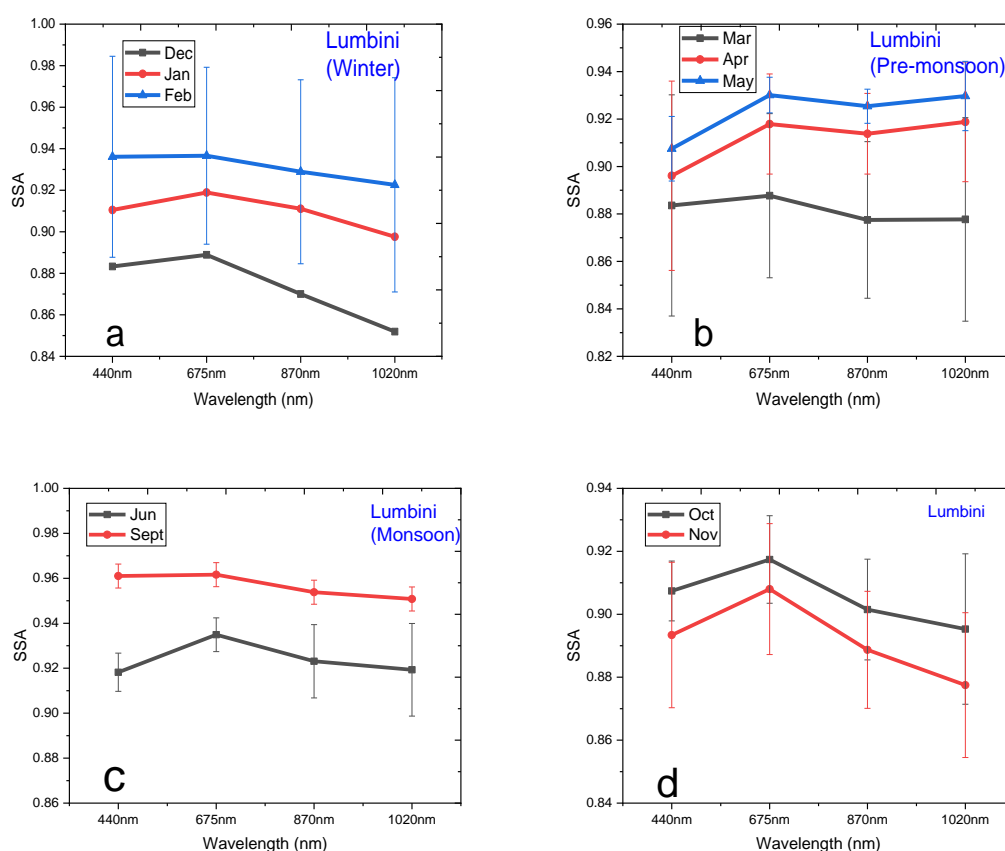


**Figure 24:** Seasonal spectral variation of monthly mean SSA at Lumbini AERONET Station for the years 2013-2014, 2017 and 2018.

The maximum value of SSA is observed (0.96 at 675 nm) in September showing the presence of scattering type aerosols whereas a minimum is observed (0.85 at 1020 nm) in December showing the presence of absorbing type of aerosols. The study performed by Wan et al. (2017), Lumbini region is heavily loaded with the absorbing aerosols like elemental carbon (EC) and black carbon (BC) in post-monsoon season. It may be due

to large amount of biomass burning in the region during the post-monsoon season. In conclusion , we can say, the aerosol particles in this region are highly absorbing in nature.

#### 4.3 Monthly variation of columnar AOD 550 nm over Nepal for the time period of 2015-2020; as analyzed from MODIS satellite data.

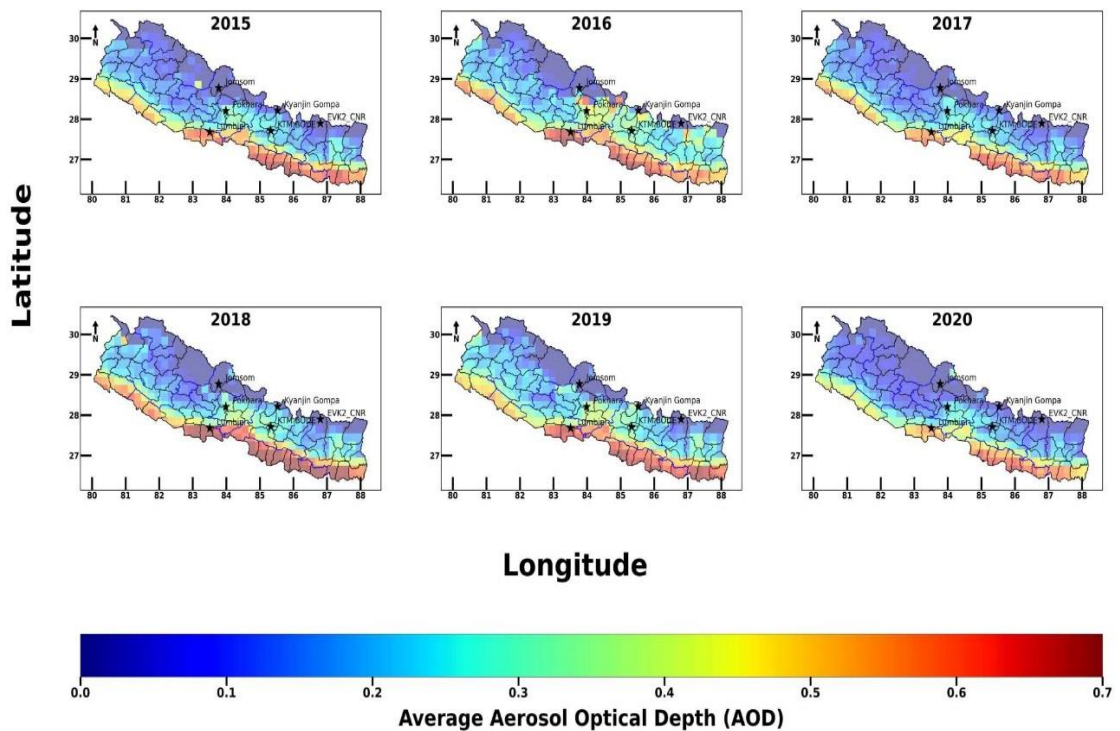


**Figure 25:** Distribution of annually averaged AOD at 550 nm over Nepal for the period of 2015 to 2020 as observed by MODIS AQUA and TERRA satellite.

We have observed the spatial variation of MODIS AOD data over Nepal for the time period of 2015-2020. It shows the higher concentration of AOD values in the southern plain (Terai region) of Nepal which borders with the Indo-Gangetic Plain (IGP); one of the densely populated and highly polluted area in the south Asia region. The eastern part of the Terai region is observed to have greater value of AOD compared to the western part. Another important pattern we can observe from these datasets is that, the value of AOD decreases gradually with the increase in altitude. The low value of AOD at higher altitude is due to the high surface reflectance. The AERONET stations under our investigation shows similar trend as that shown by MODIS AOD at 550 nm. We found the average AOD at 550 nm in different AERONET stations; Lumbini (2013-2018), Pokhara (2011-2015), KTM-Bode (2012-2014), Jomsom (2011-2013), Kyanjin-

Gompa (2017-2019) and EVK2\_CNR (2011-2013) are  $(0.71\pm0.19)$ ,  $(0.45\pm0.16)$ ,  $(0.39\pm0.09)$ ,  $(0.08\pm0.03)$ ,  $(0.06\pm0.02)$  and  $(0.04\pm0.01)$  respectively. In both the observations, Lumbini region is observed to have highest value of AOD and EVK2\_CNR experiences the least value. On evaluating the maps, we can see the year 2016 has higher values of AOD over Nepal and the year 2020 has least values. As we know the year 2020 as the year of COVID pandemic year and Nepal along-with many other countries of the world had experienced severe lockdown. It helped to minimize the emission of anthropogenic aerosols and the value of AOD significantly decreased all over Nepal which is demonstrated by various studies during that period. In almost all the years of observation, we can see that the central and western mid-hills experiencing higher values of AOD. These are the regions of increased anthropogenic activities, as big cities like Kathmandu and Pokhara are part of this region.

#### **4.4 Variability of Spectral Columnar AOD and Precipitable water of Pokhara AERONET site. (Analysis based on 10 years data-Pokhara station).**

This section presents the spectral AOD's ( $\tau$ ) temporal fluctuation to precipitable water vapor (PW) as well as its monthly and seasonal variations. Figure 26 displays the monthly mean spectral AOD ( $\tau_{AOD}$ ) values, for 2010 to 2018, at seven different wavelengths,  $0.34 \mu\text{m}$ ,  $0.38 \mu\text{m}$ ,  $0.44 \mu\text{m}$ ,  $0.50 \mu\text{m}$ ,  $0.675 \mu\text{m}$ ,  $0.87 \mu\text{m}$ , and  $1.02 \mu\text{m}$ . We removed monthly averaged aerosol data from any months with  $\tau_{AOD}$  data for less than ten days from our statistical analysis. Due to this limitation on data availability, we computed the mean values for each calendar month for the given time period. Due to data screening by clouds and the requirement that the sun photometer always be parked in a covered position anytime the rain sensor is wet, Level 2 aerosol data for the rainy season were quite scarce on the AERONET website.

As can be seen from the overall pattern of spectral fluctuations, the AOD is larger at shorter wavelengths and decreases at longer wavelengths. The spectral AOD was found to be at its peak in April, followed by March, May, February, June (January, November), (December, October), and September (August and July).



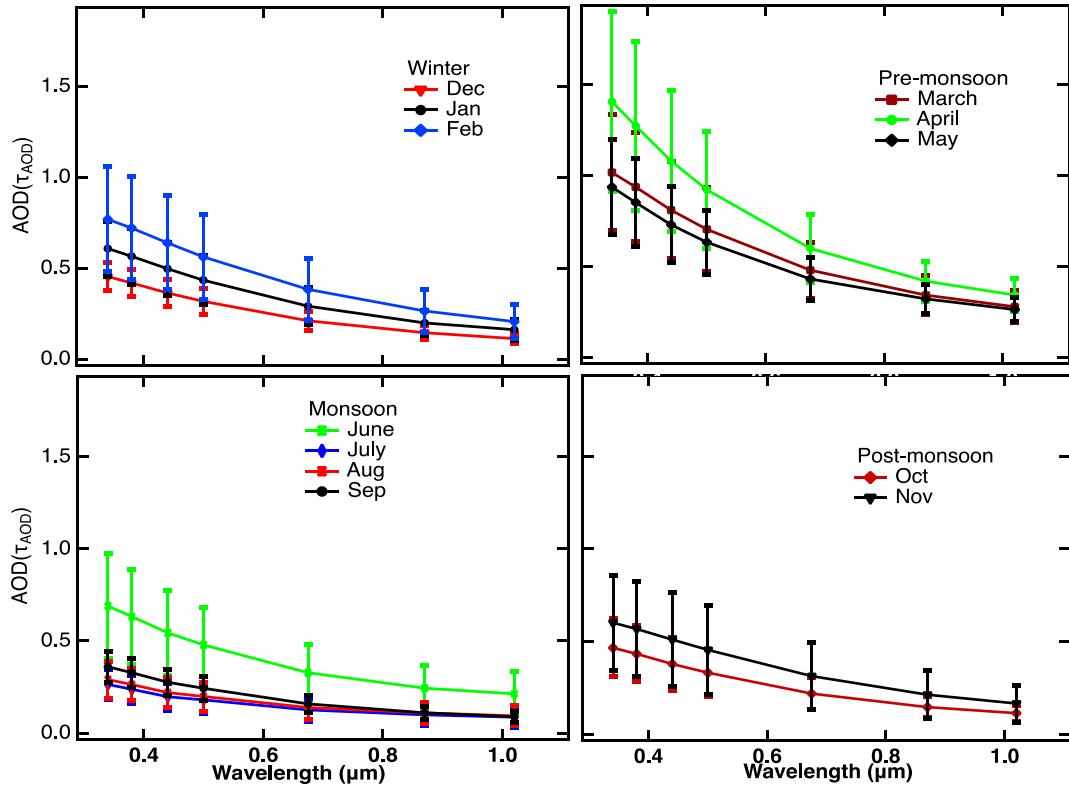


**Figure 26:** Spectral variation of monthly mean, over 9 years period between 2010-2018, aerosol optical depth representing different seasons at Pokhara (Regmi et al., 2020).

At all wavelengths, the spectral AOD for the months in parentheses is remarkably consistent. The spectral gradient at the longer wavelengths lessens during the monsoon season. The gradient in spectral AOD at the longer wavelengths decreases, which is one of the distinctive characteristics of the seasonal AOD. Figure 26 illustrates the distinctive characteristics of seasonal AOD, with the largest aerosol loading occurring during the months of pre-monsoon season, followed by winter, post-monsoon, and monsoon season. The aerosol loadings during winter and post-monsoon seems very less deviated from each other.

The temporal variation of light attenuation was analyzed using a monthly mean AOD at  $0.50 \mu\text{m}$  ( $\text{AOD}_{0.50}$ ), and column-averaged precipitable water (PW) in centimeters for various months and seasons (Figure 27). The values of  $\text{AOD}_{0.50}$ , varies from 0.31 to 0.56 in winter with an average of  $0.43 \pm 0.12$ , 0.63 to 0.92 in pre-monsoon with an average of  $0.75 \pm 0.15$ , 0.18 to 0.47 in monsoon with an average of  $0.27 \pm 0.13$ , and 0.33 to 0.45, in post-monsoon season with an average of  $0.39 \pm 0.08$ . The PW variation demonstrates a similar pattern of rainfall in Pokhara with a rise from months of winter to monsoon seasons and then a fall in the post-monsoon season (<https://>

//www.dhm.gov.np/climate). The monsoon season experiences a substantial variation on AOD<sub>0.50</sub> due to the rainfall.

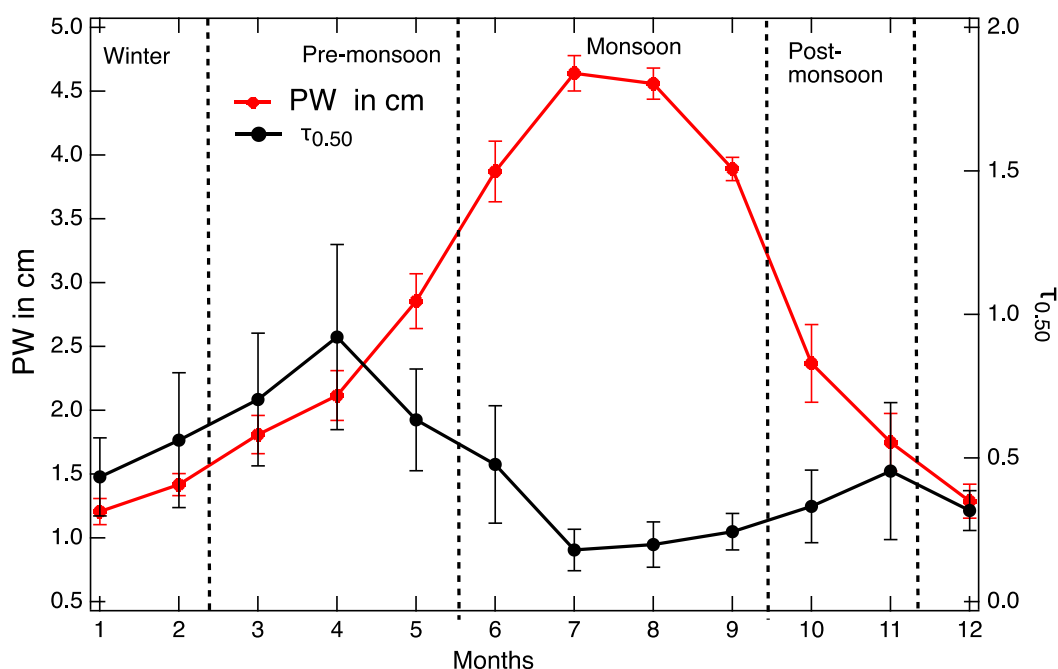


**Figure 27:** Seasonal variation (2010-2018) of monthly mean AOD 500 nm and precipitable water at Pokhara (Regmi et al., 2020).

The variations in the values of PW and AOD<sub>0.50</sub> indicates two distinct characteristics. They substantially correlated between December and April, with high  $R^2$  (0.91) and low  $p$ -values (0.01). However, when data of May were included,  $R^2$  dropped to 0.35 and  $p$ -value rose to 0.21. However, they change inversely with an  $R^2$  of 0.43 and  $p$ -value of 0.15 during the monsoon and post-monsoon months. Previous research has demonstrated that atmospheric water vapor can act as a catalyst for multiphase reactions that result in the production of gas to particle conversion and play a significant role in the hygroscopic growth of aerosols, which in turn impacts the aerosol optical properties (Altaratz et al., 2013). It suggests AOD<sub>0.50</sub>, which has a significant correlation with PW from December to April, is basically associated with the actual aerosol loading and not with the hygroscopic growth of aerosol particles. We have not performed a chemical analysis for black carbon, dust, sulfate, and organic carbon at the observation site, which may give a picture of the hygroscopic impact on AOD<sub>0.50</sub>. The effect of aerosol loading for increased AOD is supported by the analysis of Angstrom turbidity coefficient ( $\beta$ ) (explained in next section). Instead of showing the hygroscopic growth of aerosol particles, a prior study on the latitudinal change of aerosol characteristics

over the IGP region to the Central Himalayas during the pre-monsoon investigated at the AOD due to aerosol loading over the observation site.(Dumka et al., 2014).

#### **4.5 Time Series (2010-2018) Analysis of Aerosol Inversion Products (AE, Curvature of AOD Spectra, SSA, AAOD and AAE)**

Monthly and seasonal variation of spectral AOD in the wavelength ranges of 0.34  $\mu\text{m}$  to 1.02  $\mu\text{m}$  is studied using linear and second-order polynomial fit. Angstrom parameters for different types of aerosol sources like biomass burning, urban, industrial and desert dust for several AERONET sites were investigated in the past using spectral AOD to distinguish them (Eck et al., 1999). Figure 28 represents monthly Ångström parameters ( $\alpha$  and  $\beta$ ) and curvature of the spectral AOD curve ( $\alpha_2$ ). From the monthly averaged data, we found that the average seasonal  $\alpha$  was  $1.14 \pm 0.01$  in winter,  $1.17 \pm 0.07$  in the pre-monsoon,  $1.10 \pm 0.08$  in monsoon, and  $1.12 \pm 0.08$  in the post-monsoon season. Similarly,  $\alpha' (= -2\alpha_2)$  were obtained  $1.03 \pm 0.23$  for winter,  $0.55 \pm 0.14$  for pre-monsoon,  $0.23 \pm 0.38$  for monsoon, and  $1.22 \pm 0.08$  for post-monsoon seasons. The seasonal turbidity parameters,  $\beta$ , were obtained to be  $0.18 \pm 0.05$  in winter,  $0.31 \pm 0.04$  in pre-monsoon,  $0.11 \pm 0.06$  in monsoon, and  $0.16 \pm 0.04$  in post-monsoon seasons. Additionally,  $\beta$  provides an outline of aerosol loading in the vertical column, where larger  $\beta$  indicates higher aerosol loading and smaller  $\beta$  indicates lower aerosol loading. Figure 28 illustrates the seasonal fluctuations in the aerosol size spectrum, which we can see the value of  $\alpha$  are more or less the same from season to season despite a substantial variance of  $\text{AOD}_{0.50}$ .

Though the value of  $\alpha$  is found to be highest in the pre-monsoon season, followed by winter, post-monsoon and summer, the value of  $\alpha'$  is found to be different even for similar values of  $\alpha$ . It clearly indicates that the variation of aerosol microphysical properties can be better explained by the climatological pattern of  $\alpha'$ , rather than that of  $\alpha$ . Figure 29 a and b shows the significant variation of  $\alpha'$  for the months with similar values of  $\alpha$ . It is mainly observed in those months of transition of seasons, during which transition of air masses take place. Values of  $\alpha'$  greater or close to 1 in the post-monsoon and winter season indicate the contribution of fine mode particles in the columnar aerosol size distribution. Such particles originated from anthropogenic, biomass burning, urban and industrial sources. A value of  $\alpha'$  close to 0.5 during pre-monsoon

season indicates a bimodal distribution of particles and a value close to 0.2 during monsoon indicate a dominance of coarse mode particles.

From Figure 29 a, it is observed that  $AOD_{0.50}$  and  $\beta$  show a significant correlation ( $R^2 = 0.98$  and  $p\text{-value} = 4.6 \times 10^{-11}$ ). It means higher values of  $\beta$  correlating with  $AOD_{0.50}$  was associated with aerosol loading, mainly dominated by fine mode particles. The lowest values of  $\beta$  correlating with low value of  $AOD_{0.50}$ , smallest value of  $\alpha$  ( $\sim 1$ ), and  $\alpha'$  (close to 0.2) supports the contribution of coarse mode particles compared to fine mode particles on overall AOD. The lowest value of  $AOD_{0.50}$  is associated with the significant amount of rainfall during the monsoon season.

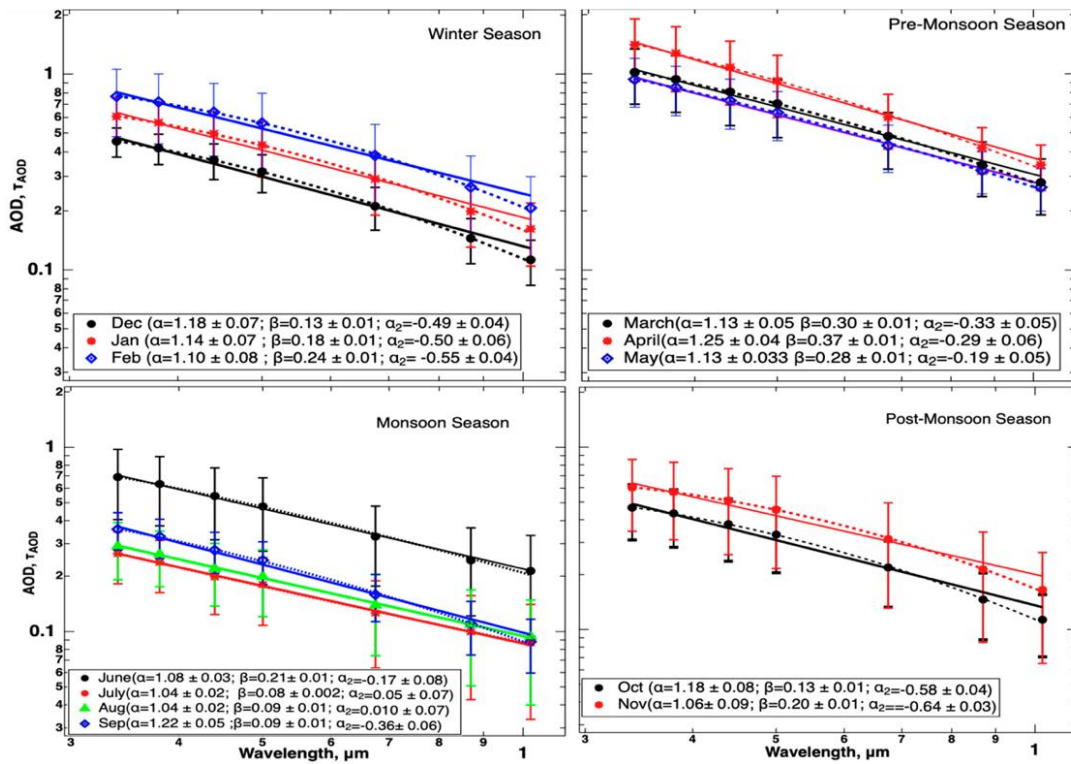


**Figure 28:** Seasonal variation (2010-2018) of Ångström parameters ( $\alpha$ ,  $\beta$ ) at Pokhara using the linear regression (solid line), and  $\alpha_2$  from second-order polynomial fit (dotted curve) of monthly mean spectral AOD (in  $\mu\text{m}$ ), in the logarithmic scale.

We analyzed  $\alpha$  computed at different spectral bands for the identification of different aerosol types, as shown in Figure 29b. It shows a significantly high difference of  $\alpha$  in post-monsoon and winter seasons at spectral bands ( $\alpha_{(0.675-0.87)} - \alpha_{(0.34-0.38)}$ ) indicating the dominance of fine mode particles. During the pre-monsoon season, this difference is found to be lower, indicating the presence of coarse mode particles; but during the monsoon season the difference is negative, which suggests the domination of coarse mode particles (Eck et al., 1999; Kaskaoutis et al., 2007).

Angstrom parameters are analyzed to observe the change in aerosol size spectrum using the AERONET data of aerosol volume size distribution from Pokhara site. Figure 30 shows the monthly mean of the volume size distribution for different seasons. The values of  $\alpha$  and  $\alpha'$  is also presented, which shows the bimodal variation of particle sizes for each month. From Figure 30, we can also observe that the volume size distribution for the months with higher value of  $\alpha'$  are dominated by accumulation mode of particles, whereas, medium value of  $\alpha'$  indicates both the modes and lower value of  $\alpha'$  suggests the coarse mode particles.

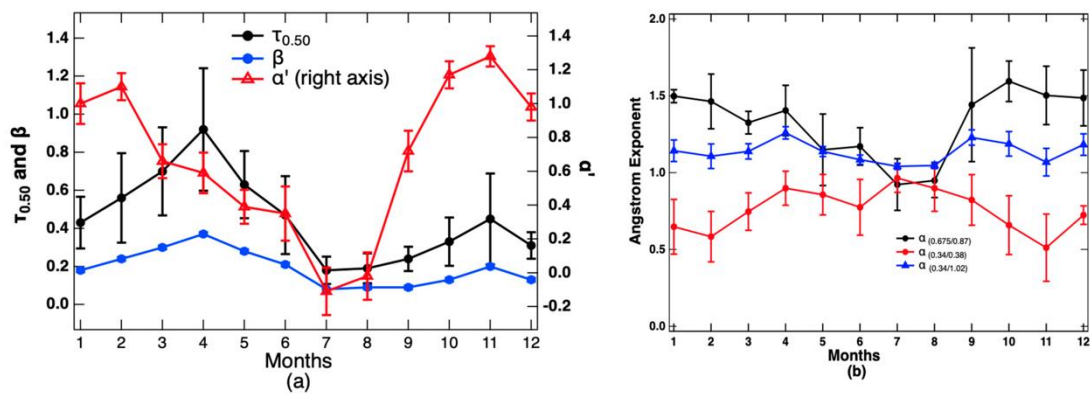


**Figure 29:** Monthly variation (2010-2018) of  $\tau_{0.50}$   $\mu\text{m}$ , Turbidity Parameter ( $\beta$ ) and curvature ( $\alpha'$ )

The volume size distribution of the aerosol particles, plotted in logarithmic scale for the particle size is shown in Figure 31. It also shows the bimodal variation of the aerosol particle sizes for all the seasons, which coincides with the symptoms of the particle sizes provided by  $\alpha$ ,  $\beta$ , and  $\alpha'$

The study of absorbing aerosols is presented in Figure 32 by the help of mean values of SSA and AAOD. We obtained the data for only five different months of winter and pre-monsoon season as per availability from the AERONET site. The figure shows the increase in the value of SSA from  $0.44 \mu\text{m}$  to  $0.675 \mu\text{m}$  and a decrease at longer wavelengths. SSA values over Pokhara are observed to be 0.89 (January), 0.88 (February), 0.87 (March), 0.87 (April), and 0.87 (May) at a wavelength  $0.44 \mu\text{m}$ , indicating the presence of reasonably strong absorbing aerosol components. Different studies in the past for various AERONET locations reported that SSA spectra with dust containing aerosols have increased SSA with increasing wavelength and it decreases with increasing wavelength for the locations dominated by urban industrial or biomass

burning (Bergstrom, Pilewskie, Russell, Redemann, Bond, Sierau, et al., 2007; Li et al., 2015; Sigdel & Ikeda, 2012).

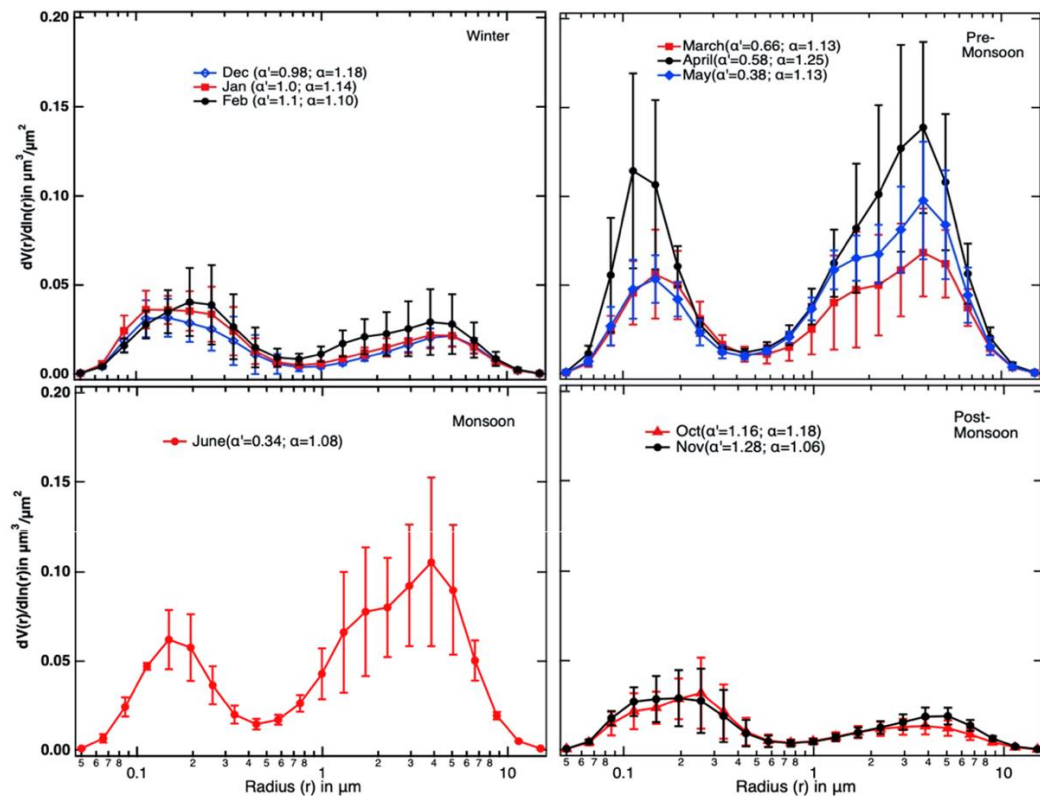


Figure 30: The seasonal variation of monthly averaged volume size distribution in logarithmic scale.

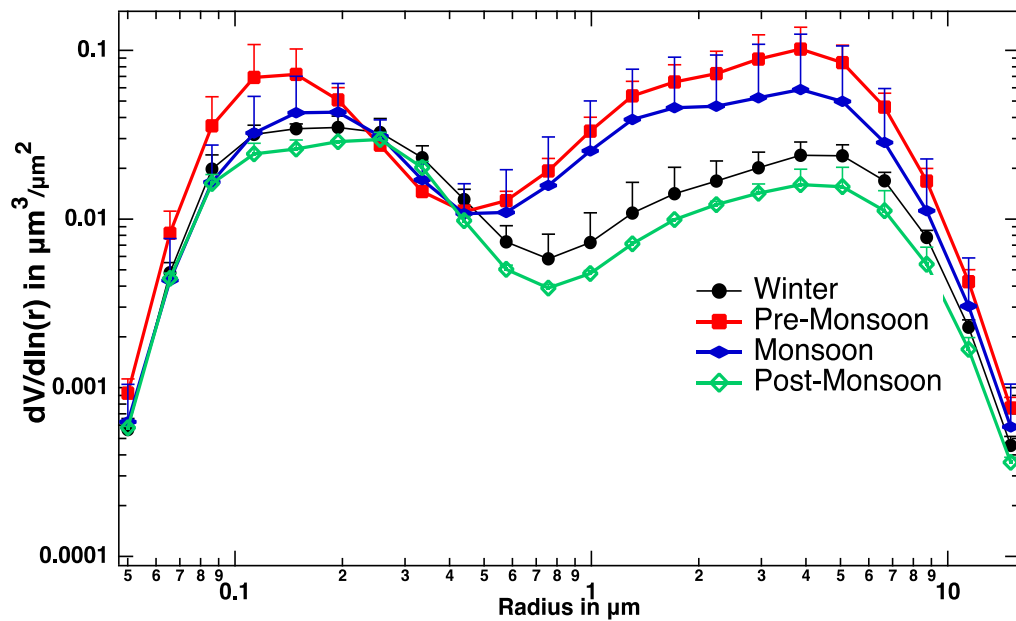
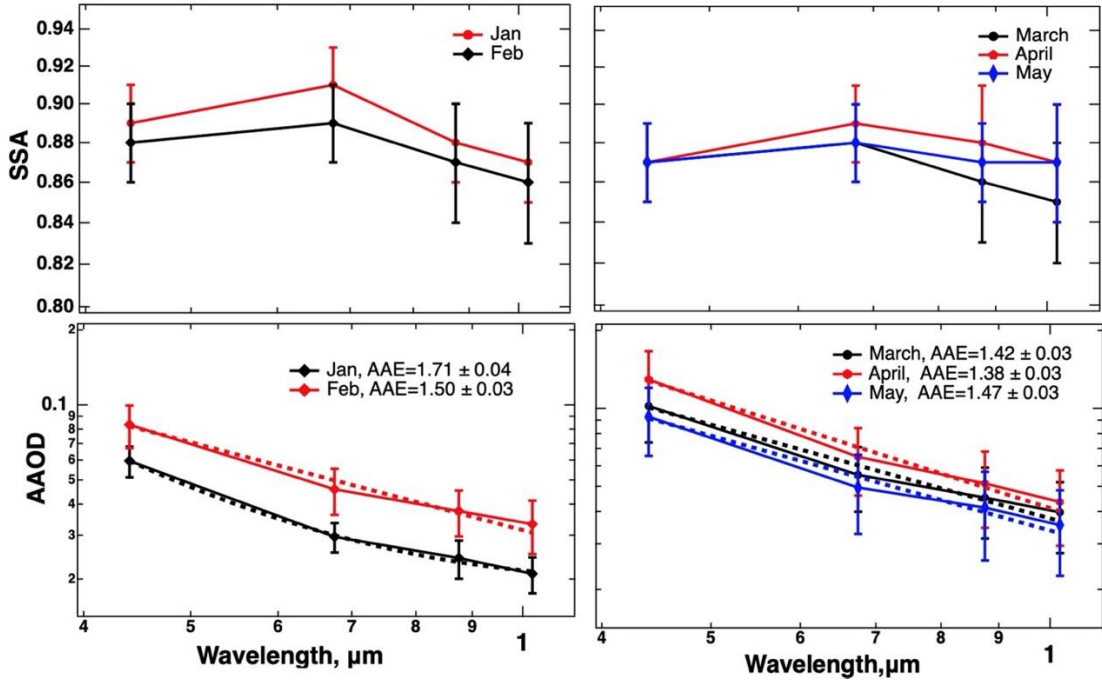


Figure 31: The seasonal volume size distribution  $dV(r)/d\ln(r)$  ( $\mu\text{m}^3/\mu\text{m}^2$ ) in the size range  $0.05 \mu\text{m} - 15 \mu\text{m}$  at Pokhara (2010-2018) (Regmi et al., 2020).

Several past studies have used this trend to distinguish carbonaceous aerosols and dust in various locations (Bergstrom, Pilewskie, Russell, Redemann, Bond, Quinn, et al., 2007). We obtained the increasing trend of SSA spectra up to 0.675  $\mu\text{m}$  which indicates the dominance of dust aerosols, and decreasing from 0.675  $\mu\text{m}$  to 1.02  $\mu\text{m}$  indicates the dominance of biomass burning, urban and industrial activities.

The Absorption Ångström Exponent (AAE) was computed from the spectral dependence of AOD( $\tau$ ) using a linear regression fit on the logarithmic scale plot (Bergstrom, Pilewskie, Russell, Redemann, Bond, Quinn, et al., 2007; Li et al., 2015; Sigdel & Ikeda, 2012). AAE data were found for January ( $1.71 \pm 0.04$ ), February ( $1.50 \pm 0.03$ ), March ( $1.42 \pm 0.03$ ), April ( $1.38 \pm 0.03$ ) and May ( $1.47 \pm 0.03$ ) with ranges 1.38 to 1.71, which assists in specifying the presence of absorbing aerosols over the atmospheric column of Pokhara. The investigations of AAE based on types of aerosols in the different locations of AERONET in the IGP region, determined the values of AAE to vary from 1.2 to 3 for dust, 0.75 to 1.3 for urban and industrial aerosols, and 1.2 to 2 for biomass burning (Bergstrom, Pilewskie, Russell, Redemann, Bond, Quinn, et al., 2007; Moody et al., 2014; Srivastava et al., 2012). Similar study performed on a different AERONET site dominated by an optical mixture of smoke, dust, and industrial and urban pollution, have reported AAE in the ranges of 1.2 to 1.8 (Eck et al., 2010). The values of AAE in our study agrees, which indicates the absorbing nature of aerosol particles contained in the mixed type of aerosols.



**Figure 32:** Monthly mean spectral SSA (top two), averaged within the months of years 2010-2018 at Pokhara, for January, February, March, April, and May and AAOD (bottom two) in the logarithmic scale with the linear fit in same scale.

#### 4.6 Investigation of Aerosol Sources and Types over Pokhara

Figure 33 shows the air mass back trajectory seasonal clusters of five days reaching to the Pokhara observation site at 500 m asl for the year 2017. The red dots are the active fire spots. Figure shows the percentage contribution of each cluster for every season. It revealed two separate pathways for the trans-boundary pollution. During winter and pre-monsoon, it enters from the western side of IGP region (Western Nepal, West India and Pakistan) when the influence of strong western disturbances occurs. The majority of the air mass during the monsoon season arrived from the Bay of Bengal side and IGP region's east. Dense fire spots were also seen over the area throughout the winter and pre-monsoon season, which could increase the amount of biomass burning emissions aerosols that are delivered to Pokhara and affect the air quality and increase AOD during that time. Studies have also reported similar seasonal fire spots and air mass flow in the past over the IGP region, supporting the results of this study (Kaskaoutis et al., 2014; Rupakheti, Kang, Cong, et al., 2018b). In addition, during post-monsoon season a large number of crop residue burning occurs in the north-west part of India. The number of active fire spots are comparatively less during the monsoon season, that



may be due to heavy rainfall and cloud cover in South Asia, caused by moist air from Arabian sea and Bay of Bengal.

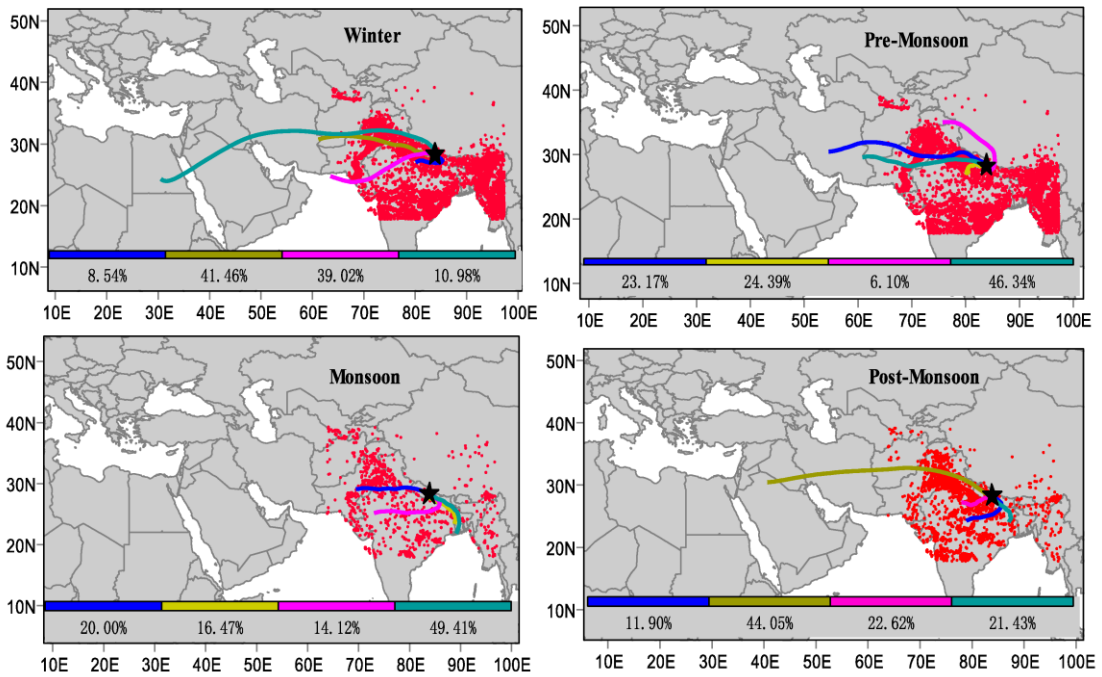


**Figure 33:** Clusters of five days air mass back trajectories computed with HYSPLIT model during four seasons of 2017 reaching Pokhara at altitude 500 m. The active fire spots are symbolized with red dots at different seasons obtained from FIRMS. The percentage contribution of each cluster is given on the bottom right corners (Regmi et al., 2020).

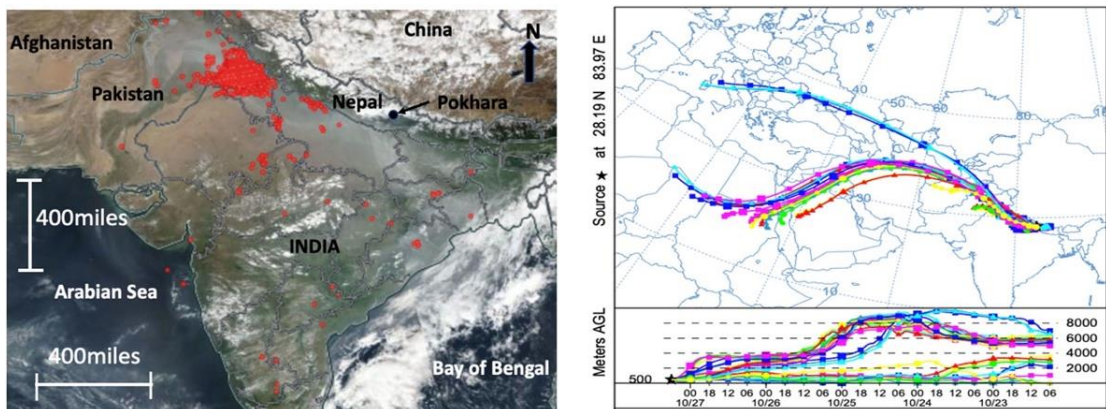


**Figure 34:** (a) The true-color image of the 27th of October, 2017 from the MODIS satellite, displays significant air pollution in the form of plumes over the IGP. (b) NOAA HYSPLIT MODEL Back Trajectories ending at Pokhara at 0600UTC on 27 October 2017 (Regmi et al.; 2020)

#### **4.7 Diurnal Variation of AOD ( $\tau_{0.50}$ ), AE coefficients and Precipitable Water during 2017 in Pokhara**

In this section, we have presented a time series of daily averaged aerosol optical properties,  $\tau_{0.50}$ , Angstrom Exponent (AE) in broadband (0.44  $\mu\text{m}$  – 0.87  $\mu\text{m}$ ) and Precipitable Water

(PW) in cm, from January to December of 2017, as shown in the Figure 35 (a, b, c) along-with the monthly averaged values of these parameters in Table 1. It shows that the aerosol loading is strong in the months from March to May with significant contribution of fine mode particles. The value of AE indicates an approximation for the dominant size of aerosol particles and previous studies in the Himalayan foothill region and Delhi reported a reference of threshold values of AOD and AE for anthropogenic 0.3-1.3 and  $> 0.9$ , for mixed type aerosols 0.4-0.7 and  $< 0.9$ , for biomass burning  $> 1.3$  and  $> 0.8$  and for dust particles  $> 0.7$  and  $< 0.6$  respectively (Rupakheti, Kang, Cong, et al., 2018a; Sharma et al., 2014). The significant deviation in the values of AOD and AE corresponds to the various types of particulate matter loading in the atmosphere (Eck et al., 1999, 2012). During the monsoon season, we observed a significant reduction in the values of AOD and a large amount of PW (Table 4). The low and stable value of AOD may have caused due to the differences in the production and flushing of the particles between dry and rainy seasons.

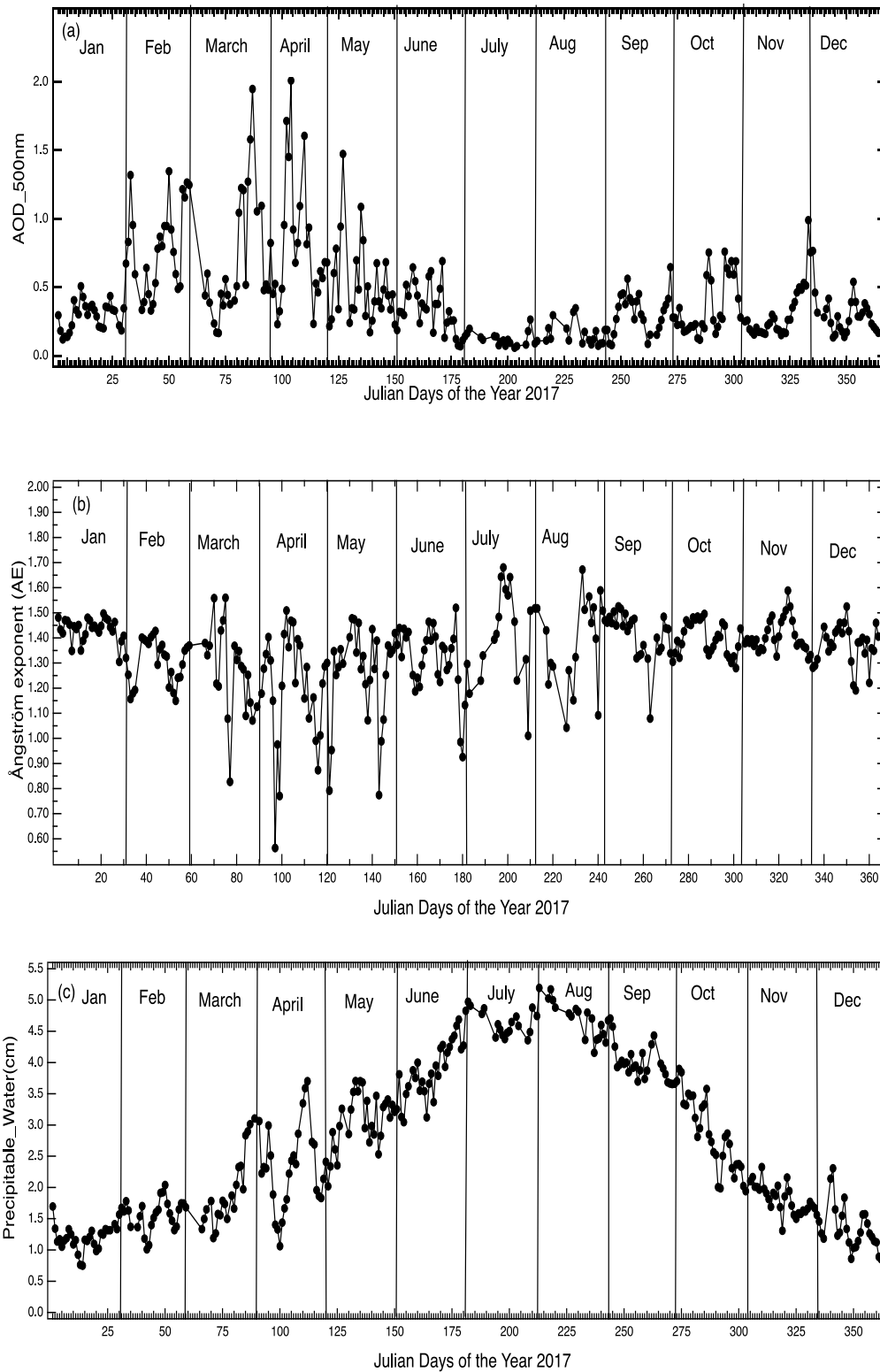


**Figure 35:** Time series of daily averaged columnar (a) AOD values at a wavelength  $0.50 \mu\text{m}$ ,  $\text{AOD}_{0.50}$  (b) AE values with in the wavelength range  $0.44 \mu\text{m} - 0.87 \mu\text{m}$  and (c) PW in cm, at Pokhara during the year 2017. The bottom scale represents Julian days.

Both AOD and AE shows a distinct seasonal trend during the months of pre- and post-monsoon seasons. It increases from the end of winter towards pre- monsoon season,

which may be due to the buildup of anthropogenic aerosols. Since this is the season of harvesting in the region, the burning of crop residue is common that hugely contributes the smoke and ash particles in the atmosphere. As evident from the Table 4, PW is highest during monsoon that gradually decreases from post- monsoon to the early pre-monsoon.

**Table 4:** Monthly average of Aerosol optical depth (AOD), Angstrom exponent (AE) and Precipitable water (PW) with standard deviation during 2017 at Pokhara station. A large variation in daily data gives significant standard deviation.

<b>Months</b>	<b>AOD_0.50<math>\mu</math>m</b>	<b>AE (0.44<math>\mu</math>m-0.87<math>\mu</math>m)</b>	<b>Precipitable-Water (PW) in cm</b>
Jan	0.30( $\pm$ 0.12)	1.43( $\pm$ 0.05)	1.21( $\pm$ 0.22)
Feb	0.79( $\pm$ 0.33)	1.30( $\pm$ 0.09)	1.56( $\pm$ 0.25)
March	0.72( $\pm$ 0.49)	1.27( $\pm$ 0.18)	1.95( $\pm$ 0.59)
April	0.79( $\pm$ 0.45)	1.21( $\pm$ 0.22)	2.31( $\pm$ 0.67)
May	0.52( $\pm$ 0.31)	1.25( $\pm$ 0.19)	3.06( $\pm$ 0.45)
June	0.34( $\pm$ 0.18)	1.31( $\pm$ 0.14)	3.91( $\pm$ 0.46)
July	0.12( $\pm$ 0.05)	1.41( $\pm$ 0.18)	4.63( $\pm$ 0.19)
Aug	0.16( $\pm$ 0.08)	1.39( $\pm$ 0.18)	4.70( $\pm$ 0.30)
Sep	0.31( $\pm$ 0.15)	1.41( $\pm$ 0.09)	3.98( $\pm$ 0.28)
Oct	0.36( $\pm$ 0.21)	1.40( $\pm$ 0.06)	2.83( $\pm$ 0.57)
Nov	0.31( $\pm$ 0.20)	1.41( $\pm$ 0.06)	1.81( $\pm$ 0.23)
Dec	0.30( $\pm$ 0.14)	1.37( $\pm$ 0.08)	1.31( $\pm$ 0.36)

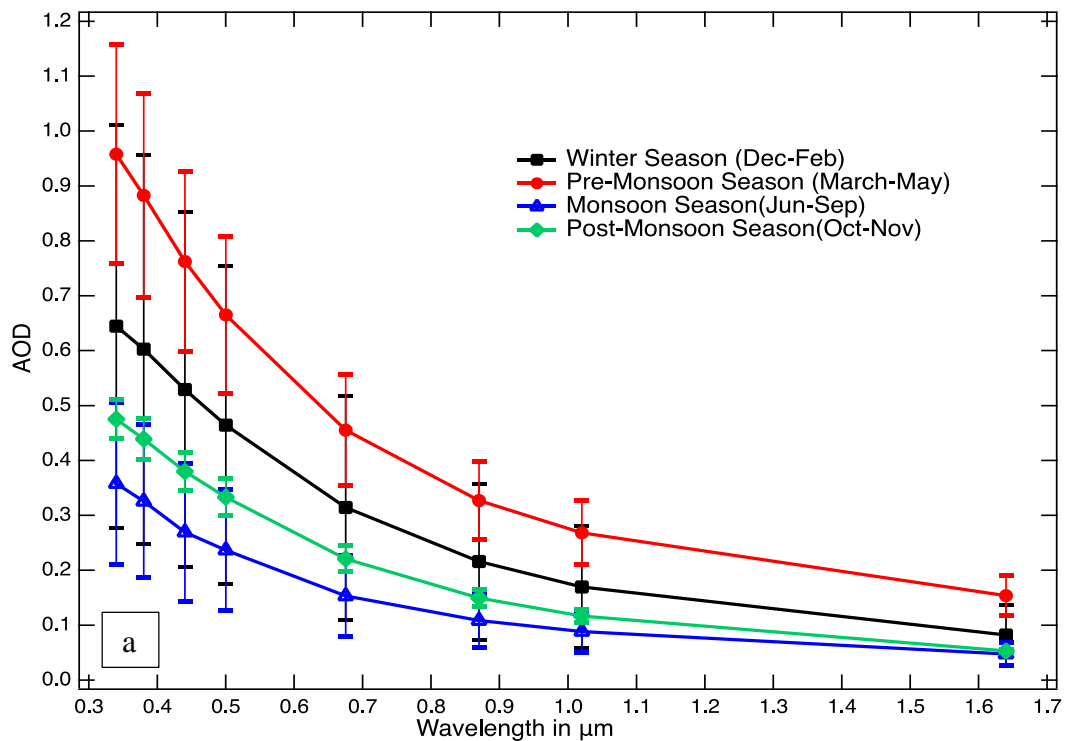
#### 4.8 Spectral dependence of AOD

AOD exhibits a considerable dependence at shorter wavelengths and gradually declines at longer wavelengths, as seen in Figure 36. It suggests the existence of particles in the fine to coarse mode. The AOD values at shorter wavelengths are increased by the fine mode particles' enhanced scattering, whereas the AOD values at longer wavelengths are decreased by the coarse mode particles (Eck et al., 1999). Additionally, it is clear that the variance in AOD exhibits a consistent pattern throughout the year. Pre-monsoon season has the greatest average value of AOD, followed by winter, post-monsoon, and monsoon season.

Characterizing change in spectral AOD curvature ( $\alpha$ ) using a single value of  $\alpha$  is simply an approximation because the value of  $\alpha$  shown in Figure 36 may be caused by the presence of many aerosol types in the atmosphere (Pedrós et al., 2003). First order

linear fit is used to study how averaged AOD based on several seasons change with wavelength in a logarithmic scale which is used to calculate Ångström exponents and turbidity parameters. Based on data from a single year, these parameters for all seasons are determined to be:  $\beta = 0.19 \pm 0.01$  and  $\alpha = 1.16 \pm 0.07$  (winter season),  $\beta = 0.29 \pm 0.01$  and  $\alpha = 1.13 \pm 0.04$  (pre-monsoon season),  $\beta = 0.09 \pm 0.03$  and  $\alpha = 1.25 \pm 0.03$  (monsoon season), and  $\beta = 0.13 \pm 0.01$  and  $\alpha = 1.22 \pm 0.07$  (post-monsoon season).

The amount of aerosol loading in the vertical column is suggested by the variation in turbidity parameter ( $\beta$ ) and it is found that the order of  $\beta$  values completely match with values of AOD variation. The AE values show the significant contribution of fine mode particles. Using the mean spectral AOD at wavelengths ranging from 0.34  $\mu\text{m}$  to 1.64  $\mu\text{m}$ , values of  $\alpha$  were calculated. The seasonal  $\alpha$  values were determined to be  $\alpha = 1.36 \pm 0.06$  for the winter season,  $1.24 \pm 0.03$  for the pre-monsoon season,  $1.37 \pm 0.05$  for the monsoon season, and  $1.40 \pm 0.01$  for the post-monsoon season based on the spectral AOD at wavelengths ranging from 0.44  $\mu\text{m}$  to 0.87  $\mu\text{m}$ . The results of our investigation, estimated using two alternative AOD wavelength ranges, reveal relatively little variation, with somewhat higher results found in the ranges of 0.34  $\mu\text{m}$  to 1.64  $\mu\text{m}$ .



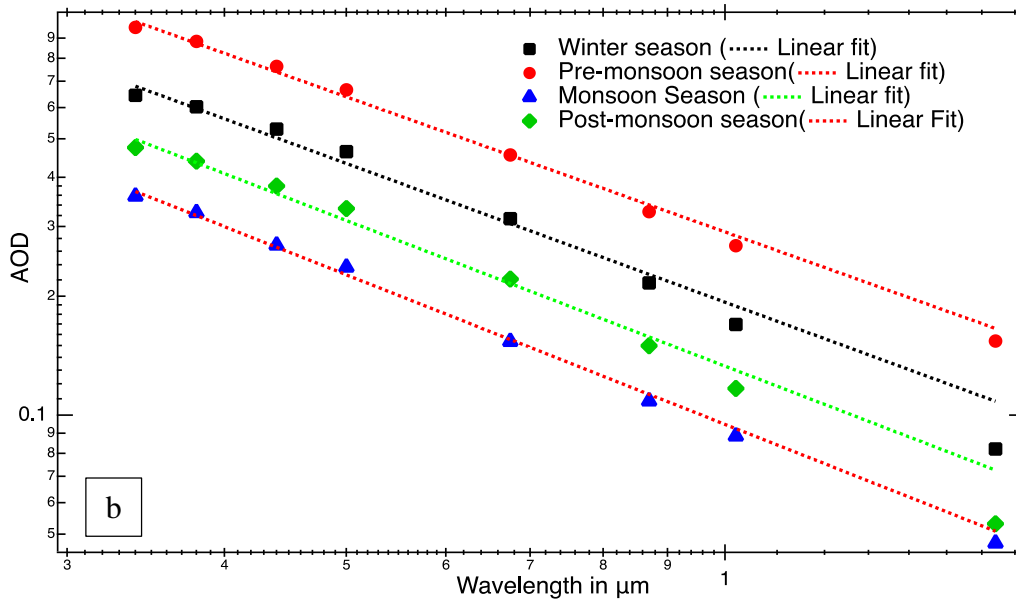


**Figure 36:** Seasonal variation of the mean AOD at Pokhara, 2017 (a) at various wavelengths ( $\lambda$ ) and (b) linear fit in logarithmic wavelength scale.

#### 4.9 Contribution of Fine and coarse mode particles on AOD

Figure 37 displays the Fine mode's partial impact on AOD. The contribution of fine mode particles to the total AOD is greater than 70% in all months, with the largest contributions of 94% in November and February and 79% in July. One of the most crucial factors for describing the aerosol particles in the atmosphere is the particle size distribution. According to Seinfeld (1998), the size distribution of atmospheric particles strongly suggests the origins of aerosols. The majority of the mechanical processes that produce the coarse mode particles, which have diameters more than 1 micrometer, and that are directly released from anthropogenic and natural processes into the atmosphere. The combustion of fuels such as wood, oil, coal, gasoline, and other substances releases fine mode particles, which have a diameter of less than 1 micrometer, into the atmosphere. Fine particles typically contain significant amounts of organic material in addition to soluble inorganics like ammonium, nitrate, and sulfate due to the nature of their sources (Moody et al., 2014).

It is therefore not surprising to discover that the fine mode fractional AOD, percentage contribution of fine mode aerosols is higher in the pre-monsoon and post-monsoon seasons compared to the summer monsoon months (Figure 37). By October, the moist air has almost entirely disappeared due to this retreat, and the weather has returned to being chilly, clear, and dry. After the pre-monsoon period, the summer monsoon, a

powerful flow of humid air from the southwest, occurs, altering the particle composition and raising the amount of water in the atmosphere. An earlier study reveals that the burning of biomass and fossil fuels has significantly increased the amount of elemental carbon in Pokhara (Tripathee et al., 2016). This demonstrates that fine mode particle concentrations are abundant in the atmosphere of Pokhara and play a substantial role in the reduction of solar radiation during the pre- and post- monsoon seasons as compared to the rainy season.

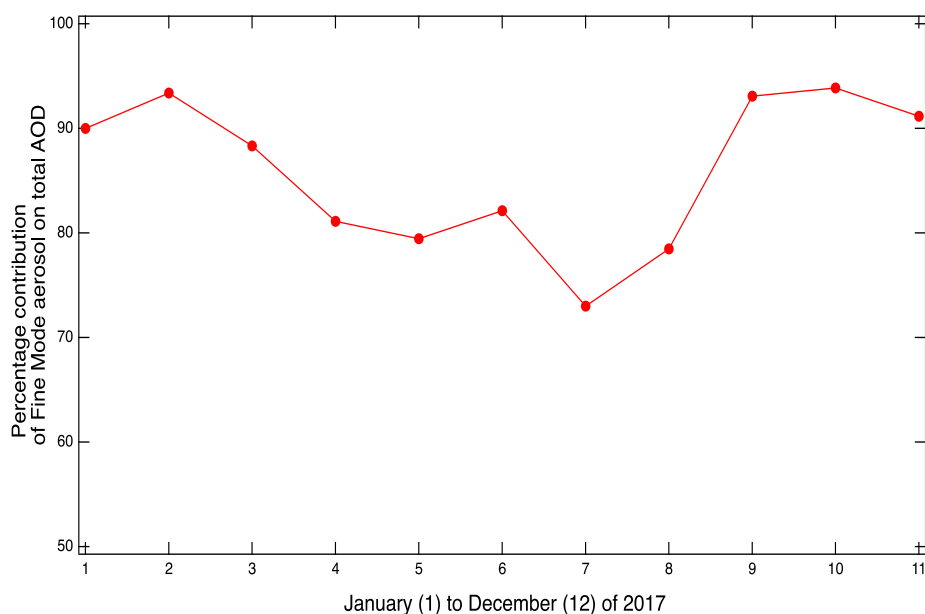


**Figure 37:** Monthly Percentage contribution of fine mode particles on total AOD over Pokhara, 2017.

Figure 38 shows the impact of aerosol on solar radiation. It is observed that the contribution of fine mode particles is increased from post-monsoon to pre- monsoon seasons. Anthropogenic aerosols must have an effect at this time, and in the summer the overall AOD drops significantly, indicating the effect of monsoon-related rainfall. Only roughly 12% of the total average AOD from February to April is contained in the two months of July and August. It indicates the significant presence of aerosol plumes in the atmosphere during pre-monsoon period.

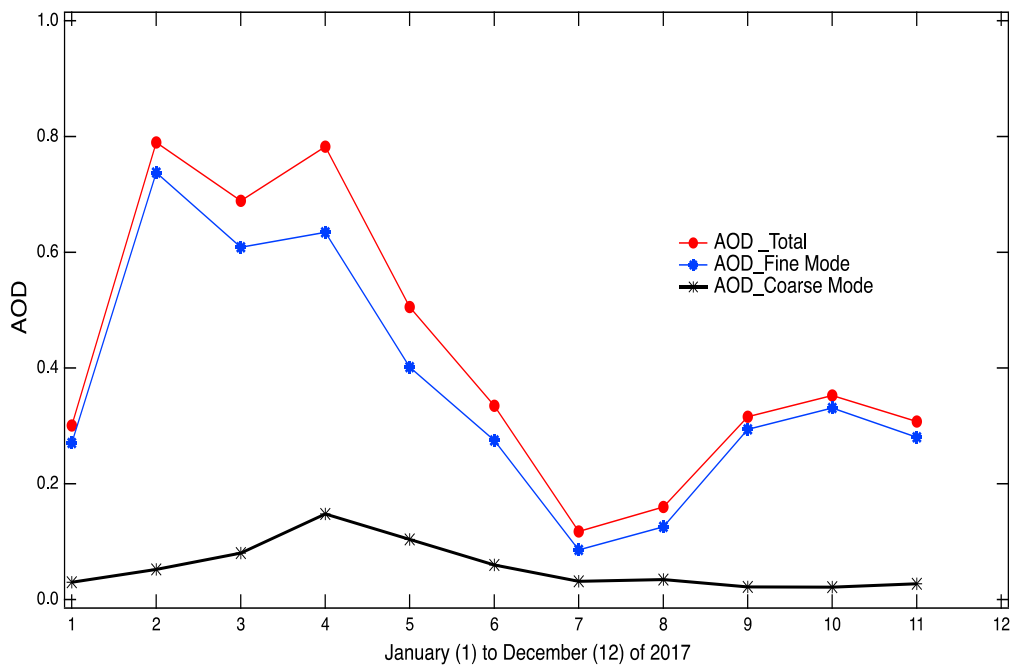


**Figure 38:** Monthly average total AOD and AODs due to fine and Coarse Mode particles in Pokhara in the year 2017.

#### 4.10 Variation of Radiative Forcing

Calculating the change in the radiative energy balance is a typical method for estimating the effects of atmospheric changes on the Earth-atmosphere system. The changes in the radiative fluxes at the top of atmosphere (TOA) and bottom of the atmosphere (BOA) gives the radiative forcing on the earth surfaces. The impact on the entire Earth-atmosphere system is summarized by TOA forcing and the impact on exchange processes between the atmosphere and the Earth's surface is explained by BOA forcing. We have analyzed the TOA and BOA forcing during pre-monsoon period of 2017 in Pokhara. The seasonal average of BOA forcing is found to be  $82.02 \pm 27.63$  and TOA forcing is  $-23.94 \pm 4.71$ . The maximum BOA forcing is observed during the month of April (111.69) and minimum during May (56.23). Similarly, the maximum TOA forcing is also observed in the month of April (-28.96) and minimum in May (-19.62) as shown in Table 5 and Figure 39 (a-e). The forcing at TOA corresponds to the cooling effect on the atmosphere that ranges from -19.62 to -28.96 during the pre-monsoon season in Pokhara that indicates presence of dust particles in significant amount in the atmosphere. Figure 40, 41 and 42 show the daily variation of radiative forcing and Flux during the year 2017 in Pokhara. It can be observed that, the radiative forcing is large during pre-monsoon season and minimum during monsoon season.



**Table 5:** Variation of Radiative Forcing during Pre- Monsoon Period of Pokhara, 2017

Month of 2017	Flux Down (BOA)	Flux Down (TOA)	Flux Up (BOA)	Flux Up (TOA)	Rad_F orcing (BOA)	Rad_F orcing (TOA)	Forcing _Eff (BOA)	Forcing _Eff (TOA)	Diffuse (BOA)	Diffuse (TOA)
March	428.96	669.79	58.32	127.06	78.64	-23.23	191.39	-65.62	1.86	159.42
April	365.37	632.95	53.12	131.08	111.19	-28.96	187.37	-52.73	1.68	167.96
May	420.35	648.89	61.86	122.60	56.23	-19.62	174.91	-60.74	1.83	149.92
Av.	404.89	650.54	57.77	126.91	82.02	-23.94	184.56	-59.70	1.79	159.92
Stdev	34.49	18.48	4.39	4.24	27.63	4.71	8.59	6.50	0.09	9.03



**Figure 39:** Variation of Radiative Forcing (a-e) in Pokhara during Pre-monsoon period of 2017.

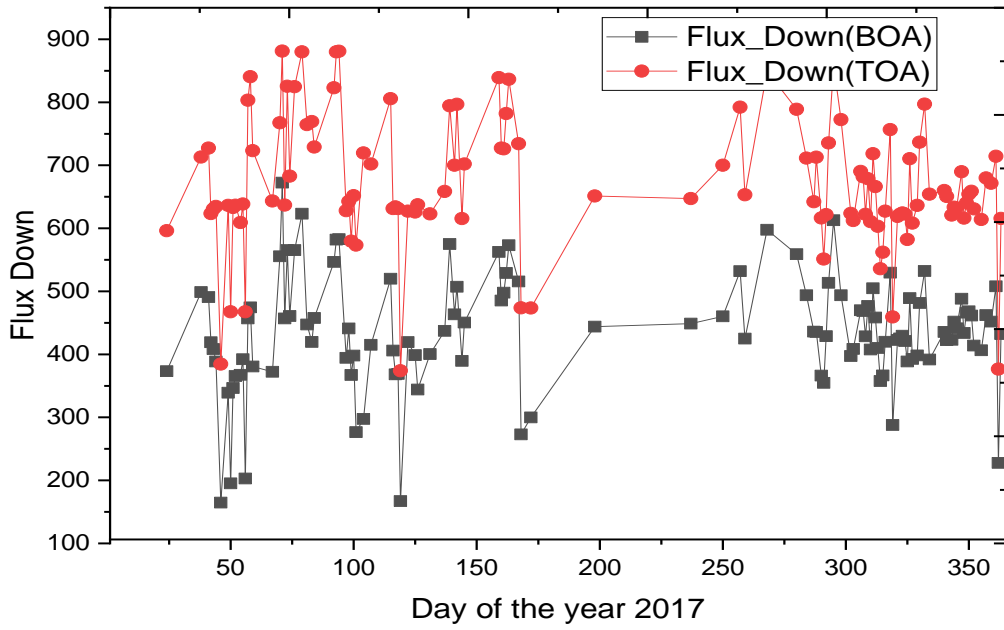


**Figure 40:** Daily variation of flux down at the top of atmosphere (TOA) and bottom of atmosphere (BOA) at Pokhara, 2017.

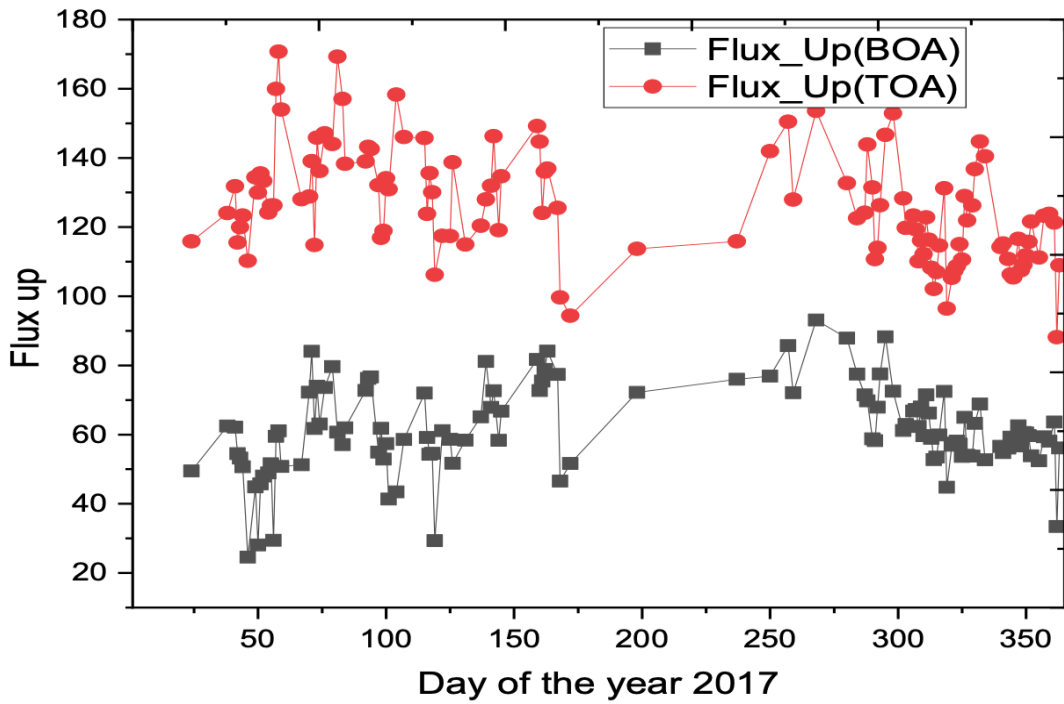


**Figure 41:** Daily variation of flux up at the top of atmosphere (TOA) and bottom of atmosphere (BOA) at Pokhara, 2017.

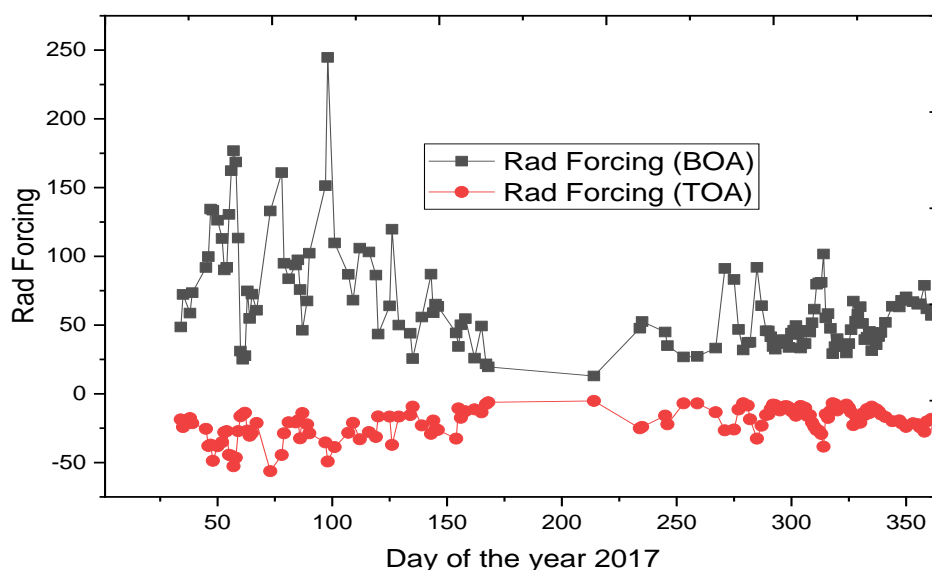


**Figure 42:** Daily Variation of Radiative forcing at the top of atmosphere (TOA) and bottom of atmosphere (BOA) during the year 2017 at Pokhara.

#### 4.11 Relationship between AOD and Radiative Forcing

We have observed the AERONET data of Pokhara station in the year 2017 to analyze the relationship between AOD and radiative forcing. As we know the magnitude of cloud cover and the duration of bright sunshine hours are the key factors that makes the significant difference in the magnitude of irradiance on the earth surface. Figure 43 shows the monthly variation of diffuse radiation (BOA) and AOD 500nm. The plot shows an increasing trend in AOD with the decreasing values of diffuse radiation. The months of post-monsoon and winter (Oct, Nov, Dec, and Jan) show higher values of diffuse radiation during which the AOD values are lower.

**Table 6:** Monthly Variation of Diffuse Radiation and AOD\_500 nm at Pokhara, 2017.

Month of 2017	AOD_500 nm	Diffuse (BOA)
JAN	0.30	2.19
FEB	0.80	1.94
MAR	0.69	1.86
APR	0.79	1.68
MAY	0.51	1.83
OCT	0.36	2.15
NOV	0.31	2.16
DEC	0.29	2.19

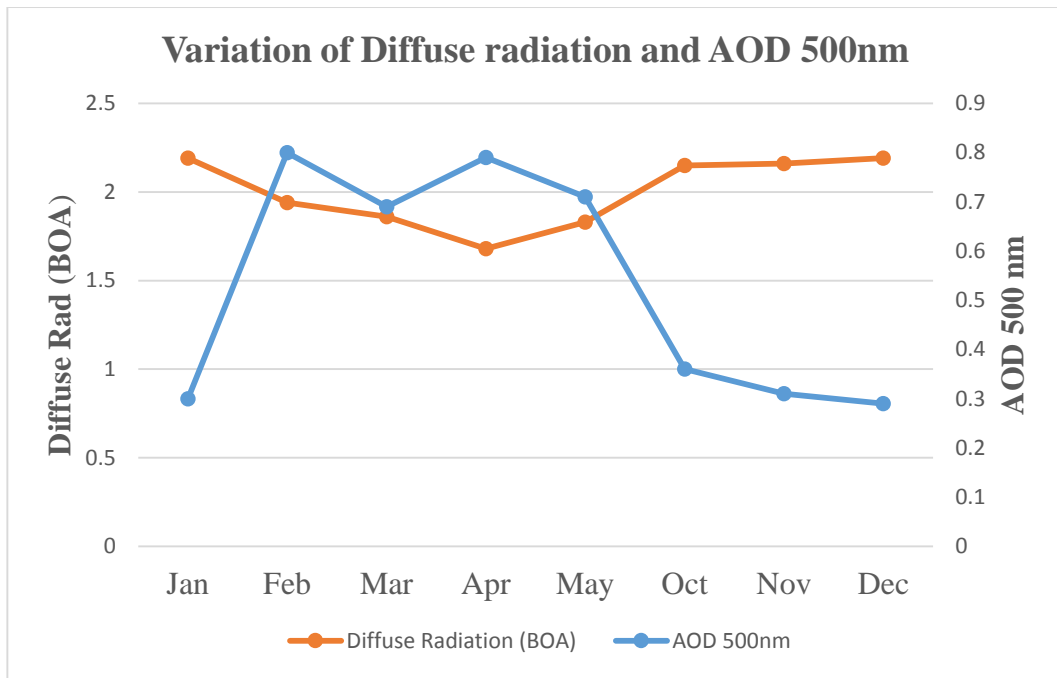


**Figure 43:** Monthly averaged Aerosol Optical Depth at 500 nm with the months of 2017.

#### 4.12 Monthly Variation of Global Solar Radiation (GSR) in Pokhara in the year 2020

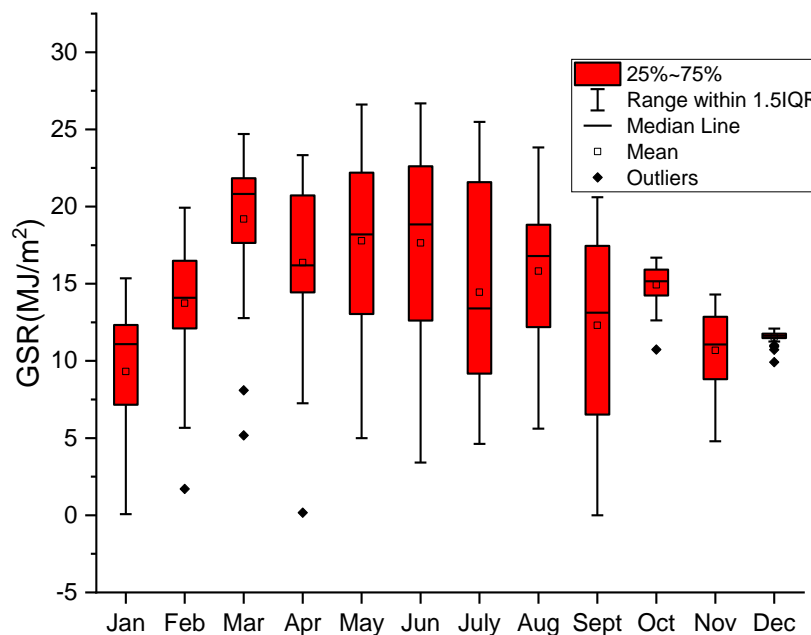


**Figure 44:** Box plot for monthly variation of GSR for the year 2020 at Pokhara

The data obtained from Pyranometer for the DHM data station Pokhara in the year 2020 was analysed using Box and Whisker plot as shown in Figure 44. The daily averaged data were used to observe monthly variation. It shows the maximum GSR values

gradually increases from January to March. A slight decrease is observed in April, which again increases up to June. From July, it gradually decreases to December. In almost all the months, mean values found to be lower than the median value of the respective months. The maximum average is observed in March  $[(19.19 \pm 4.61) \text{ MJ/m}^2]$  and a minimum average in January  $[(9.31 \pm 4.39) \text{ MJ/m}^2]$ .

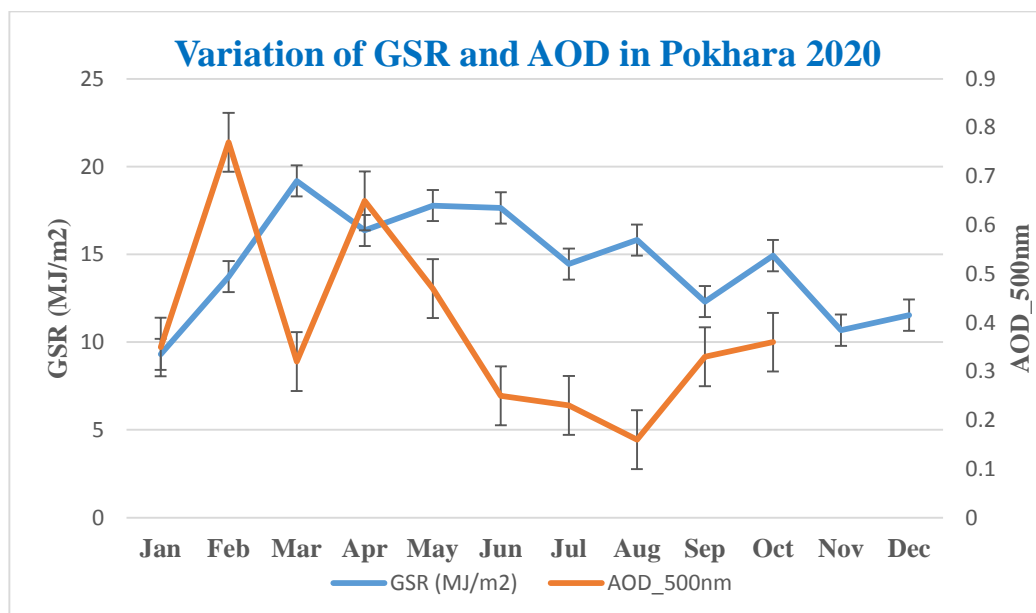


**Figure 45:** Comparative analysis of GSR data obtained from Pyranometer with aeronet AOD data for the year 2020 at Pokhara.

**Table 7:** Seasonal Meteorological Parameters for the year 2020 January to 2020 November

Season	Temperature (° C)		Relative Humidity (%)		Air Pressure (h Pa)	
	Pokhara	Pulchowk	Pokhara	Pulchowk	Pokhara	Pulchowk
Winter (Jan, Feb)	16.80	17.98	59.22	50.73	914.49	872.43
Pre-Monsoon (Mar, Apr, May)	24.22	24.01	55.80	48.76	910.40	869.55
Monsoon (June, July, Aug, Sep)	28.91	29.04	66.99	59.11	905.08	865.20
Post-Monsoon (Oct, Nov)	24.47	25.91	58.56	45.93	911.97	871.25

The GSR data was compared with AOD data obtained from AERONET Pokhara for the same time period 2020 as shown in Figure 45. It can be observed that with the increase in aerosol loading in the vertical column, the amount of solar radiation

reaching to the ground decreases. When the correlation analysis was carried out, it was found that they are negatively correlated (-0.15) which is not much significant.

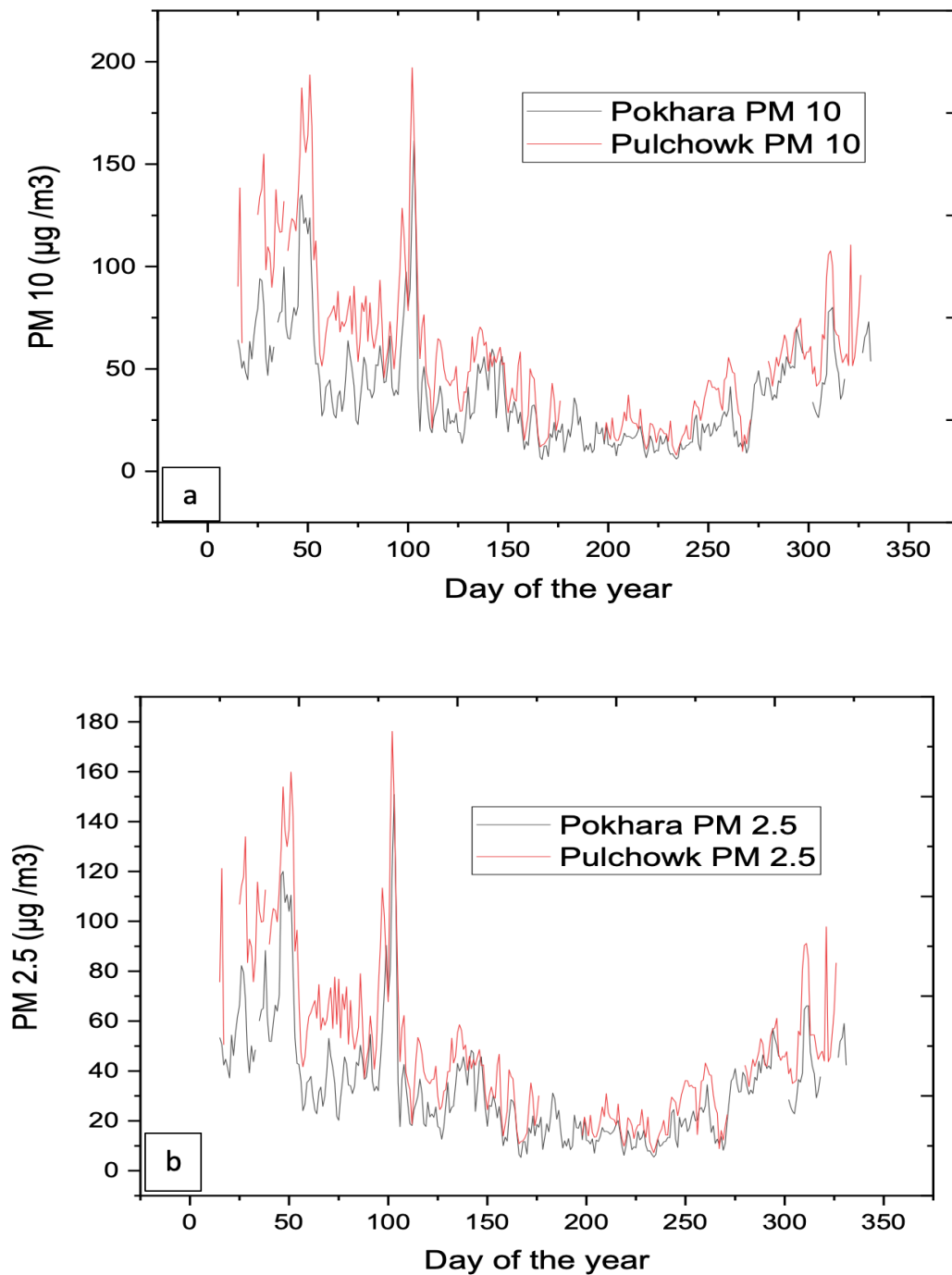


**Figure 46:** Daily mean concentrations of (a) PM<sub>10</sub> and (b) PM<sub>2.5</sub> in Pokhara and Pulchowk from January 15, 2020 to November 27, 2020.

Figure 46 (a,b) shows the daily mean concentrations of PM<sub>2.5</sub> and PM<sub>10</sub> in two large cities of Nepal, Pulchowk (Kathmandu valley) and Pokhara from January 15, 2020 to November 27, 2020 (These analysis were made on last week of November 2020). It

reveals that the concentration of PM<sub>10</sub> and PM<sub>2.5</sub> both are higher in Pulchowk than that in Pokhara throughout the year. In winter the maximum concentration of daily average for PM<sub>2.5</sub> was 115.33 in Pokhara and 159.86 in Pulchowk. In Pre-monsoon it was 155.24 in Pokhara and 176.14 in Pulchowk. But the average concentration decreased due to lockdown followed by COVID-19. However, it shows the concentration is higher during winter season and gradually decreasing till monsoon and again increasing during post-monsoon. Their values are presented in Table 8.

**Table 8:** Seasonal average concentrations of PM<sub>2.5</sub> and PM<sub>10</sub> in Pokhara and Pulchowk along with the ratio of PM<sub>2.5</sub> to PM<sub>10</sub>.

	PM <sub>2.5</sub> µg/m <sup>3</sup>		PM <sub>10</sub> µg/m <sup>3</sup>		PM <sub>2.5</sub> / PM <sub>10</sub>	
	Pokhara	Pulchowk	Pokhara	Pulchowk	Pokhara	Pulchowk
Winter	61.11±15.67	99.72± 12.65	68.05±13.03	116.39±12.87	0.89	0.86
Pre-Monsoon	38.03±20.59	55.72 ±19.95	43.57±10.91	65.49±23.86	0.87	0.85
Monsoon	17.35 ± 3.51	21.73± 5.53	18.38 ±7.77	23.56±7.67	0.94	0.92
Post-Monsoon	39.85± 9.66	52.78± 29.80	52.36± 6.60	63.54±31.72	0.76	0.83

The seasonal variation of average concentrations of PM<sub>2.5</sub> and PM<sub>10</sub> is presented in Table 8 with standard deviation. It shows Pokhara is comparatively clean than Pulchowk. The concentrations of both the fine and coarse mode particles are less in Pokhara in all the seasons than that in Pulchowk. The lowest concentration of PM<sub>2.5</sub> is observed in Pokhara during monsoon (17.35 ± 3.51) and maximum during winter (61.11±15.67). Similarly in Pulchowk, the lowest value during monsoon (21.73± 5.53) and maximum during winter (99.72± 12.65) was observed. Except in winter, the average level of PM<sub>2.5</sub> in Pokhara is below the national standard of ambient air quality (40 µg/ m<sup>3</sup> NAAQS, 2012) but in Pulchowk, it is below the safe level only during monsoon and rest of the season show a high value of PM<sub>2.5</sub>. Both the results show the significant seasonal variation in the concentration of PM<sub>2.5</sub>.

The case of PM<sub>10</sub> is also similar since the concentrations in both the stations are lowest in monsoon and highest in winter as can be seen in the Table 8.

The ratio of  $PM_{2.5} / PM_{10}$  can reflect the proportion of fine particles to coarse particles in the atmosphere of a region.

#### 4.13 Daily Variation of $PM_1$ , $PM_{2.5}$ and $PM_{10}$ in different Seasons

While comparing the concentrations of different types of PM ( $PM_1$ ,  $PM_{2.5}$  and  $PM_{10}$ ) in Pokhara, as shown in Figure 47 and Figure 48, it is found that the total contribution of particulate matter is due to mixed type of particles in all the seasons. It can be observed nearly equal contribution of  $PM_{10}$  and  $PM_{2.5}$  (coarse and fine mode) with the slight domination of coarse mode. But the contribution due to ultra fine particles ( $PM_1$ ) is comparatively very less. It may be due to less efficacy of the device as previous studies suggest that the low cost sensors are not efficient enough to track ultra fine particles. But such sensors can effectively record short lived events of pollution (Bulot et al., 2019). Similar result was obtained upon analyzing AERONET data for seasonal variation from 2010 to 2018 (Regmi et al., 2020).

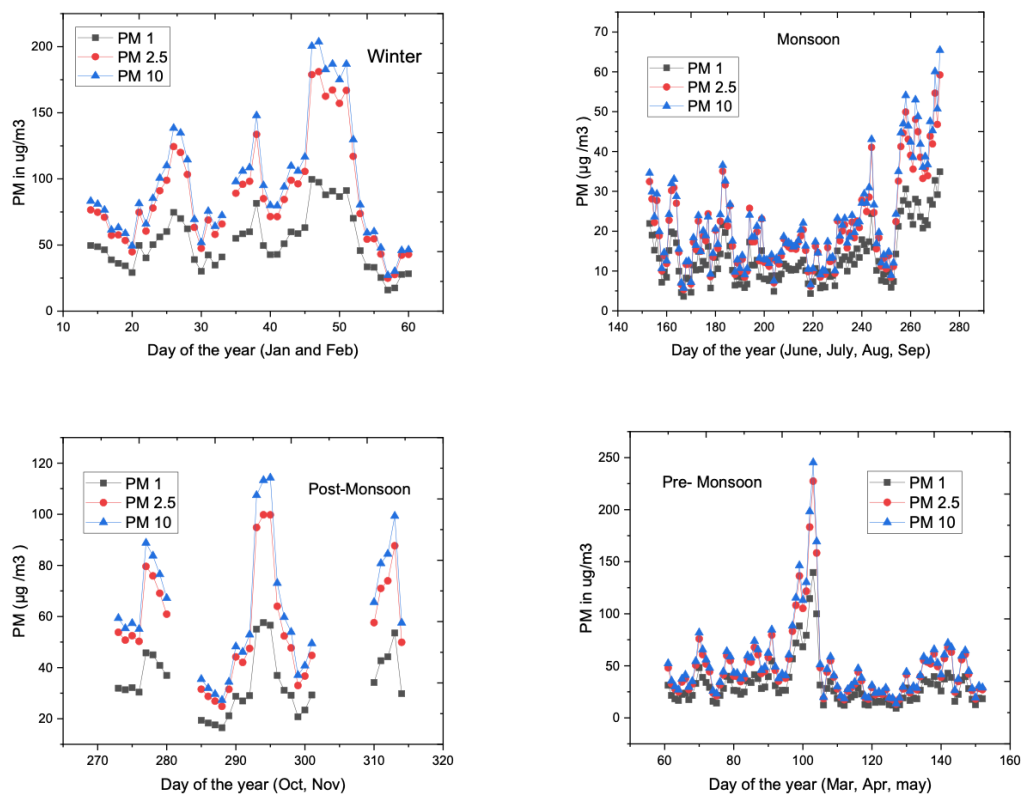


**Figure 47:** Comparison of Concentration of  $PM_1 \mu g/m^3$ ,  $PM_{2.5} \mu g/m^3$  and  $PM_{10} \mu g/m^3$  in Pokhara observation site during winter, pre-monsoon and monsoon season 2020.



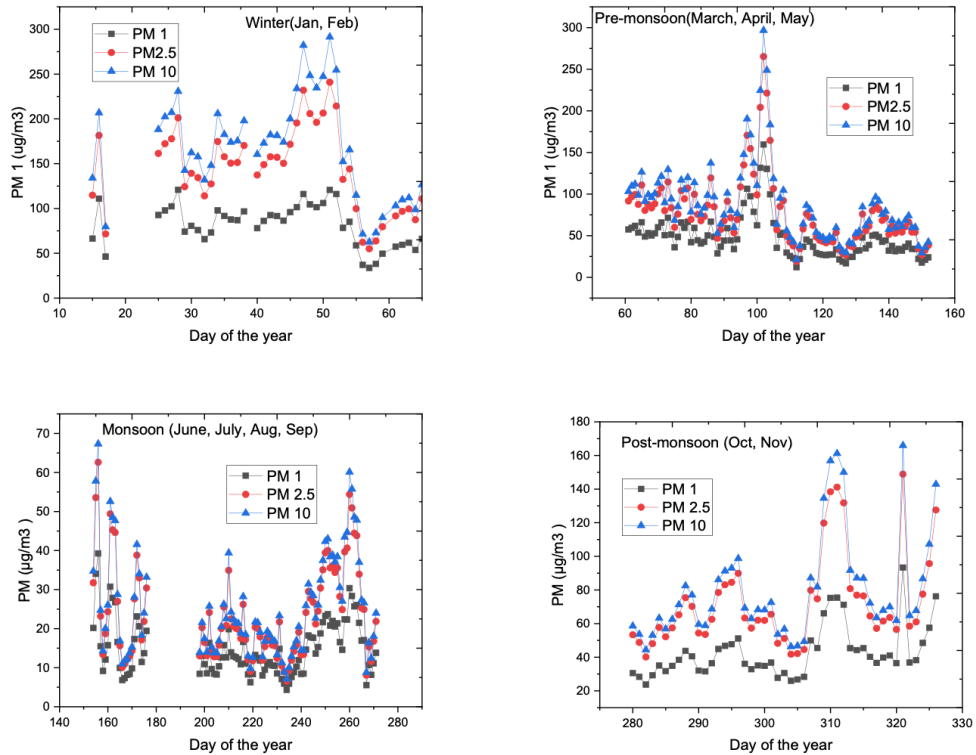


**Figure 48:** Comparison of Concentration of  $PM_1 \mu g/m^3$ ,  $PM_{2.5} \mu g/m^3$  and  $PM_{10} \mu g/m^3$  in Pulchowk observation site during winter, pre-monsoon, monsoon and post-monsoon season 2020.

#### 4.14 Seasonal Scatter Plot for $PM_{2.5}$ in Pulchowk and Pokhara

The seasonal scatterplot of the  $PM_{2.5}$  data that were simultaneously recorded between Pulchowk and Pokhara is shown in Figure 49 (a to d). The  $PM_{2.5}$  correlation coefficient in Pulchowk and Pokhara is 0.77 in the winter, 0.67 in the premonsoon, 0.62 in the monsoon, and 0.66 in the postmonsoon. Based on the availability of a year's data, the seasonal variation was examined.

There is a strong correlation between the  $PM_{2.5}$  levels in these two locations, pointing to similar air pollution from sources such as roadside dust, traffic pollution, and transboundary air pollution that is lodged in the atmosphere.

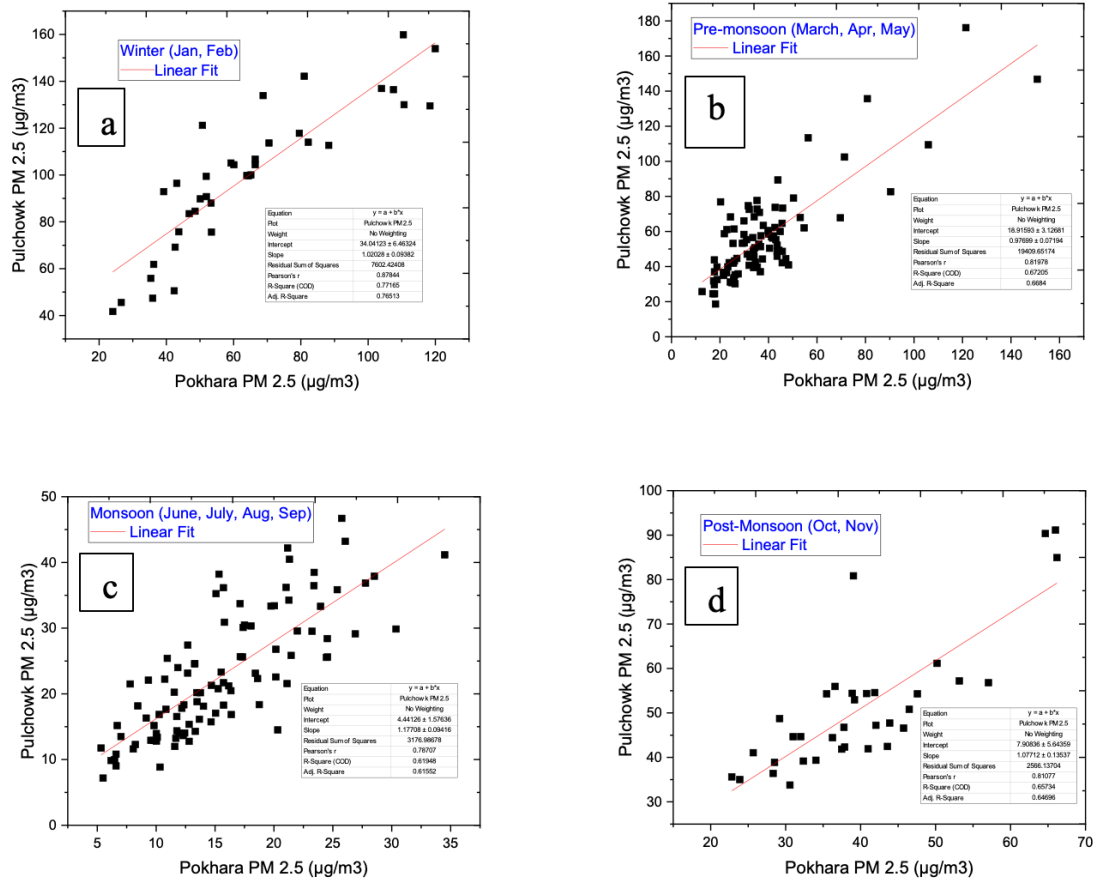


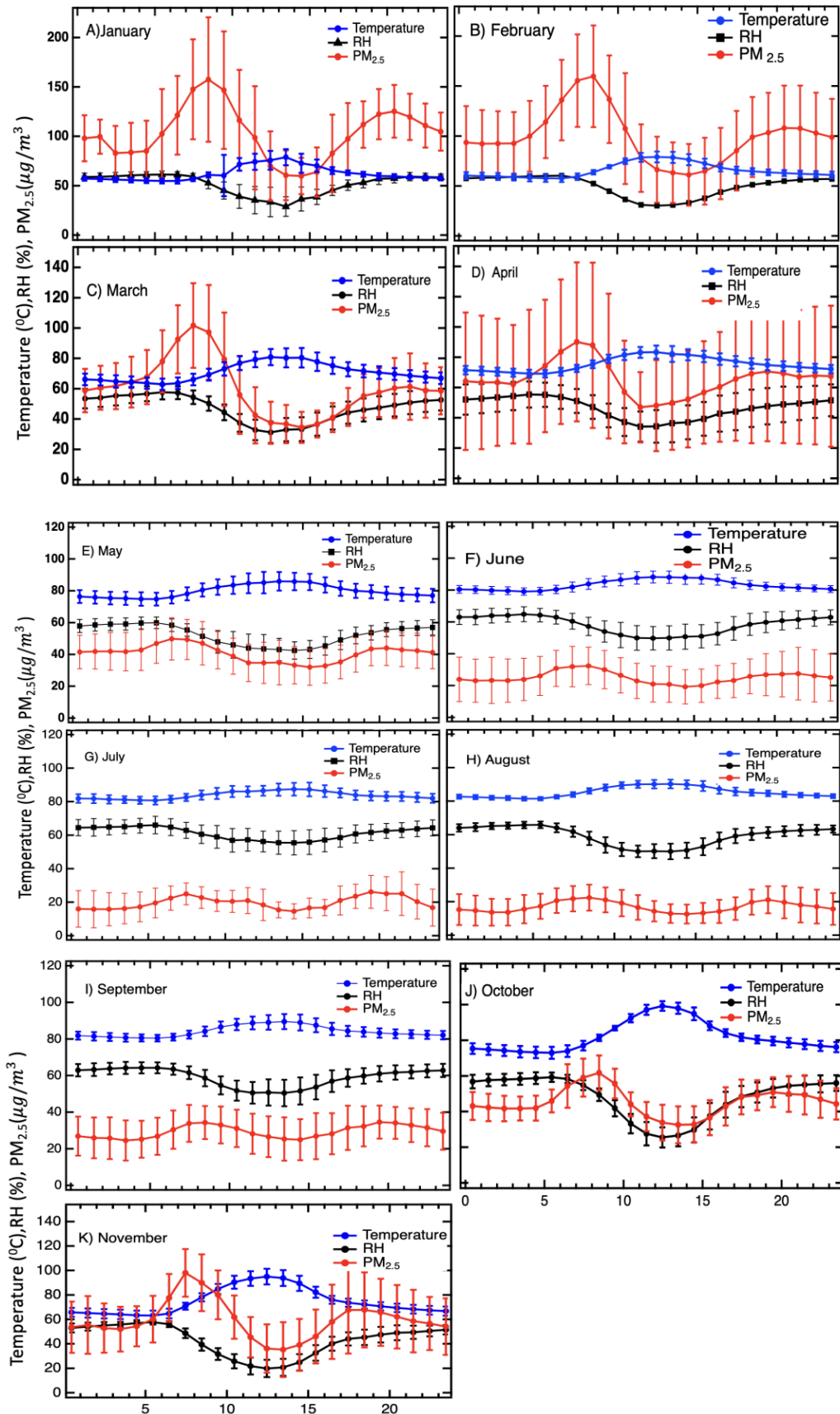
**Figure 49:** Seasonal scatter plot for PM<sub>2.5</sub> in Pulchowk and Pokhara for the year 2020

#### 4.15 Monthly Variation of Hourly Averaged PM<sub>2.5</sub> Concentration

The hourly averaged monthly concentrations of aerosols, particulate matter PM<sub>2.5</sub>, observed from January to November 2020 by PurpleAir monitor are shown in Figure 50. The particle mass concentration is visibly significant for all months during the traffic affected time, such as morning and evening. The figure also shows that during the traffic rush hours, PM<sub>2.5</sub> increases gradually and peaks at about 8 am local time. During this time, the highly detected particle concentration may be due to the formation of a new particle given by the traffic flow and low temperature, which might have affected the formation of secondary aerosols from the precursor gases (Mues et al., 2018). Low temperature enhances the nucleation and condensation of emitted condensable compounds, providing many particles that can form and successively grow to a detectable size. The lower concentration of PM<sub>2.5</sub> in the mid-days can be affected due to the convection effect in which warmer, lighter air masses, pollutants move from the ground to higher altitudes.

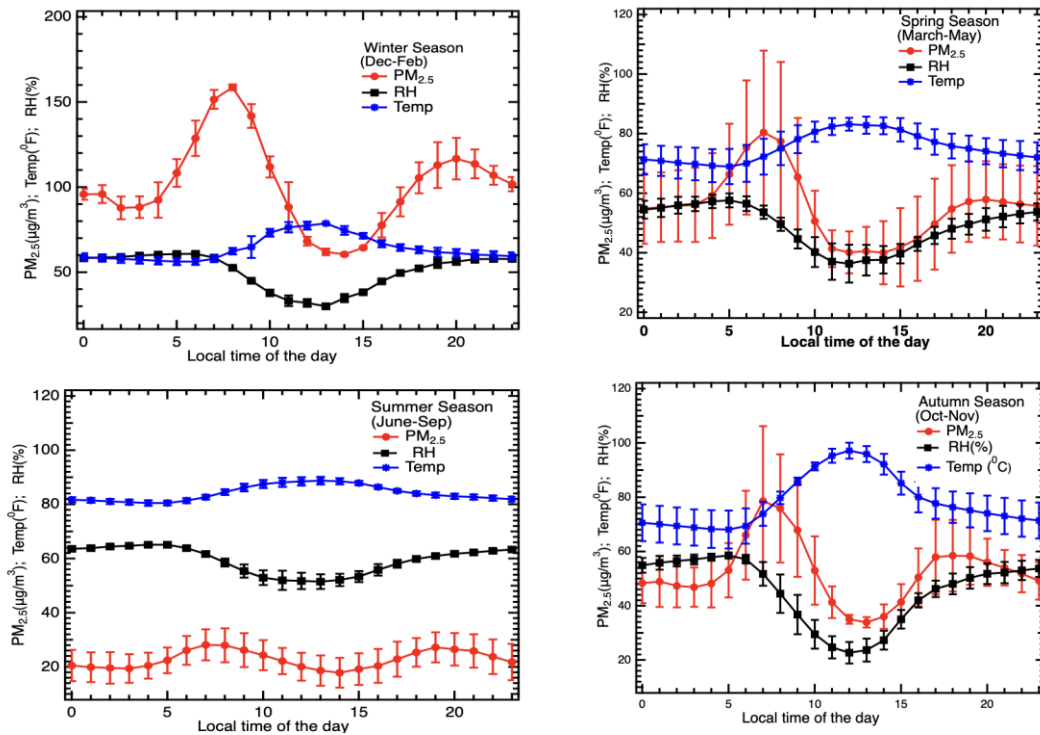
The bimodal PM<sub>2.5</sub> peaks observed in the morning and evening also coincide with the peak hours of domestic cooking or heating, such as cooking foods in the city. The frequency of PM<sub>2.5</sub> concentration patterns is similar in all months. However, the hourly observed PM<sub>2.5</sub> shows a decreasing trend after March. This trend can be due to the rise in temperature in which the surface-level particles quickly diffuse to the vertical atmosphere. The traffic flow was also significantly reduced due to the COVID lockdown period from March to July (Baral & Thapa, 2021). The monsoon also dramatically dilutes and wash away the air pollution in the Kathmandu valley from June to September (Becker et al., 2021). This study shows that surface-level PM<sub>2.5</sub> concentration at the Kathmandu valley reflects a significant local level anthropogenic effect such as traffic and domestic cooking.

Figure 50 provides hourly variations of seasonally averaged PM<sub>2.5</sub> concentration (in  $\mu\text{g}/\text{m}^3$ ) and temperature (in °F) for 2020. The error bars represent the standard deviations of the measurements. The average maximum PM<sub>2.5</sub> was observed in the winter season ( $101 \pm 26.31 \mu\text{g}/\text{m}^3$ ) while the minimum was found in summer ( $22.78 \pm 3.23 \mu\text{g}/\text{m}^3$ ) and similarly, the average concentration was observed in spring ( $55.58 \pm 11.42 \mu\text{g}/\text{m}^3$ ) and in autumn, it was observed ( $45.46 \pm 12.16 \mu\text{g}/\text{m}^3$ ). The particle mass concentration is significantly higher for all seasons during the morning and evening traffic-rush hours. However, the evolution of the hourly PM<sub>2.5</sub> pattern depicts wide variations over the four seasons of the year. In fact, the amplitude and width of PM<sub>2.5</sub> for rush hours are maximum for winter and in spring seasons. Interestingly, both patterns show a decreasing trend for Autumn and almost no significant variations for the summer season. The evolutions of PM<sub>2.5</sub> pattern exhibits the signature of local activity, such as emission from house hold cooking and from traffic emissions. It shows that during the traffic rush hours, PM<sub>2.5</sub> increases gradually and peaks at about 8 am local time.



**Figure 50:** (A to K) Hourly averaged (at local time 0:45 – 23:45 hrs, shown in the bottom scale) particle concentration (PM<sub>2.5</sub>), Relative Humidity (RH%), and temperature (°F) by using entire months' data at Pulchowk in 2020

At this time, the highly detected particle concentration may be due to the formation of a new particle given by the traffic flow and low temperature, which might have affected the formation of secondary aerosols from the precursor gases (Mues et al., 2018).



**Figure 51:** Hourly averaged (at local time) particle concentration ( $PM_{2.5}$ ), relative Humidity (RH%), and temperature ( $^{\circ}F$ ) for seasonally averaged data by using the corresponding months' data for each season at Pulchowk in 2020. The scales for all graphs are shown.

Low temperature enhances the nucleation and condensation of emitted condensable compounds, providing many particles that can also form and successively grow to a detectable size. A previous study has shown that traffic is a significant source of atmospheric pollutants in the urban area with coarse particles associated with non-exhaust sources such as road abrasion, brake, and tire wear. However, fine particles are directly associated with fuel combustion (Kumar et al., 2016; Kumar & Goel, 2016; Pant & Harrison, 2013; Singh et al., 2017).

The variation of  $PM_{2.5}$  concentration patterns is similar in all seasons, which is bimodal. The hourly averaged mass concentration decreased after the winter season up to summer and then increased in autumn. This trend can be due to the rise in temperature in which the surface-level particles quickly diffuse to the vertical atmosphere causing low concentration at the surface level. The traffic flow was also significantly reduced due to the COVID lockdown period from March to July (Baral & Thapa, 2021). The monsoon also dramatically dilutes and wash away the air pollution in the Kathmandu

valley from June to September (Becker et al., 2021a). Many research articles have shown that PM<sub>2.5</sub> is significantly contributed by commercial and household cooking in the urban areas (Balasubramanian et al., 2021; Pervez et al., 2019; Robinson et al., 2018). The use of household fuel used for cooking and heating the house contributes significantly to anthropogenic particle emissions ranging from 20-55% on a global scale (Balasubramanian et al., 2021; Pervez et al., 2019). This study concludes that surface-level PM<sub>2.5</sub> concentration at the Kathmandu valley reflects a significant local level anthropogenic effect such as traffic and domestic cooking. However, we have not analyzed the chemical components of pollutants. Table 9 shows that the mass concentration is found lowest in the early mid-day while maximum in the morning in all seasons. The lower concentration of PM<sub>2.5</sub> in the mid-days can be due to the convection effect in which warmer, lighter air masses pollutants move from the ground to higher altitudes and less use of domestic and commercial cooking in the daytime in comparison to the morning time based on the direct observation of life living pattern in Kathmandu city.

**Table 9:** The average, maximum and minimum mass concentration (PM<sub>2.5</sub>) hourly averaged data of each season at Pulchowk in 2020.

Seasons	Average ( $\pm STD$ ) $\mu g/m^3$	Max. ( $\pm STD$ ) $\mu g/m^3$	Time for Max data	Min. ( $\pm STD$ )	Time for Min data
Winter	101.29 $\pm$ 26.31	158.64 $\pm$ 1.68	8.00 am	60.52 $\pm$ 0.86	3:00 pm
Spring	55.58 $\pm$ 11.42	80.41 $\pm$ 27.47	7:00 am	40.02 $\pm$ 10.61	2:00 pm
Summer	22.78 $\pm$ 3.23	28.15 $\pm$ 5.71	7:00 am	17.86 $\pm$ 5.50	2:00 pm
Autumn	45.40 $\pm$ 12.16	58.51 $\pm$ 10.6	5:00 am	22.68 $\pm$ 3.96	12:00pm

#### 4.16 Morning and afternoon MODIS AOD and Comparison with PM<sub>2.5</sub>

As shown in Figure 52, we observed that overall Aqua (afternoon) observations slightly over-lead the Terra (morning) AOD. A similar report was also presented previously in the spatial observations of AOD using two satellites (Ichoku, 2005; Koelemeijer et al., 2006). However, Figure 4 shows the correlation between Aqua and Terra AOD by using 52 data points, and it is found that they significantly correlate  $r = 0.942$ , and  $R^2 = 0.888$ , and  $P \ll 0.001$ . These differences signal the temporal variations of aerosol loading and

possibly due to potential calibration differences between two satellite sensors. We have observed that for April, the deviation of AOD data is significant from the 1:1 line and was observed slightly higher in the afternoon (Aqua) (Green et al., 2009). It indicates some additional aerosol loading in the afternoon over the vertical column. Overall, we find that these two estimates of AOD by two satellite measurements can represent the reliable and comparable aerosol optical depth and be used for the daily average.

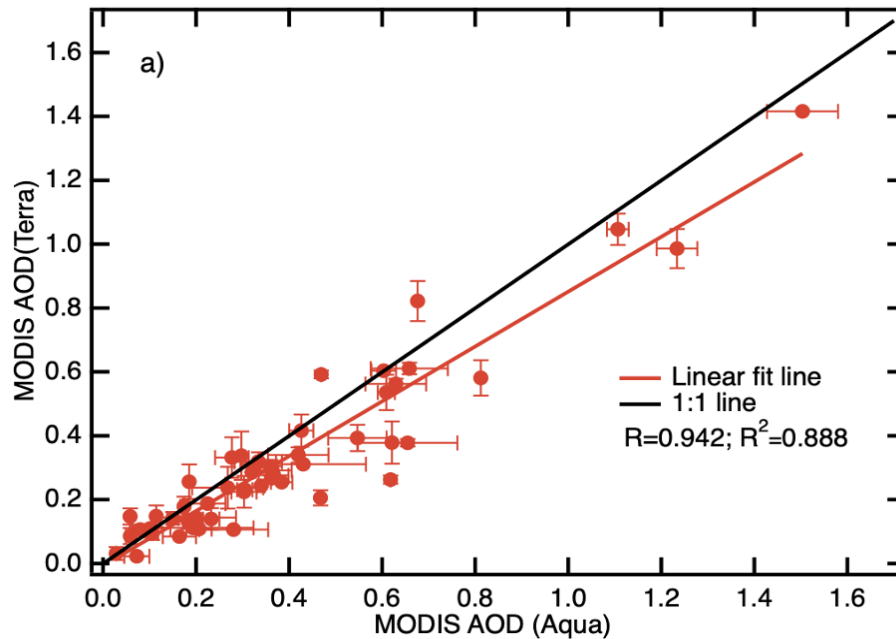


**Figure 52:** Scatter plot of a) MODIS AOD (Terra) vs MODIS AOD (Aqua) using the same day data observed from two satellites in Kathmandu, 2020 with  $3\text{km} \times 3\text{km}$  resolution. In the figure, some of the data also show the very nominal standard deviation.

The significant correlation between the morning and afternoon MODIS AOD retrieved from observed data by Aqua, and Terra depicts that the combined AOD data by two satellites can be compared to observe simultaneously with other components such as  $\text{PM}_{2.5}$ . In this study, we used three hours averaged  $\text{PM}_{2.5}$  as the mid hours coinciding with the MODIS AOD data to compare with MODIS AOD data. The standard deviation and linear best fit line are shown in Figure 53. The best fit line gives an equation,  $\text{AOD}_{550\text{nm}} = 0.038(\pm 0.037) + (0.0068 \pm 0.0006) \text{PM}_{2.5}(\text{PA})$ , and the correlation coefficient ( $R^2 = 0.407$ ) and P-values ( $\ll 0.005$ ) are also obtained from the plot.

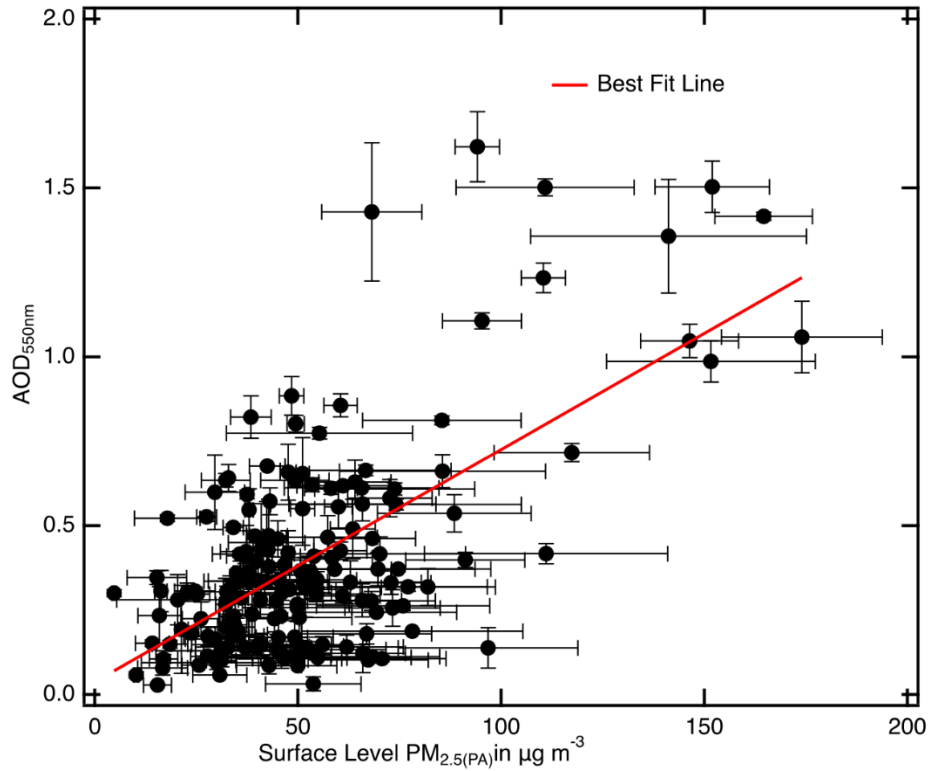


**Figure 53:** Scatter plot of MODIS AOD<sub>500 nm</sub> observed by Aqua and Terra satellites vs. PM<sub>2.5</sub> (PA) observed by PurpleAir monitor at Pulchowk in 2020 (Regmi et al., 2023).

Table 10 shows the correlation coefficients for all data and also for each season and is observed different  $R^2$  while using the correction factor  $f(RH)$ . The correlation factor has changed noticeably while using the relative humidity correction factor  $AOD/f(RH)$ . The variation on  $R^2$  indicates the higher effect of  $f(RH)$  on the season of lower temperature, however, in summer months, we have very few coinciding data available of MODIS AOD and PM<sub>2.5</sub>; therefore, these data cannot show a significant result for our analysis, although we have presented in the table. The correlation coefficient variations indicate the importance of considering the effect of atmospheric physical conditions to present the aerosol optical depth while observing from the satellite. At the lower average temperature, the aerosol particles distribute uniformly near the surface, and the planetary boundary layer will also be comparatively low than in high-temperature months (Zhang et al., 2009). At low temperature, the particle concentrations can remain close to the surface due to the temperature inversion showing the significant effect of vertical column AOD correction with  $f(RH)$ .



**Table 10:** The correlation coefficients between MODIS AOD (without and with relative humidity correction) and PM<sub>2.5</sub> for each seasons' data (2020) at Pulchowk.

Seasons/ Combined	AOD <sub>550 nm</sub> vs. PM <sub>2.5</sub> (PA)	AOD <sub>550 nm</sub> /f(RH) vs. PM <sub>2.5</sub> (PA)
All Data (172)	r = 0.638; R <sup>2</sup> = 0.407	r = 0.703; R <sup>2</sup> = 0.495
Winter (Dec-Feb) (28)	r = 0.643; R <sup>2</sup> = 0.413	r = 0.780; R <sup>2</sup> = 0.608
Spring (March-May) (77)	r = 0.653; R <sup>2</sup> = 0.426	r = 0.713; R <sup>2</sup> = 0.508
Summer (June-Sep) (9)	r = 0.134; R <sup>2</sup> = 0.018	r = 0.170; R <sup>2</sup> = 0.028
Autumn (Oct-Nov) (58)	r = 0.288; R <sup>2</sup> = 0.083	r = 0.542; R <sup>2</sup> = 0.293

#### 4.17 Comparison of hourly averaged seasonal PM<sub>2.5</sub> data from two different types of Sensors installed at Pulchowk (Lalitpur) and Phora-Durbar (Kathmandu)

For the validation of our data from PurpleAir monitor at Pulchowk, Lalitpur, we compared the data from MODIS device by collocating the data. Besides this, we also compared it with the data from Beta Attenuation Monitor (BAM) installed at Phora-Durbar Recreation Center (US Embassy) .

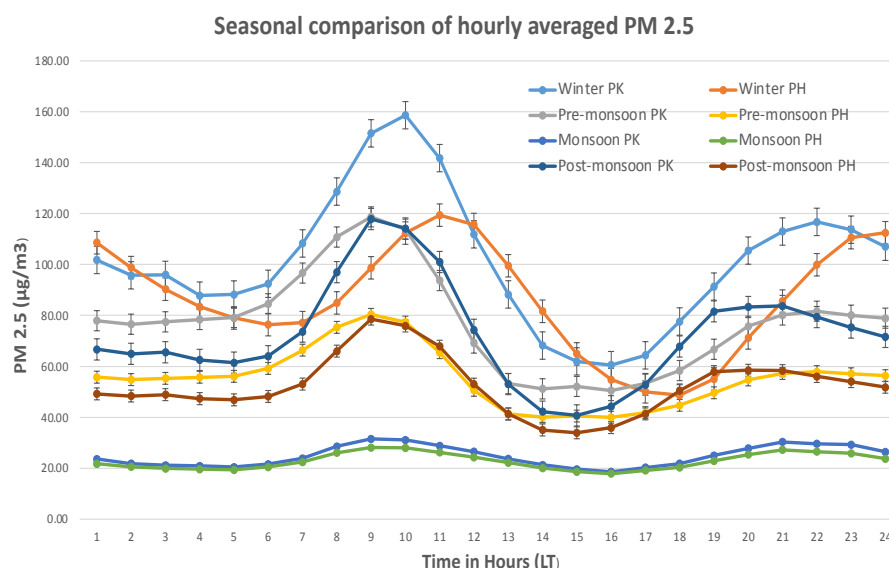


**Figure 54:** Seasonal Comparison of Hourly averaged (at local time) particle concentration (PM<sub>2.5</sub>), for two locations Pulchowk and Phora Durbar

**Table 10:** Comparison of PM<sub>2.5</sub> data from two different devices (Beta Attenuation Monitor; BAMS and PurpleAir) in two different locations: Phora Durbar(PH) and Pulchowk (PK) (Near to each other)

Time in Hours (LT)	Winter PK	Winter PH	Pre-monsoon PK	Pre-monsoon PH	Monsoon PK	Monsoon PH	Post-monsoon PK	Post-monsoon PH
0	101.79	108.58	77.95	55.77	23.64	21.79	66.68	49.20
1	95.78	98.81	76.58	54.83	21.86	20.53	64.94	48.36
2	95.96	90.33	77.51	55.31	21.20	19.91	65.55	48.90
3	87.81	83.42	78.42	55.74	20.91	19.64	62.55	47.33
4	88.23	79.03	79.21	56.10	20.51	19.39	61.49	46.87
5	92.46	76.39	84.60	59.21	21.60	20.48	64.02	48.20
6	108.29	77.18	96.67	66.39	23.92	22.45	73.66	53.07
7	128.68	84.94	110.81	75.35	28.61	26.10	97.02	66.00
8	151.54	98.70	118.73	80.42	31.52	28.15	117.87	78.58
9	158.64	112.38	113.86	77.41	31.14	27.98	114.19	75.89
10	141.80	119.41	93.73	65.42	28.83	26.21	101.01	67.89
11	111.87	115.71	69.18	50.64	26.52	24.31	74.36	53.01
12	88.27	99.52	53.23	41.37	23.66	22.17	53.06	41.31
13	68.20	81.64	51.19	40.14	21.34	20.07	42.23	35.02
14	61.97	64.90	52.14	40.51	19.65	18.63	40.74	33.92
15	60.52	54.82	50.50	40.02	18.60	17.86	44.34	35.98
16	64.35	50.05	53.27	41.84	20.27	19.17	52.79	41.33
17	77.63	48.70	58.35	44.73	21.81	20.37	67.83	50.45
18	91.35	55.10	66.74	49.63	25.06	22.89	81.63	57.95
19	105.49	71.15	75.78	54.71	27.80	25.37	83.34	58.48
20	112.97	85.66	80.21	57.20	30.33	27.21	83.74	58.32
21	116.75	99.92	81.68	57.94	29.64	26.52	79.39	56.05
22	113.70	110.57	80.13	57.13	29.25	25.87	75.25	54.03
23	107.01	112.52	78.94	56.36	26.43	23.76	71.58	51.83

The hourly averaged seasonal PM<sub>2.5</sub> values are presented in Table 10 for these two stations. It shows similar pattern of the data in both the stations with a very good

correlation. Figure 54 shows the comparison of seasonal variation of hourly averaged  $PM_{2.5}$  concentration at Phora-Durbar with that in Pulchowk, both of which are bimodal in nature. It is observed that the  $PM_{2.5}$  from PurpleAir are overrated compared to the  $PM_{2.5}$  data from BAMs as can be seen from Figure 55.

#### 4.18 Correlation between $PM_{2.5}$ at Pulchowk and $PM_{2.5}$ at Phora Durbar

The processing algorithms of the Plan-tower PMS5003 sensors (PA-PMS) used in the PurpleAir (PA) monitor configuration is unknown for public (He et al., 2020). The reliability of purpleair data  $PM_{2.5}$  is also observed by comparing the monthly averages  $PM_{2.5}$  observed from the purple air monitor at IOE, Pulchowk with the AmbientAir Quality Monitoring Station (BAM), supported by the U.S. Embassy at Phora Durbar Recreation Center.

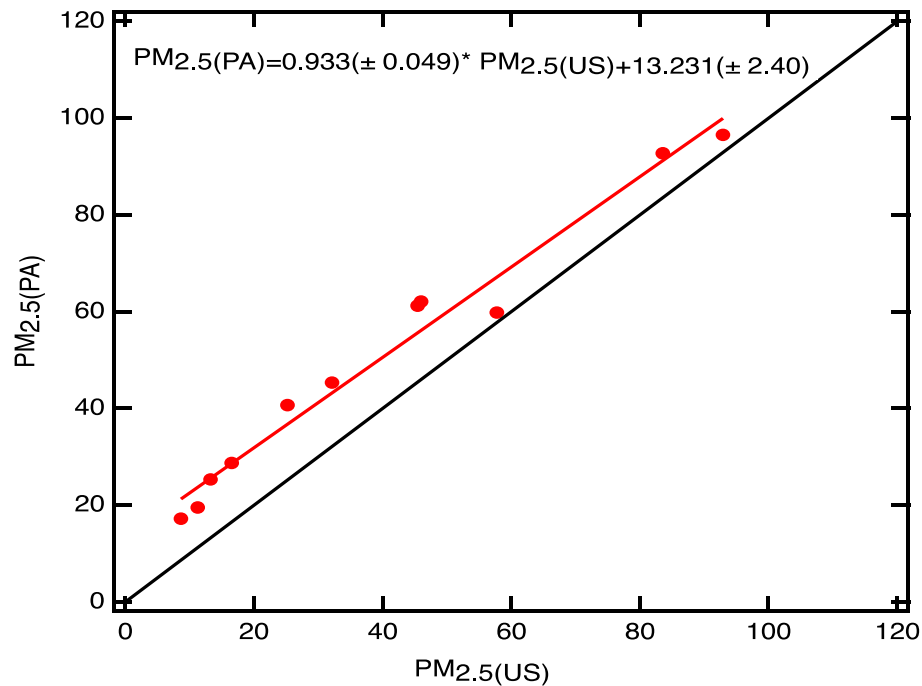


**Figure 55:** Monthly variation of Scatter plot of  $PM_{2.5}$ (US) at Phora Durbar vs.  $PM_{2.5}$ (PA) observed by purple air monitor at Pulchowk to establish correlation between them

The two data are correlated significantly. However, PurpleAir  $PM_{2.5}(PA)$  data ( $\mu g/m^3$ ) are overrated compared to the U.S. embassy data ( $PM_{2.5}(US)$  data ( $\mu g/m^3$ ), i. e. all the monthly average data observed from purple air are above the 1:1 line (Figure 55). However, in this study we have use the PurpleAir data for further analysis . The correlations between these two measurements is  $R^2 = 0.98$  with the equation,

$$PM_{2.5}(PA) = 0.933(\pm 0.0498) PM_{2.5}(US) + 13.231 (\pm 2.40).$$

#### 4.19 Seasonal Cluster Analysis

As this work compares the vertical column AOD and surface-level particle concentration therefore, we present the seasonal (winter, spring, summer, and autumn) back trajectory cluster analysis using the air mass trajectory of 2020 arrived at the observation site to indicate the additional influence of air pollution over the vertical column other than the surface level aerosols. The back trajectory of air mass for the seasonal clusters of five-day reaching over the observation area at an altitude of 500 m showing the long-range transport of air pollutants over the vertical column is presented in Figure 56.

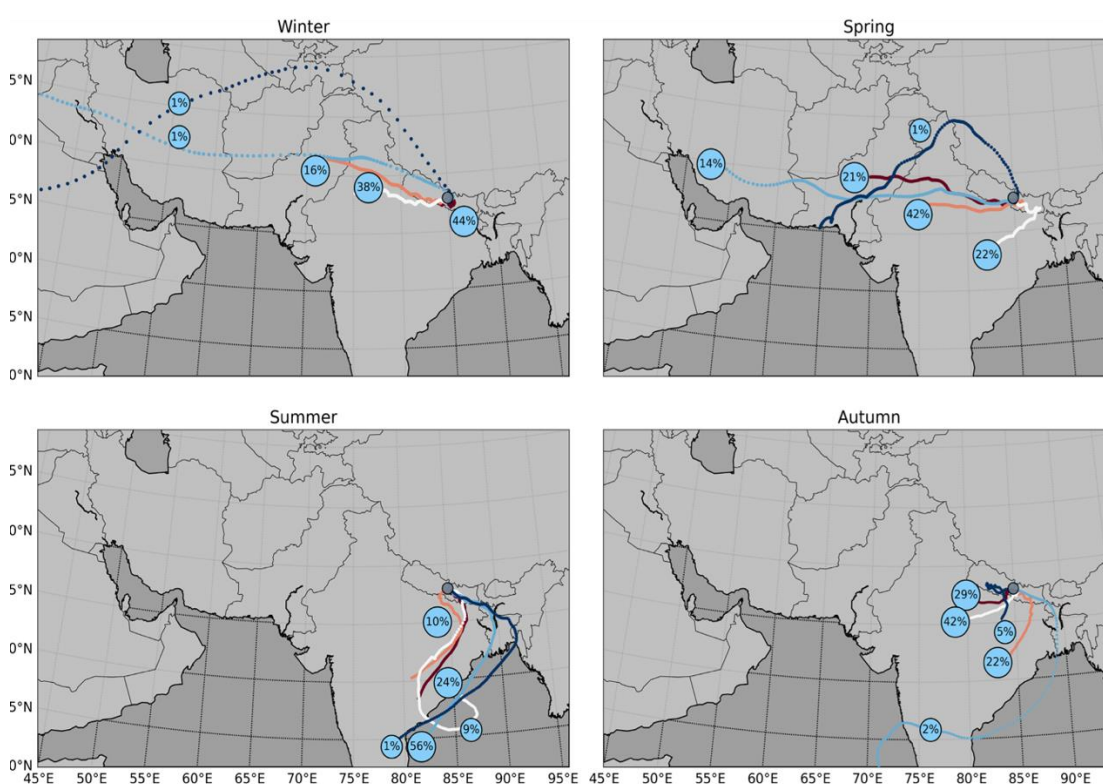


**Figure 56:** NOAA HYSPLIT Track showing the trans-boundary air pollution track showing the possible trajectories of the air parcels. The tracks are shown at 500 m asl ending at Kathmandu in 2020 (Regmi et al., 2023).

The percentage contribution for winter shows that 44% of air mass contributes from the south region, 38% from the southwest region crossing the Indo-Gangetic plain, 16% from western air mass, and the remaining 2% from the western, northwestern region. Overall, from Figure 56, it can be seen that the southwesterly air mass contribution during winter (December-February) and spring (March-May) has significantly affected the observation site. The contribution percentage and direction are shown in Figure 56.

During the monsoon (June-August), the prominent contribution is from southeasterly 24% and the main effect from the Bay of Bengal, which is 57%. In the Autumn (September-November), the southerly airmass is mainly transported from Indian inland. The previous study has also shown that the Kathmandu valley profoundly receives the air mass crossing the highly polluted region such as the Indo-Gangetic plain (Regmi et al., 2020). These air masses transported from different sources might affect the overall vertical aerosol population over Kathmandu and the column integrated AOD resulting the overall correlation factors while comparing column integrated AOD vs. surface-level  $PM_{2.5}$ .

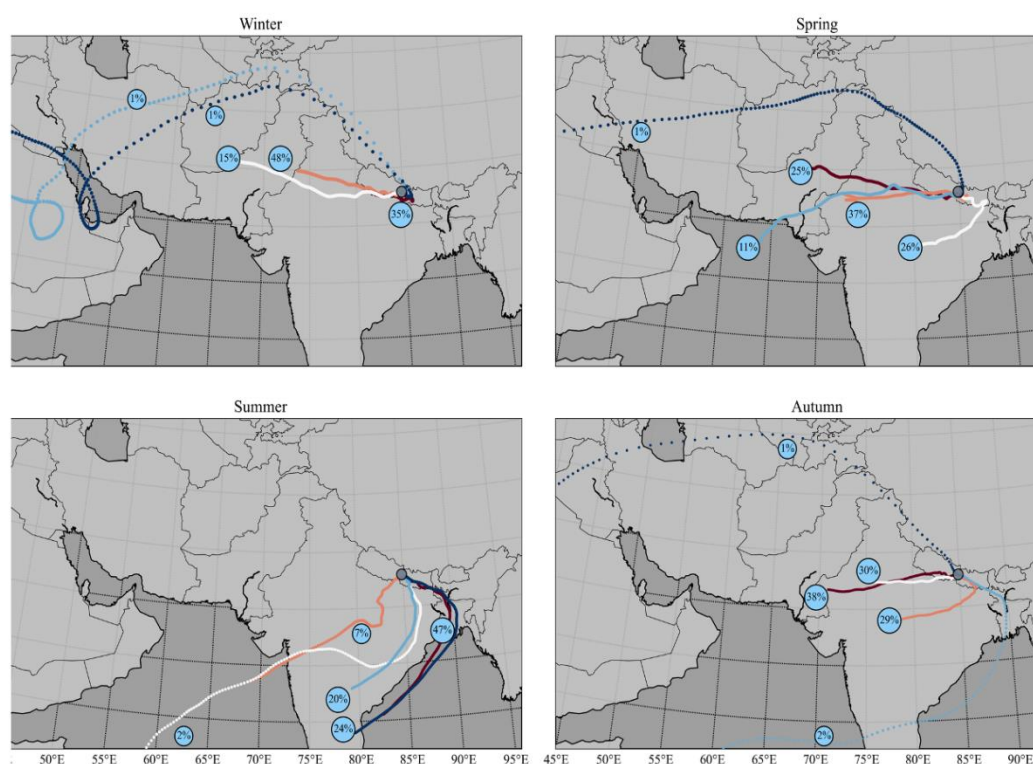


**Figure 57:** Cluster of five days air mass back trajectories computed with Analysis NOAA HYSPLIT with HYSPLIT model reaching Kathmandu valley at 1000 m asl at different seasons. The percentage contribution of each cluster is shown in different colors.

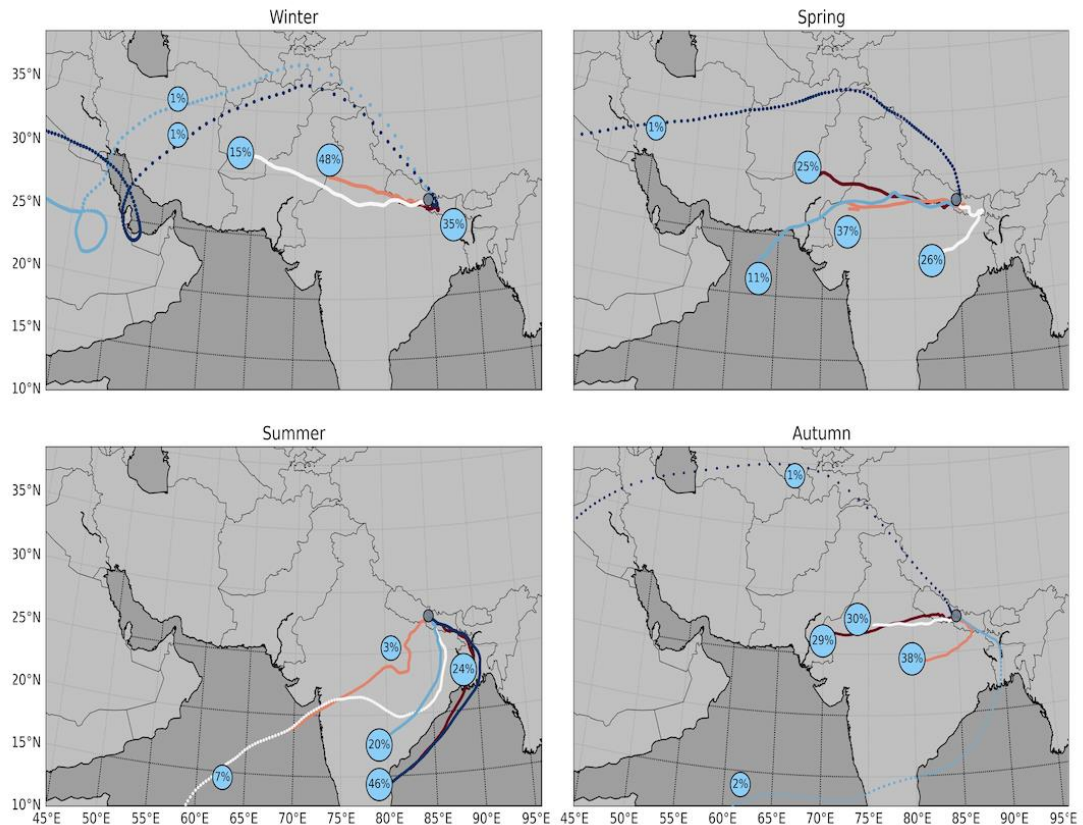


**Figure 58:** Cluster of five days air mass back trajectories computed with Analysis NOAA HYSPLIT with HYSPLIT model reaching Kathmandu valley at 1500 m asl at different seasons. The percentage contribution of each cluster is shown in different colors.

When we observe the clusters of air mass trajectory as in Figure 57 and Figure 58, there is very little difference between the prominent clusters at 1000 and 1500 meters and those at 500 meters. The air pollution at the observation point therefore travels vertically from a direction similar to that of 500 meters. On its journey to the observation site, the Kathmandu Valley, the air mass trajectory passes across the IGP region at various heights. As a result, the aerosol optical depth and the total vertical air pollution concentration are primarily affected by air pollution above the IGP region.

While summing up, we can see three major air masses pass over the Kathmandu valley every season, with five clusters having the best representation, according to percentage contributions, and three of these air masses are most common. Fast-moving air masses have a lower contribution to air pollution at the observation location, according to the cluster analysis, which ranges from 1 to 7 percent.

## CHAPTER 5

### CONCLUSIONS

This study examines the optical and microphysical characteristics of the atmospheric column at various AERONET sites in Nepal (Lumbini, Jomsom, Kathmandu Bode, and Foothills of Mount Everest, EVK2CNR) based on their geographical location, population density, and availability of AERONET aerosol retrievals. Our study examined the particulate matter of different sizes ( $PM_{10}$ ,  $PM_{2.5}$ , and  $PM_{1}$ ) using PurpleAir, and variations in aerosol optical properties based on AERONET AOD and AE, inversion products such as SSA, volume particle size distribution, HYSPLIT cluster analysis of air mass, and MODIS images and aerosol products. Using the long-term aerosol products available over Pokhara, 2010 to 2018, it is possible to predict spectral variations, aerosol distribution in the atmosphere column, and aerosol sources over Pokhara (Nepal). AERONET data from other stations also allowed us to analyze and compare aerosol concentrations, types, and transboundary aerosols, even though they were available for a shorter period of time than Pokhara's. Based on our study, we came to the following conclusions.

#### 1. Conclusions based on AERONET Data

**1.1** At shorter wavelengths, the aerosol optical depth is significantly high and shows a significant spectral variation. In highly polluted areas such as Kathmandu, the morning and evening hours aerosol loadings increase substantially compared to mid-day. All the aerosol optical depth at all AERONET sites also shows larger values during morning and evening than the afternoon data indicating the significant contribution of anthropogenic aerosols produced in the local region.

**1.2** The variation of AOD is also significantly affected by precipitation in the atmosphere, showing that rainfall is the most crucial meteorological parameter to alter the atmosphere's aerosol concentration. For example, the Pokhara site indicates that December to April strongly correlates (with a correlation coefficient of 0.96) with Precipitable Water level (PW), indicating the accumulation of aerosol and water vapor in the atmosphere increases in the months of winter and pre-monsoon season and varies inversely with a correlation coefficient of -0.61 from May to November.

**1.3** Long-range aerosol transportation plays a crucial role in the atmosphere column. AOD and other aerosol products can only be adequately analyzed over the vertical column, taking long-range transport aerosol into account. Based on the cluster analysis of Pokhara and Kathmandu, we identified that the aerosols arrive in Nepal in winter and pre-monsoon seasons from westerly, southwesterly, and northwesterly directions.

**1.4** Cluster analysis can provide a clear picture of AOD variation based on directional analysis. Based on the air mass trajectory analysis, the air mass passes over neighboring countries, which include India and Pakistan. In the monsoon season, Pokhara experiences adequate rain and a reduction in smoke fires, resulting in AOD values dropping significantly ( $<0.20$ ). As the trajectory passes toward Pokhara after the monsoon season, it passes through the North West region (mainly dust spots), the northeast, and around the IGP region (where fires are prevalent), causing AOD to rise slightly in comparison to monsoon. This season's biomass aerosols will therefore contribute to local and overall AOD.

**1.5** Overall, in Nepal, fine-mode particles contribute significantly during winter, post-monsoon, and pre-monsoon seasons. From the end of the pre-monsoon season, coarse mode particles contribute more toward the monsoon season.

**1.6** Analyzing the AERONET inversion products SSA, AAOD, and AAE with long-term data from Pokhara has been done using a spectral variation of aerosol optical properties and identifying aerosol types. From January to May, the spectral SSA of each month increases and decreases with wavelength, indicating the presence of mixed aerosols in Pokhara. Accordingly, SSA increases with the wavelength in locations dominated by desert dust and decreases with the wavelength in urban-industrial and biomass-burning areas. A higher positive slope of AAOD spectral dependence at short wavelengths indicates urban-industrial and smoke aerosols and mixed aerosols. Pokhara's AAE varies from 1.38 to 1.71, indicating biomass burning and urban industrial aerosols (mix type).

## **2. Conclusions based on Pyranometer data**

**2.1** The highest GSR values gradually grew from January to March, then declined in April, and then increased again in June, according to an analysis of daily average data for Global Solar Radiation (GSR) in Pokhara. Between July and December, it steadily



drops. In almost every month, the mean values were less than the median values. The averages for the months of March and January are respectively 19.19 and 4.61 MJ/m<sup>2</sup> and 9.31 and 4.39 MJ/m<sup>2</sup>.

**2.2** GSR and AOD data from AERONET Pokhara show that in 2020, an increase in aerosol loading in the vertical column was accompanied by a decrease in the amount of solar radiation reaching the ground. Finally, it is concluded that the atmospheric aerosols absorb the solar radiation and it reduces the solar energy budget significantly on the surface of the earth. It means that there is anticorrelation between atmospheric aerosols and solar radiation. So, it is urgent to promote clean and green renewable energy resources to solve the energy crisis all over the country.

### **3. Conclusions based on Purple Air data**

1. In Kathmandu, PM<sub>2.5</sub> concentrations swing bimodally throughout the year, with morning and evening rush hours having the highest concentrations. By comparing the column-integrated aerosol data from MODIS and the surface-level aerosol concentration, this study examines the accuracy of Purple Air measurements.

2. Using Purple Air's surface level particulate concentrations combined with satellite-based atmospheric column aerosol optical depth measurements, we can determine the relative humidity correction factor, which is a significant parameter for accurate comparison.

### **Recommendations and Future Works**

For better understanding of aerosol physical and optical properties, and their role in Earth's climate system and radiation budget, following recommendations are made.

1. Long-term Monitoring: To understand the spatio-temporal variation of aerosol properties, long-term monitoring system is to be established so that regular collection of data like size, shape, composition, and concentrations can be made.
2. Integrated Approaches: Multiple observational and modelling techniques are to be used to obtain precise result.

3. Impacts on Solar Energy: Nepal has a good potential of solar energy harvesting. Proper studies on aerosol optical properties can lead to develop robust models for the production of renewable solar energy.
4. Mitigation Strategies: To reduce negative impact of aerosol on atmosphere and to keep energy balance and climatic pattern, extensive and time series studies are to be carried out at multiple strategic locations.
5. Cloud lifetime effect: Aerosols' impact on cloud lifetime causes to alter climatic pattern so that proper modelling of aerosol-cloud interactions can be done.
6. To assess aerosol indirect and semi-direct effects from data, understanding the emission shift of aerosols and their precursors is crucial. As climatic and environmental conditions change across the globe, determining the primary emission sources will be crucial for predicting future aerosol indirect and semi-direct effects.

## CHAPTER 6

### SUMMARY

We need continuous and long-term data for analyzing local and transboundary aerosol particles because aerosol concentrations vary significantly on a spatial and temporal scale. A combination of surface-level data from PurpleAir, ground-based observations using sun photometers (AERONET provides aerosol products), and satellite observations using MODIS were used to study the physical and optical properties of aerosol particles on a daily, monthly, and seasonal basis. Study sites are carefully selected to represent an approximate picture of Nepal, from the high mountainous region EVK2\_CNR to the highly polluted lowland Lumbini. A PurpleAir monitor in Kathmandu and Pokhara analyzes daily and monthly. Seasonal variations in surface-level particle concentration reveal a high level of pollution almost in all three seasons except summer, where there is a bimodal variation with a peak in the morning at about 8 a.m. and another peak in the evening at around 7 p.m.

Pokhara and Kathmandu receive significant amounts of transboundary and local pollution, showing Nepal receives air pollution from the highly polluted region IGP and the eastern part of Pakistan. According to a time series analysis of Pokhara data for nine years (2010-2018), aerosol volume size distributions in the pre-monsoon season are both accumulation mode and coarse mode, contributing to the highest mean AOD, whereas fine mode particles dominate during the winter and post-monsoon seasons. As the pre-monsoon season draws to close, coarse mode particles begin to contribute significantly to the monsoon season. SSA, AAOD, and AAE aerosol inversion products are analyzed to compute the spectral variation and identify the aerosol types in Pokhara, revealing mixed aerosols showing how the size distribution has a vital role in aerosol optical properties.

Based on spatial variation in MODIS AOD images across Nepal, the Terai region, which borders the densely populated and heavily polluted Indo-Gangetic Plain (IGP), has a greater concentration of AOD values. Terai's eastern portion has a higher AOD value than its western portion. Another significant trend in these data sets is the gradual decline in the value of AOD as elevation increases.

The analysis of the daily average data for global solar radiation (GSR) reveals that maximum GSR values gradually rose from January to March, then fell in April, and then rose once more in June. From July to December, it steadily drops. The mean values for almost every month were less than their median values.

## REFERENCES

- Adhikari, P., & Mejjia, J. F. (2022). Impact of Transported Dust Aerosols on Precipitation over the Nepal Himalayas Using Convection-Permitting WRF-Chem Simulation. *Atmospheric Environment: X*, **15**: 1–13. <https://doi.org/10.1016/j.aeaoa.2022.100179>
- Altaratz, O., Bar-Or, R. Z., Wollner, U., & Koren, I. (2013). Relative Humidity and Its Effect on Aerosol Optical Depth in the Vicinity of Convective Clouds. *Environmental Research Letters*, **8**(3): 1–6. <https://doi.org/10.1088/1748-9326/8/3/034025>
- Ångström, A. (1961). Techniques of Determining the Turbidity of the Atmosphere. *Tellus B*, **13**(2): <https://doi.org/10.3402/tellusb.v13i2.12984>
- Aryal, R. K., Lee, B., Karki, R., Gurung, A., Baral, B., & Byeon, S. (2009). *Dynamics of PM 2.5 Concentrations in Kathmandu Valley, Nepal*. **168**: 732–738. <https://doi.org/10.1016/j.jhazmat.2009.02.086>
- Aryal, R. P., Voss, K. J., Terman, P. A., Keene, W. C., Moody, J. L., Welton, E. J., & Holben, B. N. (2014). Comparison of Surface and Column Measurements of Aerosol Scattering Properties over the Western North Atlantic Ocean at Bermuda. *Atmospheric Chemistry and Physics*, **14**(14): 7617–7629. <https://doi.org/10.5194/acp-14-7617-2014>
- Balasubramanian, S., Domingo, N. G. G., Hunt, N. D., Gittlin, M., Colgan, K. K., Marshall, J. D., Robinson, A. L., Azevedo, I. M. L., Thakrar, S. K., Clark, M. A., Tessum, C. W., Adams, P. J., Pandis, S. N., & Hill, J. D. (2021). The Food We Eat, the Air We Breathe: A Review of the Fine Particulate Matter-induced Air Quality Health Impacts of the Global Food System. *Environmental Research Letters*, **16**(10): <https://doi.org/10.1088/1748-9326/ac065f>
- Baral, B. D., & Thapa, K. (2021). Effect of the COVID-19 Lockdown on Ambient Air Quality in Major Cities of Nepal. *Journal of Health and Pollution*, **11**(29): <https://doi.org/10.5696/2156-9614-11.29.210211>
- Barnes, J., & Mauersberger, K. (1987). Temperature Dependence of the Ozone Absorption Cross Section at the 253.7-nm Mercury Line. *Journal of Geophysical Research*, **92**(14): 861-875. <https://doi.org/https://doi.org/10.1029/JD092iD12p14861>

- Becker, S., Sapkota, R. P., Pokharel, B., Adhikari, L., Pokhrel, R. P., Khanal, S., & Giri, B. (2021). Particulate Matter Variability in Kathmandu Based on In-situ Measurements, Remote Sensing, and Reanalysis Data. *Atmospheric Research*, **258**: 1–14. <https://doi.org/10.1016/j.atmosres.2021.105623>
- Bergstrom, R. W., Pilewskie, P., Russell, P. B., Redemann, J., Bond, T. C., Quinn, P. K., & Sierau, B. (2007). Spectral Absorption Properties of Atmospheric Aerosols. *Atmospheric Chemistry and Physics*, **7**(23): 5937–5943. <https://doi.org/10.5194/acp-7-5937-2007>
- Bergstrom, R. W., Pilewskie, P., Schmid, B., & Russell, P. B. (2003). Estimates of the Spectral Aerosol Single Scattering Albedo and Aerosol Radiative Effects during SAFARI 2000. *Journal of Geophysical Research D: Atmospheres*, **108**(13): 1–11. <https://doi.org/10.1029/2002jd002435>
- Bhattarai, B. C., Burkhart, J. F., Stordal, F., & Xu, C. Y. (2019). Aerosol Optical Depth Over the Nepalese Cryosphere Derived from an Empirical Model. *Frontiers in Earth Science*, **7**(July): 1–17. <https://doi.org/10.3389/feart.2019.00178>
- Bhattarai, B. K., Kjeldstad, B., Thorseth, T. M., & Bagheri, A. (2006). Aerosol Climatology in Kathmandu Using Sun Photometry. *Remote Sensing of Clouds and the Atmosphere XI*, 6362, 636204. <https://doi.org/10.1117/12.688963>
- Bhattarai, B. K., Kjeldstad, B., Thorseth, T. M., & Bagheri, A. (2007). Erythemal Dose in Kathmandu, Nepal Based on Solar UV Measurements from Multichannel Filter Radiometer, Its Deviation from Satellite and Radiative Transfer Simulations. *Atmospheric Research*, **85**(1): 112–119. <https://doi.org/10.1016/j.atmosres.2006.11.006>
- Blumthaler, M., Ambach, W., & Ellinger, R. (1997). Increase in Solar UV Radiation with Altitude. *Journal of Photochemistry and Photobiology B: Biology*, **39**(2): 130–134. [https://doi.org/https://doi.org/10.1016/S1011-1344\(96\)00018-8](https://doi.org/https://doi.org/10.1016/S1011-1344(96)00018-8)
- Bonasoni, P., Laj, P., Angelini, F., Arduini, J., Bonafè, U., Calzolari, F., Cristofanelli, P., Decesari, S., Facchini, M. C., Fuzzi, S., Gobbi, G. P., Maione, M., Marinoni, A., Petzold, A., Roccatò, F., Roger, J. C., Sellegri, K., Sprenger, M., Venzac, H. Vuillermoz, E. (2008). The ABC-Pyramid Atmospheric Research Observatory in Himalaya for Aerosol, Ozone and Halocarbon Measurements. *Science of the Total Environment*, **391**(2–3): 252–261. <https://doi.org/10.1016/j.scitotenv.2007.10.024>

- Bonasoni, P., Laj, P., Marinoni, A., Sprenger, M., Angelini, F., Arduini, J., Bonafè, U., Calzolari, F., Colombo, T., Decesari, S., di Biagio, C., di Sarra, A. G., Evangelisti, F., Duchi, R., Facchini, M.C., Fuzzi, S., Gobbi, G. P., Maione, M., Panday, A., Cristofanelli, P. (2010). Atmospheric Brown Clouds in the Himalayas: First Two Years of Continuous Observations at the Nepal Climate Observatory-Pyramid (5079m). *Atmospheric Chemistry and Physics*, **10**(15): 7515–7531. <https://doi.org/10.5194/acp-10-7515-2010>
- Boucher, O. (2015). *Atmospheric Aerosols: Properties and Climate Impacts* (1st Ed.). Springer Netherlands. <https://doi.org/10.1007/978-94-017-9649-1>
- Brock, C. A., Froyd, K. D., Dollner, M., Williamson, C. J., Schill, G., Murphy, D. M., Wagner, N. J., Kupc, A., Jimenez, J. L., Campuzano-Jost, P., Nault, B. A., Schroder, J. C., Day, D. A., Price, D. J., Weinzierl, B., Schwarz, J. P., Katich, J. M., Wang, S., Zeng, L., ... Wofsy, S. C. (2021). Ambient Aerosol Properties in the Remote Atmosphere from Global-scale in situ Measurements. *Atmospheric Chemistry and Physics*, **21**(19): 15023–15063. <https://doi.org/10.5194/acp-21-15023-2021>
- Brock, C. A., Wagner, N. L., Anderson, B. E., Attwood, A. R., Beyersdorf, A., Campuzano-Jost, P., Carlton, A. G., Day, D. A., Diskin, G. S., Gordon, T. D., Jimenez, J. L., Lack, D. A., Liao, J., Markovic, M. Z., Middlebrook, A. M., Ng, N. L., Perring, A. E., Richardson, M. S., Schwarz, J. P., ... Murphy, D. M. (2016). Aerosol Optical Properties in the Southeastern United States in Summer- Part 1: Hygroscopic Growth. *Atmospheric Chemistry and Physics*, **16**(8): 4987–5007. <https://doi.org/10.5194/acp-16-4987-2016>
- Bulot, F. M. J., Johnston, S. J., Basford, P. J., Easton, N. H. C., Apetroaie-Cristea, M., Foster, G. L., Morris, A. K. R., Cox, S. J., & Loxham, M. (2019). Long-Term Field Comparison of Multiple Low-Cost Particulate Matter Sensors in an Outdoor Urban Environment. *Scientific Reports*, **9**(1): 1–13. <https://doi.org/10.1038/s41598-019-43716-3>
- Chatterjee, A., Ghosh, S. K., Adak, A., Singh, A. K., Devara, P. C. S., & Raha, S. (2012). Effect of Dust and Anthropogenic Aerosols on Columnar Aerosol Optical Properties over Darjeeling (2200 m asl), Eastern Himalayas, India. *Plos One*, **7**(7): 1–10. <https://doi.org/10.1371/journal.pone.0040286>
- Chen, P., Li, C., Kang, S., Yan, F., Zhang, Q., Ji, Z., Tripathi, L., Rupakheti, D., Rupakheti, M., Qu, B., & Sillanpää, M. (2016). Source Apportionment of Particle-

- Bound Polycyclic Aromatic Hydrocarbons in Lumbini, Nepal by Using the Positive Matrix Factorization Receptor Model. *Atmospheric Research*, **182**: 46–53. <https://doi.org/10.1016/j.atmosres.2016.07.011>
- Cho, C., Kim, S. W., Rupakheti, M., Park, J. S., Panday, A., Yoon, S. C., Kim, J. H., Kim, H., Jeon, H., Sung, M., Mann Kim, B., Hong, S. K., Park, R. J., Rupakheti, D., Singh Mahata, K., Siva Praveen, P., Lawrence, M. G., & Holben, B. (2017). Wintertime Aerosol Optical and Radiative Properties in the Kathmandu Valley during the SusKat-ABC Field Campaign. *Atmospheric Chemistry and Physics*, **17**(20): 12617–12632. <https://doi.org/10.5194/acp-17-12617-2017>
- Christoph Kleinschmitt. (2017). *Climate Engineering with Stratospheric Sulphate Aerosol: Development and Application of a Global Atmosphere-Aerosol Model for Studying Potential Efficacy and Impacts* [Natural Sciences]. Pierre and Marie Curie University.
- CMP6 - Pyranometer (Kipp and Zonen). (2019). <https://www.kippzonen.com/Product/12/CMP6-Pyranometer>
- Dahlback, A. (1996). Measurements of Biologically Effective UV Doses, Total Ozone Abundances, and Cloud Effects with Multichannel, Moderate Bandwidth Filter Instruments. *Applied Optics*, **35**(33): 6514–6521.
- Dhungel, S., Kathayat, B., Mahata, K., & Panday, A. (2018). Transport of Regional Pollutants through a Remote Trans-Himalayan Valley in Nepal. *Atmospheric Chemistry and Physics*, **18**(2): 1203–1216. <https://doi.org/10.5194/acp-18-1203-2018>
- Draxler, R. R., & Hess, G. D. (1998). An Overview of the HYSPLIT\_4 Modelling System for Trajectories, Dispersion and Deposition. *Australian Meteorological Magazine*, **47**(4): 295–308.
- Dubovik, O., Holben, B., Eck, T. F., Smirnov, A., Kaufman, Y. J., King, M. D., Tanré, D., & Slutsker, I. (2002). Variability of Absorption and Optical Properties of Key Aerosol Types Observed in Worldwide Locations. *Journal of Atmospheric Sciences*, **59**: 590–608. [https://doi.org/10.1175/1520-0469\(2002\)059<0590:voaaop>2.0.co;2](https://doi.org/10.1175/1520-0469(2002)059<0590:voaaop>2.0.co;2)
- Dubovik, O., & King, D. (2000). A Flexible Inversion Algorithm for Retrieval of Aerosol Optical Properties from Sun and Sky Radiance Measurements. *Journal of Geophysical Research*, **105**(D16): 673–690. <https://doi.org/https://doi.org/10.1029/2000JD900282>



- Duffie, J. A., & Beckman, W. A. (2013). *Solar engineering of thermal processes*. Wiley.
- Dumka, U. C., Tripathi, S. N., Misra, A., Giles, D. M., Eck, T. F., Sagar, R., & Holben, B. N. (2014). Latitudinal Variation of Aerosol Properties from Indo-Gangetic Plain to Central Himalayan Foothills during TIGERZ Campaign. *Journal of Geophysical Research*, **119**(8): 4750–4769. <https://doi.org/10.1002/2013JD021040>
- Eck, T. F., Holben, B. N., Dubovik, O., Smirnov, A., Slutsker, I., Lobert, J. M., & Ramanathan, V. (2001). Column-Integrated Aerosol Optical Properties over the Maldives during the Northeast Monsoon for 1998-2000. *Journal of Geophysical Research Atmospheres*, **106**(D22): 28555–28566. <https://doi.org/10.1029/2001JD000786>
- Eck, T. F., Holben, B. N., Reid, J. S., Dubovik, O., Smirnov, A., O'Neill, N. T., Slutsker, I., & Kinne, S. (1999). Wavelength Dependence of the Optical Depth of Biomass Burning, Urban, and Desert Dust Aerosols. *Journal of Geophysical Research Atmospheres*, **104**(D24): 31333–31349. <https://doi.org/10.1029/1999JD900923>
- Eck, T. F., Holben, B. N., Reid, J. S., Giles, D. M., Rivas, M. A., Singh, R. P., Tripathi, S. N., Bruegge, C. J., Platnick, S., Arnold, G. T., Krotkov, N. A., Carn, S. A., Sinyuk, A., Dubovik, O., Arola, A., Schafer, J. S., Artaxo, P., Smirnov, A., Chen, H., & Goloub, P. (2012). Fog- and cloud-induced aerosol modification observed by the Aerosol Robotic Network (AERONET). **117**, 1–18. <https://doi.org/10.1029/2011JD016839>
- Eck, T. F., Holben, B. N., Sinyuk, A., Pinker, R. T., Goloub, P., Chen, H., Chatenet, B., Li, Z., Singh, R. P., Tripathi, S. N., Reid, J. S., Giles, D. M., Dubovik, O., O'Neill, N. T., Smirnov, A., Wang, P., & Xia, X. (2010). Climatological Aspects of the Optical Properties of Fine/Coarse Mode Aerosol Mixtures. *Journal of Geophysical Research Atmospheres*, **115**(19): 1–20. <https://doi.org/10.1029/2010JD014002>
- El-Metwally, M., Alfaro, S. C., Wahab, M. M. A., Favez, O., Mohamed, Z., & Chatenet, B. (2011). Aerosol Properties and Associated Radiative Effects over Cairo (Egypt). *Atmospheric Research*, **99**(2): 263–276. <https://doi.org/10.1016/j.atmosres.2010.10.017>

- Fioletov, V. E., Kerr, J. B., McArthur, L. J. B., Wardle, D. I., & Mathews, T. W. (2002). Estimating UV Index Climatology over Canada. *Journal of Applied Meteorology*, **42**(3): 417–433. [https://doi.org/10.1175/1520-0450\(2003\)042<0417:EUICOC>2.0.CO;2](https://doi.org/10.1175/1520-0450(2003)042<0417:EUICOC>2.0.CO;2)
- Gautam, M. R., Timilsina, G. R., & Acharya, K. (2013). Climate Change in the Himalayas: Current State of Knowledge. *Policy Research Working Paper*, **6516**: 1–47.
- Gautam, R., Hsu, N. C., Tsay, S. C., Lau, K. M., Holben, B., Bell, S., Smirnov, A., Li, C., Hansell, R., Ji, Q., Payra, S., Aryal, D., Kayastha, R., & Kim, K. M. (2011). Accumulation of Aerosols over the Indo-Gangetic Plains and Southern Slopes of the Himalayas: Distribution, Properties and Radiative Effects during the 2009 Pre-monsoon Season. *Atmospheric Chemistry and Physics*, **11**(24): 12841–12863. <https://doi.org/10.5194/acp-11-12841-2011>
- Giles, D. M., Holben, B. N., Eck, T. F., Sinyuk, A., Smirnov, A., Slutsker, I., Dickerson, R. R., Thompson, A. M., & Schafer, J. S. (2012). An Analysis of AERONET Aerosol Absorption Properties and Classifications Representative of Aerosol Source Regions. *Journal of Geophysical Research Atmospheres*, **117**(17): 1–16. <https://doi.org/10.1029/2012JD018127>
- Gobbi, G. P., Angelini, F., Bonasoni, P., Verza, G. P., Marinoni, A., & Barnaba, F. (2010). Sunphotometry of the 2006-2007 Aerosol Optical/Radiative Properties at the Himalayan Nepal Climate Observatory-Pyramid (5079ma.s.l.). *Atmospheric Chemistry and Physics*, **10**(22): 11209–11221. <https://doi.org/10.5194/acp-10-11209-2010>
- Green, M., Kondragunta, S., Ciren, P., & Xu, C. (2009). Comparison of GOES and MODIS Aerosol Optical Depth (AOD) to Aerosol Robotic Network (AERONET) AOD and IMPROVE PM<sub>2.5</sub> Mass at Bondville, Illinois. *Journal of the Air and Waste Management Association*, **59**(9): 1082–1091. <https://doi.org/10.3155/1047-3289.59.9.1082>
- Gregory, L. (2011). *Cimel Sunphotometer (CSPHOT) Handbook*.
- Guo, J., Kang, S., Huang, J., Zhang, Q., Rupakheti, M., Sun, S., Tripathee, L., Rupakheti, D., Panday, A. K., Sillanpää, M., & Paudyal, R. (2017). Characterizations of Atmospheric Particulate-Bound Mercury in the Kathmandu Valley of Nepal, South Asia. *Science of the Total Environment*, **579**: 1240–1248. <https://doi.org/10.1016/j.scitotenv.2016.11.110>

- Han, S., Bian, H., Zhang, Y., Wu, J., Wang, Y., Tie, X., Li, Y., Li, X., & Yao, Q. (2012). Effect of Aerosols on Visibility and Radiation in Spring 2009 in Tianjin, China. *Aerosol and Air Quality Research*, **12**(2): 211–217. <https://doi.org/10.4209/aaqr.2011.05.0073>
- He, M., Kuerbanjiang, N., & Dhaniyala, S. (2020). Performance Characteristics of the Low-Cost Plan tower PMS Optical Sensor. *Aerosol Science and Technology*, **54**(2), 232–241. <https://doi.org/10.1080/02786826.2019.1696015>
- Hinds, W. C. (1999). Aerosol Technology: Properties, Behavior, and Measurement of Airborne Particles. In *Aerosol Technology* (2nd Ed.), John Wiley & Sons, Inc.
- Hobbs, P. V. (1993). Aerosol-Cloud Interactions. *International Geophysics*, **54**(C): 33–73. [https://doi.org/10.1016/S0074-6142\(08\)60211-9](https://doi.org/10.1016/S0074-6142(08)60211-9)
- Holben, B. N., Eck, T. F., Slutsker, I., Smirnov, A., Sinyuk, A., Schafer, J., Giles, D., & Dubovik, O. (2006). Aeronet's Version 2.0 Quality Assurance Criteria. *Remote Sensing of the Atmosphere and Clouds*, **6408**: 64080Q. <https://doi.org/10.1117/12.706524>
- Holben, B. N., Eck, T. F., Slutsker, I., Tanré, D., Buis, J. P., Setzer, A., Vermote, E., Reagan, J. A., Kaufman, Y. J., Nakajima, T., Lavenu, F., Jankowiak, I., & Smirnov, A. (1998a). AERONET-A Federated Instrument Network and Data Archive for Aerosol Characterization of a New Sun-Sky Scanning Radiometer System That. *ENVIRON*, **66**: 1–16. <http://capita.wustl.edu/capita/capitareports/coretriaval/AERONET.pdf>
- Holben, B. N., Eck, T. F., Slutsker, I., Tanré, D., Buis, J. P., Setzer, A., Vermote, E., Reagan, J. A., Kaufman, Y. J., Nakajima, T., Lavenu, F., Jankowiak, I., & Smirnov, A. (1998b). AERONET - A Federated Instrument Network and Data Archive for Aerosol Characterization. *Remote Sensing of Environment*, **66**(1): 1–16. [https://doi.org/10.1016/S0034-4257\(98\)00031-5](https://doi.org/10.1016/S0034-4257(98)00031-5)
- Holben, B. N., Tanré, D., Smirnov, A., Eck, T. F., Slutsker, I., Abuhassan, N., Newcomb, W. W., Schafer, J. S., Chatenet, B., Lavenu, F., Kaufman, Y. J., Castle, J. vande, Setzer, A., Markham, B., Clark, D., Frouin, R., Halthore, R., Karneli, A., O'Neill, N. T., ... Zibordi, G. (2001). An Emerging Ground-Based Aerosol Climatology: Aerosol Optical Depth from AERONET. *Journal of Geophysical Research: Atmospheres*, **106**(D11): 12067–12097. <https://doi.org/10.1029/2001JD900014>

- Hsu, N. C., Tsay, S. C., King, M. D., & Herman, J. R. (2004). Aerosol Properties over Bright-Reflecting Source Regions. *IEEE Transactions on Geoscience and Remote Sensing*, **42**(3): 557–569. <https://doi.org/10.1109/TGRS.2004.824067>
- Ichoku, C. (2005). Correction to “Quantitative Evaluation and Intercomparison of Morning and Afternoon Moderate Resolution Imaging Spectroradiometer (MODIS) Aerosol Measurements from Terra and Aqua.” *Journal of Geophysical Research*, **110**(D10): 1–23. <https://doi.org/10.1029/2005jd005897>
- Iqbal, M. (1983). *An Introduction to Solar Radiation*. Academic Press.
- Islam, M. R., Jayarathne, T., Simpson, I. J., Werden, B., Maben, J., Gilbert, A., Praveen, P. S., Adhikari, S., Panday, A. K., Rupakheti, M., Blake, D. R., Yokelson, R. J., Decarlo, P. F., Keene, W. C., & Stone, E. A. (2020). Ambient Air Quality in the Kathmandu Valley, Nepal, During the Pre-monsoon: Concentrations and Sources of Particulate Matter and Trace Gases. *Atmospheric Chemistry and Physics*, **20**(5): 2927–2951. <https://doi.org/10.5194/acp-20-2927-2020>
- Jaenicke, R. (1993). Tropospheric Aerosols. *International Geophysics*, **54**(C): 1–31. [https://doi.org/10.1016/S0074-6142\(08\)60210-7](https://doi.org/10.1016/S0074-6142(08)60210-7)
- Jethva, H., Torres, O., Field, R. D., Lyapustin, A., Gautam, R., & Kayetha, V. (2019). Connecting Crop Productivity, Residue Fires, and Air Quality over Northern India. *Scientific Reports*, **9**(1): 1–11. <https://doi.org/10.1038/s41598-019-52799-x>
- Kaskaoutis, D. G., & Kambezidis, H. D. (2006). Investigation into the Wavelength Dependence of the Aerosol Optical Depth in the Athens Area. *Quarterly Journal of the Royal Meteorological Society*, **132**(620): 2217–2234. <https://doi.org/10.1256/qj.05.183>
- Kaskaoutis, D. G., & Kambezidis, H. D. (2008). Comparison of the Ångström Parameters Retrieval in Different Spectral Ranges with the Use of Different Techniques. *Meteorology and Atmospheric Physics*, **99**(3–4): 233–246. <https://doi.org/10.1007/s00703-007-0279-y>
- Kaskaoutis, D. G., Kambezidis, H. D., Hatzianastassiou, N., Kosmopoulos, P. G., & Badarinath, K. V. S. (2007). Aerosol Climatology: Dependence of the Angstrom Exponent on Wavelength over Four AERONET Sites. *Atmospheric Chemistry and Physics Discussions*, **7**(3): 7347–7397. <https://doi.org/10.5194/acpd-7-7347-2007>
- Kaskaoutis, D. G., Kumar, S., Sharma, D., Singh, R. P., Kharol, S. K., Sharma, M., Singh, A. K., Singh, S., Singh, A., & Singh, D. (2014). Effects of Crop Residue Burning on Aerosol Properties, Plume Characteristics, and Long-Range Transport

- over Northern India. *Journal of Geophysical Research*, **119**(9): 5424–5444.  
<https://doi.org/10.1002/2013JD021357>
- Kaufman, J. (1993). Aerosol Optical Thickness and Atmospheric Path Radiance. *Journal of Geophysical Research*, **98**: 2677–2692.
- Kaufman, Y. J., Tanré, D., & Boucher, O. (2002). A Satellite View of Aerosols in the Climate System. *Nature*, **419**(6903): 215–223.  
<https://doi.org/10.1038/nature01091>
- Kaufman, Y. J., Wald, A. E., Remer, L. A., Gao, B.-C., Li, R.-R., & Flynn, L. (1997). The MODIS 2.1-m Channel-Correlation with Visible Reflectance for Use in Remote Sensing of Aerosol. *IEEE Transactions on Geoscience and Remote Sensing*, **35**(5): 1286-1298.
- Kedia, S., Ramachandran, S., Holben, B. N., & Tripathi, S. N. (2014). Quantification of Aerosol Type, and Sources of Aerosols over the Indo-Gangetic Plain. *Atmospheric Environment*, **98**: 607–619.  
<https://doi.org/10.1016/j.atmosenv.2014.09.022>
- Kerr, J. B. (2005). Understanding the Factors that Affect Surface Ultraviolet Radiation. *Optical Engineering*, **44**(4): 041002. <https://doi.org/10.1117/1.1886817>
- Kim, B. M., Park, J. S., Kim, S. W., Kim, H., Jeon, H., Cho, C., Kim, J. H., Hong, S., Rupakheti, M., Panday, A. K., Park, R. J., Hong, J., & Yoon, S. C. (2015). Source Apportionment of PM10 Mass and Particulate Carbon in the Kathmandu Valley, Nepal. *Atmospheric Environment*, **123**: 190–199.  
<https://doi.org/10.1016/j.atmosenv.2015.10.082>
- Kim, S., Yoon, S., Kim, J., & Kim, S. (2007). *Seasonal and monthly variations of columnar aerosol optical properties over east Asia determined from multi-year MODIS , LIDAR , and AERONET Sun / sky radiometer measurements*, **41**: 1634–1651. <https://doi.org/10.1016/j.atmosenv.2006.10.044>
- King, D. M., & Byrne, M. D. (1976). A Method for Inferring Total Ozone Content from the Spectral Variation of Total Optical Depth Obtained with a Solar Radiometer. *Journal of Atmospheric Sciences*, **33**: 2242–2251.  
[https://doi.org/https://doi.org/10.1175/1520-0469\(1976\)033<2242:AMFITO>2.0.CO;2](https://doi.org/https://doi.org/10.1175/1520-0469(1976)033<2242:AMFITO>2.0.CO;2)
- Kitada, T., & Regmi, R. P. (2003). Dynamics of Air Pollution Transport in Late Wintertime over Kathmandu Valley, Nepal: As Revealed with Numerical

- Simulation. *Journal of Applied Meteorology*, **42**(12): 1770–1798. [https://doi.org/10.1175/1520-0450\(2003\)042<1770:DOAPTI>2.0.CO;2](https://doi.org/10.1175/1520-0450(2003)042<1770:DOAPTI>2.0.CO;2)
- Koelemeijer, R. B. A., Homan, C. D., & Matthijsen, J. (2006). Comparison of Spatial and Temporal Variations of Aerosol Optical Thickness and Particulate Matter over Europe. *Atmospheric Environment*, **40**(27): 5304–5315. <https://doi.org/10.1016/j.atmosenv.2006.04.044>
- Kotchenruther, R. A., & Hobbs, P. v. (1998). Humidification Factors of Aerosols from Biomass Burning in Brazil. *Journal of Geophysical Research Atmospheres*, **103**(D24): 32081–32089. <https://doi.org/10.1029/98JD00340>
- Kumar, M., Singh, R. K., Murari, V., Singh, A. K., Singh, R. S., & Banerjee, T. (2016). Fireworks induced particle pollution: A Spatio-Temporal Analysis. *Atmospheric Research*, **180**: 78–91. <https://doi.org/10.1016/j.atmosres.2016.05.014>
- Kumar, P., & Goel, A. (2016). Concentration Dynamics of Coarse and Fine Particulate Matter at and around Signalized Traffic Intersections. *Environmental Science: Processes and Impacts*, **18**(9): 1220–1235. <https://doi.org/10.1039/c6em00215c>
- Kylling, A., Dahlback, A., & Mayer, B. (2000). The Effect of Clouds and Surface Albedo on UV Irradiances at a High Latitude Site. *Geophysical Research Letters*, **27**(9): 1411–1414. <https://doi.org/https://doi.org/10.1029/1999GL011015>
- Latha, K. M., & Badarinath, K. V. S. (2004). Correlation between Black Carbon Aerosols, Carbon Monoxide and Tropospheric Ozone over a Tropical Urban Site. *Atmospheric Research*, **71**(4): 265–274. <https://doi.org/https://doi.org/10.1016/j.atmosres.2004.06.004>
- Lawrence, M. G., & Lelieveld, J. (2010). Atmospheric Pollutant Outflow from Southern Asia: A Review. *Atmospheric Chemistry and Physics*, **10**(22): 11017–11096. <https://doi.org/10.5194/acp-10-11017-2010>
- Levy, R. C., Munchak, L. A., Mattoo, S., Patadia, F., Remer, L. A., & Holz, R. E. (2015). Towards a Long-Term Global Aerosol Optical Depth Record: Applying a Consistent Aerosol Retrieval Algorithm to MODIS and VIIRS-Observed Reflectance. *Atmospheric Measurement Techniques*, **8**(10): 4083–4110. <https://doi.org/10.5194/amt-8-4083-2015>
- Li, J., Carlson, B. E., & Lacis, A. A. (2015). Using Single-Scattering Albedo Spectral Curvature to Characterize East Asian Aerosol Mixtures. *Journal of Geophysical Research: Atmospheres*, 2037–2052. <https://doi.org/10.1002/2014JD022433>

- Liou, K. (2002). *An Introduction to Atmospheric Radiation Second Edition* (R. Dmowska, J. R. Holton, & H. T. Rossby, Eds. Vol. 84). Academic Press.
- Liou, K. N., Lee, J. L., Ou, S. C., Fu, Q., & Takano, Y. (1991). Ice Cloud Microphysics, Radiative Transfer and Large-Scale Cloud Processes. *Meteorology and Atmospheric Physics*, **46**: 41–50. <https://doi.org/10.1007/BF01026622>
- Liu, Y., Jia, R., Dai, T., Xie, Y., & Shi, G. (2014). A Review of Aerosol Optical Properties and Radiative Effects. *Journal of Meteorological Research*, **28**(6): 1003–1028. <https://doi.org/10.1007/s13351-014-4045-z>
- Lüthi, Z. L., Škerlak, B., Kim, S.-W., Lauer, A., Mues, A., Rupakheti, M., & Kang, S. (2015). Atmospheric Brown Clouds Reach the Tibetan Plateau by Crossing the Himalayas. *Atmospheric Chemistry and Physics*, **15**(11): 6007–6021. <https://doi.org/10.5194/acp-15-6007-2015>
- Madronich, S. (1993). *The Atmosphere and UV-B Radiation at Ground Level* (Madronich Sasha, Ed.). [https://doi.org/10.1007/978-1-4899-2406-3\\_1](https://doi.org/10.1007/978-1-4899-2406-3_1)
- Mahapatra, P. S., Puppala, S. P., Adhikary, B., Shrestha, K. L., Dawadi, D. P., Paudel, S. P., & Panday, A. K. (2019). Air Quality Trends of the Kathmandu Valley: A Satellite, Observation and Modeling Perspective. *Atmospheric Environment*, **201**: 334–347. <https://doi.org/10.1016/j.atmosenv.2018.12.043>
- Mallet, M., Dubovik, O., Nabat, P., Dulac, F., Kahn, R., Sciare, J., Paronis, D., & Léon, J. F. (2013). Absorption Properties of Mediterranean Aerosols Obtained from Multi-Year Ground-Based Remote Sensing Observations. *Atmospheric Chemistry and Physics*, **13**(18): 9195–9210. <https://doi.org/10.5194/acp-13-9195-2013>
- McKenzie, R. L., Kotkamp, M., & Ireland, W. (1996). Upwelling UV Spectral Irradiances and Surface Albedo Measurements at Lauder, New Zealand. *Geophysical Research Letters*, **23**(14): 1757–1760. <https://doi.org/10.1029/96GL01668>
- Molina, L. T., & Molina, M. J. (1986). Absolute Absorption Cross Sections of Ozone in the 185-to 350-nm Wavelength Range. *Journal of Geophysical Research*, **91**(D13): 501–515. <https://doi.org/10.1029/JD091iD13p14501>
- Moody, J. L., Keene, W. C., Cooper, O. R., Voss, K. J., Aryal, R., Eckhardt, S., Holben, B., & Maben, J. R. (2014). *Flow climatology for physicochemical properties of dichotomous aerosol over the western North Atlantic Ocean at Bermuda*. 691–717. <https://doi.org/10.5194/acp-14-691-2014>

- Mues, A., Lauer, A., Lupascu, A., Rupakheti, M., Kuik, F., & Lawrence, M. G. (2018). WRF and WRF-Chem v3.5.1 Simulations of Meteorology and Black Carbon Concentrations in the Kathmandu Valley. *Geoscientific Model Development*, **11**: 2067–2091. <https://doi.org/10.5194/gmd-11-2067-2018>
- Myhre, G., & Shindell, D. (2013). Anthropogenic and Natural Radiative Forcing. In D. Jacob, A. R. Ravishankara, & K. Shine (Eds.), *Climate Change 2013 the Physical Science Basis: Working Group I Contribution to the Fifth Assessment Report of the Intergovernmental Panel on Climate Change* (2013th ed., Vol. 9781107057), Cambridge University Press, Cambridge, United Kingdom and New York, Ny, USA. <https://doi.org/10.1017/CBO9781107415324.018>
- Ng, D. H. L., Li, R., Raghavan, S. v., & Liong, S. Y. (2017). Investigating the relationship between Aerosol Optical Depth and Precipitation over Southeast Asia with Relative Humidity as an influencing factor. *Scientific Reports*, **7**(1): 1–13. <https://doi.org/10.1038/s41598-017-10858-1>
- O'Neill, N. T., Eck, T. F., Holben, B. N., Smirnov, A., Dubovik, O., & Royer, A. (2001). Bimodal Size Distribution Influences on the Variation of Angstrom Derivatives in Spectral and Optical Depth Space. *Journal of Geophysical Research Atmospheres*, **106**(D9): 9787–9806. <https://doi.org/10.1029/2000JD900245>
- Panday, A. K., & Prinn, R. G. (2009). *Diurnal cycle of air pollution in the Kathmandu Valley, Nepal : Observations*. **114**: 1–19. <https://doi.org/10.1029/2008JD009777>
- Pant, P., & Harrison, R. M. (2013). Estimation of the Contribution of Road Traffic Emissions to Particulate Matter Concentrations from Field Measurements: A Review. *Atmospheric Environment*, **77**: 78–97. <https://doi.org/10.1016/j.atmosenv.2013.04.028>
- Papadimas, C. D., Hatzianastassiou, N., Matsoukas, C., Kanakidou, M., Mihalopoulos, N., & Vardavas, I. (2012). The Direct Effect of Aerosols on Solar Radiation over the Broader Mediterranean Basin. *Atmospheric Chemistry and Physics*, **12**(15): 7165–7185. <https://doi.org/10.5194/acp-12-7165-2012>
- Pedrós, R., Martínez-Lozano, J. A., Utrillas, M. P., Gómez-Amo, J. L., & Tena, F. (2003). Column-Integrated Aerosol Optical Properties from Ground-Based Spectroradiometer Measurements at Barrax (Spain) during the Digital Airborne Imaging Spectrometer Experiment (DAISEX) Campaigns. *Journal of*



*Geophysical Research: Atmospheres*, **108**(18): 1–17.  
<https://doi.org/10.1029/2002jd003331>

- Pervez, S., Verma, M., Tiwari, S., Chakrabarty, R. K., Watson, J. G., Chow, J. C., Panicker, A. S., Deb, M. K., Siddiqui, M. N., & Fatima Pervez, Y. (2019). Household Solid Fuel Burning Emission Characterization and Activity Levels in India. *Science of the Total Environment*, **654**: 493–504. <https://doi.org/https://doi.org/10.1016/j.scitotenv.2018.11.019>
- Pesava, P., Horvath, H., & Kasahara, M. (2001). A Local Optical Closure Experiment in Vienna. *Aerosol Science*, **32**: 1249–1267. [www.elsevier.com/locate/jaerosci](http://www.elsevier.com/locate/jaerosci)
- Pillai, P. S., & Moorthy, K. K. (2004). Size Distribution of Near-Surface Aerosols and Its Relation to the Columnar Aerosol Optical Depths. *Annales Geophysicae*. <https://doi.org/10.5194/angeo-22-3347-2004>
- Poudyal, K., de Vito, L., Bhattarai, B. K., Sapkota, B., Poudyal, K. N., Daponte, P., & Bhattarai, B. K. (2010). Study of Variation of Global Solar Radiation at Different Altitudes at Himalaya Region-A Case Study in Nepal. *Study of Variation of Global Solar Radiation at Different Altitudes at Himalaya Region-A Case Study in Nepal*, 1–7. <https://www.researchgate.net/publication/268809027>
- Poudyal, K. N., Bhattarai, B. K., Sapkota, B. K., Kjeldstad, B., & Karki, N. R. (2014). Estimation of Global Solar Radiation Using Pyranometer and NILU-UV Irradiance Meter at Pokhara Valley in Nepal. *Journal of the Institute of Engineering*. <https://doi.org/10.3126/jie.v9i1.10672>
- Poudyal, K. N., Bhattarai, B. K., Sapkota, B., & Kjeldstad, B. (2012). Estimation of Global Solar Radiation Using Clearness Index and Cloud Transmittance Factor at Trans-Himalayan Region in Nepal. *Energy and Power Engineering*, **04**(06): 415–421. <https://doi.org/10.4236/epe.2012.46055>
- Putero, D., Marinoni, A., Bonasoni, P., Calzolari, F., Rupakheti, M., & Cristofanelli, P. (2018). Black Carbon and Ozone Variability at the Kathmandu Valley and at the Southern Himalayas: A Comparison between a “Hot Spot” and a Downwind High-Altitude Site. *Aerosol and Air Quality Research*, **18**(3): 623–635. <https://doi.org/10.4209/aaqr.2017.04.0138>
- Rai, M., Mahapatra, P. S., Gul, C., Kayastha, R. B., Panday, A. K., & Puppala, S. P. (2019). Aerosol Radiative Forcing Estimation over a Remote High-altitude Location (~4900 masl) near Yala Glacier, Nepal. *Aerosol and Air Quality Research*, **19**(8): 1872–1891. <https://doi.org/10.4209/aaqr.2018.09.0342>

- Ramachandran, S., & Rupakheti, M. (2020). Inter-Annual and Seasonal Variations in Columnar Aerosol Characteristics and Radiative Effects over the Pokhara Valley in the Himalayan Foothills – Composition, Radiative Forcing, and Atmospheric Heating. *Environmental Pollution*, **264**: 1–14. <https://doi.org/10.1016/j.envpol.2020.114799>
- Ramachandran, S., & Rupakheti, M. (2021). Inter-Annual and Seasonal Variations in Optical and Physical Characteristics of Columnar Aerosols over the Pokhara Valley in the Himalayan Foothills. *Atmospheric Research*, **248**: 1–15. <https://doi.org/10.1016/j.atmosres.2020.105254>
- Ramachandran, S., Rupakheti, M., & Lawrence, M. G. (2020). Black Carbon Dominates the Aerosol Absorption over the Indo-Gangetic Plain and the Himalayan Foothills. *Environment International*, **142**: <https://doi.org/10.1016/j.envint.2020.105814>
- Ranabhat, C. L., Kim, C., Kim, C., Jha, N., Deepak, K. C., & Connel, F. A. (2015). *Consequence of indoor air pollution in rural area of Nepal: a simplified measurement approach*. **3**: 1–6. <https://doi.org/10.3389/fpubh.2015.00005>
- Regmi, J., Poudyal, K. N., Pokhrel, A., Gyawali, M., Barinelli, A., & Aryal, R. (2021). Analysis of Aerosol Optical Depth and Angstrom Exponents over an AERONET site at Pokhara, Nepal. *Bibechana*, **18**(1): 118–127. <https://doi.org/10.3126/bibechana.v18i1.29448>
- Regmi, J., Poudyal, K. N., Pokhrel, A., Gyawali, M., Tripathy, L., Panday, A., Barinelli, A., & Aryal, R. (2020). Investigation of Aerosol Climatology and Long-Range Transport of Aerosols over Pokhara, Nepal. *Atmosphere*, **11**(8): 1–16. <https://doi.org/doi:10.3390/atmos11080874>
- Regmi, J., Poudyal, K., Pokhrel, A., Barinelli, A., & Aryal, R. (2019). Aerosol Optical Properties of Size Segregated Aerosol Particles and Radiative Forcing over Pokhara valley. *Himalayan Physics*, **8**: 1–10.
- Reid, J. S., Hobbs, P. v., Rangno, A. L., & Hegg, D. A. (1999). Relationships between Cloud Droplet Effective Radius, Liquid Water Content, and Droplet Concentration for Warm Clouds in Brazil Embedded in Biomass Smoke. *Journal of Geophysical Research Atmospheres*, **104**(D6): 6145–6153. <https://doi.org/10.1029/1998JD200119>
- Remer, L. A., Kaufman, Y. J., Tanré, D., Mattoo, S., Chu, D. A., Martins, J. v, Li, R.-R., Ichoku, C, Levy, R. C., Kleidman, R. G., Eck, T. F., Vermote, E, Holben, B.

- N., & Ichoku, C. (2005). The MODIS Aerosol Algorithm, Products, and Validation. *Journal of the Atmospheric Sciences*, **62**: 947–973. <https://www.researchgate.net/publication/336142036>
- Robinson, E. S., Gu, P., Ye, Q., Li, H. Z., Shah, R. U., Apte, J. S., Robinson, A. L., & Presto, A. A. (2018). Restaurant Impacts on Outdoor Air Quality: Elevated Organic Aerosol Mass from Restaurant Cooking with Neighborhood-Scale Plume Extents. *Environmental Science and Technology*, **52**(16): 9285–9294. <https://doi.org/10.1021/acs.est.8b02654>
- Rupakheti, D., Adhikary, B., Praveen, P. S., Rupakheti, M., Kang, S., Mahata, K. S., Naja, M., Zhang, Q., Panday, A. K., & Lawrence, M. G. (2017). Pre-Monsoon Air Quality over Lumbini, a World Heritage Site along the Himalayan Foothills. *Atmospheric Chemistry and Physics*, **17**(18): 11041–11063. <https://doi.org/10.5194/acp-17-11041-2017>
- Rupakheti, D., Kang, S., Cong, Z., Rupakheti, M., Tripathee, L., Panday, A. K., & Holben, B. (2018a). Study of Aerosol Optical Properties over Two Sites in the Foothills of the Central Himalayas. *International Archives of the Photogrammetry, Remote Sensing and Spatial Information Sciences - ISPRS Archives*, **42**(3): 1493–1497. <https://doi.org/10.5194/isprs-archives-XLII-3-1493-2018>
- Rupakheti, D., Kang, S., Rupakheti, M., Cong, Z., Tripathee, L., Panday, A. K., & Holben, B. N. (2018). Observation of Optical Properties and Sources of Aerosols at Buddha's Birthplace, Lumbini, Nepal: Environmental Implications. *Environmental Science and Pollution Research*, **25**(15): 14868–14881. <https://doi.org/10.1007/s11356-018-1713-z>
- Russell, P. B., Bergstrom, R. W., Shinozuka, Y., Clarke, A. D., Decarlo, P. F., Jimenez, J. L., Livingston, J. M., Redemann, J., Dubovik, O., & Strawa, A. (2010). Absorption Angstrom Exponent in AERONET and Related Data as an Indicator of Aerosol Composition. *Atmospheric Chemistry and Physics*, **10**(3): 1155–1169. <https://doi.org/10.5194/acp-10-1155-2010>
- Sabburg, J., & Wong, J. (2000). The Effect of Clouds on Enhancing UVB Irradiance at the Earth's Surface: A One Year Study. *Geophysical Research Letters*, **27**(20): 3337–3340. <https://doi.org/10.1029/2000GL011683>
- Saikawa, E., Panday, A., Kang, S., Gautam, R., Zusman, E., Cong, Z., Somanathan, E., & Adhikary, B. (2019). *Air Pollution in the Hindu Kush Himalaya* (P., M. A., M.

- A., S. A. Wester, Ed.; 1st ed., Vol. 1). Springer International Publishing.  
<https://doi.org/10.1007/978-3-319-92288-1>
- Salby, M. L. (1995). *Fundamentals of Atmospheric Physics*. Academic Press.
- Sarkar, C., Sinha, V., Sinha, B., Panday, A. K., & Rupakheti, M. (2017). Source Apportionment of NMVOCs in the Kathmandu Valley during the SusKat-ABC International Field Campaign using Positive Matrix Factorization. *Atmos. Chem. Phys.*, **17**(13): 8129–8156. <https://doi.org/10.5194/acp-17-8129-2017>
- Savtchenko, A., Ouzounov, D., Ahmad, S., Acker, J., Leptoukh, G., Koziana, J., & Nickless, D. (2004). Terra and Aqua MODIS Products Available from NASA GES DAAC. *Advances in Space Research*, **34**(4): 710–714. <https://doi.org/10.1016/j.asr.2004.03.012>
- Schuster, G. L., Dubovik, O., & Holben, B. N. (2006). Angstrom Exponent and Bimodal Aerosol Size Distributions. *Journal of Geophysical Research Atmospheres*, **111**(7): 1–14. <https://doi.org/10.1029/2005JD006328>
- Seckmeyer, G., Erb, R., & Albold, A. (1996). Transmittance of a Cloud is Wavelength-Dependent in the UV-Range. *Geophysical Research Letters*, **23**(20): 2753–2755. <https://doi.org/10.1029/96GL02614>
- Seinfeld, J., & Pandis, S. (2006). *Atmospheric chemistry and physics: from air pollution to climate change*, (Second). Wiley, Inc., New Jersey, USA.
- Sellegrri, K., Laj, P., Venzac, H., Boulon, J., Picard, D., Villani, P., Bonasoni, P., Marinoni, A., Cristofanelli, P., & Vuillermoz, E. (2010). Seasonal Variations of Aerosol Size Distributions Based on Long-Term Measurements at the High Altitude Himalayan Site of Nepal Climate Observatory-Pyramid (5079 m), Nepal. *Atmospheric Chemistry and Physics*, **10**(21): 10679–10690. <https://doi.org/10.5194/acp-10-10679-2010>
- Sharma, M., Kaskaoutis, D. G., Singh, R. P., & Singh, S. (2014). Seasonal Variability of Atmospheric Aerosol Parameters over Greater Noida using Ground Sun photometer Observations. *Aerosol and Air Quality Research*, **14**(3): 608–622. <https://doi.org/10.4209/aaqr.2013.06.0219>
- Shrestha, P. M., Regmi, J., Joshi, U., Poudyal, K. N., Chapagain, N. P., & Karki, I. B. (2020). Study of Affecting Factors of Meteorological Parameters on Solar Radiation on Pokhara. *Himalayan Physics*, **9**: 45–52.

- Shrestha, S., Puppala, S. P., Adhikary, B., & Shrestha, K. L. (2017). *Influence of semi-volatile aerosols on physical and optical properties of aerosols in the Kathmandu Valley*, 1–33. <https://doi.org/10.5194/acp-2017-287>
- Sigdel, M., & Ikeda, M. (2012). Earth Science & Climatic Change Summer Monsoon Rainfall over Nepal Related with Large-Scale Atmospheric Circulations. *Journal of Earth Science & Climatic Change*, **3**(2): 112. <https://doi.org/10.4172/2157-7617.1000112>
- Singh, A., Mahata, K. S., Rupakheti, M., Junkermann, W., & Panday, A. K. (2019). An Overview of Airborne Measurement in Nepal – Part 1 : Vertical Profile of Aerosol Size, Number, Spectral Absorption, and Meteorology. *Atmos. Chem. Phys.*, **19**(1): 245–258. <https://doi.org/https://doi.org/10.5194/acp-19-245-2019>
- Singh, N., Banerjee, T., Raju, M. P., Deboudt, K., Sorek-Hamer, M., Singh, R. S., & Mall, R. K. (2018). Aerosol Chemistry, Transport and Climatic Implications during Extreme Biomass Burning Emissions over Indo-Gangetic Plain. *Atmospheric Chemistry and Physics Discussions*, 1–37. <https://doi.org/10.5194/acp-2018-446>
- Singh, N., Murari, V., Kumar, M., Barman, S. C., & Banerjee, T. (2017). Fine Particulates over South Asia: Review and Meta-Analysis of PM<sub>2.5</sub> Source Apportionment through Receptor Model. *Environmental Pollution*, **223**(2016): 121–136. <https://doi.org/10.1016/j.envpol.2016.12.071>
- Smirnov, A., Holben, B. N., Eck, T. F., Dubovik, O., & Slutsker, I. (2000). Cloud-Screening and Quality Control Algorithms for the AERONET Database. *Remote Sensing of Environment*, **73**(3): 337–349. [https://doi.org/10.1016/S0034-4257\(00\)00109-7](https://doi.org/10.1016/S0034-4257(00)00109-7)
- Srivastava, A. K., Dey, S., & Tripathi, S. N. (2012). Aerosol Characteristics over the Indo-Gangetic Basin: Implications to Regional Climate. *Atmospheric Aerosols - Regional Characteristics - Chemistry and Physics*. <https://doi.org/10.5772/47782>
- Stein, A. F., Draxler, R. R., Rolph, G. D., Stunder, B. J. B., Cohen, M. D., & Ngan, F. (2015). NOAA's HYSPLIT Atmospheric Transport and Dispersion Modeling System. In *Bulletin of the American Meteorological Society*, **96**(12): American Meteorological Society. <https://doi.org/10.1175/BAMS-D-14-00110.1>
- Tanre D., Kaufman Y.J., Herman M., & Mattoo S. (1997). Remote Sensing of Aerosol Properties over Oceans using the MODIS/EOS Spectral Radiances. *Journal of*

- Geophysical Research*, **102**(D14): 16971–16988.  
<https://doi.org/https://doi.org/10.1029/96JD03437>
- Tomasi, C., & Lupi, A. (2017). Primary and Secondary Sources of Atmospheric Aerosol. In C. Tomasi, S. Fuzzi, & Kokhanovsky (Eds.), *Atmospheric Aerosols: Life Cycles and Effects on Air Quality and Climate* (First, 1–86). Willey- VCH Verlag GmbH & Co. KGaA.  
<https://doi.org/https://doi.org/10.1002/9783527336449.ch1>
- Tripathee, L., Kang, S., Rupakheti, D., Zhang, Q., Huang, J., & Sillanpää, M. (2016). Water-Soluble Ionic Composition of Aerosols at Urban Location in the Foothills of Himalaya, Pokhara Valley, Nepal. *Atmosphere*, **7**(8): 102.  
<https://doi.org/10.3390/atmos7080102>
- Tripathi, S. N., Pattnaik, A., & Dey, S. (2007). Aerosol Indirect Effect over Indo-Gangetic plain. *Atmospheric Environment*, **41**(33): 7037–7047.  
<https://doi.org/10.1016/j.atmosenv.2007.05.007>
- Van de Hulst H.C. (1981). *Light Scattering by Small Particles* (1981st ed.). Dover Publications, Inc.
- Wan, X., Kang, S., Li, Q., Rupakheti, D., Zhang, Q., Guo, J., Chen, P., Tripathee, L., Rupakheti, M., Panday, A. K., Wang, W., Kawamura, K., Gao, S., Wu, G., & Cong, Z. (2017). Organic Molecular Tracers in the Atmospheric Aerosols from Lumbini, Nepal, in the Northern Indo-Gangetic Plain: Influence of Biomass Burning. *Atmospheric Chemistry and Physics*, **17**(14): 8867–8885.  
<https://doi.org/10.5194/acp-17-8867-2017>
- Wang, J., Zhang, L., Dai, A., van Hove, T., & van Baelen, J. (2007). A Near-Global, 2-Hourly Data Set of Atmospheric Precipitable Water from Ground-Based GPS Measurements. *Journal of Geophysical Research Atmospheres*, **112**(11): 1–17.  
<https://doi.org/10.1029/2006JD007529>
- Wang, Y. Q., Zhang, X. Y., & Draxler, R. R. (2009). TrajStat: GIS-Based Software that uses Various Trajectory Statistical Analysis Methods to Identify Potential Sources from Long-Term Air Pollution Measurement Data. *Environmental Modelling and Software*, **24**(8): 938–939. <https://doi.org/10.1016/j.envsoft.2009.01.004>
- Xu, C., Ma, Y. M., Panday, A., Cong, Z. Y., Yang, K., Zhu, Z. K., Wang, J. M., Amatya, P. M., & Zhao, L. (2014). Similarities and Differences of Aerosol Optical Properties between Southern and Northern Sides of the Himalayas. *Atmospheric*

- Chemistry and Physics*, **14**(6): 3133–3149. <https://doi.org/10.5194/acp-14-3133-2014>
- Xu, X., & Zhang, C. (2020a). Estimation of Ground-Level PM 2.5 Concentration using MODIS AOD and Corrected Regression Model over Beijing, China. *Plos One*, **15**(10): 3–15. <https://doi.org/10.1371/journal.pone.0240430>
- Xu, X., & Zhang, C. (2020b). Estimation of Ground-Level PM2.5 Concentration using MODIS AOD and Corrected Regression Model over Beijing, China. *Plos One*, **15**, 1–15. <https://doi.org/10.1371/journal.pone.0240430>
- Zhang, H., Hoff, R. M., & Engel-Cox, J. A. (2009). The Relation between Moderate Resolution Imaging Spectroradiometer (MODIS) Aerosol Optical Depth and PM2.5 over the United States: A Geographical Comparison by U.S. Environmental Protection Agency Regions. *Journal of the Air and Waste Management Association*, **59**(11): 1358–1369. <https://doi.org/10.3155/1047-3289.59.11.1358>
- Zhang, Q., Xin, J., Yin, Y., Wang, L., & Wang, Y. (2016). The Variations and Trends of MODIS C5 & C6 Products' Errors in the Recent Decade over the Background and Urban Areas of North China. *Remote Sensing*, **8**(9): 1–17. <https://doi.org/10.3390/rs8090754>
- Zhao, G., Zhao, C., Kuang, Y., Bian, Y., Tao, J., Shen, C., & Yu, Y. (2018). Calculating the Aerosol Asymmetry Factor Based on Measurements from the Humidified Nephelometer System. *Atmospheric Chemistry and Physics*, **18**(12): 9049–9060. <https://doi.org/10.5194/acp-18-9049-2018>
- Zheng, T., Bergin, M. H., Johnson, K. K., Tripathi, S. N., Shirodkar, S., Landis, M. S., Sutaria, R., & Carlson, D. E. (2018). Field Evaluation of Low-Cost Particulate Matter Sensors in High and Low Concentration Environments. *Atmospheric Measurement Techniques Discussions*, **11**(8), 4823–4846. <https://doi.org/https://doi.org/10.5194/amt-11-4823-2018>

## APPENDIX

### Academic Activities

#### A. Attended courses offered by IoST

##### First semester:

PHS 911, Philosophy of Science (Cr. Hrs. 3)

PHS 912, Research Methodology (Cr. Hrs. 3)

PHS 913, Seminar (Cr. Hrs. 3)

##### Second semester:

PHS 951, Advanced Research Methodology (Cr. Hrs. 3)

PHS 957, Advanced Plasma Physics (Cr. Hrs. 3)

PHS 952, Seminar (Cr. Hrs. 3)

#### B. Paper publications

##### International

1. Regmi, J., Poudyal, K. N., Pokhrel, A., Gyawali, M., Tripathee, L., Panday, A., Barinelli, A., & Aryal, R. (2020). Investigation of Aerosol Climatology and Long-Range Transport of Aerosols over Pokhara , Nepal. *Atmosphere*, 11(8), 1–16. <https://doi.org/doi:10.3390/atmos11080874>
2. Regmi, J., Poudyal, K.N., Pokhrel, A., Wilson, K., & Aryal, A. (2021). Variability of Particulate Matter in Kathmandu and Pokhara Valley using Purple Air Sensor and an Overview of Origin of Pollutants, *Bulletin of the American Physical Society, APS March Meeting Abstracts, 2021*. <https://ui.adsabs.harvard.edu/>
3. Regmi, J., Poudyal, K.N., Pokhrel, A., Malakar, N., Gyawali, M., Tripathee, L., Rai, M., Ramachandran, S., Wilson, K., Aryal, R. (2023). Analysis of Surface Level PM<sub>2.5</sub> Measured by Low-Cost Sensor and Satellite-Based Column Aerosol Optical Depth (AOD) over Kathmandu. *Aerosol Air Qual. Res.* <https://doi.org/10.4209/aaqr.220311>



## National

1. Regmi, J., Poudyal, K., Pokhrel, A., Barinelli, A., & Aryal, R. (2019). Aerosol optical properties of size segregated aerosol particles and radiative forcing over Pokhara valley. *Himalayan Physics*, 8(December), 1–10.  
<https://doi.org/10.3126/hp.v8i0.29939>
2. Regmi, J., Poudyal, K. N., Pokhrel, A., Gyawali, M., Barinelli, A., & Aryal, R. (2021). Analysis of Aerosol Optical Depth and Angstrom Exponents over an AERONET site at Pokhara, Nepal. *Bibechana*, 18(1), 118–127.  
<https://doi.org/10.3126/bibechana.v18i1.29448>
3. Regmi, J., Poudyal, K. N., Pokhrel, A., Wilson, K., & Aryal, R. (2022). Variability of Surface Level Particulate Matter in Kathmandu and Pokhara and an Overview of Origin of Pollutants. *Journal of Engineering and Sciences*, 1(1), 1–12.  
<https://journal.ioepas.edu.np>

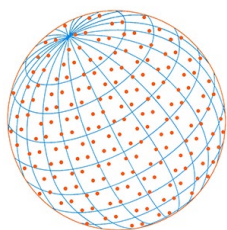
## C. Participations

1. Participated and presented the poster on, “Seasonal Variation of Aerosol optical depth and Angstrom Exponent and its Impact on Climate in Pokhara Valley” in “The 8<sup>th</sup> Asian Conference on Colloid & Interface Science”, Sept. 24-27, 2019 in IoE, Pulchowk, Lalitpur. <http://www.nims.go.jp/mana/accis2019>.
2. Participated in “Workshop on Space Weather and Upper Atmosphere Physics (WSWUAP)” September 23 –27, 2019 Organized by, Department of Physics, Amrit Campus, Kathmandu.
3. Presented an oral presentation on, “Scientific Evaluation of Air Pollution Over Two Big Cities in Nepal” in Regional Meeting & 2<sup>nd</sup> Knowledge Conference, Americas held on 5-7 September, 2020.
4. Presented a poster on, “Variability of particulate matter in Kathmandu and Pokhara Valley using Purple Air Sensor and an Overview of Origin of Pollutants” for APS March meeting 2021 on 19<sup>th</sup> March virtually.
5. Participated in a webinar on, “An Update on Low-Cost Sensors for the Measurement of Atmospheric Composition” organized by World Meteorological Organization on February 16, 2021.

6. Presented a popular talk on Nobel Prize in Physics 2021: “A Concern for Predictability of the Climate of the Chaotic, Coupled- behavior of the Atmosphere, Oceans and Land surfaces” Organized by Nepal Physical Society, Gandaki Province and Department of Physics, Prithvi Narayan Campus Pokhara, on 24<sup>th</sup> Asoj, 2078.
7. Participated on a webinar organized by Nepal Physical Society on, “Satellite Remote Sensing of Atmospheric Aerosols: Algorithms, Datasets, Access and Applications.” By Dr. Pawan Gupta, Senior Scientist, Earth Sciences Universities Space Research Association, NASA Marshall Space Flight Center, USA on July 30, 2021.
8. Presented an oral presentation on, “Comparison of Aerosol Particle Concentration and Aerosol Optical Properties Obtained from a Variety of Aerosol Optical Measurement Techniques” in ANPA Conference 2021 held on July 16-18, 2021.
9. Participated in “International Conference on Frontiers of Physics (ICFP)-2022” and presented a talk on, “Relative Humidity as a Correcting Factor on Comparing Surface Level Particle Concentration and Column Integrated Aerosol Optical Properties,” Organized by Nepal Physical Society, Kathmandu on Jan (22 – 24), 2022.
10. Participated in the four-days virtual regional workshop on, “Two Punjab, One Atmosphere” (31 Jan-3 Feb 2022) Organized by ICIMOD and the US Embassy.
11. An oral presentation was delivered on “Evaluation of Aerosol Extinction Efficiency Factors Using Lorentz-Mie Theory” in “National Conference on Recent Trends in Science, Technology and Innovation (RTSTI)” (29 – 30 May, 2022) Organized by Research Management Unit, Paschimanchal Campus, IOE, TU.
12. Participated in the Training cum Workshop on, “Capacity Building on Geo-Information Technology for University Teaching and Research Human Resources” (June 15 to 19, 2022) Organized by Department of Geography, Prithvi Narayan Campus, Pokhara, TU (Supported by UGC, Nepal).

13. Participated and presented an oral presentation (in person) on, “Comparing Surface and Column Integrated Aerosol Loadings with Relative Humidity as a Correction Factor” in American Physical Society March Meeting 2023 held in Las Vegas, Nevada, USA from March 5 to 10.

**Published Papers:**



# Analysis of Surface Level PM<sub>2.5</sub> Measured by Low-Cost Sensor and Satellite-Based Column Aerosol Optical Depth (AOD) over Kathmandu

Jeevan Regmi<sup>1,2</sup>, Khem N. Poudyal<sup>3</sup>, Amod Pokhrel<sup>4</sup>, Nabin Malakar<sup>5</sup>,  
Madhu Gyawali<sup>6</sup>, Lekhendra Tripathi<sup>7</sup>, Mukesh Rai<sup>7</sup>,  
Srikanthan Ramachandran<sup>8</sup>, Katrina Wilson<sup>9</sup>, Rudra Aryal<sup>9\*</sup>

<sup>1</sup>Prithvi Narayan Campus, Tribhuvan University (TU), Pokhara, Nepal

<sup>2</sup>Central Department of Physics, Tribhuvan University, Kirtipur, Nepal

<sup>3</sup>Department of Applied Sciences, IOE Pulchowk Campus, Tribhuvan University, Lalitpur, Nepal

<sup>4</sup>University of California Berkeley, California, USA

<sup>5</sup>Worcester State University, Massachusetts, USA

<sup>6</sup>Department of Physics, San Jacinto College, South Campus, Houston, TX 77089, USA

<sup>7</sup>State Key Laboratory of Cryospheric Science, Northwest Institute of Eco-Environment and Resources, Chinese Academy of Sciences, Lanzhou 730000, China

<sup>8</sup>Physical Research Laboratory, Ahmedabad, India

<sup>9</sup>Franklin Pierce University, Rindge, NH, USA

## ABSTRACT

A low-cost PurpleAir PA-II sensor was installed, in 2020 at the Institute of Engineering (IOE) Pulchowk Campus, TU located in Kathmandu valley, Nepal, to measure particulate matter with an aerodynamic diameter equal to or smaller than 2.5  $\mu\text{m}$  (PM<sub>2.5</sub>). The observation shows that hourly averaged PM<sub>2.5</sub> fluctuates bimodally in four seasons (Winter: December, January, and February; Spring: March–May; Summer: June–September; and Autumn: October–November), with the highest levels occurring during morning and evening rush hours. PurpleAir records PM<sub>2.5</sub> with a maximum average of  $101 \pm 26.31 \mu\text{g m}^{-3}$ , in winter,  $55.58 \pm 11.42 \mu\text{g m}^{-3}$ , in spring,  $45.46 \pm 12.16 \mu\text{g m}^{-3}$ , in autumn, and a minimum of  $22.78 \pm 3.23 \mu\text{g m}^{-3}$ , in the summer. Due to rain and diffusion in the vertical atmosphere, PM<sub>2.5</sub> levels are lowest during the summer. The  $\pm$  number for each season represents the standard deviation from the hourly average. AOD<sub>550nm</sub> data collected by MODIS (Moderate Resolution Imaging Spectroradiometer) onboard two NASA satellites, Terra and Aqua, are compared with simultaneously observed PM<sub>2.5</sub>. With humidity correction factor  $f(\text{RH})$ ,  $R^2$  increases from 0.413 to 0.608 (in winter), 0.426 to 0.508 (in spring), and 0.083 to 0.293 (in autumn). The summer AOD data and PM<sub>2.5</sub> are not compared due to a lack of AOD observations. By comparing the column-integrated aerosol data with the surface-level aerosol concentration, this study illustrates the relevance of atmospheric parameters while investigating the reliability of PurpleAir measurements. A cluster analysis of five-day back trajectories of air masses arriving at different altitudes in different seasons indicates that long-range transport of air pollution contributes to MODIS's column integrated AOD by adding aerosol population.

**Keywords:** Aerosol optical depth, MODIS, PM<sub>2.5</sub>, PurpleAir, Transboundary aerosols

## OPEN ACCESS

**Received:** September 20, 2022

**Revised:** November 28, 2022

**Accepted:** December 15, 2022

\* **Corresponding Author:**

aryalr@franklinpierce.edu

**Publisher:**

Taiwan Association for Aerosol  
Research

ISSN: 1680-8584 print

ISSN: 2071-1409 online

 **Copyright:** The Author(s).

This is an open access article distributed under the terms of the [Creative Commons Attribution License \(CC BY 4.0\)](https://creativecommons.org/licenses/by/4.0/), which permits unrestricted use, distribution, and reproduction in any medium, provided the original author and source are cited.

## 1 INTRODUCTION

The study of atmospheric aerosols, particulate matter, is important since they influence Earth's radiation budget by scattering and absorbing incoming solar radiation and altering cloud microphysical properties (Haywood and Boucher, 2000; Ramanathan *et al.*, 2001). Their ability to affect Earth's radiation budget and their effects on health, air quality, and clouds are strongly



related to their size (Dusek *et al.*, 2006; Ruzer and Harley, 2005). A PM<sub>2.5</sub> particle has an aerodynamic diameter of less than 2.5 micrometers. Particulates of this size can be either natural or anthropogenic, and their composition varies according to their sources (Devi *et al.*, 2020). Human-produced particles are generally smaller in size, while naturally produced particles are larger. PM<sub>2.5</sub> is also one of the most common pollutants contributing to global health burdens (Lim *et al.*, 2012). According to Shiraiwa *et al.* (2017), these particles penetrate deeply into the lungs of humans and cause adverse health effects depending on their chemical composition. Statistical analysis shows a strong correlation between hospitalizations, and deaths and exposure to high PM<sub>2.5</sub> concentrations (Di *et al.*, 2017; Schwartz *et al.*, 1996; Klemm and Mason, 2000). As a result, a comprehensive measurement and analysis of particle concentration in the atmosphere are essential for protecting local health and studying atmospheric conditions.

Several studies highlight the importance of low-cost air quality monitoring instruments, such as PurpleAir Monitors, for determining both spatial and temporal air quality, since traditional real-time air quality monitors lack this capability due to their high installation and maintenance costs (Kumar *et al.*, 2018; Munir *et al.*, 2019). Because of their availability, size, and price, PurpleAir monitors are being widely used in almost every continent to measure PM concentrations on surfaces, as well as for assessing air pollution (Quimette *et al.*, 2022).

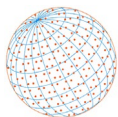
These monitors work on the light scattering principle in which a fan draws air particles into the chamber and passes along the laser path. The sensor's photodiode detector converts scattered light into voltage pulses from light. These pulses use to count the number of particles of sizes 0.3, 0.5, 1, 2.5, 5, and 10  $\mu\text{m}$  and determine mass concentrations of PM<sub>1.0</sub>, PM<sub>2.5</sub>, and PM<sub>10</sub> by using an algorithm for PM concentration (Ardon-Dryer *et al.*, 2020; Sayahi *et al.*, 2019); <https://www2.purpleair.com/community/faq>). In a variety of environmental conditions, PurpleAir monitors were evaluated for measuring atmospheric particle concentrations (Morawska *et al.*, 2018; Stavroulas *et al.*, 2020; Zhang *et al.*, 2009). Ardon-Dryer *et al.* (2020) showed that PurpleAir PM<sub>2.5</sub> data significantly correlated with PM<sub>2.5</sub> measured by AQMS (Air Quality Monitoring Stations) operated by the Environmental Protection Agency. This study will also aid in investigating the low-cost monitors for measuring air pollution by comparing them with other reliable reference data, such as satellite-based aerosol optical properties. The simultaneous measurements of aerosols at ground level and those based on remote sensing provide reliable information about air pollutant loading over the observation site (Baral and Thapa, 2021; Segura *et al.*, 2017). Comparison of surface and atmospheric level aerosol data can also be used as a statistical basis to extrapolate regional aerosol data (Aryal *et al.*, 2014; Moody *et al.*, 2014).

In atmospheric column observations, satellites provide long-term data and global coverage, providing insights into regional air quality and climate variations through the precise timing and spatial resolution of PM<sub>2.5</sub> concentrations (Karagulian *et al.*, 2015; Schwarze *et al.*, 2006; Zhong *et al.*, 2015). Satellites, however, view the entire atmosphere column, which makes it difficult to distinguish surface-level particle concentrations. Therefore, ground-based measurements and comparisons with satellite-based aerosol data can lower the uncertainty associated with local and external aerosols, and meteorological parameters (Kumar *et al.*, 2007).

The use of low-cost sensors in surface measurements can alleviate the limitations of human resources and can enable setting up multiple ground-based measurement stations easier, regardless of a lack of funding and/or technical expertise. A correlative analysis based on satellite-based aerosol optical depth (AOD) data and ground-level particle concentration can be conducted to evaluate the proposed method for estimating PM<sub>2.5</sub> in areas that lack ground-level observations (van Donkelaar *et al.*, 2015).

Several studies have examined the air quality and aerosol loading trend over the Kathmandu Valley (Aryal *et al.*, 2009; Islam *et al.*, 2020; Mahapatra *et al.*, 2019). MODIS-equipped Earth observation satellites Terra and Aqua pass over the Kathmandu valley every morning and afternoon (at about 10:30 am and 1:00 pm local time, respectively), and MODIS' AOD data (3 km  $\times$  3 km) can be used to compare with surface level PM<sub>2.5</sub> (Ramachandran and Kedia, 2013).

This paper will present and analyze the hourly variability of PM<sub>2.5</sub> observed by PurpleAir monitor at the Pulchowk Engineering Campus (TU), located about a hundred meters from the bus station, for each season and compare surface-level particle concentrations with satellite-based AODs using relative humidity correction factor. Relative humidity influences aerosol particle growth and refractive index, affecting aerosol mass concentration (Altaratz *et al.*, 2013; Hagan and Kroll,



2020; Malm *et al.*, 2000). Kathmandu valley's bowl-shaped structure and surrounding mountains make it a unique case study for investigating air pollution (Kitada and Regmi, 2003; Panday and Prinn, 2009; Shakya *et al.*, 2017; Shrestha *et al.*, 2017). This paper also presents the local and regional aspects of long-range air pollution transport over Kathmandu Valley using cluster analysis of back trajectory air masses arriving over the observation site.

## 2 MATERIALS AND METHODS

### 2.1 Site Description

A PurpleAir sensor was deployed in the Kathmandu valley (Pulchowk Engineering Campus, IOE, Lalitpur, Lat. 27.68°N, Long. 85.31°E, and Alt. 1350 m Fig. 1) to measure real-time PM<sub>2.5</sub> concentration data. The city of Kathmandu is Nepal's largest metropolitan area and is highly polluted. Nepal is surrounded by the Indo-Gangetic Plain in the south and the large Himalayas in the north (Shakya *et al.*, 2017; Regmi *et al.*, 2020). High mountains surround the Kathmandu valley, ranging from 2000 meters to 2800 meters, and the valley is shaped like a bowl, trapping pollution.

This city is experiencing rapid urbanization and population growth. The region is characterized by haphazard construction, unmanaged industries, brick and kiln production, and solid waste and biomass burning. Kathmandu also experiences significant amount of transboundary air pollution (Kitada and Regmi, 2003). Transported dust aerosols impact the cloud microphysical properties significantly. As a result of biomass burning and dust storms in the Indo-Gangetic Plain region, and long-range transportation, aerosols accumulate over Nepal, which, when combined with local pollution sources, contributes to high levels of pollution (Adhikari and Mejia, 2022; Becker *et al.*, 2021; Das *et al.*, 2021; Jethva *et al.*, 2019; Regmi *et al.*, 2020).

### 2.2 PurpleAir, Sampling Methods and MODIS AOD

PurpleAir's website (<https://www2.purpleair.com/>) provides real-time PM<sub>2.5</sub> (in  $\mu\text{g m}^{-3}$ ) data. Microprocessor-based circuits are used to calculate equivalent particle diameters and the number of particles with different diameters per unit volume (Ouimette *et al.*, 2022; Yong, 2016). The processing algorithms for the Plan-tower PMS5003 sensors (PA-PMS) used in the PurpleAir (PA) monitor configuration are provided in He *et al.* (2020). The remainder of this paper uses the

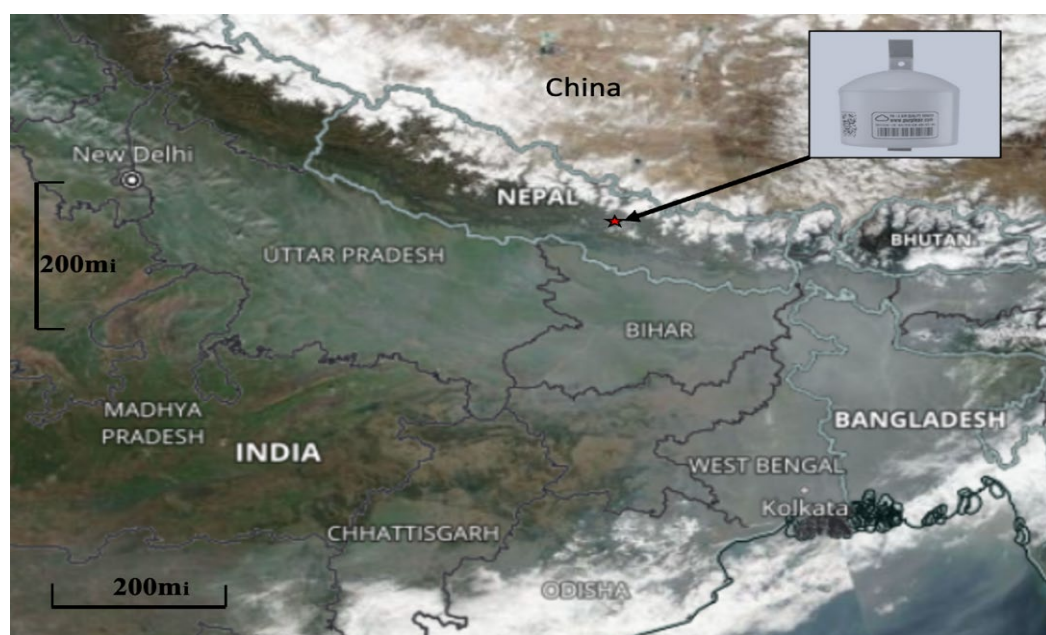


**Fig. 1.** As seen in the MODIS image (taken by NASA's Terra satellite on February 9, 2020), there is a noticeable accumulation of haze on the foothills of the Himalayan range. The top right corner of the figure shows a PurpleAir monitor located at Kathmandu Valley.

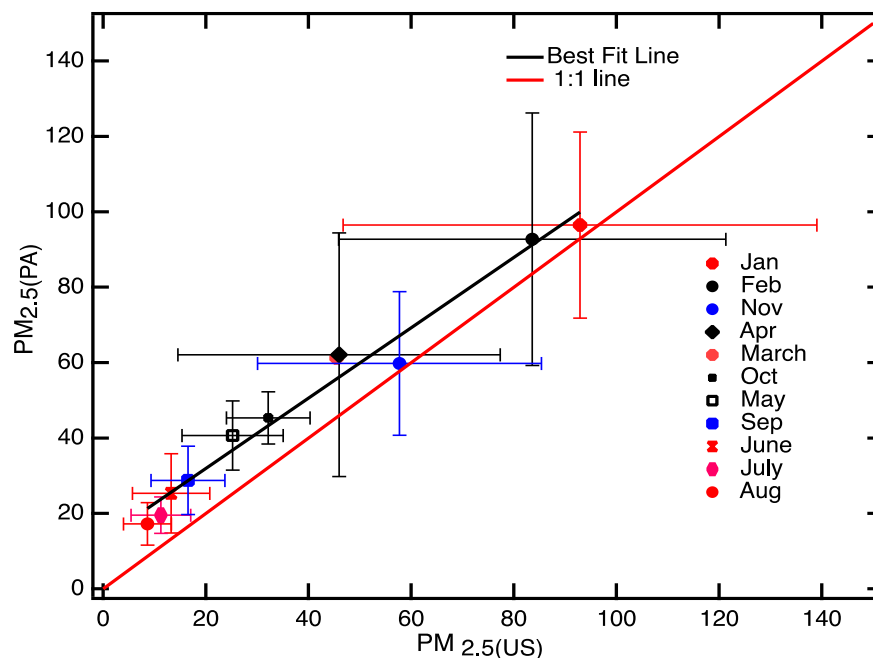
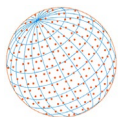


**Fig. 2.** The scatter plot shows the monthly averages for  $PM_{2.5(PA)}$  and  $PM_{2.5(US)}$  in unit of  $\mu g m^{-3}$ . Based on the legend in the figure, the symbols are ordered from higher to lower  $PM_{2.5}$  for the different months. December month is discarded for comparison due to a lack of data availability.

symbol  $PM_{2.5(PA)}$  for  $PM_{2.5}$  observed by a PurpleAir monitor. Additionally, we compare  $PM_{2.5(PA)}$  data with  $PM_{2.5(US)}$  data to indicate the reliability of PurpleAir.  $PM_{2.5(US)}$  is monitored by the Ambient Air Quality Monitoring Station (Beta Attenuation Monitor, BAM) at the Phora Durbar Recreation Center, 3 km from the PurpleAir monitoring site and supported by the United States Embassy (Edwards *et al.*, 2021). The BAM 1022 measures and records airborne PM concentrations in  $\mu g m^{-3}$  at local temperatures and atmospheric pressures by utilizing beta-ray attenuation (Magi *et al.*, 2020). The manufacturer's website provides a complete description of the BAM 1022's operation (<https://metone.com/air-quality-particulate-measurement/regulatory/bam-1022/>).

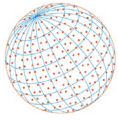
A significant correlation exists between  $PM_{2.5(PA)}$  and  $PM_{2.5(US)}$  data sets with a coefficient of determination ( $R^2$ ) of 0.98. The best fit line equation is  $PM_{2.5(PA)} = 0.93(\pm 0.04) PM_{2.5(US)} + 13.23 (\pm 2.40)$  as shown in Fig. 2.

However, the two sets are not validated individually against other nearby reference optical devices. In Fig. 2, the scatter plot shows that PurpleAir data  $PM_{2.5(PA)}$  near the bus station is slightly above the 1:1 line compared to  $PM_{2.5(US)}$  at Phora Durbar and shows that  $PM_{2.5(PA)}$  provides usable data representing the atmosphere of Kathmandu valley.

In this study,  $PM_{2.5(PA)}$  is compared with NASA's MODIS column integrated Aerosol Optical Depth (AOD at 550 nm) product, which is corrected for relative humidity. The rest of this paper uses  $AOD_{550nm}$  to represent AOD retrieved from Satellite data.  $AOD_{550nm}$  aerosol products collected from MODIS Aqua and Terra at  $3 km \times 3 km$  is analyzed in this study. The  $3 km \times 3 km$  algorithm differs from the  $10 km \times 10 km$  algorithm simply in the way reflectance pixels are ingested, organized, and selected (Levy *et al.*, 2013). PurpleAir provides optical data matching the products of aerosol optical devices such as cell reciprocal and TSI 3563 integrating nephelometers, according to Calvello *et al.* (2008) and Ouimette *et al.* (2022).

## 2.4 Model Description

The relationship between PM and AOD is illustrated by a simplified linear equation with a relative humidity correction factor. To express a statistical model, we have written the particle concentration (PM) in general, observed at the ground level with the dry sample, which can be expressed quantitatively (Xu and Zhang, 2020) as



$$PM = \frac{4}{3} \pi \rho \int_0^{\infty} r^3 n_{dry}(r) dr \quad (1)$$

$n_{dry}(r)$  denotes the number of particles per unit volume in atmospheric space per unit particle radius and  $\rho$  is the aerosol particle density. Based on the hypothesis of spherical particles, the columnar AOD can be calculated using the Mie scattering theory with the equation (Calvello *et al.*, 2008), and can be written as,

$$AOD = \int_0^{\infty} dh \int_0^{\infty} \pi r^2 Q_{ext,amb}(r) n_{amb}(r, h) dr \quad (2)$$

where  $r$  is the radius of the assumed spherical particles,  $Q_{ext}$  is the extinction efficiency factor defined by van de Hulst (1981), and  $n_{amb}(r, h)$  represents the aerosol size distribution giving a concentration of particles per unit volume per particle radius at height  $h$ , which is factorized in two parts based on height.

$$(n_{amb}(r, h)) = n_{amb}(r)n(h) = n_0 n_{amb}(r) \exp(-h/H) \quad (3)$$

where  $n_0$  is the particle concentration at the surface level and  $H$  is the aerosol scale height, then the equation for AOD can be expressed as given by Calvello *et al.* (2008).

$$AOD = n_0 H \int_0^{\infty} \pi r^2 Q_{ext,amb}(r) n(r) dr \quad (4)$$

Several models explain the relationship between  $f(RH)$  and Relative humidity (RH) (Brock *et al.*, 2016, 2021; Chen *et al.*, 2016; Kasten, 1969; Kotchenruther and Hobbs, 1998; Zheng *et al.*, 2017). This work utilizes the  $f(RH)$  expression (Brock *et al.*, 2021; Zheng *et al.*, 2017) to examine aerosol light extinction induced by hygroscopic growth.

$$f(RH) = \frac{AOD}{AOD_{dry}} = \left( 1 + \frac{RH}{100 - RH} \right) \quad (5)$$

where  $AOD_{dry}$  represents the aerosol optical depth with dehydration adjustment. Then the expression for AOD in terms of the dry condition can be expressed as,

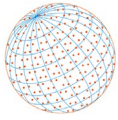
$$AOD = n_0 H f(RH) \int_0^{\infty} \pi r^2 Q_{ext,dry}(r) n(r) dr \quad (6)$$

To investigate the AOD vs. PM relation, the size distribution and extinction efficiency  $\langle Q_{ext} \rangle$  and effective aerosol radius  $r_{eff}$  are expressed (Xu and Zhang, 2020) as,

$$\langle Q_{ext} \rangle = \frac{\int_0^{\infty} Q_{ext}(r) n(r) r^2 dr}{\int_0^{\infty} n(r) r^2 dr} \quad (7)$$

And, the effective radius of aerosol particles is given as,





$$r_{eff} = \frac{\int_0^{\infty} n(r)r^3 dr}{\int_0^{\infty} n(r)r^2 dr} \quad (8)$$

Based on the above Eqs. (2), (4), (7), and (8) a relation between AOD/f(RH) and PM can be obtained as

$$AOD = \frac{3}{4} n_0 \cdot H \cdot f(RH) \cdot PM \frac{\langle Q_{ext,dry}(r) \rangle}{\rho r_{eff}} \quad (9)$$

Thus Eq. (9) provides, assuming H as a constant for all data for this study, f(RH) as the correcting factor to study the correlation between AOD/(f(RH)) vs. PM.

## 2.4 Statistical Analysis

AOD<sub>550nm</sub> obtained from two satellite measurements, Aqua and Terra, is compared with the hourly averaged PurpleAir data PM<sub>2.5(PA)</sub>. For comparison with ground based PM<sub>2.5(PA)</sub>, the AOD<sub>550nm</sub> are corrected by dividing with f(RH), where RH is ambient relative humidity. At different humidity levels, aerosol particles with different chemical compositions but the same mass concentration exhibit different aerosol optical properties (Jin *et al.*, 2022). Accordingly, this correlation study investigates the correlation between aerosol extinction and mass concentration using relative humidity correction factor, f(RH).

MOD04 and MYD04\_3K data (MOD04 for Terra, MYD04 for Aqua), 3 km × 3 km AOD<sub>550nm</sub> data were extracted and correlated with a temporal variation of PM<sub>2.5(PA)</sub> from PurpleAir sensors at ground level. AOD<sub>550nm</sub> measurements from two satellites, Aqua and Terra, were observed simultaneously with PM<sub>2.5(PA)</sub> measurements. We performed the graphical analysis using the Levenberg-Marquardt least orthogonal distance method implemented in IGOR (<https://www.wavemetrics.com/>). The data were then analyzed using linear regression analysis, and a coefficient of determination (R<sup>2</sup>) was obtained. A two-tailed P statistic and a coefficient of correlation coefficient (R) was calculated to determine the significance of the correlation. Data with confidence levels (based on P values) < 95% were disregarded for statistical significance.

## 2.5 Cluster Analysis

The aerosol particle trajectories arriving at Kathmandu at 500 m, 1000 m, and 1500 m asl were analyzed using cluster analysis to understand the origin of aerosol particles over Kathmandu Valley's vertical column. For each season, seasonal clusters were generated by analyzing five days of air mass trajectories starting at 500 m, 1000 m, and 1500 m asl over Kathmandu (Lat. 27.68°N, Long. 85.31°E) at 0:00, 6:00, 12:00, and 18:00 UTC each day. In this study, the cluster calculations were conducted using the free software Traj-stat (Regmi *et al.*, 2020; Wang, 2014).

# 3 RESULTS AND DISCUSSION

## 3.1 The Hourly Variation of the Seasonally Averaged PM<sub>2.5</sub>

Fig. 3 shows hourly variations of PM<sub>2.5(PA)</sub> concentrations (in μg m<sup>-3</sup>) for each season in 2020. The average maximum PM<sub>2.5(PA)</sub> is observed to be 101 ± 26.31 μg m<sup>-3</sup> in the winter season, while the minimum is seen in summer (22.78 ± 3.23 μg m<sup>-3</sup>). Similarly, the average concentration of 55.58 ± 11.42 μg m<sup>-3</sup> is observed in the spring and 45.46 ± 12.16 μg m<sup>-3</sup> in the autumn. The ± 1 σ standard deviation obtained from hourly averaged measurements for each season are given adjacent to the seasonal mean values. Kathmandu is a bowl-shaped urban basin in Nepal, and during winter, the planetary boundary layer is thinner due to the dense, cooler air near the surface. A layer of cooler air sits beneath the warm air above, forming a kind of lid in the atmosphere referred to as winter inversion. Only within this layer does vertical air mixing occur, so pollutants

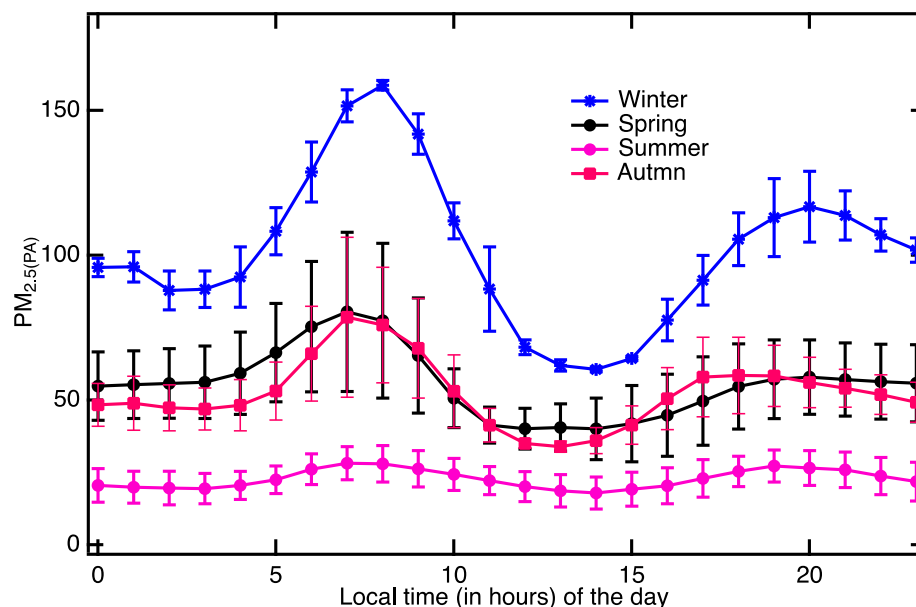
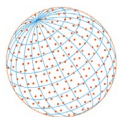


**Fig. 3.** Hourly averaged (at local time) averaged particle concentration ( $PM_{2.5(PA)}$ ) in  $\mu g m^{-3}$  for each season by using the corresponding months' data for each season.

cannot disperse in the atmosphere. Kathmandu relies mainly on wood for heating in winter, and wood burning contributes significantly to air pollution. Kotchenruther (2020) found elevated levels of  $PM_{2.5}$  during the winter in the Northwest U.S. According to the study, residential wood combustion, motor vehicle emissions, gaseous  $NO_x$  emissions, and particulate sulfate emissions are the primary sources of  $PM_{2.5}$  during winter.

For all seasons, particle mass concentrations are bimodal, significantly higher in the mornings (around 8:00 am) and evenings (around 7:00 pm). Fig. 3 shows the seasonal variations of hourly averaged  $PM_{2.5(PA)}$ , which are bimodal in all seasons. The amplitude and width of  $PM_{2.5(PA)}$  is maximum during the winter seasons, and the patterns are similar during spring, summer, and autumn. No significant variation in hourly averaged  $PM_{2.5(PA)}$  is seen during summer. A signature of local activity can be seen in  $PM_{2.5(PA)}$ , such as during the household cooking and traffic emissions time. Many studies have shown that household and commercial cooking significantly contribute to  $PM_{2.5}$  pollution in urban areas (Balasubramanian *et al.*, 2021; Pervez *et al.*, 2019; Robinson *et al.*, 2018). Earlier studies have also shown that traffic and cooking contribute to air pollution in Kathmandu valley during rush hours (morning and evening) and off hours in the afternoon (Islam *et al.*, 2020).

$PM_{2.5(PA)}$  increases gradually during rush hours in traffic. On a global scale, cooking and heating fuels contribute 20–55% to anthropogenic particle emissions (Balasubramanian *et al.*, 2021; Pervez *et al.*, 2019). The study concludes that domestic cooking and traffic are significant anthropogenic factors affecting the Kathmandu valley's surface-level  $PM_{2.5(PA)}$  concentrations. Previously, it has been shown that traffic contributes significantly to air pollution in different urban areas, with coarse particles originating from non-exhaust sources like road abrasion, brake wear, and tire wear, while fine particles are emitted directly from fuel combustion (Kumar and Goel, 2016; Pant and Harrison, 2013). Low temperatures can lead to the formation of secondary aerosols during the winter months (Duan *et al.*, 2020; Mues *et al.*, 2018). Previous studies have shown the importance of secondary organic aerosols (SOA) in contributing to  $PM_{2.5}$  (Bui *et al.*, 2022; Mancilla *et al.*, 2015).

Fig. 3 also shows that the average particle concentration at hourly averaged  $PM_{2.5(PA)}$  decreases from winter to summer, then increases again in autumn as the seasons change. A rise in temperature in the summer causes surface-level particles to diffuse rapidly in the vertical atmosphere, resulting in lower surface concentrations. PurpleAir record shows an average temperature of  $17.77 \pm 4.00^\circ C$  in winter,  $24.08 \pm 2.65^\circ C$  in summer, and  $28.96 \pm 1.65^\circ C$  in autumn. The summer also brings significant amounts of rain, which helps removal of aerosol particles from the atmosphere (Becker *et al.*, 2021). June to September are rainy monsoon months in Kathmandu, which can



significantly reduce air pollution. Thus, the monsoon rain also plays a crucial role in reducing the surface level air pollution in Kathmandu in the summer months from June to September. The COVID lockdown period from March to July also significantly reduced traffic flow, which might have affected particle concentrations in the atmosphere (Baral and Thapa, 2021).

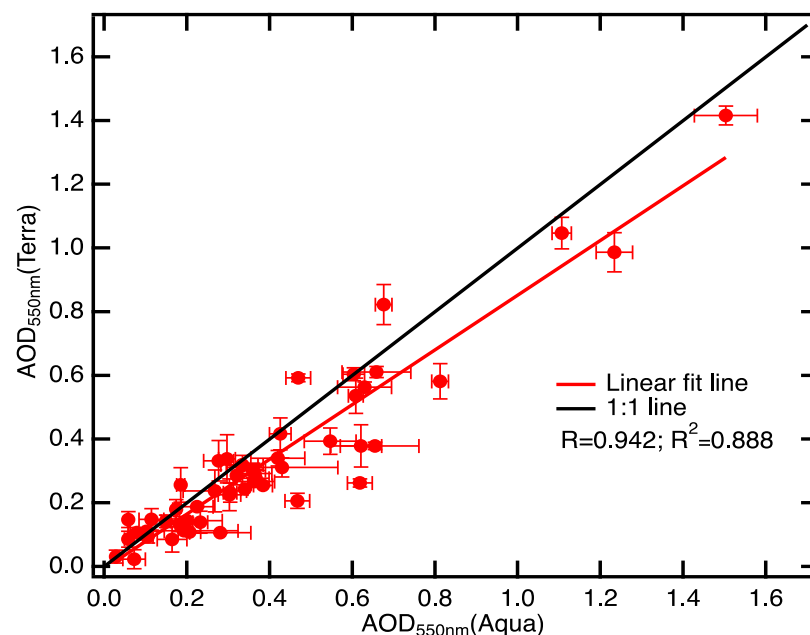
### 3.2 Comparison of MODIS AOD with PM<sub>2.5(PA)</sub>

Fig. 4 illustrates the correlation between Aqua and Terra AOD<sub>550nm</sub> and reveals  $R = 0.942$ ,  $R^2 = 0.888$ , and  $P < 0.005$ . The calibration of two satellite sensors and the retrieval algorithm for MODIS AOD<sub>550nm</sub> during spatial observations may cause some deviations in the AOD data collected by the two satellites (Green *et al.*, 2009; Gupta *et al.*, 2020; Ichoku *et al.*, 2005; Koelemeijer *et al.*, 2006). However, a significant high correlation indicates that AOD<sub>550nm</sub> by two satellite measurements can represent reliable and comparable aerosol optical depth, and it can be used for daily averages and combined to compare with other concurrently observed aerosol concentrations such as PM<sub>2.5(PA)</sub>.

Fig. 5 presents a comparison of the hourly average of PM<sub>2.5(PA)</sub> with the AOD data observed by two satellites at 550 nm wavelength, AOD<sub>550nm</sub>, without relative humidity correction factor. Fig. 5 also shows the standard deviation and linear best fit line. The best fit line provides an equation,  $AOD_{550nm} = 0.038(\pm 0.037) + (0.0068 \pm 0.0006) PM_{2.5(PA)}$ , and the correlation coefficient ( $R = 0.638$ ,  $R^2 = 0.407$ ) and  $P$ -values ( $\ll 0.005$ ) are also obtained from the plot. Based on the correlation between these two parameters, Fig. 5 indicates that surface air pollution, PM<sub>2.5(PA)</sub>, significantly influences aerosol optical depth (AOD<sub>550nm</sub>).

According to Table 1, the correlation coefficients between AOD<sub>550nm</sub> and corresponding PM<sub>2.5(PA)</sub> are improved by dividing AOD<sub>550nm</sub> by  $f(RH)$ . In seasons of low temperature,  $f(RH)$  has a greater effect on the  $R^2$  than in seasons of higher temperatures. As a result of the temperature inversion at low temperatures, particle concentrations can remain close to the surface due to the significant effect of vertical column AOD correction with  $f(RH)$ . In low-temperature months, aerosol particles will distribute uniformly near the surface. In summer, however, very few AOD<sub>550nm</sub> coincide with the corresponding hourly averaged PM<sub>2.5(PA)</sub> due to persistent monsoon clouds. Correlation results obtained in summer are also given in the table which, however, are less reliable owing to a smaller number of data points on account of monsoon clouds.

Based on the variations in correlation coefficients, meteorological parameters such as relative humidity should be considered when retrieving aerosol optical depths from satellite data (Zhang *et al.*, 2009).



**Fig. 4.** Scatter plot of MODIS AOD<sub>550nm</sub> (Terra) vs. MODIS AOD<sub>550nm</sub> (Aqua) comparing the same day data observed from two satellites in the morning and afternoon.

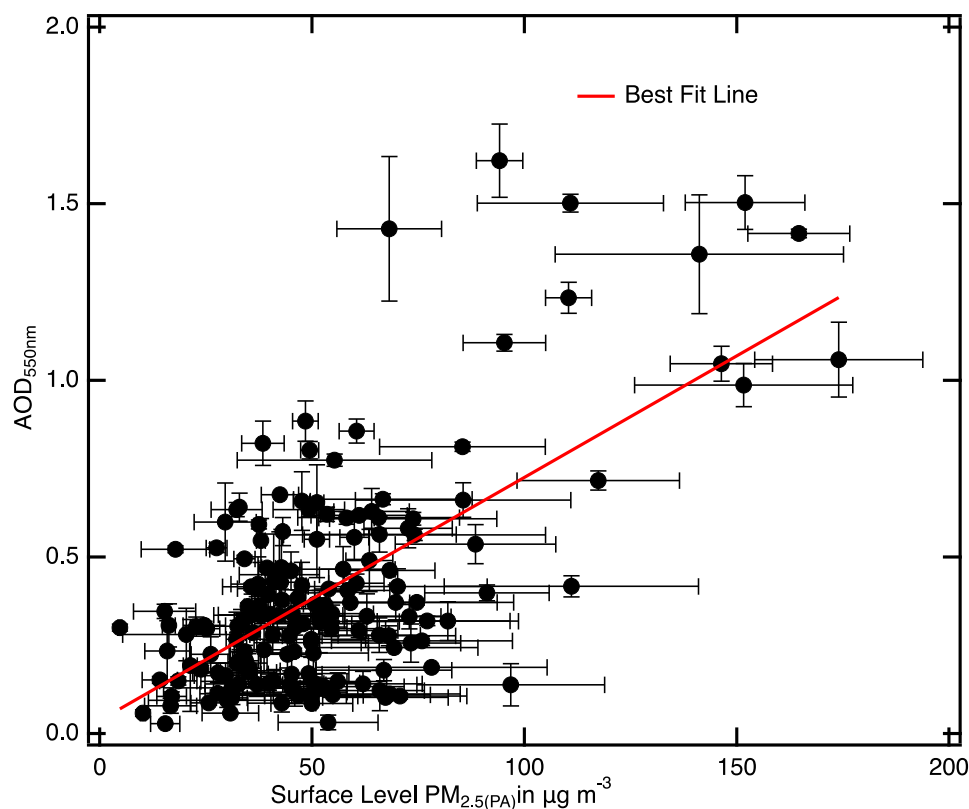
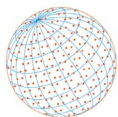


**Fig. 5.** A comparison between Aqua and Terra Satellites' spatially averaged AOD at 550 nm ( $AOD_{550nm}$ ) and PurpleAir Monitor's hourly average  $PM_{2.5(PA)}$  around the satellite overpass.

**Table 1.** The correlation coefficients for each seasons using the available one-year 2020 data without and with the  $f(RH)$  corrected AOD data vs.  $PM_{2.5(PA)}$ .

Seasons/Combined	$AOD_{550nm}$ vs. $PM_{2.5(PA)}$	$AOD_{550nm}/f(RH)$ vs. $PM_{2.5(PA)}$
All Data (172)	$R = 0.638$ ; $R^2 = 0.407$	$R = 0.703$ ; $R^2 = 0.495$
Winter (Dec–Feb) (28)	$R = 0.643$ ; $R^2 = 0.413$	$R = 0.780$ ; $R^2 = 0.608$
Spring (March–May) (77)	$R = 0.653$ ; $R^2 = 0.426$	$R = 0.713$ ; $R^2 = 0.508$
Summer (June–Sep) (9)	$R = 0.134$ ; $R^2 = 0.018$	$R = 0.170$ ; $R^2 = 0.028$
Autumn (Oct–Nov) (58)	$R = 0.288$ ; $R^2 = 0.083$	$R = 0.542$ ; $R^2 = 0.293$

### 3.3 Seasonal Cluster Analysis

Fig. 6 and supplementary figures Fig. S1 and Fig. S2 show the seasonal clusters of five-day back trajectories over Kathmandu Valley during four seasons at 500 meters, 1000 meters and 1500 meters.

According to percentage contributions, three predominant air masses reach over the Kathmandu valley every season, with five clusters exhibiting the best representation. The cluster analysis shows that fast-moving air masses contribute less, ranging from 1 to 7 percent, to air pollution at the observation site.

At 500 meters, 44% of the winter air mass comes from the Indo-Gangetic plain (IGP), Nepal's south, 38% from the southwest, 16% from the west, and 2% from the west (Fig. 6). The IGP is densely populated, and its aerosol loading is high due to industrial and urban pollution, dust, biomass burning, and the flat land of southern Nepal that lines its northern edge (Regmi *et al.*, 2020). Fig. 6 illustrates the dominance of southerly and southwesterly air masses in winter (December–February) and spring (March–May). The trajectory also indicates that south-easterly air masses from the Bay of Bengal contribute significantly and prominently in summer (June–August), whereas southerly air masses dominate in autumn (September–November). According

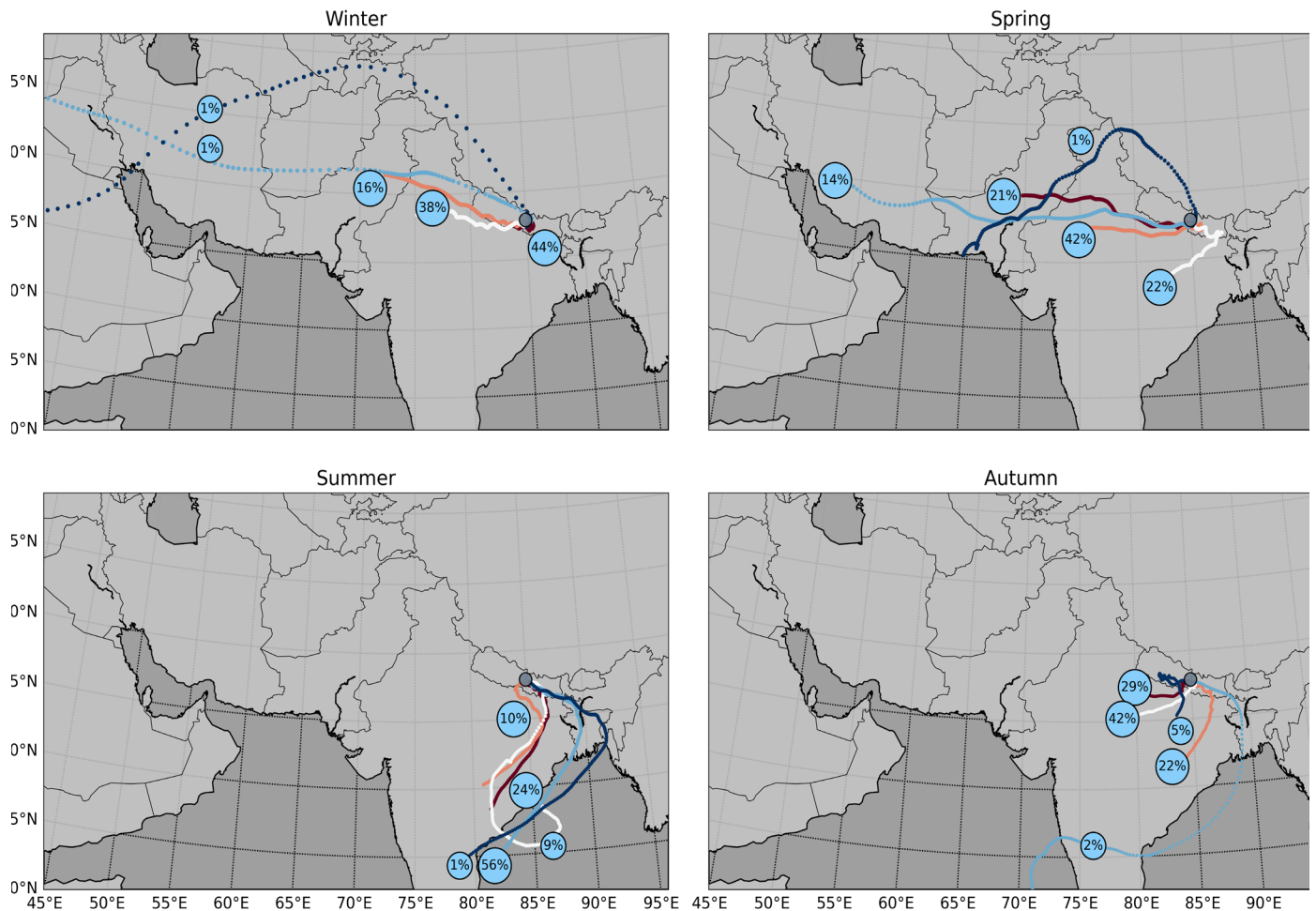
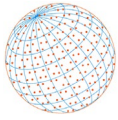


**Fig. 6.** An analysis of five-day air mass back trajectories computed with Analysis NOAA HYSPLIT and HYSPLIT model reaching Kathmandu at 500 m at different seasons. For each season's cluster analysis, the percentage contribution is presented.

to supplementary figures, Fig. S1 and Fig. S2, the dominant clusters at 1000 meters and 1500 meters are not significantly different from those at 500 meters. Therefore, the air pollution at the observation site is transported vertically from a similar direction to that of 500 meters. At different altitudes, the air mass trajectory crosses the IGP region on its way to the observation site, Kathmandu Valley. As a result, air pollution over the IGP region mainly impacts the aerosol optical depth and the overall vertical air pollution concentration.

## 4 CONCLUSIONS

The PurpleAir sensor was installed in the Kathmandu Valley, a Himalayan foothill, to determine its capability to measure surface-level small-size particles whose aerodynamic diameter is equal to or smaller than 2.5 micrometers ( $PM_{2.5}$ ). The observation shows that the bimodal particulate concentrations ( $PM_{2.5}$ ) peak at about 8 am and 7 pm, coincident with the density of traffic and other anthropogenic pollutants events, such as cooking and heating, which indicates Kathmandu has significant local sources of outdoor air pollution. In winter, temperature inversion causes particles to remain close to the surface rather than disperse vertically, showing the highest concentrations. During the summer, which is monsoon season,  $PM_{2.5}$  levels are low and bimodal variations are smaller. PurpleAir's surface-level  $PM_{2.5}$  and MODIS's AOD measurements correlate better with the relative humidity correction factor. For further analyzing the comparison between  $PM_{2.5}$  and AOD, boundary layer height (BLH) data can be used, but these data are not available for this study. An air mass cluster analysis shows that transboundary air pollution over different



altitudes at Kathmandu valley is received from different directions and source regions. The contribution of directional air mass varies with the season. The Indo-Gangetic Plain pollutes the atmosphere over Kathmandu during winter, spring, and autumn. In addition to contributing to aerosols over the atmospheric column and, eventually, to column integrated AOD<sub>550nm</sub>, transboundary air pollution might bias the comparison between PM<sub>2.5(PA)</sub> and AOD<sub>550nm</sub>. Moreover, the study establishes that simultaneous measurements of particle concentration at the surface level and AOD over a vertical column allow for the extrapolation of surface-level concentrations using satellite-based AOD, thereby, calling for a more robust and comprehensive analysis of spatial and temporal distribution of PM<sub>2.5</sub> concentration characteristics and columnar aerosol optical depth.

## ACKNOWLEDGMENTS

The authors acknowledge NOAA-ARL and NASA for providing HYSPLIT air mass back trajectories, MODIS satellite air quality data, and Franklin Pierce University for providing the PurpleAir monitor.

## DISCLOSURE

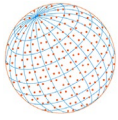
Any reference to companies or specific commercial products does not constitute a recommendation, support, or endorsement and we have no conflict of interest to disclose.

## SUPPLEMENTARY MATERIAL

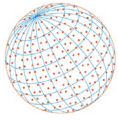
Supplementary material for this article can be found in the online version at <https://doi.org/10.4209/aaqr.220311>

## REFERENCES

- Adhikari, P., Mejjia, J.F. (2022). Impact of transported dust aerosols on precipitation over the Nepal Himalayas using convection-permitting WRF-Chem simulation. *Atmos. Environ.*: X 15, 100179. <https://doi.org/10.1016/j.aeaoa.2022.100179>
- Altartaz, O., Bar-Or, R.Z., Wollner, U., Koren, I. (2013). Relative humidity and its effect on aerosol optical depth in the vicinity of convective clouds. *Environ. Res. Lett.* 8, 034025. <https://doi.org/10.1088/1748-9326/8/3/034025>
- Ardon-Dryer, K., Dryer, Y., Williams, J.N., Moghimi, N. (2020). Measurements of PM<sub>2.5</sub> with PurpleAir under atmospheric conditions. *Atmos. Meas. Tech.* 13, 5441–5458. <https://doi.org/10.5194/amt-13-5441-2020>
- Aryal, R.K., Lee, B.K., Karki, R., Gurung, A., Baral, B., Byeon, S.H. (2009). Dynamics of PM<sub>2.5</sub> concentrations in Kathmandu Valley, Nepal. *J. Hazard. Mater.* 168, 732–738. <https://doi.org/10.1016/j.jhazmat.2009.02.086>
- Aryal, R.P., Voss, K.J., Terman, P.A., Keene, W.C., Moody, J.L., Welton, E.J., Holben, B.N. (2014). Comparison of surface and column measurements of aerosol scattering properties over the western North Atlantic Ocean at Bermuda. *Atmos. Chem. Phys.* 14, 7617–7629. <https://doi.org/10.5194/acp-14-7617-2014>
- Balasubramanian, S., Domingo, N.G.G., Hunt, N.D., Gittlin, M., Colgan, K.K., Marshall, J.D., Robinson, A.L., Azevedo, I.M.L., Thakrar, S.K., Clark, M.A., Tessum, C.W., Adams, P.J., Pandis, S.N., Hill, J.D. (2021). The food we eat, the air we breathe: A review of the fine particulate matter-induced air quality health impacts of the global food system. *Environ. Res. Lett.* 16, 103004. <https://doi.org/10.1088/1748-9326/ac065f>
- Baral, B.D., Thapa, K. (2021). Effect of the COVID-19 lockdown on ambient air quality in major cities of Nepal. *J. Health Pollut.* 11, 210211. <https://doi.org/10.5696/2156-9614-11.29.210211>
- Becker, S., Sapkota, R.P., Pokharel, B., Adhikari, L., Pokhrel, R.P., Khanal, S., Giri, B. (2021). Particulate matter variability in Kathmandu based on in-situ measurements, remote sensing, and reanalysis data. *Atmos. Res.* 258, 105623. <https://doi.org/10.1016/j.atmosres.2021.105623>
- Brock, C.A., Wagner, N.L., Anderson, B.E., Attwood, A.R., Beyersdorf, A., Campuzano-Jost, P.,

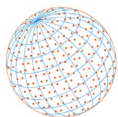


- Carlton, A.G., Day, D.A., Diskin, G.S., Gordon, T.D., Jimenez, J.L., Lack, D.A., Liao, J., Markovic, M.Z., Middlebrook, A.M., Ng, N.L., Perring, A.E., Richardson, M.S., Schwarz, J.P., Washenfelder, R.A., *et al.* (2016). Aerosol optical properties in the southeastern United States in summer – Part 1: Hygroscopic growth. *Atmos. Chem. Phys.* 16, 4987–5007. <https://doi.org/10.5194/acp-16-4987-2016>
- Brock, C.A., Froyd, K.D., Dollner, M., Williamson, C.J., Schill, G., Murphy, D.M., Wagner, N.J., Kupc, A., Jimenez, J.L., Campuzano-Jost, P., Nault, B.A., Schroder, J.C., Day, D.A., Price, D.J., Weinzierl, B., Schwarz, J.P., Katich, J.M., Wang, S., Zeng, L., Weber, R., *et al.* (2021). Ambient aerosol properties in the remote atmosphere from global-scale in situ measurements. *Atmos. Chem. Phys.* 21, 15023–15063. <https://doi.org/10.5194/acp-21-15023-2021>
- Bui, T.H., Nguyen, D.L., Nguyen, H.H. (2022). Study of aerosol optical properties at two urban areas in the north of Vietnam with the implication for biomass burning impacts. *Environ. Sci. Pollut. Res.* 29, 41923–41940. <https://doi.org/10.1007/s11356-021-15608-5>
- Calvello, M., Esposito, F., Leone, L., Pavese, G., Restieri, R. (2008). High resolution measurement of aerosol equivalent scale height over wide range. 16, 443–448.
- Chen, P., Li, C., Kang, S., Yan, F., Zhang, Q., Ji, Z., Tripathi, L., Rupakheti, D., Rupakheti, M., Qu, B., Sillanpää, M. (2016). Source apportionment of particle-bound polycyclic aromatic hydrocarbons in Lumbini, Nepal by using the positive matrix factorization receptor model. *Atmos. Res.* 182, 46–53. <https://doi.org/10.1016/j.atmosres.2016.07.011>
- Das, M., Das, A., Sarkar, R., Mandal, P., Saha, S., Ghosh, S. (2021). Exploring short term spatio-temporal pattern of PM<sub>2.5</sub> and PM<sub>10</sub> and their relationship with meteorological parameters during COVID-19 in Delhi. *Urban Clim.* 39, 100944. <https://doi.org/10.1016/j.uclim.2021.100944>
- Devi, N.L., Kumar, A., Yadav, I.C. (2020). PM<sub>10</sub> and PM<sub>2.5</sub> in Indo-Gangetic Plain (IGP) of India: Chemical characterization, source analysis, and transport pathways. *Urban Clim.* 33, 100663. <https://doi.org/10.1016/j.uclim.2020.100663>
- Di, Q., Wang, Y., Zanobetti, A., Wang, Y., Koutrakis, P., Choirat, C., Dominici, F., Schwartz, J.D. (2017). Air Pollution and Mortality in the Medicare Population. *N. Engl. J. Med.* 376, 2513–2522. <https://doi.org/10.1056/nejmoa1702747>
- Duan, J., Huang, R.J., Li, Y., Chen, Q., Zheng, Y., Chen, Y., Lin, C., Ni, H., Wang, M., Ovadnevaite, J., Ceburnis, D., Chen, C., Worsnop, D.R., Hoffmann, T., O’Dowd, C., Cao, J. (2020). Summertime and wintertime atmospheric processes of secondary aerosol in Beijing. *Atmos. Chem. Phys.* 20, 3793–3807. <https://doi.org/10.5194/acp-20-3793-2020>
- Dusek, U., Frank, G.P., Hildebrandt, L., Curtius, J., Schneider, J., Walter, S., Chand, D., Drewnick, F., Hings, S., Jung, D., Borrmann, S., Andreae, M.O. (2006). Size matters more than chemistry for cloud-nucleating ability of aerosol particles. *Science* 312, 1375–1378. <https://doi.org/10.1126/science.1125261>
- Edwards, L., Rutter, G., Iverson, L., Wilson, L., Chadha, T.S., Wilkinson, P., Milojevic, A. (2021). Personal exposure monitoring of PM<sub>2.5</sub> among US diplomats in Kathmandu during the COVID-19 lockdown, March to June 2020. *Sci. Total Environ.* 772, 144836. <https://doi.org/10.1016/j.scitotenv.2020.144836>
- Green, M., Kondragunta, S., Ciren, P., Xu, C. (2009). Comparison of GOES and MODIS aerosol optical depth (AOD) to aerosol robotic network (AERONET) AOD and IMPROVE PM<sub>2.5</sub> mass at Bondville, Illinois. *J. Air Waste Manage. Assoc.* 59, 1082–1091. <https://doi.org/10.3155/1047-3289.59.9.1082>
- Gupta, P., Remer, L.A., Patadia, F., Levy, R.C., Christopher, S. A. (2020). High-resolution gridded level 3 aerosol optical depth data from MODIS. *Remote Sens.* 12, 2847. <https://doi.org/10.3390/rs12172847>
- Hagan, D.H., Kroll, J.H. (2020). Assessing the accuracy of low-cost optical particle sensors using a physics-based approach. *Atmos. Meas. Tech.* 13, 6343–6355. <https://doi.org/10.5194/amt-13-6343-2020>
- Haywood, J., Boucher, O. (2000). Estimates of the direct and indirect radiative forcing due to tropospheric aerosols: A review. *Rev. Geophys.* 38, 513–543. <https://doi.org/10.1029/1999RG000078>
- He, M., Kuerbanjiang, N., Dhaniyala, S. (2020). Performance characteristics of the low-cost Plantower PMS optical sensor. *Aerosol Sci. Technol.* 54, 232–241. <https://doi.org/10.1080/02786826.2019.1696015>



- Ichoku, C., Remer, L.A., Eck, T.F. (2005). Correction to “Quantitative evaluation and intercomparison of morning and afternoon Moderate Resolution Imaging Spectroradiometer (MODIS) aerosol measurements from Terra and Aqua.” *J. Geophys. Res.* 110, D10S99. <https://doi.org/10.1029/2005JD005897>
- Islam, M.R., Jayarathne, T., Simpson, I.J., Werden, B., Maben, J., Gilbert, A., Praveen, P.S., Adhikari, S., Panday, A.K., Rupakheti, M., Blake, D.R., Yokelson, R.J., DeCarlo, P.F., Keene, W.C., Stone, E.A. (2020). Ambient air quality in the Kathmandu Valley, Nepal, during the pre-monsoon: Concentrations and sources of particulate matter and trace gases. *Atmos. Chem. Phys.* 20, 2927–2951. <https://doi.org/10.5194/acp-20-2927-2020>
- Jethva, H., Torres, O., Field, R.D., Lyapustin, A., Gautam, R., Kayetha, V. (2019). Connecting crop productivity, residue fires, and air quality over Northern India. *Sci. Rep.* 9, 16594. <https://doi.org/10.1038/s41598-019-52799-x>
- Jin, X., Li, Z., Wu, T., Wang, Y., Cheng, Y., Su, T., Wei, J., Ren, R., Wu, H., Li, S., Zhang, D., Cribb, M. (2022). The different sensitivities of aerosol optical properties to particle concentration, humidity, and hygroscopicity between the surface level and the upper boundary layer in Guangzhou, China. *Sci. Total Environ.* 803, 150010. <https://doi.org/10.1016/j.scitotenv.2021.150010>
- Karagulian, F., Belis, C.A., Dora, C.F.C., Prüss-Ustün, A.M., Bonjour, S., Adair-Rohani, H., Amann, M. (2015). Contributions to cities’ ambient particulate matter (PM): A systematic review of local source contributions at global level. *Atmos. Environ.* 120, 475–483. <https://doi.org/10.1016/j.atmosenv.2015.08.087>
- Kasten, F. (1969). Visibility forecast in the phase of pre-condensation. *Tellus A* 21, 631. <https://doi.org/10.3402/tellusa.v21i5.10112>
- Kitada, T., Regmi, R.P. (2003). Dynamics of air pollution transport in late wintertime over Kathmandu Valley, Nepal: As revealed with numerical simulation. *J. Appl. Meteorol.* 42, 1770–1798. [https://doi.org/10.1175/1520-0450\(2003\)042<1770:DOAPTI>2.0.CO;2](https://doi.org/10.1175/1520-0450(2003)042<1770:DOAPTI>2.0.CO;2)
- Koelemeijer, R.B.A., Homan, C.D., Matthijsen, J. (2006). Comparison of spatial and temporal variations of aerosol optical thickness and particulate matter over Europe. *Atmos. Environ.* 40, 5304–5315. <https://doi.org/10.1016/j.atmosenv.2006.04.044>
- Kotchenruther, R.A., Hobbs, P.V. (1998). Humidification factors of aerosols from biomass burning in Brazil. *J. Geophys. Res.* 103, 32081–32089. <https://doi.org/10.1029/98JD00340>
- Kotchenruther, R.A. (2020). Recent changes in winter PM<sub>2.5</sub> contributions from wood smoke, motor vehicles, and other sources in the Northwest U.S. *Atmos. Environ.* 237, 117724. <https://doi.org/10.1016/j.atmosenv.2020.117724>
- Kumar, N., Chu, A., Foster, A. (2007). An empirical relationship between PM<sub>2.5</sub> and aerosol optical depth in Delhi Metropolitan. *Atmos. Environ.* 41, 4492–4503. <https://doi.org/10.1016/j.atmosenv.2007.01.046>
- Kumar, A., Singh, N., Anshumali, Solanki, R. (2018). Evaluation and utilization of MODIS and CALIPSO aerosol retrievals over a complex terrain in Himalaya. *Remote Sens. Environ.* 206, 139–155. <https://doi.org/10.1016/j.rse.2017.12.019>
- Kumar, P., Goel, A. (2016). Concentration dynamics of coarse and fine particulate matter at and around signalised traffic intersections. *Environ. Sci.: Processes Impacts* 18, 1220–1235. <https://doi.org/10.1039/C6EM00215C>
- Levy, R.C., Mattoo, S., Munchak, L.A., Remer, L.A., Sayer, A.M., Patadia, F., Hsu, N.C. (2013). The Collection 6 MODIS aerosol products over land and ocean. *Atmos. Meas. Tech.* 6, 2989–3034. <https://doi.org/10.5194/amt-6-2989-2013>
- Lim, S.S., Vos, T., Flaxman, A.D., Danaei, G., Shibuya, K., Adair-Rohani, H., AlMazroa, M.A., Amann, M., Anderson, H.R., Andrews, K.G., Aryee, M., Atkinson, C., Bacchus, L.J., Bahalim, A.N., Balakrishnan, K., Balmes, J., Barker-Collo, S., Baxter, A., Bell, M.L., Blore, J.D., *et al.* (2012). A comparative risk assessment of burden of disease and injury attributable to 67 risk factors and risk factor clusters in 21 regions, 1990–2010: A systematic analysis for the Global Burden of Disease Study 2010. *Lancet* 380, 2224–2260. [https://doi.org/10.1016/S0140-6736\(12\)61766-8](https://doi.org/10.1016/S0140-6736(12)61766-8)
- Magi, B.I., Cupini, C., Francis, J., Green, M., Hauser, C. (2020). Evaluation of PM<sub>2.5</sub> measured in an urban setting using a low-cost optical particle counter and a Federal Equivalent Method Beta Attenuation Monitor. *Aerosol Sci. Technol.* 54, 147–159. <https://doi.org/10.1080/02786826.2019.1619915>





- Mahapatra, P.S., Puppala, S.P., Adhikary, B., Shrestha, K.L., Dawadi, D.P., Paudel, S.P., Panday, A.K. (2019). Air quality trends of the Kathmandu Valley: A satellite, observation and modeling perspective. *Atmos. Environ.* 201, 334–347. <https://doi.org/10.1016/j.atmosenv.2018.12.043>
- Malm, W.C., Day, D.E., Kreidenweis, S.M. (2000). Light scattering characteristics of aerosols as a function of relative humidity: Part I—A comparison of measured scattering and aerosol concentrations using the theoretical models. *J. Air Waste Manage. Assoc.* 50, 686–700. <https://doi.org/10.1080/10473289.2000.10464117>
- Mancilla, Y., Herckes, P., Fraser, M.P., Mendoza, A. (2015). Secondary organic aerosol contributions to PM<sub>2.5</sub> in Monterrey, Mexico: Temporal and seasonal variation. *Atmos. Res.* 153, 348–359. <https://doi.org/10.1016/j.atmosres.2014.09.009>
- Moody, J.L., Keene, W.C., Cooper, O.R., Voss, K.J., Aryal, R., Eckhardt, S., Holben, B., Maben, J.R., Izaguirre, M.A., Galloway, J.N. (2014). Flow climatology for physicochemical properties of dichotomous aerosol over the western North Atlantic Ocean at Bermuda. *Atmos. Chem. Phys.* 14, 691–717. <https://doi.org/10.5194/acp-14-691-2014>
- Morawska, L., Thai, P.K., Liu, X., Asumadu-Sakyi, A., Ayoko, G., Bartonova, A., Bedini, A., Chai, F., Christensen, B., Dunbabin, M., Gao, J., Hagler, G.S.W., Jayaratne, R., Kumar, P., Lau, A.K.H., Louie, P.K.K., Mazaheri, M., Ning, Z., Motta, N., Mullins, B., *et al.* (2018). Applications of low-cost sensing technologies for air quality monitoring and exposure assessment: How far have they gone? *Environ. Int.* 116, 286–299. <https://doi.org/10.1016/j.envint.2018.04.018>
- Mues, A., Lauer, A., Lupascu, A., Rupakheti, M., Kuik, F., Lawrence, M.G. (2018). WRF and WRF-Chem v3.5.1 simulations of meteorology and black carbon concentrations in the Kathmandu Valley. *Geosci. Model Dev.* 11, 2067–2091. <https://doi.org/10.5194/gmd-11-2067-2018>
- Munir, S., Mayfield, M., Coca, D., Jubb, S.A., Osammor, O. (2019). Analysing the performance of low-cost air quality sensors, their drivers, relative benefits and calibration in cities—A case study in Sheffield. *Environ. Monit. Assess.* 191, 94. <https://doi.org/10.1007/s10661-019-7231-8>
- Ouimette, J.R., Malm, W.C., Schichtel, B.A., Sheridan, P.J., Andrews, E., Ogren, J.A., Arnott, W.P. (2022). Evaluating the PurpleAir monitor as an aerosol light scattering instrument. *Atmos. Meas. Tech.* 15, 655–676. <https://doi.org/10.5194/amt-15-655-2022>
- Panday, A.K., Prinn, R.G. (2009). Diurnal cycle of air pollution in the Kathmandu Valley, Nepal: Observations. *J. Geophys. Res.* 114, D09305. <https://doi.org/10.1029/2008JD009777>
- Pant, P., Harrison, R.M. (2013). Estimation of the contribution of road traffic emissions to particulate matter concentrations from field measurements: A review. *Atmos. Environ.* 77, 78–97. <https://doi.org/10.1016/j.atmosenv.2013.04.028>
- Pervez, S., Verma, M., Tiwari, S., Chakrabarty, R.K., Watson, J.G., Chow, J.C., Panicker, A.S., Deb, M.K., Siddiqui, M.N., Pervez, Y.F. (2019). Household solid fuel burning emission characterization and activity levels in India. *Sci. Total Environ.* 654, 493–504. <https://doi.org/10.1016/j.scitotenv.2018.11.019>
- Ramachandran, S., Kedia, S. (2013). Aerosol optical properties over South Asia from ground-based observations and remote sensing: A review. *Climate* 1, 84–119. <https://doi.org/10.3390/cli1030084>
- Ramanathan, V., Crutzen, P.J., Kiehl, J.T., Rosenfeld, D. (2001). Aerosols, climate, and the hydrological cycle. *Science* 294, 2119–2124. <https://doi.org/10.1126/science.1064034>
- Regmi, J., Poudyal, K.N., Pokhrel, A., Gyawali, M., Tripathi, L., Panday, A., Barinelli, A., Aryal, R. (2020). Investigation of aerosol climatology and long-range transport of aerosols over Pokhara, Nepal. *Atmosphere* 11, 874. <https://doi.org/10.3390/atmos11080874>
- Robinson, E.S., Gu, P., Ye, Q., Li, H.Z., Shah, R.U., Apte, J.S., Robinson, A.L., Presto, A.A. (2018). Restaurant impacts on outdoor air quality: Elevated organic aerosol mass from restaurant cooking with neighborhood-scale plume extents. *Environ. Sci. Technol.* 52, 9285–9294. <https://doi.org/10.1021/acs.est.8b02654>
- Ruzer, L.S., Harley, N.H. (2005). *Aerosols handbook: measurement, dosimetry, and health effects*. CRC press.
- Sarkar, C., Sinha, V., Sinha, B., Panday, A.K., Rupakheti, M., Lawrence, M.G. (2017). Source apportionment of NMVOCs in the Kathmandu Valley during the SusKat-ABC international field campaign using positive matrix factorization. *Atmos. Chem. Phys.* 17, 8129–8156. <https://doi.org/10.5194/acp-17-8129-2017>
- Sayahi, T., Butterfield, A., Kelly, K.E. (2019). Long-term field evaluation of the Plantower PMS low-



- cost particulate matter sensors. *Environ. Pollut.* 245, 932–940. <https://doi.org/10.1016/j.envpol.2018.11.065>
- Schwartz, J., Dockery, D.W., Neas, L.M. (1996). Is daily mortality associated specifically with fine particles? *J. Air Waste Manage. Assoc.* 46, 927–939. <https://doi.org/10.1080/10473289.1996.10467528>
- Schwarze, P.E., Øvrevik, J., Låg, M., Refsnes, M., Nafstad, P., Hetland, R.B., Dybing, E. (2006). Particulate matter properties and health effects: Consistency of epidemiological and toxicological studies. *Hum. Exp. Toxicol.* 25, 559–579. <https://doi.org/10.1177/096032706072520>
- Segura, S., Estellés, V., Utrillas, M.P., Martínez-Lozano, J.A. (2017). Long term analysis of the columnar and surface aerosol relationship at an urban European coastal site. *Atmos. Environ.* 167, 309–322. <https://doi.org/10.1016/j.atmosenv.2017.08.012>
- Shakya, K.M., Rupakheti, M., Shahi, A., Maskey, R., Pradhan, B., Panday, A., Puppala, S.P., Lawrence, M., Peltier, R.E. (2017). Near-road sampling of PM<sub>2.5</sub>, BC, and fine-particle chemical components in Kathmandu Valley, Nepal. *Atmos. Chem. Phys.* 17, 6503–6516. <https://doi.org/10.5194/acp-17-6503-2017>
- Shiraiwa, M., Ueda, K., Pozzer, A., Lammel, G., Kampf, C.J., Fushimi, A., Enami, S., Arangio, A.M., Fröhlich-Nowoisky, J., Fujitani, Y., Furuyama, A., Lakey, P.S.J., Lelieveld, J., Lucas, K., Morino, Y., Pöschl, U., Takahama, S., Takami, A., Tong, H., Weber, B., *et al.* (2017). Aerosol health effects from molecular to global scales. *Environ. Sci. Technol.* 51, 13545–13567. <https://doi.org/10.1021/acs.est.7b04417>
- Shrestha, S., Puppala, S.P., Adhikary, B., Shrestha, K.L., Panday, A.K. (2017). Influence of semi-volatile aerosols on physical and optical properties of aerosols in the Kathmandu Valley. *Atmos. Chem. Phys. Discuss.* [preprint], <https://doi.org/10.5194/acp-2017-287>
- Stavroulas, I., Grivas, G., Michalopoulos, P., Liakakou, E., Bougiatioti, A., Kalkavouras, P., Fameli, K., Hatzianastassiou, N., Mihalopoulos, N., Gerasopoulos, E. (2020). Field Evaluation of Low-Cost PM Sensors (Purple Air PA-II) Under Variable Urban Air Quality Conditions, in Greece. *Atmosphere* 11, 926. <https://doi.org/10.3390/atmos11090926>
- van de Hulst, H.C. (1981). *Light Scattering by Small Particles* (1981st ed.). Dover Publications, Inc.
- van Donkelaar, A., Martin, R.V., Brauer, M., Boys, B.L. (2015). Use of satellite observations for long-term exposure assessment of global concentrations of fine particulate matter. *Environ. Health Perspect.* 123, 135–143. <https://doi.org/10.1289/ehp.1408646>
- Wang, Y.Q. (2014). Meteoinfo: GIS software for meteorological data visualization and analysis. *Meteorol. Appl.* 21, 360–368. <https://doi.org/10.1002/met.1345>
- Xu, X., Zhang, C. (2020). Estimation of ground-level PM<sub>2.5</sub> concentration using MODIS AOD and corrected regression model over Beijing, China. *PLoS One*, 15, 3–15. <https://doi.org/10.1371/journal.pone.0240430>
- Yong, Z. (2016). Plantower PMS5003 Data Manual. 3. [http://www.aqmd.gov/docs/default-source/aq-spec/resources-page/plantower-pms5003-manual\\_v2-3.pdf](http://www.aqmd.gov/docs/default-source/aq-spec/resources-page/plantower-pms5003-manual_v2-3.pdf)
- Zhang, H., Hoff, R.M., Engel-Cox, J.A. (2009). The relation between moderate resolution imaging spectroradiometer (MODIS) aerosol optical depth and PM<sub>2.5</sub> over the United States: A geographical comparison by U.S. Environmental Protection Agency regions. *J. Air Waste Manage. Assoc.* 59, 1358–1369. <https://doi.org/10.3155/1047-3289.59.11.1358>
- Zheng, C., Zhao, C., Zhu, Y., Wang, Y., Shi, X., Wu, X., Chen, T., Wu, F., Qiu, Y. (2017). Analysis of influential factors for the relationship between PM<sub>2.5</sub> and AOD in Beijing. *Atmos. Chem. Phys.* 17, 13473–13489. <https://doi.org/10.5194/acp-17-13473-2017>
- Zhong, S., Qian, Y., Zhao, C., Leung, R., Yang, X.Q. (2015). A case study of urbanization impact on summer precipitation in the Greater Beijing Metropolitan Area: Urban heat island versus aerosol effects. *J. Geophys. Res.* 120, 10903–10914. <https://doi.org/10.1002/2015JD023753>

Article

# Investigation of Aerosol Climatology and Long-Range Transport of Aerosols over Pokhara, Nepal

Jeevan Regmi <sup>1</sup>, Khem N Poudyal <sup>2</sup>, Amod Pokhrel <sup>3</sup>, Madhu Gyawali <sup>4</sup>, Lekhendra Tripathi <sup>5</sup> , Arnico Panday <sup>6</sup>, Anthony Barinelli <sup>7</sup> and Rudra Aryal <sup>7,\*</sup>

<sup>1</sup> Central Department of Physics, Tribhuvan University Kirtipur, Kirtipur, Nepal; jeevan@pncampus.edu.np

<sup>2</sup> Department of Applied Sciences, Institute of Engineering Tribhuvan University, Lalitpur, Nepal; khem@ioe.edu.np

<sup>3</sup> School of Public Health, University of California Berkeley, Berkeley, CA 94720, USA; amod@berkeley.edu

<sup>4</sup> Department of Physics, San Jacinto College, South Campus, 13735 Beamer Rd, Houston, TX 77089, USA; madhu.gyawali@sjcd.edu

<sup>5</sup> State Key Laboratory of Cryospheric Science, Northwest Institute of Eco-Environment and Resources, Chinese Academy of Sciences, Lanzhou 730000, China; lekhendra@lzb.ac.cn

<sup>6</sup> Ullens Education Foundation, Lalitpur, Nepal; arnico@ullens.edu.np

<sup>7</sup> College of Health & Natural Sciences, Franklin Pierce University, 40 University Drive, Rindge, NH 03461, USA; Barinellia15@live.franklinpiercedu

\* Correspondence: aryalr@franklinpiercedu

Received: 20 July 2020; Accepted: 13 August 2020; Published: 17 August 2020



**Abstract:** This study presents the spectral monthly and seasonal variation of aerosol optical depth ( $\tau_{\text{AOD}}$ ), single scattering albedo (SSA), and aerosol absorption optical depth (AAOD) between 2010 and 2018 obtained from the Aerosol Robotic Network (AERONET) over Pokhara, Nepal. The analysis of these column-integrated aerosol optical data suggests significant monthly and seasonal variability of aerosol physical and optical properties. The pre-monsoon season (March to May) has the highest observed  $\tau_{\text{AOD}}$  ( $0.75 \pm 0.15$ ), followed by winter (December to February,  $0.47 \pm 0.12$ ), post-monsoon (October and November,  $0.39 \pm 0.08$ ), and monsoon seasons (June to September,  $0.27 \pm 0.13$ ), indicating seasonal aerosol loading over Pokhara. The variability of Ångström parameters,  $\alpha$ , and  $\beta$ , were computed from the linear fit line in the logarithmic scale of spectral  $\tau_{\text{AOD}}$ , and used to analyze the aerosol physical characteristics such as particle size and aerosol loading. The curvature of spectral  $\tau_{\text{AOD}}$ ,  $\alpha'$ , computed from the second-order polynomial fit, reveals the domination by fine mode aerosol particles in the post-monsoon and winter seasons, with coarse mode dominating in monsoon, and both modes contributing in the pre-monsoon. Analysis of air mass back trajectories and observation of fire spots along with aerosol optical data and aerosol size spectra suggest the presence of mixed types of transboundary aerosols, such as biomass, urban-industrial, and dust aerosols in the atmospheric column over Pokhara.

**Keywords:** aerosol climatology; spectral aerosol optical depth; single scattering albedo; aerosol absorption optical depth; Ångström parameters; turbidity; long range transportation; back trajectory; aerosol absorption exponent

## 1. Introduction

Atmospheric aerosols have a significant impact on the Earth's atmospheric radiation budget, due to their direct scattering and absorption characteristics, as well as an indirect impact on microphysics and clouds' formation [1–3]. In recent decades, there has been increasing concern about aerosols' impact on melting snow and ice in the high Himalaya and over the Tibetan Plateau [4–6], with indications that a significant portion of the aerosols arrived from the Indo-Gangetic Plains [7,8]. To date, though, there

have been only limited studies of aerosols over the Himalayan foothills immediately south of high Himalaya, on their route from the IGP towards the high mountains [5,9].

The measurement of atmospheric aerosol physical and optical properties can provide knowledge of understanding the role of aerosols in the climate system. In the last few decades, various techniques have been used to measure and characterize the atmospheric aerosols from ground, aircraft, and satellite measurements [10–14]. Aerosol Robotic Network (AERONET) is one of the global ground-based networks used to monitor atmospheric aerosol optical properties and is maintained by the National Aeronautics and Space Administration (NASA). It has adopted the robotic Cimel Sun photometer throughout its network, to measure direct and diffuse solar radiation, which is then used to retrieve the aerosol products on the AERONET website [12,15]. The network provides a readily accessible public domain database of atmospheric column integrated aerosol optical properties, such as aerosol optical depth ( $\tau_{\text{AOD}}$ ) measured in the ultraviolet to infrared wavelengths. Moreover,  $\tau_{\text{AOD}}$  represents the columnar aerosol content resulting from the different aerosol populations in the atmospheric column above the measurement site [12,14,16]. The spectral variation of  $\tau_{\text{AOD}}$ , which can be characterized by the Ångström parameters ( $\alpha$  and  $\beta$ ), can give a picture of aerosol size distribution and aerosol loading in the atmospheric column [14,16,17]. These are important parameters in the determination of aerosol size distribution. The variability of aerosol size distribution is a good indicator for the sources of aerosols, such as those generated from urban and industrial, biomass burning, combustion of fossil fuels, and airborne soil particles [17]. Many investigations have previously used the information on particle size and spectral aerosol optical characteristics to validate the dominant aerosol type [17–19].

Remote sensing techniques are important tools to monitor aerosol optical properties globally, by validating the accuracy of measurements [12,20,21]. The establishment of AERONET sites has provided an opportunity to study the aerosol loading due to local and long-range transportation over the region [13,18]. A combined analysis of ground-based column integrated aerosol optical data, atmospheric simulations such as the back trajectory analysis from Hybrid Single-Particle Lagrangian Integrated Trajectory Model (HYSPLIT) and the Moderate Resolution Imaging Spectroradiometer (MODIS) satellite observation data of atmospheric pollutants can be used to study the spatial and temporal variation of aerosol optical properties, aerosol types, and source [13,22,23]

Previous studies in Nepal have presented aerosol characteristics, but did not investigate long-term aerosol optical properties and aerosol sizes based on the spectral aerosol optical depth [24–27]. A number of studies have shown that Nepal's atmosphere is affected by a variety of emissions, such as those produced by biomass burning, agricultural burning, and domestic uses of biofuels, which are taking place in its large neighboring countries [28,29]. Particularly the Terai—the flat part of southern Nepal that lines the northern edge of the Indo-Gangetic Plains (IGP)—is heavily affected by trans-boundary pollution from the rest of the IGP. The IGP is a densely populated region with high aerosol loading from both anthropogenic and natural sources. Past studies have shown that major sources of aerosol loading over IGP include biomass burning, desert dust, and pollution from industrial and urban activities [26,29,30].

The AERONET observation site in Pokhara, Nepal, was established in January 2010 and has continuously provided various long-term aerosol products. After a decade of operation, it has now accumulated the longest continuous atmospheric observation data site in Nepal. While previous studies have shown the influence of transboundary air pollution over the Himalayan region of Nepal [4–9,24], this is the first detailed analysis of the seasonal variation of aerosol transport over the Nepal Himalaya using a long-term aerosol dataset, combined with computer simulation and satellite data analysis, providing us with a comprehensive picture of aerosols across temporal and spatial scales. Analysis of aerosol climatology over Pokhara in the foothill of Himalayas, along with its transboundary aerosol sources, provides glimpses of regional aerosols that reach more remote locations in the high Himalayas and Tibetan plateau.

In this study, we have used monthly averaged aerosol optical properties between 2010 and 2018, such as spectral aerosol optical depth ( $\tau_{\text{AOD}}$ ) from ultraviolet to infrared, 0.34  $\mu\text{m}$  to 1.02  $\mu\text{m}$ , to examine

the seasonal Angstrom exponents and characterize the aerosol types. Level 2 AERONET inversion products single scattering albedo (SSA), and absorption angstrom exponent (AAE) at four different wavelengths—0.44  $\mu\text{m}$ , 0.675  $\mu\text{m}$ , 0.87  $\mu\text{m}$ , and 1.02  $\mu\text{m}$ —are investigated to identify absorbing aerosols. HYSPLIT back trajectory analysis, combined with MODIS satellite images of fire spots, have been used to identify the origins and types of aerosols transported to the receptor site, Pokhara.

## 2. Methodology

### 2.1. Site Description

The Pokhara AERONET site is located at 28.19° N, 83.97° E in the Pokhara Sub-Metropolitan city of Nepal. Pokhara is Nepal's second-largest city after Kathmandu, with a population of about two hundred sixty thousand [31]. The Cimel Sun Photometer is located on the roof of Shangrila Village Resort, in the south-western suburbs of Pokhara.

The site is approximately at an altitude of 805 m above sea level, and about 140 km west of Kathmandu. It is surrounded by hills, between 1000 to 2000 m above sea level. The IGP is about 90 km to the south, while to the north, the elevation rises quickly to over 7000 m in the span of 35 km. The presence of high mountains near Pokhara assists in lifting the humid air-masses, mainly in the summertime, resulting in a large amount of precipitation, which can significantly affect the aerosol concentration in the atmosphere [9,25,27,32]. Figure 1 shows the location of Pokhara, along with the potential source regions of air masses over its atmospheric column from Nepal and outside the region, such as from IGP, along with other parts of Asia, including the Punjab region of Pakistan and the Thar Desert [33].



**Figure 1.** The map with the aerosol ground monitoring station (Pokhara, Nepal) has an inset in the bottom right corner that shows the Aerosol Robotic Network (AERONET) sun photometer in Pokhara (photo by Arnico Panday) and a compass rose on the left corner. This image is adopted from online resources, and horizontal and vertical scales in 200 miles are shown on the map.

### 2.2. Cimel Sun Photometer

An automatic sun-and-sky scanning Cimel Sun Photometer is located on the roof of the Shangrila Village Resort in Pokhara's south-western suburbs, as a part of AERONET. Descriptions of this network and methods for retrieving aerosol optical data have been published before [12,14,20].

The sun photometer measures direct sun radiances at 0.34  $\mu\text{m}$ , 0.38  $\mu\text{m}$ , 0.44  $\mu\text{m}$ , 0.50  $\mu\text{m}$ , 0.675  $\mu\text{m}$ , 0.87  $\mu\text{m}$ , 1.02  $\mu\text{m}$  and 1.64  $\mu\text{m}$  wavelengths during the daytime. The aerosol optical depth ( $\tau_{\text{AOD}}$ ) is derived by correcting attenuation due to Rayleigh scattering, absorption by ozone, and gaseous

components in direct spectral measurements [12,14,15]. In addition, the sun photometer also measures diffuse sky radiance at four wavelengths 0.44 μm, 0.675 μm, 0.87 μm, and 1.02 μm [14,16,20]. These solar extinction measurements are used to retrieve aerosol columnar inversion products, such as volume size distribution and single scattering albedo. Three data quality levels, Level 1.0 (unscreened), Level 1.5 (cloud screened), and Level 2.0 (cloud-screened and quality-assured), are provided for analysis of aerosol data [16,20], with Level 2.0 data made available after the instrument is returned to NASA during annual swap outs. All products of AERONET are automatically computed and made available within the AERONET website [15]. The estimated uncertainty in computed AOD is reported to range from ±0.01 to ±0.02, which is spectrally dependent, and is found higher on the UV region [12,16,23].

### 2.3. Basic Equations and Definitions

The spectral  $\tau_{AOD}$  is guided by Ångström exponent ( $\alpha$ ), as given by power-law equation [34].

$$\tau_{AOD} = \beta \lambda^{-\alpha} \tag{1}$$

In logarithmic format can be written as:

$$\ln \tau_{AOD}(\lambda) = \ln \beta - \alpha \ln \lambda \tag{2}$$

This gives the values of Ångström parameters  $\alpha$  and  $\beta$

The Ångström exponent  $\alpha$  can be further defined from the spectral AOD( $\lambda$ ) as

$$\alpha = -\frac{d \ln \tau_{AOD}(\lambda)}{d \ln \lambda} = -\frac{\ln\left(\frac{\tau_{AOD}(\text{at } \lambda_2)}{\tau_{AOD}(\text{at } \lambda_1)}\right)}{\ln\left(\frac{\lambda_2}{\lambda_1}\right)} \tag{3}$$

The deviation of observed data from the linear fit line can be tested by using a second-order polynomial fit, with coefficients of the polynomial fit  $\alpha_2, \alpha_1$ , and  $\alpha_0$ , as defined in previous studies [17–19].

$$\ln \tau_{AOD}(\lambda) = \alpha_2(\ln \lambda)^2 + \alpha_1(\ln \lambda) + \alpha_0 \tag{4}$$

We define  $\alpha'$  at wavelength ( $\lambda$ ) and this can also be found in previous articles [17,18].

$$\alpha' = \frac{d\alpha}{d \ln \lambda} = -\frac{d}{d \ln \lambda} \left[ \frac{d \ln \tau_{AOD}(\lambda)}{d \ln \lambda} \right] = -2\alpha_2 \tag{5}$$

The aerosol absorption characteristics can be exhibited by using SSA, aerosol absorption optical depth (AAOD) and AAE, and are related as below [2,3,35],

$$AAOD(\lambda) = AOD(\lambda) [1 - SSA(\lambda)] \tag{6}$$

and,

$$AAOD = K\lambda^{-AAE} \tag{7}$$

### 2.4. Tools Used for Backward Trajectories and Fire Spots

Four clusters were generated for each season by calculating five days backward air mass trajectories, starting at 500 m over the receptor site Pokhara (28.19° N, 83.19° E), for every day at 0:00, 6:00, 12:00, and 18:00 UTC, based on the HYSPLIT model [13]. A free software plugin called TrajStat was used from MeteoInfo for the calculations [36]. Fire spots were obtained from NASA’s Fire Information for Resource Management System (FIRMS), which allows visualizing large scale bio-mass burning activities around the region. These active fire data were observed from NASA’s Moderate Resolution Imaging Spectroradiometer (MODIS) and NASA’s Visible Infrared Imaging Radiometer Suite (VIIRS),

however, these satellite images will not provide the household level of biomass burning. A combination of satellite images of fire spots with air masses back trajectory will be presented to demonstrate a significant picture of aerosol climatology over the region [37–39].

In this study, we have used the data of the year 2017 to present a cluster analysis for indicating the seasonal aerosol sources’ characterization over the observation site Pokhara.

### 3. Results and Discussion

#### 3.1. Variability of Spectral Columnar AOD and Precipitable Water

In this section, we present the monthly and seasonal variability of spectral AOD and the temporal variability of AOD, by comparing with columnar precipitable water vapor (PW). Figure 2 shows the monthly mean spectral AOD values,  $\tau_{AOD}$ , over the 9 years from 2010 to 2018, at seven different wavelengths—0.34  $\mu\text{m}$ , 0.38  $\mu\text{m}$ , 0.44  $\mu\text{m}$ , 0.50  $\mu\text{m}$ , 0.675  $\mu\text{m}$ , 0.87  $\mu\text{m}$ , and 1.02  $\mu\text{m}$ . Our statistical analysis excluded monthly averaged aerosol data from any months that had  $\tau_{AOD}$  data for less than ten days.

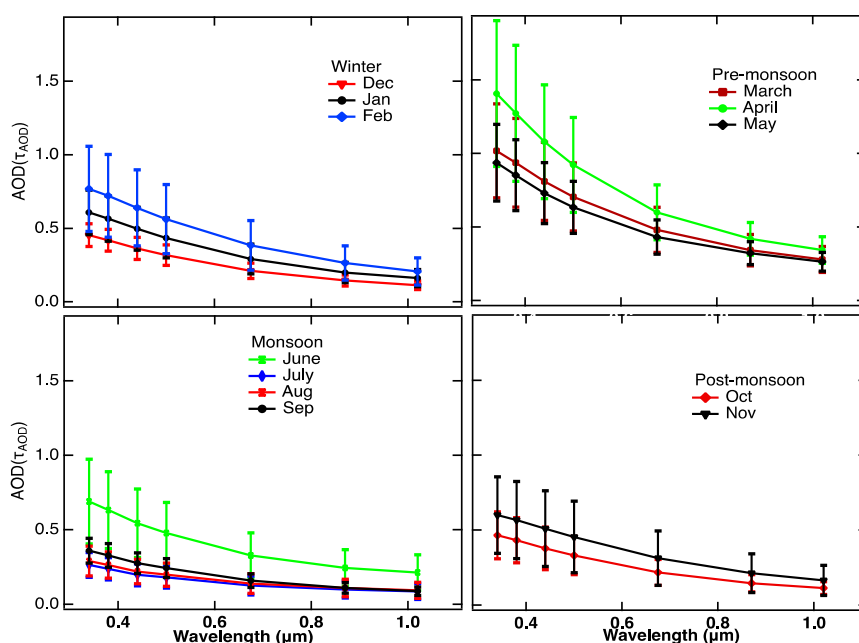


**Figure 2.** Spectral variation of monthly mean aerosol optical depth (AOD), over nine years between 2010–2018, in different seasons.

Due to the above constraint on data availability, the mean values for each calendar month across the nine years were computed from a varying number of months, as given in the parenthesis: January (6), February (8), March (8), April (7), May (8), June (5), July (4), August (3), September (4), October (6), November (6), and December (7). Level 2 aerosol data were very scarce on the AERONET website for the rainy season months of June, July, and August, due to cloud screening of the data and the requirement for the sun photometer to remain parked in a protected position whenever the rain sensor was wet.

The general trend of spectral variations shows that the  $\tau_{AOD}$  is higher at a shorter wavelength and decreases at longer wavelengths. We found the spectral  $\tau_{AOD}$  highest in April, followed by March, May, February, June (January, November), (December, October) September and (August and July). Months placed in parentheses have almost identical spectral  $\tau_{AOD}$  at all wavelengths. In the monsoon season, the gradient of spectral  $\tau_{AOD}$  in the longer wavelength decreases. Distinct features of seasonal  $\tau_{AOD}$  can be observed in Figure 2, with the highest aerosol loading in the months of pre-monsoon

season followed by winter, post-monsoon, and monsoon season. In the months of two seasons, winter and post-monsoon, the aerosol loadings are not significantly deviated from each other.

The temporal variation of light attenuation is also observed using a monthly mean AOD at  $0.50 \mu\text{m}$  ( $\tau_{0.50}$ ), along with a column-averaged precipitable water level (PW) in centimeters for different months and seasons (Figure 3). The  $\tau_{0.50}$ , ranges from 0.31 to 0.56 in winter season with average value of  $0.43 \pm 0.12$ , 0.63 to 0.92 in pre-monsoon season with average value of  $0.75 \pm 0.15$ , 0.18 to 0.47 in monsoon season with average value of  $0.27 \pm 0.13$ , and 0.33 to 0.45, in post-monsoon season with average value of  $0.39 \pm 0.08$ . Variation of PW shows a similar trend of rainfall in Pokhara with an increase from months of winter to monsoon seasons, and then decreasing in post-monsoon season [40]. In monsoon season, the variation on  $\tau_{0.50}$  is significantly affected by the rainfall.

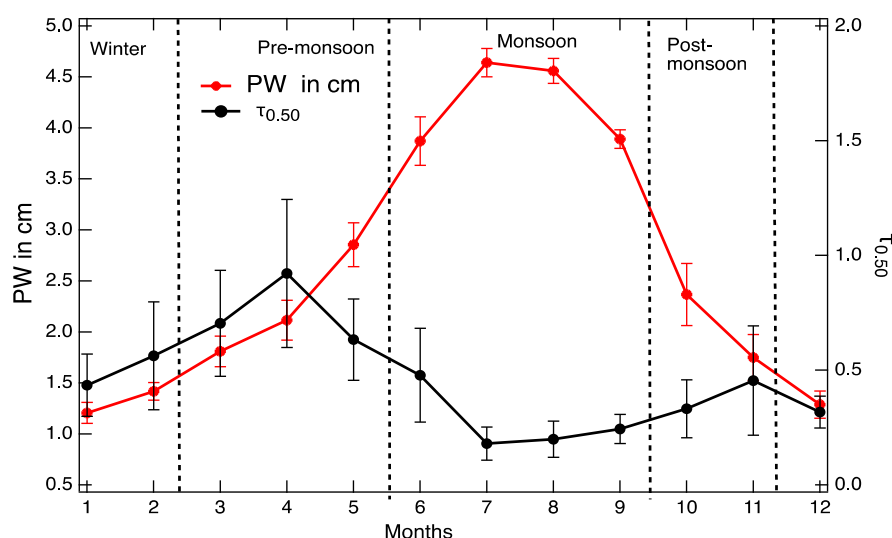


**Figure 3.** Temporal variation, monthly mean  $\tau_{0.50}$  (right axis), and precipitable water level in cm (left axis). The vertical dotted lines indicate the boundaries between different seasons.

The variations of  $\tau_{0.50}$  and PW show two different characters. Between December and April, these two parameters correlate significantly, with high  $R^2$  (0.91) and low  $p$ -values (0.01), and while including data of May  $R^2$  drops to 0.35 and  $p$ -value increases to 0.21. However, in monsoon and the post-monsoon months, they vary inversely with  $R^2$  equal to 0.43 and  $p$ -value 0.15. Previous studies have shown that atmospheric water vapor can serve as a medium for igniting multiphase reaction to the formation of gas to particle transformation, and play a key role for hygroscopic growth of aerosols, which ultimately affects the aerosol optical properties [41,42]. In this study, we argue that  $\tau_{0.50}$ , which has a significant correlation with PW, from December to April, is mainly associated with the actual aerosol loading, and might not be linked with aerosol particles' hygroscopic effect growth. However, a chemical analysis of aerosols over the observation site, such as the observation of black carbon, dust, sulfate, and organic carbon concentrations due to their hygroscopic characters, can give a picture of the aerosol hygroscopic impact on  $\tau_{0.50}$ , which we have not done in this study. A study of aerosol loading based on the Ångström turbidity coefficient ( $\beta$ ) is also presented in the next section, that will support the effect of aerosol loading for higher AOD. A previous study on the latitudinal variation of aerosol optical properties over the IGP region to the Central Himalayas during the pre-monsoon season has also explored the AOD due to aerosol loading over the observation site, rather than depicting hygroscopic growth of aerosol particles [43].

### 3.2. Angstrom Exponents, Curvature of AOD Spectra, SSA, AAOD and AAE

This section uses linear and second-order polynomial fit to study monthly and seasonal variation of spectral AOD in the wavelength ranges of 0.34 to  $1.02 \mu\text{m}$ . Ångström parameters have been



investigated in the past, by using spectral  $\tau_{AOD}$  by distinguishing several AERONET sites with a variety of individual aerosol types such as biomass burning, urban and industrial, and desert dust [17].

Figure 4 shows monthly Ångström parameters ( $\alpha$  and  $\beta$ ) and curvature of the spectral AOD curve ( $\alpha_2$ ). We observed that the average seasonal  $\alpha$  as  $1.14 \pm 0.01$  in winter,  $1.17 \pm 0.07$  in the pre-monsoon season,  $1.10 \pm 0.08$  in monsoon, and  $1.22 \pm 0.08$  in the post-monsoon season, based on the monthly mean data. Similarly,  $\alpha \nu (= -2\alpha_2)$  were obtained  $1.03 \pm 0.23$  for winter,  $0.55 \pm 0.14$  for pre-monsoon,  $0.23 \pm 0.38$  for monsoon, and  $1.22 \pm 0.08$  for post-monsoon seasons. The seasonal turbidity parameters,  $\beta$ , were also found  $0.18 \pm 0.05$  in winter,  $0.31 \pm 0.04$  in pre-monsoon,  $0.11 \pm 0.06$  in monsoon, and  $0.16 \pm 0.04$  in post-monsoon seasons. Moreover,  $\beta$  gives a picture of aerosol loading with the higher the value, the higher the aerosol loading, and similarly, smaller  $\beta$  shows lower aerosol loading. We observe from Figure 4 that  $\alpha$  shows more or less the same from one season to another, even though with a significant variation of  $\tau_{0.50}$ , by indicating the seasonal differences of the aerosol size spectrum.

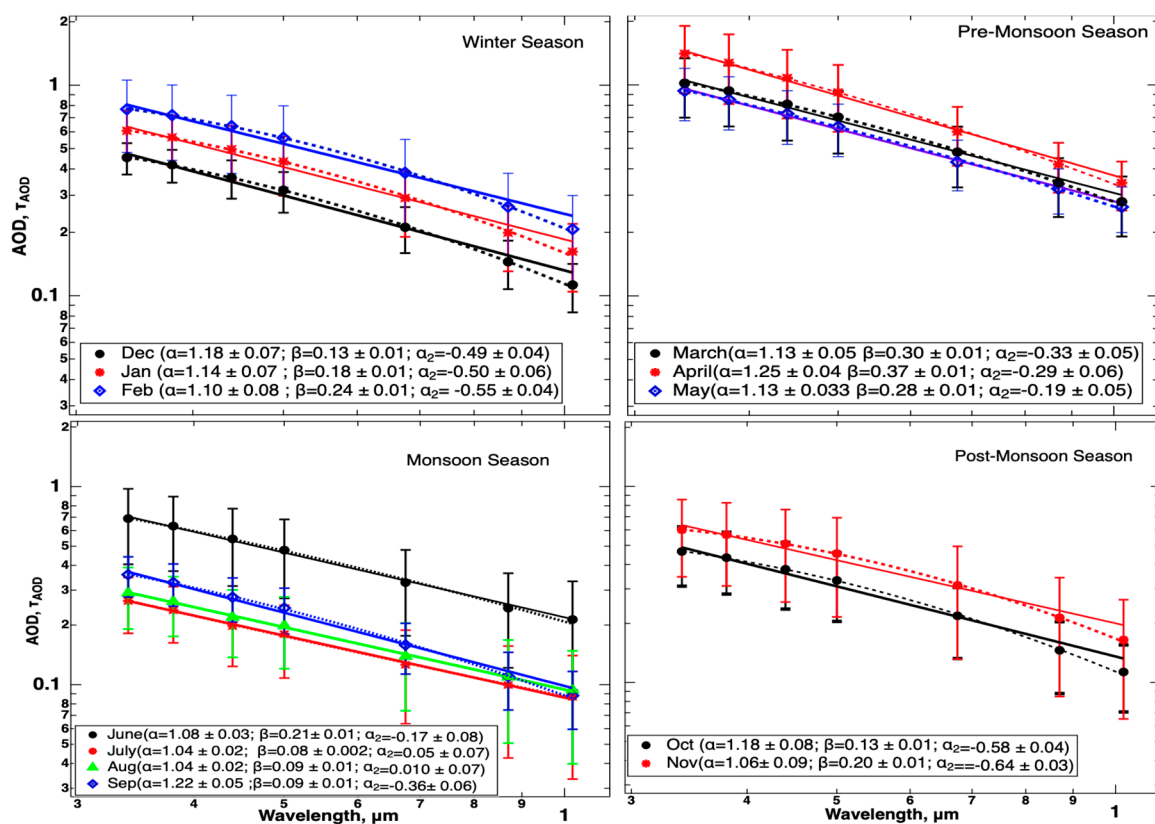


**Figure 4.** Ångström parameters ( $\alpha$ ,  $\beta$ ) computed by using the linear regression (solid line), and  $\alpha_2$  from second-order polynomial fit (dotted curve) of monthly mean spectral AOD, between years 2010–2018, in the logarithmic scale for different seasons, as indicated.

However,  $\alpha$  can be seen to be the highest in post-monsoon, followed by pre-monsoon, winter, and monsoon. We found different values of  $\alpha \nu$ , even for a similar value of  $\alpha$ , which indicates that the variation of aerosol microphysical properties can be presented by a climatological pattern of  $\alpha \nu$  rather than  $\alpha$ . Figure 5a,b show that the significant variation on  $\alpha \nu$  are observed for the months even with the similar  $\alpha$ . It was observed mainly in the months of a shift from one season to another season, in which prevailing air masses will also be in transition. Higher values of  $\alpha \nu$  (greater or close to 1) in the post-monsoon season followed by winter season provide a picture of columnar aerosol size distribution showing strong contribution by fine mode particles, which are mainly originated from anthropogenic, biomass burning, urban and industrial sources. The medium values (close to 0.5) in the

pre-monsoon indicate a bimodal distribution of particles, and while the lowest values of  $\alpha'$  (close to 0.2) in monsoon season indicate a dominance by coarse mode particles.

The monthly mean variation of  $\tau_{0.50}$  and  $\beta$  is shown in Figure 5a. We found that  $\tau_{0.50}$  and  $\beta$  show a significant correlation ( $R^2 = 0.98$  and  $p\text{-value} = 4.6 \times 10^{-11}$ , scatter plot is not shown). This result shows that higher values of  $\beta$  correlating with  $\tau_{0.50}$  was associated with aerosol loading, mainly dominated by fine mode aerosols. In July and August (peak monsoon) of monsoon, we observed lowest  $\beta$  along with low  $\tau_{0.50}$ , and smallest values of  $\alpha' (\sim 1)$ , and  $\alpha'$  (smallest, closest to 0.2) supports the contribution of coarse mode particles compared to fine mode particles on overall AOD. The significantly low  $\tau_{0.50}$  in monsoon compared to other seasons is associated with significant rainfall in this season [25,44].

We also analyzed  $\alpha$  computed at different spectral bands, as shown in Figure 5b to identify the aerosol types. The difference in  $\alpha$  at spectral bands ( $\alpha_{(0.675-0.87)} - \alpha_{(0.34-0.38)}$ ) was significantly higher in post-monsoon and winter seasons, indicating a size distribution dominated by fine modes (Figure 5b). The difference lowers in months of pre-monsoon seasons, supporting the company of coarse mode as well. This difference is negative in the monsoon season, which indicated domination by coarse mode aerosols [17,19].

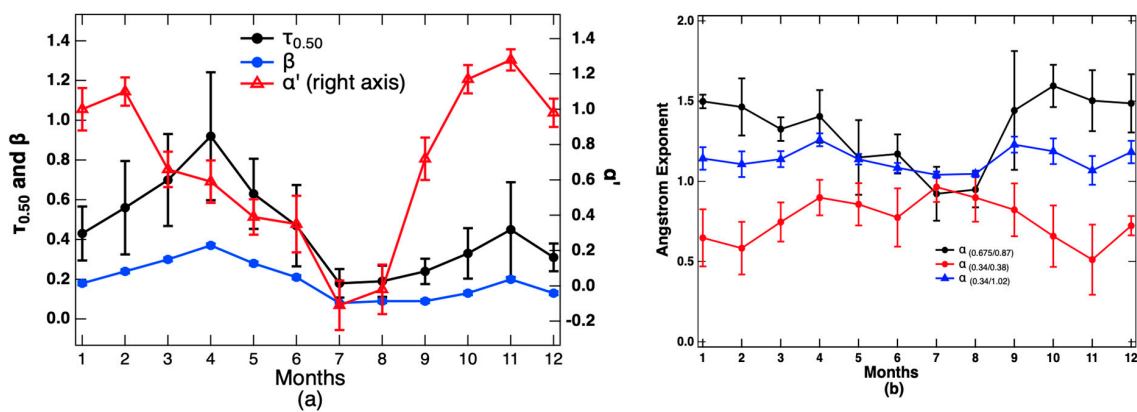


**Figure 5.** Time series of (a) Aerosol Optical Depth at 0.50  $\mu\text{m}$  and Ångström Turbidity Parameter  $\beta$  and curvature of the curve. (b) Ångström Exponent in different wavelength pairs.

The aspect of change in aerosol size spectrum, based on Angstrom parameters, is also examined by using aerosol volume size distribution data obtained from AERONET over Pokhara site. July to September data are not analyzed due to the limitation of availability of data in AERONET. Figure 6 shows the monthly mean of the aerosol volume size distribution for different seasons, along with  $\alpha'$  and  $\alpha$ , and reveals a bimodal structure of aerosol sizes for each month. It is observed from Figure 6 that the volume size distribution for the months are significantly dominated by accumulation mode of aerosols (with higher  $\alpha'$ ), both modes of aerosol sizes (with the medium  $\alpha'$ ), and coarse modes (with smaller  $\alpha'$ ). For this study, July to September volume size distribution data are not available for comparison.

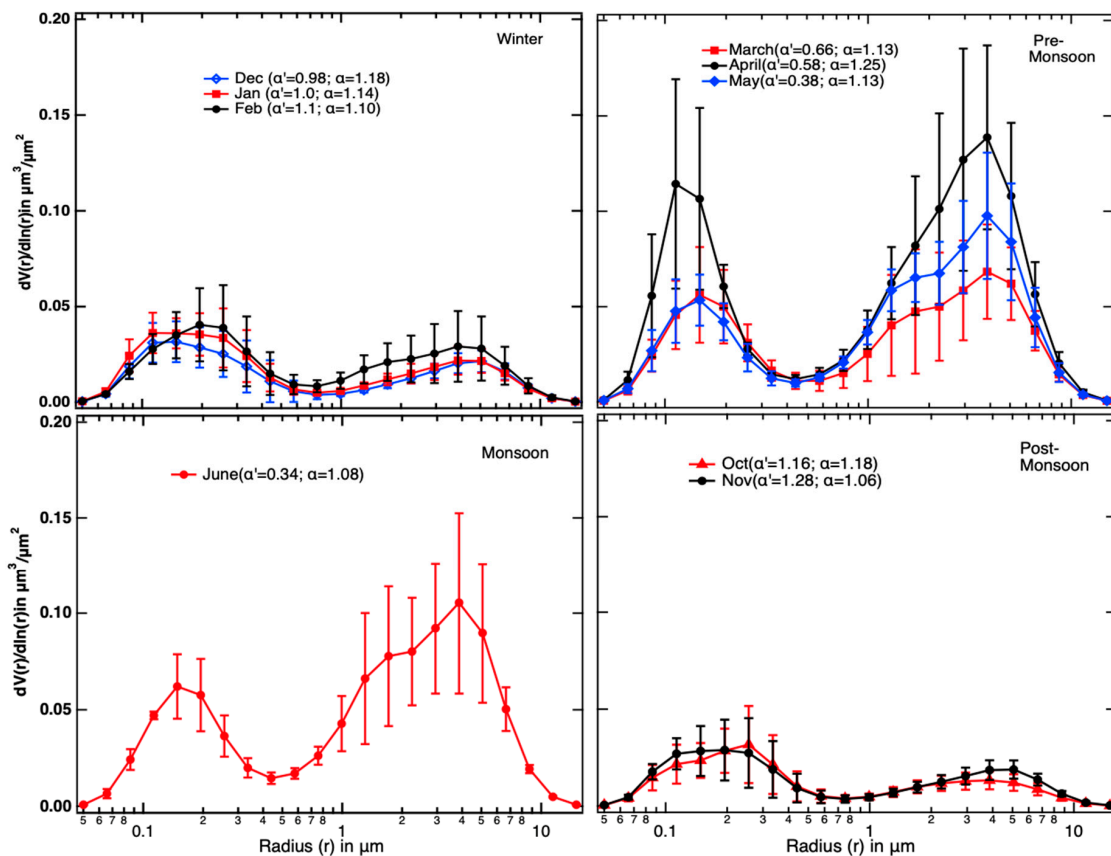


**Figure 6.** The monthly averaged columnar volume particle size distribution in the range of sizes  $0.05 \mu\text{m} \leq r \leq 15 \mu\text{m}$ , for different seasons, as indicated.

Figure 7 shows mean values of SSA and AAOD for five different months of winter and pre-monsoon season to study absorbing aerosols. These months are chosen because of the data availability in the AERONET site. SSA’s spectral variation, the top two figures, shows that SSA increases from 0.44 to  $0.675 \mu\text{m}$ , and then decreases at higher wavelengths. SSA values are found as 0.89 (January), 0.88 (February), 0.87 (March), 0.87 (April), and 0.87 (May) at wavelength  $0.44 \mu\text{m}$ , and indicate the presence of reasonably strong absorbing aerosol components. Figure 7, bottom two figures, shows AAOD spectra. Previous studies reported that SSA spectra of different AERONET locations with dust containing aerosols have increased SSA with increasing wavelength, while locations dominated by urban industrial or biomass burning decrease with increasing wavelength [2,4,45,46]. This trend was also used in the past studies to differentiate between carbonaceous aerosols and dust in different locations [2,10,47,48].

The behaviors of increasing of SSA spectra up to  $0.675 \mu\text{m}$  resemble aerosol components from dust aerosols, and decreasing from  $0.675 \mu\text{m}$  to  $1.02 \mu\text{m}$  shows similar to that of aerosol products of biomass burning, urban and industrial activities. Similar results can also be found in previous studies to define a mixed type of aerosols [45,46].

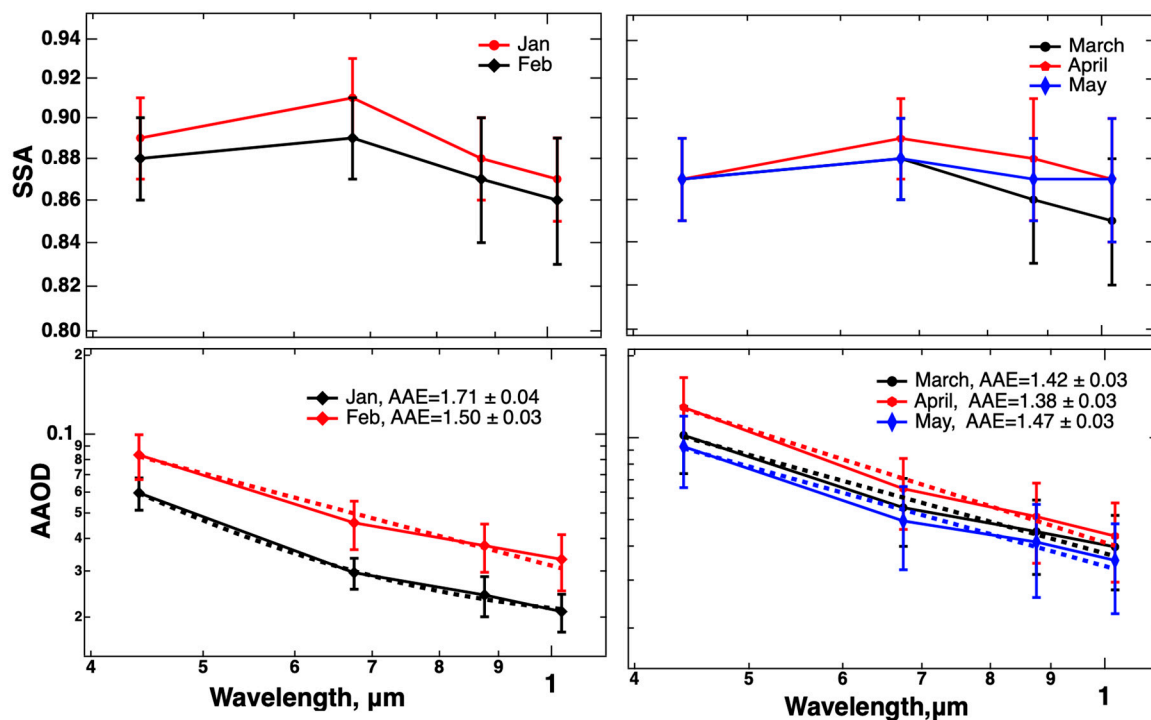
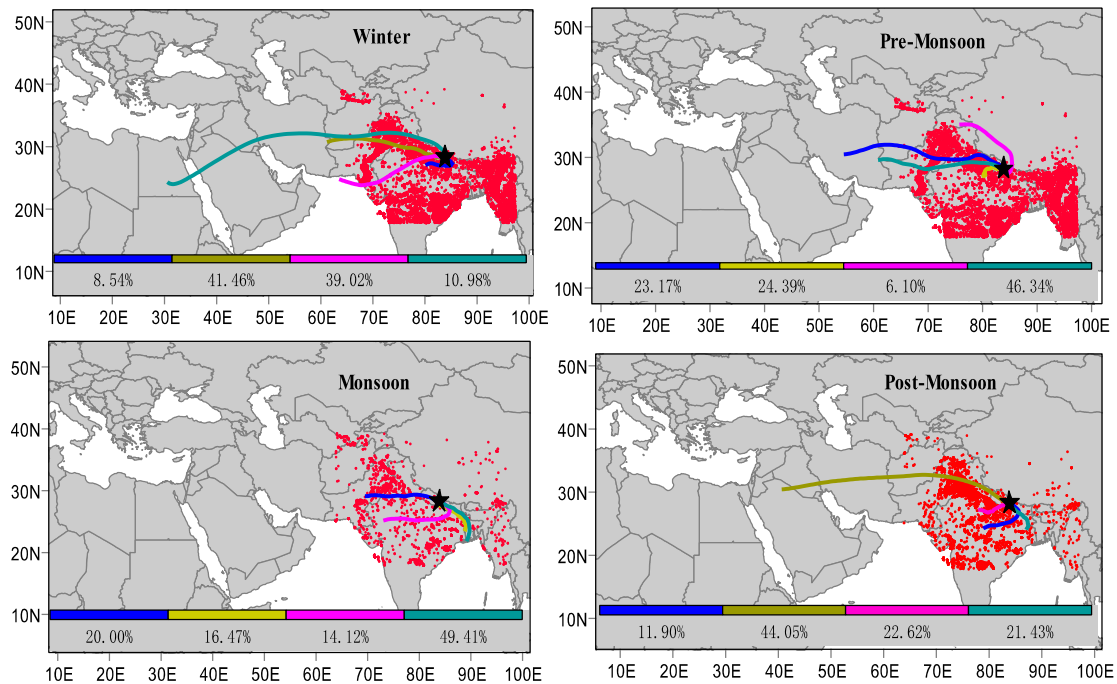


**Figure 7.** Monthly mean spectral SSA (**top two figures**), averaged within the months of the study period of years 2010–2018, from January to May, along with AOD (**bottom two figures**) in the logarithmic scale. The dotted lines are the linear fit of spectral AOD in the logarithmic scale.

The spectral dependence of AOD was also used to compute the absorption Ångström exponent (AAE), using a linear regression fit on the logarithmic scale plot [2,45,46]. AAE data were found for January ( $1.71 \pm 0.04$ ), February ( $1.50 \pm 0.03$ ), March ( $1.42 \pm 0.03$ ), April ( $1.38 \pm 0.03$ ) and May ( $1.47 \pm 0.03$ ), with ranges 1.38 to 1.71. Various studies have been done in the IGP region and different locations of AERONET to investigate the AAE based on types of aerosols [2,49–51]. These previous investigations have shown that AAE values vary from 1.2 to 3 for dust, 0.75 to 1.3 for urban and industrial aerosols, and 1.2 to 2 for biomass burning. Similarly, in different studies on the AERONET sites dominated by an optical mixture of smoke, dust, and industrial and urban pollution, have reported AAE in the ranges of 1.2 to 1.8 [52]. AAE observed in this study also lies in the range, indicating the absorbing behavior of aerosol components obtained in the mixed type of aerosols.

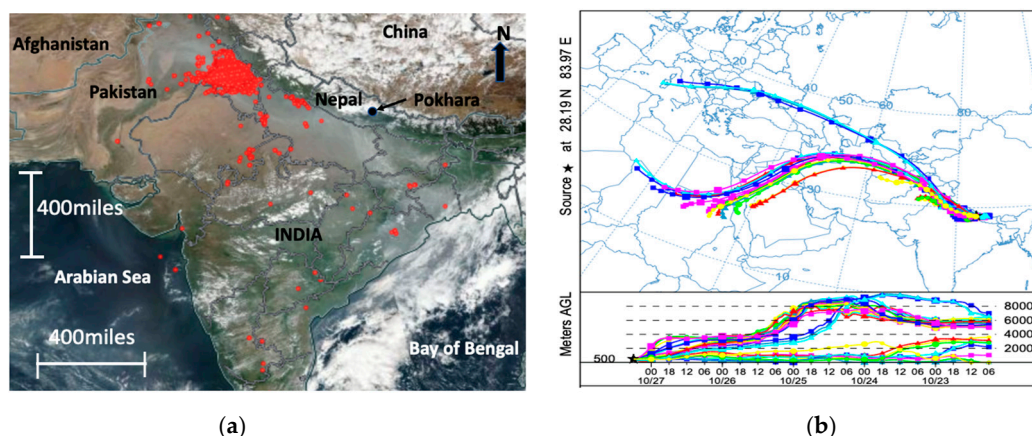
### 3.3. Investigation of Aerosol Sources and Types

Figure 8 shows the seasonal clusters of five days air mass back trajectories arriving at the observation site Pokhara at an altitude of 500 m and active fire spots (red dots) for 2017. The percentage contribution of each cluster is also shown in the figure for each season. The air masses reaching Pokhara valley follow two distinctive pathways from the Indo Gangetic Plain (IGP) region, during winter and pre-monsoon (Western Nepal, West India, and Pakistan), when the influence of strong western disturbances occur. During monsoon, majority of air masses arrived from the eastern IGP region and Bay of Bengal. Dense fire spots are observed during winter and pre-monsoon period over the region, which can enhance the emission of aerosols from biomass burning, that could be transported to Pokhara and influence the air quality and enhance AOD during that period [53]. In addition, during the post-monsoon, widespread crop residue burning occurs in the north-west part of India [54]. Comparatively few active fire spots are detected during the monsoon season, which might be due to cloud cover and heavy rainfall in South Asia, caused by moist air from the Arabian Sea and Bay of Bengal.



**Figure 8.** Clusters of five days air mass back trajectories computed with HYSPLIT model reaching Pokhara and at altitude 500 m and all active fire spots; each season is symbolized with red dots at different seasons (winter, pre-monsoon, monsoon and post-monsoon) of 2017. The percentage contributions of each cluster are shown in different colors.

It is evident from previous analyses of aerosol chemical composition over the Himalayan foothill in Nepal that the emission from crop-residue burning over the IGP has a significant impact on the air quality over the regions [24,28,46,55–59]. The cluster analysis of trajectories in this study also indicates the high likelihood that the aerosol population’s physical and optical properties over the Pokhara valley could be influenced significantly by the regional transport of air masses from polluted regions of South Asia. This could be further confirmed by looking at MODIS visible imagery, showing continuous aerosol haze layers extending up from the IGP into the Himalayan valleys (Figure 9a,b). The MODIS satellite image taken on 27 October 2017 reasonably shows emissions from biomass burning. The biomass burning smoke funnels through the densely populated and industrialized areas on IGP, and after mixing with anthropogenic pollution background, it comfortably transports to Nepal’s Pokhara valley, and is also suggested by the HYSPLIT back trajectory analysis (Figure 9b).



**Figure 9.** (a) The corrected reflectance true-color MODIS satellite image of the day 27 October 2017, shows intensive air pollution plumes over the IGP. (b) NOAA HYSPLIT MODEL Back Trajectories ending at 0600UTC on 27 October 2017. Horizontal and vertical scales of 400 miles on the left figure are shown.

#### 4. Conclusions

We have been able to study a cluster analysis of the aerosol climatology over Pokhara, an AERONET site located on a Himalayan foothill, based on long-term aerosol optical properties, size spectra and regional aerosol sources, and the long-range transport of aerosols over the observation site. The variation of AOD spectra and the magnitude of AOD are strongly associated with the change in seasons that brings different air masses over the observation site.

The maximum  $\tau_{0.50}$  in the pre-monsoon season ( $0.75 \pm 0.15$ ), followed by winter ( $0.43 \pm 0.12$ ), post-monsoon ( $0.39 \pm 0.08$ ), and monsoon ( $0.27 \pm 0.13$ ) seasons, show different aerosol loading, by a varying amount of wind-driven long-range transport of aerosols (mainly dust and aerosols from biomass burning, urban-industrial activities). The strong correlation between  $\tau_{0.50}$  and  $\beta$  also shows the association of seasonal aerosol loadings to influence the  $\tau_{0.50}$ . The air masses back trajectory and local and regional fire spots were supported, to investigate the effect of transboundary air pollution, from different sectors over Pokhara. We find that Pokhara receives dominating westerly air masses during the post-monsoon season, indicating a significant effect of biomass burning, such as crop residue burning over the northeast part of Pakistan. Both westerly and southwesterly air masses crossing over the Thar desert of India affect the area during the pre-monsoon and winter seasons. The pre-monsoon season (April and May) is mainly crop harvesting time, such as wheat, in the northwest area of Pakistan, and the smoke of burning crop residue easily diffuses to the atmosphere to be transported to Pokhara. The monsoon season is significantly associated with the transport of aerosols from the side of the Bay of Bengal. The trajectory analysis provides a unique background knowledge of aerosol components, which arrives over Pokhara by mixing with anthropogenic pollution background and natural aerosols, while passing over the heavily polluted IGP or coming from the IGP.

The study of spectral variation of AOD by using  $\alpha'$ , the first derivative of the angstrom exponent ( $\alpha$ ) with the wavelength in log scale distinguishes the aerosol size distribution, even with a similar value of  $\alpha$ . Furthermore,  $\alpha'$  is found to be more sensitive for months when there is a transition from one season to another. This investigation suggests that the analysis of  $\alpha'$  gives a more sensible complement of  $\alpha$  to characterize more fully wavelength dependence of AOD and the comparative influence of aerosol size spectra of two modes in aerosol loading. Intermediate AAE values range from 1.38 to 1.78, and the increasing and decreasing nature of SSA with wavelengths (analyzed only for winter and pre-monsoon seasons due to limitations of availability of data) proved beneficial for identifying the aerosols over Pokhara as a mixed type of aerosols, such as dust, aerosols from biomass burning and urban-industrial activities.

We consider the presented methodology as a useful tool for the calibration of aerosol optical properties, and advancing knowledge on aerosol climatology over the Himalaya region of Nepal.

**Author Contributions:** J.R. is the prime author of this paper and was involved in preparing the manuscript, data and graphical analysis. A.B. was responsible for analyzing aerosol data and supporting the preparation of the manuscript. A.P. (Arnico Panday), the Pokhara AERONET site's Principal Investigator, was responsible for the site's establishment of and also critically reviewed the manuscript. L.T. supported the cluster Analysis and fire spots. R.A., M.G., A.P. (Amod Pokhrel), and K.N.P. supported manuscript review and analyzing the results. All authors have read and agreed to the published version of the manuscript.

**Funding:** This research work has received no external funding.

**Acknowledgments:** Authors are thankful to AERONET group of NASA, USA for providing the online aerosol optical data. We are also thankful to the National Oceanic Atmospheric Administration Air Resources Laboratory (NOAA-ARL) for providing the HYSPLIT air mass back trajectories, and MODIS satellite fire spots data. The authors also thank Hotel Shangrila Village in Pokhara for providing space on the hotel roof for the AERONET station, and Gupta Giri for ongoing technical support. We are also thankful to the anonymous reviewers for their thoughtful comments and suggestions, which helped us improve the manuscript.

**Conflicts of Interest:** The authors declare no conflict of interest.

## References

1. Myhre, G.; Berglen, T.F.; Johnsrud, M.; Hoyle, C.R.; Berntsen, T.K.; Christopher, S.A.; Fahey, D.W.; Isaksen, I.S.A.; Jones, T.A.; Kahn, R.A.; et al. Modelled radiative forcing of the direct aerosol effect with multi-observation evaluation. *Atmos. Chem. Phys.* **2009**, *9*, 1365–1392. [[CrossRef](#)]
2. Bergstrom, R.W.; Pilewskie, P.; Russell, P.B.; Redemann, J.; Bond, T.C.; Quinn, P.K.; Sierau, B. Spectral absorption properties of atmospheric aerosols. *Atmos. Chem. Phys.* **2007**, *7*, 5937–5943. [[CrossRef](#)]
3. Russell, P.B.; Bergstrom, R.W.; Shinzuka, Y.; Clarke, A.D.; DeCarlo, P.F.; Jimenez, J.L.; Livingston, J.M.; Redemann, J.; Dubovik, O.; Strawa, A. Absorption Angstrom Exponent in AERONET and related data as an indicator of aerosol composition. *Atmos. Chem. Phys.* **2010**, *10*, 1155–1169. [[CrossRef](#)]
4. Li, C.; Chen, P.; Kang, S.; Yan, F.; Tripathi, L.; Wu, G.; Qu, B.; Sillanpää, M.; Yang, D.; Dittmar, T.; et al. Fossil fuel combustion emission from South Asia influences precipitation dissolved organic carbon reaching the remote Tibetan plateau: Isotopic and molecular evidence. *J. Geophys. Res. Atmos.* **2018**, *123*, 6248–6258. [[CrossRef](#)]
5. Dhungel, S.; Kathayat, B.; Mahata, K.; Panday, A. Transport of regional pollutants through a remote trans-Himalayan valley in Nepal. *Atmos. Chem. Phys.* **2018**, *18*, 1203–1216. [[CrossRef](#)]
6. Xu, B.; Cao, J.; Hansen, J.; Yao, T.; Joswita, D.R.; Wang, N.; Wu, G.; Wang, M.; Zhao, H.; Yang, W.; et al. Black soot and the survival of Tibetan glaciers. *Proc. Natl. Acad. Sci. USA* **2010**, *106*, 22114–22118. [[CrossRef](#)]
7. Li, C.; Bosch, C.; Kang, S.; Andersson, A.; Chen, P.; Zhang, Q.; Cong, Z.; Bing, C.; Qin, D.; Gustafsson, Ö. Sources of black carbon to the Himalayan–Tibetan Plateau glaciers. *Nat. Commun.* **2016**, *7*, 12574. [[CrossRef](#)]
8. Zhang, R.; Wang, H.; Qian, Y.; Rasch, P.J.; Easter, R.C.; Ma, P.L.; Singh, B.; Huang, J. Quantifying sources, transport, deposition, and radiative forcing of black carbon over the Himalayas and Tibetan Plateau. *Atmos. Chem. Phys.* **2015**, *15*, 77–121. [[CrossRef](#)]
9. Singh, A.; Mahata, K.S.; Rupakheti, M.; Junkermann, W.; Panday, A.K. An overview of airborne measurement in Nepal—Part 1: Vertical profile of aerosol size, number, spectral absorption, and meteorology. *Atmos. Chem. Phys.* **2019**, *19*, 245–258. [[CrossRef](#)]
10. Kaskaoutis, D.G.; Sifakis, N.; Retalis, A.; Kambezidis, H.D. Aerosol monitoring over Athens using satellite and ground-based measurements. *Adv. Meteorol.* **2010**, *12*. [[CrossRef](#)]
11. Aryal, R.P.; Voss, K.J.; Terman, P.A.; Keene, W.C.; Moody, J.L.; Welton, E.J.; Holben, B.N. Comparison of surface and column measurements of aerosol scattering properties over the western North Atlantic Ocean at Bermuda. *Atmos. Chem. Phys.* **2014**, *14*, 7617–7629. [[CrossRef](#)]
12. Holben, B.; Eck, T.; Slutsker, I.; Tanre, D.; Buis, J.; Setzer, A.; Vermote, E.; Reagan, J.; Kaufman, Y.; Nakajima, T.; et al. AERONET—A federated instrument network and data archive for aerosol characterization. *Remote Sens. Environ.* **1998**, *66*, 1–16. [[CrossRef](#)]
13. Stein, A.F.; Draxler, R.R.; Rolph, G.D.; Stunder, B.J.B.; Cohen, M.D.; Ngan, F. NOAA's HYSPLIT atmospheric transport and dispersion modeling system. *Bull. Am. Meteor. Soc.* **2015**, *96*, 2059–2077. [[CrossRef](#)]

14. Holben, B.; Tanre, D.; Smirnov, A.; Eck, T.; Slutsker, I.; Abuhassan, N.; Newcomb, W.; Schafer, J.; Chatenet, B.; Lavenu, F.; et al. An emerging ground-based aerosol climatology: Aerosol optical depth from AERONET. *J. Geophys. Res.* **2001**, *106*, 12067–12097. [[CrossRef](#)]
15. AERONET. Available online: <http://aeronet.gsfc.nasa.gov/> (accessed on 1 April 2015).
16. Dubovik, O.; King, M.A. Flexible inversion algorithm for retrieval of aerosol optical properties from sun and sky radiance measurements. *J. Geophys. Res.* **2000**, *105*, 20673–20696. [[CrossRef](#)]
17. Eck, T.F.; Holben, B.N.; Reid, J.S.; Dubovik, O.; Smirnov, A.; O’Neill, N.T.; Slutsker, I.; Kinne, S. Wavelength Dependence of the Optical Depth of Bio Mass Burning, Urban, and Desert Dust Aerosols. *J. Geophys. Res.* **1999**, *104*, 31333–31349. [[CrossRef](#)]
18. Schuster, G.L.; Dubovik, O.; Holben, B.N. Ångström exponent and bimodal aerosol size distributions. *J. Geophys. Res. Atmos.* **2006**, *111*, 1–14. [[CrossRef](#)]
19. Kaskaoutis, D.G.; Kambezidis, H.D.; Hatzianastassiou, N.; Kosmopoulos, P.G.; Badarinath, K.V.S. Aerosol climatology: Dependence of the Angstrom exponent on wavelength over four AERONET sites. *Atmos. Chem. Phys. Discuss.* **2007**, *7*, 7347–7397. [[CrossRef](#)]
20. Holben, B.; Eck, T.; Slutsker, I.; Smirnov, A.; Schafer, J.; Giles, D.; Dubovik, O. AERONET’s Version 2.0 quality assurance criteria. *Proc. SPIE* **2006**, *6408*, 64080Q.
21. Giles, D.M.; Sinyuk, M.S.; Sorokin, J.S.; Schafer, A.; Smirnov, I.; Slutsker, T.F.; Eck, B.N.; Holben, J.R.; Lewis, J.R.; Campbell, E.J.; et al. Advancements in the Aerosol Robotic Network (AERONET) Version 3 database—automated near real-time quality control algorithm with improved cloud screening for Sun photometer aerosol optical depth measurements. *Atmos. Meas. Tech.* **2019**, *12*, 169–209. [[CrossRef](#)]
22. HYSPLIT. Available online: [https://www.ready.noaa.gov/HYSPLIT\\_traj.php/](https://www.ready.noaa.gov/HYSPLIT_traj.php/) (accessed on 2 April 2020).
23. Kim, S.W.; Yoon, S.C.; Kim, J.; Kim, S.Y. Seasonal and monthly variations of columnar aerosol optical properties over East Asia determined from multi-year MODIS, LiDAR, and AERONET sun/sky radiometer measurements. *Atmos. Environ.* **2007**, *41*, 1634–1651. [[CrossRef](#)]
24. Tripathi, L.; Kang, S.C.; Rupakheti, D.; Zhang, Q.G.; Huang, J.; Sillanpää, M. Water-soluble ionic composition of aerosols at urban location in the foothills of Himalaya, Pokhara Valley, Nepal. *Atmosphere* **2016**, *7*, 102. [[CrossRef](#)]
25. Bhattarai, B.C.; Burkhart, J.F.; Stordal, F.; Xu, C.-Y. Aerosol Optical Depth Over the Nepalese Cryosphere Derived from an Empirical Model. *Front. Earth Sci.* **2019**, *7*, 178. [[CrossRef](#)]
26. Xu, C.; Ma, Y.M.; Pandey, A.; Cong, Z.Y.; Yang, K.; Zhu, Z.K.; Wang, J.M.; Amatya, P.M.; Zhao, L. Similarities and differences of aerosol optical properties between southern and northern slopes of the Himalayas. *Atmos. Chem. Phys.* **2014**, *14*, 3133–3149. [[CrossRef](#)]
27. Ranabhat, C.L.; Kim, C.-B.; Kim, C.-S.; Jha, N.; Deepak, K.C.; Connel, F.A. Consequence of indoor air pollution in rural area of Nepal: A simplified measurement approach. *Front. Public Health* **2015**, *3*, 5. [[CrossRef](#)]
28. Wan, X.; Kang, S.; Li, Q.; Rupakheti, D.; Zhang, Q.; Guo, J.; Chen, P.; Tripathi, L.; Rupakheti, M.; Panday, A.K.; et al. Organic molecular tracers in the atmospheric aerosols from Lumbini, Nepal, in the northern Indo-Gangetic Plain: Influence of biomass burning. *Atmos. Chem. Phys.* **2017**, *17*, 8867–8885. [[CrossRef](#)]
29. Gautam, R.; Hsu, N.C.; Lau, K.M. Premonsoon aerosol characterization and radiative effects over the Indo-Gangetic Plains: Implications for regional climate warming. *J. Geophys. Res.* **2010**, *115*, 1383–1392. [[CrossRef](#)]
30. Kumar, M.; Parmar, K.S.; Kumar, D.B.; Mhawish, A.; Broday, D.M.; Mall, R.K.; Banerjee, T. Long-term aerosol climatology over Indo-Gangetic Plain: Trend, prediction and potential source fields. *Atmos Environ.* **2018**, *180*, 37–50. [[CrossRef](#)]
31. National Population and Housing Census 2011. Available online: <https://unstats.un.org/unsd/demographic-social/census/documents/Nepal/Nepal-Census-2011-Vol1.pdf> (accessed on 10 August 2020).
32. Poudyal, K.N.; Bhattarai, B.K.; Sapkota, B.K.; Kjeldstad, B.; Karki, N.R. Estimation of Global Solar Radiation using Pyranometer and NILU-UV Irradiance Meter at Pokhara Valley in Nepal. *J. Inst. Eng.* **2014**, *9*, 69–78. [[CrossRef](#)]
33. Home. Available online: <https://www.pinterest.com/pin/259238522278164839/> (accessed on 12 August 2020).
34. Ångström, A. Techniques of Determining the Turbidity of the Atmosphere. *Tellus B* **1961**, 214–223. [[CrossRef](#)]



35. Gyawali, M.; Arnott, W.P.; Lewis, K.; Moosmüller, H. In situ aerosol optics in Reno, NV, 5 USA during and after the summer 2008 California wildfires and the influence of absorbing and non-absorbing organic coatings on spectral light absorption. *Atmos. Chem. Phys.* **2009**, *9*, 8007–8015. [[CrossRef](#)]
36. Wang, Y. MeteoInfo: GIS software for meteorological data visualization and analysis. *Meteorol. Appl.* **2014**, *21*, 360–368. [[CrossRef](#)]
37. Morton, D.C.; Defries, R.S.; Randerson, J.T.; Giglio, L.; Schroeder, W.; van der Werf, G.R. Agricultural intensification increases deforestation fire activity in Amazonia. *Glob. Chang. Biol.* **2008**, *14*, 2262–2275. [[CrossRef](#)]
38. Zhang, X.; Kondragunta, S.; Ram, J.; Schmidt, C.; Huang, H.C. Near real time global biomass burning emissions product from geostationary satellite constellation. *Geophys. Res. Atmos.* **2012**, *117*. [[CrossRef](#)]
39. Li, J.; Li, X.; Carlson, B.E.; Kahn, R.A.; Laci, A.A.; Dubovik, O.; Nakajima, T. Reducing multi-sensor satellite monthly mean aerosol optical depth uncertainty, Part I: Objective assessment of current AERONET locations. *J. Geophys. Res. Atmos.* **2016**, *121*, 13609–13626. [[CrossRef](#)]
40. Government of Nepal, Ministry of Energy, Water Resources and Irrigation. Available online: <https://www.dhm.gov.np/climate/> (accessed on 10 July 2020).
41. Herrmann, H.; Schaefer, T.; Tilgner, A.; Styler, S.A.; Weller, C.; Teich, M.; Otto, T. Tropospheric aqueous-phase chemistry: Kinetics, mechanisms, and its coupling to a changing gas phase. *Chem. Rev.* **2015**, *115*, 4259–4334. [[CrossRef](#)]
42. Altaratz, O.R.; Bar-Or, Z.; Wollner, U.; Koren, I. Relative humidity and its effect on aerosol optical depth in the vicinity of convective clouds. *Environ. Res. Lett.* **2013**, *8*, 034025. [[CrossRef](#)]
43. Dumka, U.C.; Tripathi, S.N.; Misra, A.; Giles, D.M.; Eck, T.F.; Sagar, R.; Holben, B.N. Latitudinal variation of aerosol properties from Indo-Gangetic Plain to central Himalayan foothills during TIGERZ campaign. *J. Geophys. Res.* **2014**, *119*, 4750–4769. [[CrossRef](#)]
44. Sigdel, M.; Ikeda, M. Summer Monsoon Rainfall over Nepal Related with Large-Scale Atmospheric Circulations. *J. Earth Sci Climate Change* **2012**, *3*, 112. [[CrossRef](#)]
45. Li, J.; Carlson, B.E.; Laci, A.A. Using Single Scattering Albedo Spectral Curvature to Characterize East Asian Aerosol Mixtures. *J. Geophys. Res. Atmos.* **2015**, *120*, 2037–2052. [[CrossRef](#)]
46. Mallet, M.; Dubovik, O.; Nabat, P.; Dulac, F.; Kahn, R.; Sciare, J.; Paronis, D.; Léon, J.F. Absorption properties of Mediterranean aerosols obtained from multi-year ground-based remote sensing observations. *Atmos. Chem. Phys.* **2013**, *13*, 9195–9210. [[CrossRef](#)]
47. Collaud Coen, M.; Weingartner, E.; Schaub, D.; Hueglin, C.; Corrigan, C.; Henning, S.; Schwikowski, M.; Baltensperger, U. Saharan dust events at the jungfrauoch: Detection by wavelength dependence of the single scattering albedo and first climatology analysis. *Atmos. Chem. Phys.* **2004**, *4*, 2465–2480. [[CrossRef](#)]
48. Meloni, D.; di Sarra, A.; Pace, G.; Monteleone, F. Aerosol optical properties at Lampedusa (Central Mediterranean). 2. Determination of single scattering albedo at two wavelengths for different aerosol types. *Atmos. Chem. Phys.* **2006**, *6*, 715–727. [[CrossRef](#)]
49. Srivastava, A.K.; Tripathi, S.N.; Dey, S.; Kanawade, V.P.; Tiwari, S. Inferring Aerosol Types over the Indo-Gangetic Basin from Ground Based Sunphotometer Measurements. *Atmos. Res.* **2012**, *109–110*, 64–75. [[CrossRef](#)]
50. Giles, D.; Holben, B.; Tripathi, S.; Eck, T.; Newcomb, W.; Slutsker, I.; Dickerson, R.; Thomsson, A.; Mattoo, S.; Wang, S.H.; et al. Aerosol properties over the Indo-Gangetic Plain: A mesoscale perspective from the TIGERZ experiment. *J. Geophys. Res.* **2011**, *11*. [[CrossRef](#)]
51. Moody, J.L.; Keene, W.C.; Cooper, O.R.; Voss, K.J.; Aryal, R.; Eckhardt, S.; Holben, B.; Maben, J.R.; Izaguirre, M.A.; Galloway, J.N. Flow climatology for physicochemical properties of dichotomous aerosol over the western North Atlantic Ocean at Bermuda. *Atmos. Chem. Phys.* **2014**, *14*, 691–717. [[CrossRef](#)]
52. Eck, T.F.; Holben, B.N.; Sinyuk, A.; Pinker, R.T.; Goloub, P.; Chen, H.; Chatenet, B.; Li, Z.; Singh, R.P.; Tripathi, S.N. Optical properties of fine/coarse mode aerosol mixtures. *J. Geophys. Res. Atmos.* **2010**, *115*, 5548–5554. [[CrossRef](#)]
53. Kaskaoutis, D.G.; Kumar, S.; Sharma, D.; Singh, R.P.; Kharol, S.K.; Sharma, M.; Singh, A.K.; Singh, S.; Singh, A.; Singh, D. Effects of crop residue burning on aerosol properties, plume characteristics, and long-range transport over northern India. *J. Geophys. Res. Atmos.* **2013**, *119*, 5424–5444. [[CrossRef](#)]

54. Guo, J.; Ram, K.; Tripathee, L.; Kang, S.; Huang, J.; Chen, P.; Ghimire, P.S. Study on Mercury in PM10 at an Urban Site in the Central Indo-Gangetic Plain: Seasonal Variability and Influencing Factors. *Aerosol Air Qual. Res.* **2020**, in press. [[CrossRef](#)]
55. Rupakheti, D.; Kang, S.; Rupakheti, M.; Cong, Z.; Tripathee, L.; Panday, A.K.; Holben, B.N. Observation of optical properties and sources of aerosols at Buddha's birthplace, Lumbini, Nepal: Environmental implications. *Environ. Sci. Pollut. Res. Int.* **2018**, *25*, 14868–14881. [[CrossRef](#)]
56. Kulshrestha, U.; Kumar, B. Airmass Trajectories and Long Range Transport of Pollutants: Review of Wet Deposition Scenario in South Asia. *Adv. Meteorol.* **2014**, *2014*, 596041. [[CrossRef](#)]
57. Tripathee, L.; Guo, J.; Kang, S.; Paudyal, R.; Huang, J.; Sharma, C.M.; Zhang, Q.; Chen, P.; Ghimire, P.S.; Sigdel, M. Spatial and temporal distribution of total mercury in atmospheric wet precipitation at four sites from the Nepal-Himalayas. *Sci. Total Environ.* **2019**, *655*, 1207–1217. [[CrossRef](#)] [[PubMed](#)]
58. Gautam, R.; Hsu, N.C.; Tsay, S.C.; Lau, K.M.; Holben, B.; Bell, S.; Smirnov, A.; Li, C.; Hansell, R.; Ji, Q.; et al. Accumulation of aerosols over the Indo-Gangetic plains and southern slopes of the Himalayas: Distribution, properties and radiative effects during the 2009 pre-monsoon season. *Atmos. Chem. Phys.* **2011**, *11*, 12841–12863. [[CrossRef](#)]
59. Tripathee, L.; Kang, S.; Rupakheti, D.; Cong, Z.; Zhang, Q.; Huang, J. Chemical characteristics of soluble aerosols over the central Himalayas: Insights into spatiotemporal variations and sources. *Environ. Sci. Pollut. Res.* **2017**, *24*, 24454–24472. [[CrossRef](#)]



© 2020 by the authors. Licensee MDPI, Basel, Switzerland. This article is an open access article distributed under the terms and conditions of the Creative Commons Attribution (CC BY) license (<http://creativecommons.org/licenses/by/4.0/>).

# BIBECHANA

ISSN 2091-0762 (Print), 2382-5340 (Online)

Journal homepage: <http://nepjol.info/index.php/BIBECHANA>

Publisher: Department of Physics, Mahendra Morang A.M. Campus, TU, Biratnagar, Nepal

## Analysis of Aerosol Optical Depth and Angstrom Exponents over an AERONET site at Pokhara, Nepal

Jeevan Regmi<sup>1\*</sup>, Khem N Poudyal<sup>2</sup>, Amod Pokhrel<sup>3</sup>, Madhu Gyawali<sup>4</sup>, Anthony Barinelli<sup>5</sup>, Rudra Aryal<sup>5</sup>

<sup>1</sup>Central Department of Physics, Tribhuvan University Kirtipur, Nepal

<sup>2</sup>Dept. of Applied Sciences, Institute of Engineering Tribhuvan University, Lalitpur, Nepal

<sup>3</sup>University of California Berkeley, California, USA

<sup>4</sup>San Jacinto College, South Campus, 13735 Beamer Rd, Houston, TX 77089

Franklin Pierce University, 40 University Drive, Rindge, NH, USA

\*Email: [jsregmi28@gmail.com](mailto:jsregmi28@gmail.com)

### Article Information:

Received: June 14, 2020

Accepted: July 27, 2020

### Keywords:

Aerosol

Aerosol optical depth

Angstrom exponent

Monthly variations

### ABSTRACT

The monthly variability of Aerosol Optical Depth at 0.50  $\mu\text{m}$  ( $\text{AOD}_{0.50}$ ) and Ångström exponents (AE) based on spectral AODs over an Aerosol Robotic Network (AERONET) site Pokhara, are analyzed by using aerosol data of the year 2017. The  $\text{AOD}_{0.50}$  are characterized by low average values ( $0.21 \pm 0.12$ ) in monsoon, and highest values in pre- monsoon ( $0.67 \pm 0.14$ ) followed by winter ( $0.46 \pm 0.28$ ) and post- monsoon ( $0.33 \pm 0.02$ ) with an overall mean of  $0.43 \pm 0.02$ . The average AE obtained by using AODs at 0.44  $\mu\text{m}$  and 0.87  $\mu\text{m}$  are  $1.20 \pm 0.04$  in pre- monsoon,  $1.37 \pm 0.05$  in monsoon,  $1.41 \pm 0.01$  in post- monsoon, and  $1.37 \pm 0.07$  in winter with an annual average value of  $1.35 \pm 0.08$ . These overall variations of AE indicate that the majority of aerosol loading during the study period was mixture of fine and coarse mode aerosols and the influence of anthropogenic aerosols. The monthly average AOD suggest low aerosol loading in the months of the monsoon season (June to September) than other months of pre-monsoon season (March to May) and post-monsoon season (October and November).

DOI: <https://doi.org/10.3126/bibechana.v18i1.29448>

This work is licensed under the Creative Commons CC BY-NC License. <https://creativecommons.org/licenses/by-nc/4.0/>

## 1. Introduction

Aerosols are fine solid or liquid particles suspended in the atmosphere, which are embedded by

anthropogenic and natural processes, have a strong contribution to perturb the overall solar radiative forcing [1-3]. Hence, the sources, nature of aerosols, and its climatic impact are a topic of

significant interest in the climate. Commonly known natural aerosols are dust, sea salt, forest exudates, while anthropogenic aerosols are particulate air pollutants produced from human activities [4]. The importance of studying and measurement of aerosol physical, optical, and chemical properties have increased dramatically since the last few decades as aerosol loading is significantly growing due to urbanization and industrialization, high population density, or biomass burning.

The atmosphere over the urban areas contains a concentration of particles with diameters from a few nanometers to around 100 micrometers produced mainly from a combination of primary particulate emissions from transportations, industries, power generation, and natural sources, and gases to particles conversion [5, 6]. Aerosol particles from combustion sources, such as automobiles, wood burning, and power generation, can be small and are considered up to the size range of 1 micrometer ( $\mu\text{m}$ ). The variability of climate is associated directly with aerosols by scattering and absorbing solar radiation and indirectly by modifying cloud properties [7]. Most of the aerosols are scattering type and cause a cooling effect but some aerosols like black carbon, mineral dust and few organic carbons are absorber of radiation which causes warming effect in the atmosphere [8]. The aerosol produced by human activities has also contributed significantly to climate change [9, 10]. The analysis of aerosol optical properties along with meteorological parameters such as precipitation, relative humidity will give a picture of aerosol types over the aerosol observation sites [11-13]. Ground-based measurement and analysis of aerosol optical properties are important for the quantitative measure of the extinction of solar radiation by aerosol scattering and absorption. Since the last two decades, the direct measurement of aerosol optical properties from ground-based is increasing worldwide. The Aerosol Robotic Network (AERONET) is one of the network which provides

long-term aerosol optical data in many different areas of the world, and it has also established in Pokhara. This site is one of the fast urbanizing cities of Nepal with a lot of construction works, growing industrialization and rapid increase in population[14][2]. It causes to deposit anthropogenic aerosols in the atmosphere which requires a systematic, continuous and long term analysis of physical and chemical properties[15]. But there are very few studies in this region to address the impact of aerosol on climate change, crop productivity, visibility and human health. This work provides an overview of aerosol type by the analysis of Aerosol Optical Depth (AOD) and Angstrom Exponents (AE). A number of previous studies have classified aerosol types from ground based observations and remote sensing from satellites[16,17]. The spectral variation of AOD which can be characterized by Angstrom's parameters gives an idea of particle size and aerosol loading in the atmosphere [18, 19].

### 1.1 Theoretical background

The aerosol characteristics are commonly determined by using the Angstrom's parameters,  $\alpha$  and  $\beta$  [20] and are related to AOD as;

$$\tau(\lambda) = \beta\lambda^{-\alpha} \quad (1)$$

where  $\alpha$  is the wavelength exponent that represents columnar aerosol size distribution in the atmosphere and used as a qualitative indicator of aerosol particle size and chemical composition. Angstrom exponent values greater than 2 indicate small particles associated with combustion byproducts, and values less than 1 indicate large particles [21, 22] like sea salt and soil dust. The detection of high values of  $\alpha$  is always associated with the small anthropogenic particles [23].  $\beta$  is the turbidity coefficient that shows the aerosol number concentration in the vertical column of the atmosphere. The value of  $\beta$  generally varies from 0.0 to 0.5. The atmosphere is clean when  $\beta$  is less than 0.1 and turbid when it is greater than this.  $\alpha$  at wavelengths 0.34, 0.38, 0.44, 0.5, 0.67, 0.87, and 1.02  $\mu\text{m}$  are sensitive to the volume fraction of

aerosols with radii less than 0.6  $\mu\text{m}$  but not to the fine mode effective radius. Long wavelengths 0.67  $\mu\text{m}$  and, 0.87  $\mu\text{m}$  are sensitive to fine mode volume fraction of aerosols, but not fine mode effective radius, while short wavelengths 0.38  $\mu\text{m}$  and, 0.44  $\mu\text{m}$  are sensitive to the fine mode effective radius but not the fine mode volume fraction [24].

At a wavelength,  $\lambda = 1 \mu\text{m}$ , we have  $\tau(\lambda) = \beta$ , which is related to the aerosol column burden.

The linear equation in logarithmic format is given by

$$\ln \tau(\lambda) = \ln \beta - \alpha \ln \lambda \quad (2)$$

Equation 2 gives the values of Angstrom's parameters  $\alpha$  and  $\beta$  by least square analysis.

## 2. Experiments and Discussion

### Research Site and Instrumentation

The observation site Pokhara is one of the important geophysical cities and an important tourist destination of Nepal. It is situated at an altitude of 800.0 m above the sea level and about 200 km, by road, west of the capital city, Kathmandu. The valley is surrounded by hills about 1000-2000 m high. The elevation rises from 800.0 m to over 7500.0 m over an aerial span of 25.0 km. Pokhara is the region of highest precipitation rates in the country (3350 mm/year to 5000 mm/year). Due to this sharp rise in altitude, the climate of the city is sub-tropical; however, the elevation keeps the temperatures moderate [25]. Summers are humid and mild, and most precipitation occurs during the monsoon season (July - September), winter and spring skies are generally clear and sunny. The mixing of dry westerly air masses with heated moist air masses from the Bay of Bengal produces strong convection over the Pokhara Valley, and thus results in strong updrafts. These strong convective activities are frequent in the pre-monsoon and monsoon seasons but do not occur during the winter season [26].

AEROSOL ROBOTIC NETWORK (AERONET), a federation of ground-based remote sensing aerosol networks established by NASA and PHOTONS, site in Pokhara is situated on the rooftop of hotel Sangrila, which is near to Pokhara Airport and uses ([https://aeronet.gsfc.nasa.gov/cgi-bin/draw\\_map\\_display\\_inv\\_v3](https://aeronet.gsfc.nasa.gov/cgi-bin/draw_map_display_inv_v3)).CIMEL

Sunphotometer, which is a ground-based device to measure vertical profiles, as shown in the figure 1.



**Fig. 1:** Map of Nepal showing the location of Pokhara (Red icon) (obtained from <https://www.google.com/url: nepalforeignaffairs.com>). The Sunphotometer used for the study is shown in inset. (Photo: Arnico Panday)

CIMEL sun and sky radiometer operate in two modes, direct sun measurements at 0.34  $\mu\text{m}$ , 0.38  $\mu\text{m}$ , 0.44  $\mu\text{m}$ , 0.50  $\mu\text{m}$ , 0.675  $\mu\text{m}$ , 0.87  $\mu\text{m}$ , 1.02  $\mu\text{m}$ , 1.64  $\mu\text{m}$  wavelengths and sky measurements at 0.44  $\mu\text{m}$ , 0.675  $\mu\text{m}$ , 0.87  $\mu\text{m}$ , 1.02  $\mu\text{m}$  [3, 26]. This radiometer makes direct Sun measurements with a 1.2° full field of view every 15 min. These solar extinction measurements were used to compute aerosol optical depth (AOD), which were automatically computed by using software and are available in the AERONET website. 0.94  $\mu\text{m}$  channel is used to retrieve total precipitable water in centimeters. A study has reported the estimated uncertainty in computed AOD approximately  $\pm 0.01$  to  $\pm 0.02$ , which is spectrally dependent with higher errors in the UV region [12]. These data are available on the AERONET website, and since now, we name it as AERONET data. Level 2

AERONET aerosol optical data are cloud-screened and are used in this study. Since the data are cloud screened and quality assured, data will not be available during cloudy days and when the sensor is wet. For this reason it is very difficult to obtain data during monsoon season.

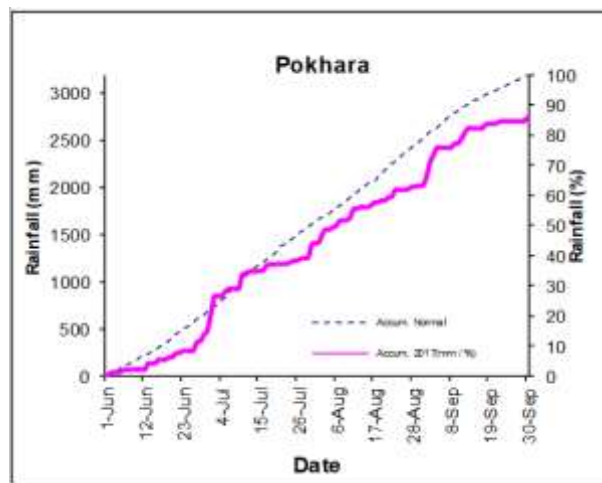


**Fig. 2:** Accumulated Rainfall during Monsoon 2017 as monitored by DHM, Nepal. The plot is retrieved from website of DHM weather on 7/21/2020.

[http://www.dhm.gov.np/uploads/getforecast/1797220298sep%202017\\_final.docx](http://www.dhm.gov.np/uploads/getforecast/1797220298sep%202017_final.docx)

As reported by DHM Nepal, the average rainfall during monsoon season (June, July, August and September) are 670 mm, 932.5 mm, 767 mm and 714.2 mm respectively. The average maximum and minimum temperature during the monsoon season were 30.97 and 22.57 respectively. The annual rainfall in the year 2017 was 3743.3 mm. It means a significant amount of rainfall takes place in the monsoon season that can easily flush out larger aerosol particles from the atmosphere causing a larger drop in the value of AOD.

Angstrom exponents, which were obtained by two pairs of wavelengths 0.44  $\mu\text{m}$  and 0.87  $\mu\text{m}$  are analyzed. Daily averaged aerosol optical depth at 0.50  $\mu\text{m}$ ,  $\text{AOD}_{0.50}$  and angstrom exponents based on wavelengths ranges, 0.40  $\mu\text{m}$  to 0.87  $\mu\text{m}$  are

downloaded from AERONET Pokhara site and analyzed for different months.

### 3. Results

#### 3.1. Variability of $\text{AOD}_{0.50}$ , AE coefficients and Precipitable Water

The time series of daily averaged aerosol optical properties, namely AOD at 0.50  $\mu\text{m}$  ( $\text{AOD}_{0.50}$ ), calculated Ångström exponents (AE) in a broadband (0.44  $\mu\text{m}$ -0.87 $\mu\text{m}$ ) and precipitable water (PW) in cm, from January to December of 2017 are presented in figure 2 (a, b and c). The monthly averages of  $\text{AOD}_{0.50}$ , AE, and PW (in cm) along with monthly standard deviation are presented in Table 1. It shows that aerosol loading is strong in the months from March to May with significant fine particles. Angstrom exponent data indicate the approximation of the dominant size of fine particles in aerosol loading in all seasons. For our general reference we considered the threshold value of AOD and AE for nearby region (Delhi) for anthropogenic, mixed type, biomass burning and dust were taken as 0.3-1.3 and  $> 0.9$ , 0.4-0.7 and  $< 0.9$ ,  $> 1.3$  and  $> 0.8$ , and  $> 0.7$  and  $< 0.6$  respectively [27,28]. The significant standard deviation in the AOD and AE represents for the different types of particulate components loading into the atmosphere [19, 29]. As expected in the monsoon period (June to September), the air is clean with low and stable AOD. In the rainy season, in which we find a large amount of PW in the atmosphere (Table 1), the monsoon period, the reduced values of AOD may have been caused by differences in the production and flushing of aerosol from the atmosphere due to rain between dry and rainy seasons.

Both AOD and AE exhibit a distinct seasonal trend, mainly in the months of pre and post- monsoon seasons. From the end of winter towards pre-monsoon season (March to May), the AOD has an increasing trend and may be mainly due to the buildup of anthropogenic aerosols, burning of crop residue such as wheat in the regions as this season is the time of harvesting. PW is an essential

parameter of the atmosphere for the overall climate change. Monthly mean values, along with standard deviations (Table 1), show that PW is decreasing from post- monsoon seasons to the early stage of pre-monsoon.

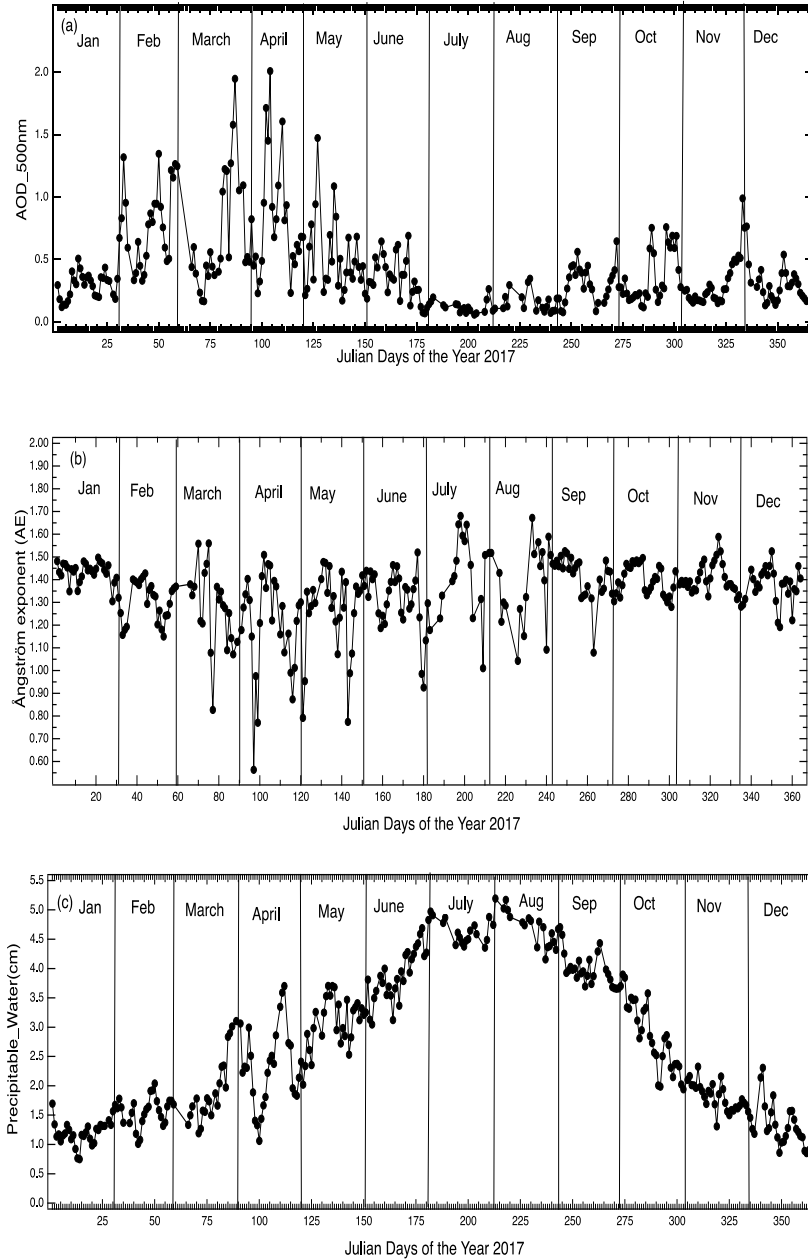


**Fig. 2:** Time series of daily averaged columnar (a) AOD values at a wavelength 500 nm ( $0.50 \mu\text{m}$ ),  $\text{AOD}_{0.50}$ (b) Ångström exponent (AE) with broad band  $0.44 \mu\text{m} / 0.87 \mu\text{m}$  and (c) Precipitable water in cm, measured over Pokhara from Jan to December of 2017. The bottom scale is in Julian day with 1 for January first and 365 for last day of December.

**Table 1.** Monthly average of AOD, AE and Precipitable water (PW) and standard deviation in parenthesis for each month. The standard deviation is significant due to daily variability of aerosol optical properties and PW.

Months	AOD_0.50 $\mu$ m	AE (0.44/0.87)	Precipitable_Water (PW) in cm
Jan	0.30( $\pm$ 0.12)	1.43( $\pm$ 0.05)	1.21( $\pm$ 0.22)
Feb	0.79( $\pm$ 0.33)	1.30( $\pm$ 0.09)	1.56( $\pm$ 0.25)
March	0.72( $\pm$ 0.49)	1.27( $\pm$ 0.18)	1.95( $\pm$ 0.59)
April	0.79( $\pm$ 0.45)	1.21( $\pm$ 0.22)	2.31( $\pm$ 0.67)
May	0.52( $\pm$ 0.31)	1.25( $\pm$ 0.19)	3.06( $\pm$ 0.45)
June	0.34( $\pm$ 0.18)	1.31( $\pm$ 0.14)	3.91( $\pm$ 0.46)
July	0.12( $\pm$ 0.05)	1.41( $\pm$ 0.18)	4.63( $\pm$ 0.19)
Aug	0.16( $\pm$ 0.08)	1.39( $\pm$ 0.18)	4.70( $\pm$ 0.30)
Sep	0.31( $\pm$ 0.15)	1.41( $\pm$ 0.09)	3.98( $\pm$ 0.28)
Oct	0.36( $\pm$ 0.21)	1.40( $\pm$ 0.06)	2.83( $\pm$ 0.57)
Nov	0.31( $\pm$ 0.20)	1.41( $\pm$ 0.06)	1.81( $\pm$ 0.23)
Dec	0.30( $\pm$ 0.14)	1.37( $\pm$ 0.08)	1.31( $\pm$ 0.36)

### 3.2. Spectral dependence of AOD

The spectral values of AOD decrease with an increased value of wavelength of light. The figure 3 shows the strong dependence of AOD at a shorter wavelength and gradually decreases towards the longer wavelengths indicating the presence of fine to coarse aerosol particles. The fine mode particles are responsible for enhancing scattering that causes to make the values of AOD high at a shorter wavelength, whereas coarse mode particles are responsible for lower values of AOD at longer wavelength [19].

It can also be observed from the graph that the variation of AOD with wavelength follows a similar trend for different seasons, as indicated in figure 3. The average value of AOD is highest at

pre-monsoon season followed by winter, post-monsoon, and monsoon season.

The change in curvature in spectral AOD in figure 3 could be due to the presence of more than one type of aerosol in the atmosphere, so characterizing them using a single value of  $\alpha$  is only an approximation [30]. The variation of averaged AOD based on different seasons with wavelength in logarithmic scale is investigated by using first order linear fit, given by equation, and calculated angstrom exponents and turbidity parameters.

The Ångström exponent and turbidity parameters for these different seasons based on a single year data are found as  $\beta = 0.19 \pm 0.01$  and  $\alpha = 1.16 \pm 0.07$  (winter season),  $\beta = 0.29 \pm 0.01$  and  $\alpha = 1.13 \pm 0.04$  (pre-monsoon season),  $\beta = 0.09 \pm 0.03$  and  $\alpha = 1.25 \pm 0.03$  (monsoon season), and  $\beta = 0.13 \pm 0.01$  and  $\alpha = 1.22 \pm 0.07$  (post-monsoon season). The variation



of turbidity parameters indicates for the aerosol loadings, and the order of  $\beta$  values perfectly matches the variation of AOD values. The Ångström exponents indicate for a significant contribution of fine mode particles. These  $\alpha$  values were calculated using the mean spectral aerosol optical depth (AOD) at wavelengths,  $\lambda$ , from 0.34  $\mu\text{m}$  to 1.64  $\mu\text{m}$ . On the other hand, the seasonal  $\alpha$

based on the spectral AOD at wavelengths ranges 0.44  $\mu\text{m}$  to 0.87  $\mu\text{m}$  were found as  $\alpha = 1.36 \pm 0.06$  (winter season),  $1.24 \pm 0.03$  (pre-monsoon season),  $1.37 \pm 0.05$  (monsoon season), and  $1.40 \pm 0.01$  (post-monsoon season). In our study,  $\alpha$  calculated using two different wavelength ranges of AOD shows very little differences, with slightly higher  $\alpha$  obtained in the ranges 0.34  $\mu\text{m}$  to 1.64  $\mu\text{m}$ .

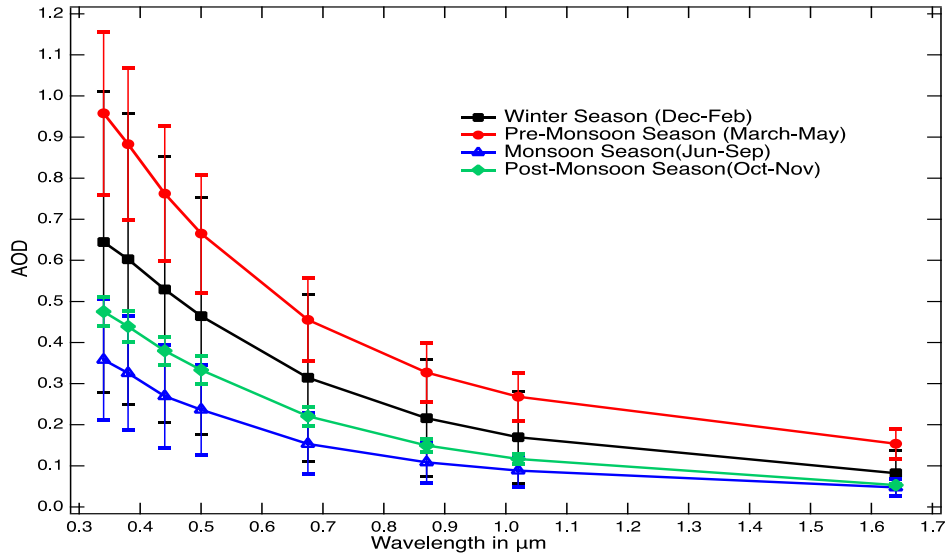


Fig. 3: Spectral Variation of AOD.

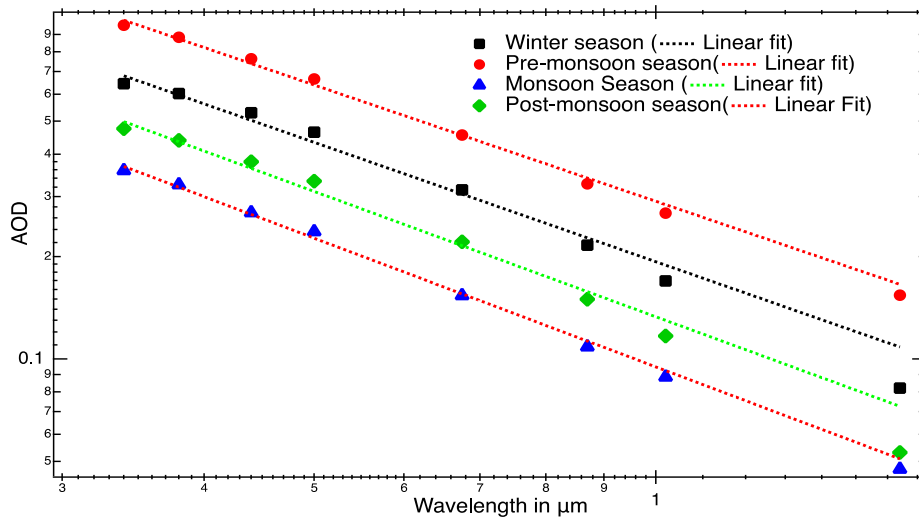


Fig. 4: Spectral variation of the mean aerosol optical depth (AOD) at six wavelengths,  $\lambda$ , from 0.44  $\mu\text{m}$  to 1.64  $\mu\text{m}$  for different seasons and linear fit in logarithmic wavelength scale.

#### 4. Conclusions

The monthly averaged AOD over the Pokhara AERONET device data shows that aerosol concentration is lower in the months from July to September than in the pre and post-monsoon season. It is associated with the regular rainfall in the region during this period. This study shows that the lower AOD on these months is due to the heavy rainfall, as indicated by higher precipitable water levels during the monsoon season. The lowest columnar AOD at 0.50  $\mu\text{m}$  (AOD<sub>0.50</sub>) characterize the lowest aerosol loading in monsoon, and highest average values in pre-monsoon followed by winter and post-monsoon. Previous studies suggest that the higher value of AOD during pre-monsoon and post-monsoon is due to the accumulation of aerosol loading from biomass burning and trans-boundary pollution from IGP (Indo Gangetic Plain). AE's Comparison obtained at two wavelength ranges, 0.44 to 0.87  $\mu\text{m}$  and 0.34 to 1.64  $\mu\text{m}$ , indicates that AE observed in the ultraviolet to infrared ranges can estimate aerosol sizes and shows that the aerosol has comparatively less impact on the infrared region. This analysis presented only one-year aerosol optical data to represent monthly variation along with seasonal variation. Therefore this study also sees the importance of further analysis of aerosol optical properties by using multi-year aerosol data along with back trajectory analysis of air masses to identify trans-boundary aerosols and source of air pollution over Pokhara.

#### Acknowledgments

Authors are thankful to Dr. Arnico Panday, Nepal, and AERONET group of NASA, USA for sun/sky radiometers data (<http://aeronet.gsfc.nasa.gov/>) from Pokhara site.

#### Conflicts of Interest

The authors declare no conflict of interest.

#### References

- [1] R. P. Aryal, K. J. Voss, P. A. Terman, W. C. Keene, J. L. Moody, E. J. Welton, and B.N. Holben, Comparison of surface and column

measurements of aerosol scattering properties over the western North Atlantic Ocean at Bermuda, *Atmos. Chem. Phys.* 14 (2014) 7617-7629.

- [2] <http://doi.org/10.5194/acp-14-7617-2014>.  
T. C. Bond, S. J. Doherty, D.W. Fahey, P. M. Forster, T. Berntsen B. J. DeAngelo, M. G. Flanner, S. Ghan, B. Kärcher, D. Koch, S. Kinne, Y. Kondo, P. K. Quinn, M. C. Sarofim, M.G. Schultz, M. Schulz, C. Venkataraman, H. Zhang, S. Zhang, N. Bellouin, S. K. Guttikunda, P.K. Hopke, M. Z. Jacobson, J. W. Kaiser, Z. Klimont, U. Lohmann, J. P. Schwarz, D. Shindell, T. Storelvmo, S. G. Warren, and C. S. Zender, Bounding the role of black carbon in the climate system: A scientific assessment, *J. Geophys. Res.* 118 (2013) 5380–5552.  
<http://doi.org/doi:10.1002/jgrd.50171>.
- [3] B. N. Holben, T. F. Eck, I. Slutsker, A. Smirnov, J. Sinyuk, A. Schafer, D. Giles, and O. Dubovik. Aeronet's Version 2.0 quality assurance criteria, *Proc. SPIE Remote Sens. Atmos., Clouds*, (2006) 6408, 64080Q.  
<https://doi.org/10.1117/12.706524>.
- [4] William C. Hinds, *Aerosol Technology* (2nd ed.). Wiley-Interscience, Iqbal Muhammad, An introduction to Solar Radiation, Academic Press, New York (1999). ISBN 978-0471-19410-1
- [5] M. Salby. *Fundamentals of Atmospheric Physics*, Academic Press, California (1996). ISBN: 9780126151602
- [6] J. Seinfeld, and S. Pandis. *Atmospheric chemistry and physics: from air pollution to climate change*, Wiley, Inc., New Jersey, USA (2006) p. 450.
- [7] B. Verheggen and E. P. Weijers, *Climate change and the impact of Aerosol: Energy Research Centre of the Netherlands (ECN)* (2010) ECN-E--09-095.
- [8] G. Myhre, C. E. L. Myhre, B. H. Samset and T. Storelvmo, *Aerosols and their Relation to Global Climate and Climate Sensitivity*, *Nature Education Knowledge* 4(5) (2013)7.
- [9] O. Boucher, *Atmospheric Aerosols Properties and Climate Impacts*, Springer, Netherlands (2015). ISBN978-94-017-9648-4
- [10] J. A. Duffie, and W. A. Beckman. *Solar engineering of Thermal Processes*, Fourth Edition. 2013, John Wile & Sons, Inc. (2013). ISBN: 0-471-51056-4.

- [11] S. Fuzzi, U. Baltensperger, K. Carslaw, S. Decesari, H. Denier van der Gon, M. C. Facchini, D. Fowler, I. Koren, B. Langford, U. Lohmann, E. Nemitz, S. Pandis, I. Riipinen, Y. Rudich, M. Schaap, J.G. Slowik, D. V. Spracklen, E. Vignati, M. Wild, M. Williams, and S. Gilardoni, Particulate matter, air quality and climate: lessons learned and future needs, *Atmos. Chem. Phys.* 15 (2015) 8217–8299. <https://doi.org/10.5194/acp-15-8217-2015>.
- [12] B. N. Holben, T. F. Eck, I. Slutsker, D. Tanre, J. P. Buis, A. Setzer, E. Vermote, J. A. Reagan, Y. J. Kaufman, T. Nakajima, F. Lavenu, I. Jankowiak, and A. Smirnov et al. AERONET—A federated instrument network and data archive for aerosol characterization, *Remote Sens. Environ.* 66(1) (1998) 1–16. [https://doi.org/10.1016/S0034-4257\(98\)00031-5](https://doi.org/10.1016/S0034-4257(98)00031-5).
- [13] D. Putero, P. Cristofanelli, A. Marinoni, B. Adhikary, R. Duchi, S. D. Shrestha, G. P. Verza, T. C. Landi, F. Calzolari, M. Busetto, G. Agrillo, F. Biancofiore, P. Di Carlo, A. K. Panday, M. Rupakheti, and P. Bonasoni, Seasonal variation of ozone and black carbon observed at Paknajol, an urban site in the Kathmandu Valley, Nepal, *Atmos. Chem. Phys.* 15 (2015) 13957–13971. <https://doi.org/10.5194/acp-15-13957-2015>.
- [14] R. Gautam, N. C. Hsu, S. C. Tsay, K. M. Lau, B. Holben, S. Bell, A. Smirnov, C. Li, R. Hansell, Q. Ji, S. Payra, D. Aryal, R. Kayastha, and K. M. Kim, “Accumulation of aerosols over the Indo-Gangetic plains and southern slopes of the Himalayas: Distribution, properties and radiative effects during the 2009 pre-monsoon season,” *Atmos. Chem. Phys.* 11 (24) (2011) 12841–12863. <https://doi.org/10.5194/acp-11-12841-2011>.
- [15] P. Tian, X. Cao, L. Zhang, N. Sun, L. Sun, T. Logan, J. Shi, Y. Wang, Y. Ji, Y. Lin, Z. Huang, T. Zhou, Y. Shi, and R. Zhang, “Aerosol vertical distribution and optical properties over China from longterm satellite and ground-based remote sensing,” *Atmos. Chem. Phys.* 17 (4) (2017) 2509–2523. <https://doi.org/10.5194/acp-17-2509-2017>.
- [16] O. Dubovik, B. Holben, T. F. Eck, A. Smirnov, Y. J. Kaufman, M. D. King, D. Tanre and I. Slutsker, “Variability of absorption and optical properties of key aerosol types observed in worldwide locations”, *J. Atmos. Sci.* 59 ( 3 ) (2002) 590–608. 2002. [https://doi.org/10.1175/15200469\(2002\)059<0590:VOAAOP>2.0.CO;2](https://doi.org/10.1175/15200469(2002)059<0590:VOAAOP>2.0.CO;2)
- [17] D. G. Kaskaoutis, K. V. S. Badarinath, S. K. Kharol, A. R. Sharma, and H. D. Kambezidis, “Variations in the aerosol optical properties and types over the tropical urban site of Hyderabad, India”, *J. Geophys. Res. Atmos.* 114 (22) (2009) 1–20. <https://doi.org/10.1029/2009JD012423>
- [18] B. N. Holben, D. Tanré, A. Smirnov, T. F. Eck, I. Slutsker, N. Abuhassan, W.W. Newcomb, J. S. Schafer, B. Chatenet, F. Lavenu, Y. J. Kaufman et al. “An emerging ground-based aerosol climatology: Aerosol optical depth from AERONET” *J. Geophys. Res. Atmos.* 106 ( D11) (2001) 12067–12097.
- [19] T. F. Eck, B. N. Holben, J. S. Reid, O. Dubovik, A. Smirnov, N. T. O’Neill, I. Slutsker and S. Kinne., Wavelength dependence of the optical depth of biomass burning, urban, and desert dust aerosol, *J. Geophys. Res.* 104 (31) (1999) 333–349. <https://doi.org/10.1029/1999JD900923>
- [20] A. Angstrom. Techniques of Determining the Turbidity of the Atmosphere, *Tellus* 13 (1961) 214-223. <https://doi.org/10.1111/j.2153-3490.1961.tb00078.x>.
- [21] M. Gyawali, W. P. Arnott, K. Lewis, and H. Moosmüller. Photoacoustic optical properties at UV, VIS, and near IR wavelengths for laboratory generated and winter time ambient urban aerosols, *Atmos. Chem. Phys.* 12 (2012) 2587–2601. <https://doi.org/10.5194/acp12-2587>
- [22] H. Moosmuller, R. K. Chakrabarty, K. M. Ehlers, and W. P. Arnott. Absorption Angstrom coefficient, brown carbon, and aerosols: basic concepts, bulk matter, and spherical particles, *Atmos. Chem. Phys.* 11 (2011) 1217–1225. <https://doi.org/10.5194/acp-11-1217-2011>.
- [23] N. T. O’Neill, T. F. Eck, A. Smirnov, B. N. Holben, and S. Thulasiraman. Spectral discrimination of coarse and fine mode optical depth, *Journal of Geophysical Research.* (2003) 108. <https://doi.org/10.1029/2002JD002975>.
- [24] G. L. Schuster, O. Dubovik, and B. N. Holben. Angstrom exponent and bimodal aerosol size

- distributions, *J. Geophys. Res.* 111 (2006) D07207, <https://doi.org/10.1029/2005JD006328>
- [25] K. N. Poudyal, B. K. Bhattarai, B. K. Sapkota, B. Kjeldstad, and N. R. Karki. Estimation of Global Solar Radiation using Pyranometer and NILU-UV Irradiance Meter at Pokhara Valley in Nepal. *Journal of the Institute of Engineering.* 9(1) (2003) 69-78.
- [26] A. Singh, K. S. Mahata, M. Rupakheti, W. Junkermann, A. K. Panday, and M. G. Lawrence. An overview of airborne measurement in Nepal– Part 1: Vertical profile of aerosol size, number, spectral absorption, and meteorology, *Atmospheric Chemistry and Physics.* 19(1) (2019) 245-258. <https://doi.org/10.5194/acp-19-245-2019>.
- [27] M. Sharma, D. G. Kaskaoutis, R. P. Singh, and S. Singh, “Seasonal variability of atmospheric aerosol parameters over greater Noida using ground sunphotometer observations”, *Aerosol Air Qual. Res.* 14 (3) (2014) 608–622. <https://doi.org/10.4209/aaqr.2013.06.0219>
- [28] D. Rupakheti, S. Kang, Z. Cong, M. Rupakheti, L. Tripathee, A. K. Panday and B. N. Holben, “Study of aerosol optical properties over two sites in the foothills of the central himalayas”, *Int. Arch. Photogramm. Remote Sens. Spat. Inf. Sci. -ISPRS Arch.* 42 (3) (2018) 1493–1497. <https://doi.org/10.5194/isprs-archives-XLII-3-1493-2018>
- [29] T. F. Eck, B. N. Holben, J. S. Reid, D. M. Giles, M. A. Rivas, R. P. Singh, S. N. Tripathi, C. J. Bruegge, S. Platnick, G. T. Arnold, N. A. Krotkov, S. A. Carn, A. Sinyuk, O. Dubovik, A. Arola, J. S. Schafer, P. Artaxo, A. Smirnov, H. Chen, and P. Goloub. Fog-and cloudinduced aerosol modification observed by the Aerosol Robotic Network (AERONET), *J. Geophys. Res.* 117(2012)D07206. <https://doi.org/10.1029/2011JD016839>
- [30] R. Pedrós, J. A. Martínez-Lozano, M. P. Utrillas, J. L. Gómez-Amo, and F. Tena, Column-integrated aerosol, optical properties from ground-based spectro radiometer measurements at Barrax (Spain) during the Digital Airborne Imaging Spectrometer Experiment (DAISEX) campaigns. *J. Geophys. Res.* 108 (D18) (2003)4571–4587. <https://doi.org/10.1029/2002JD003331>

# Variability of Surface Level Particulate Matter in Kathmandu and Pokhara and an Overview of Origin of Pollutants

Jeevan Regmi<sup>1,2</sup>, Khem N Poudyal<sup>3</sup>, Amod Pokhrel<sup>4</sup>, Katrina Wilson<sup>5</sup>, and Rudra Aryal<sup>5</sup>

*1 Prithvi Narayan Campus, Tribhuvan University, Pokhara, Nepal*

*2 Central Department of Physics Tribhuvan University, Kirtipur, Nepal*

*3 Dept. of Applied Sciences, Institute of Engineering Tribhuvan University, Lalitpur, Nepal*

*4 University of California Berkeley, California, USA*

*5 Franklin Pierce University, 40 University Drive, Rindge, NH, USA*

*Corresponding e-mail: [jeevan.regmi@prnc.tu.edu.np](mailto:jeevan.regmi@prnc.tu.edu.np)*

*(Manuscript Received 16/08/2022; Review: 15/09/2022; Revised 30/09/2022; Accepted 05/10/2022)*

## Abstract

The concentration of fine and coarse particulate matter at the surface level in Pokhara and Pulchowk (Kathmandu Valley) of Nepal was monitored from January to September 2020 using particulate matter sensors. Size-segregated particulate matter with diameters less than or equal to 1 micrometer (PM 1.0), PM 2.5, and PM 10 are analyzed hourly, daily, and seasonally. Pokhara is observed to be less polluted than Pulchowk, with an average of 58.96  $\mu\text{g}/\text{m}^3$  during winter and 38.50  $\mu\text{g}/\text{m}^3$  pre-monsoon. Pulchowk PM 2.5 averaged 99.64  $\mu\text{g}/\text{m}^3$  during the winter season, December to February, and 55.94  $\mu\text{g}/\text{m}^3$  during the pre-monsoon season, March to May. PM concentrations vary bimodally and decrease significantly in the daytime until 5 pm local time. There was a significant decrease in PM 2.5 after the last week of March in both cities, resulting from the COVID-19 lockdown, which indicates that most surface-level aerosol particles are anthropogenic such as traffic and cooking activities in the evenings and mornings might have significantly affected particulate matter concentrations. Based on seasonal variation, Pulchowk PM 2.5 leads to Pokhara by 1.63 times in winter, 1.46 times in pre-monsoon, 1.25 times in summer, and 1.32 times in post-monsoon, indicating Pokhara is less polluted than Pulchowk. In both cities, PM 2.5 contributes equally to PM 10, with fraction of 0.89 (0.86), 0.87 (0.85), 0.94 (0.92), and 0.76 (0.83), with the numbers in parenthesis representing Pulchowk and Pokhara, respectively.

## Keywords:

*Coarse Mode; Fine Mode; Particulate Matter (PM 2.5, PM 10); Spatio-Temporal Variation.*

## 1. INTRODUCTION

Aerosol particles with an effective aerodynamic diameter of 2.5  $\mu\text{m}$  or less are called Particulate Matter (PM<sub>2.5</sub>) [1]. Particles like these have various health effects and play a significant role in climate change. PM is a chemically non-specific pollutant with different chemical compositions depending on its source [2]. The most important sources of such PM are biomass and fossil fuel combustion, along with diverse energy sources used in household activities [3].

Ground observations of aerosol particles are crucial as the level of uncertainty is very high due to various local and external factors [4]. Even though satellite observations can provide long-term and global coverage, they may not be as precise as surface measurements. As satellites view the entire atmospheric column, it is difficult to distinguish surface particles from those at a height [5]. It is

necessary to update satellite data retrievals by considering regional bias corrections because satellite detection of surface-level and geographic data reduces its accuracy [6]. It is necessary to take multiple ground-based measurements at various locations to validate satellite and model-generated data. Further, establishing many ground-based measurement stations worldwide will be costly, and skilled human resources will be hard to come by. Low-cost sensors like Purple Air Monitor, which can be operated with general technical knowledge and transported to multiple locations quickly, can fill this gap.

In our study, we studied Kathmandu (the most polluted city in Nepal) and Pokhara (comparatively clean among Nepalese cities). Combined with rapid population growth, they are rapidly urbanizing. Pokhara has a population

density of 4,626.3 / km<sup>2</sup>, while Kathmandu has a population density of 19726 / km<sup>2</sup> (CBS, 2011). Apart from this, human activities such as the unplanned expansion of the city, the increase in vehicles, the haphazard construction of buildings, unmanaged industries, and biomass burning contribute to the pollution of the environment.

In the Environmental Performance Index (EPI) 2022, Nepal ranks 178th for air quality and 162<sup>nd</sup> in EPI (it was 145th in 2020) among 180 countries (Figure 1 a, b and c). It means the air quality is very poor and threatening, and mitigation is urgent. Statistics are essential for developing long- and short-term strategies. Only continuous and sufficient research will be able to accomplish this. The Kathmandu valley has had few studies analyzing PM 2.5 concentrations in the past. Aryal et al. (2009) reported that the valley has very high pollution levels, which peak in the morning and evening with higher values[7]. During winter mornings, pollutants remain within the inversion layer due to mixing layer activity under weak wind flow and basin topography of the valley [8]. Several other studies have also reported similar results [9]–[12]. However, a continuous and long-term study is always desirable to understand and know how air pollution is progressing. Kathmandu's source apportionment studies showed that 40% of it is from brick kilns, 37% from motor vehicles, and 22% from biomass/garbage burning) is Elemental Carbon, 47% from motor vehicles, 32% from biomass/garbage burning, and 13 percent from soil dust [13].

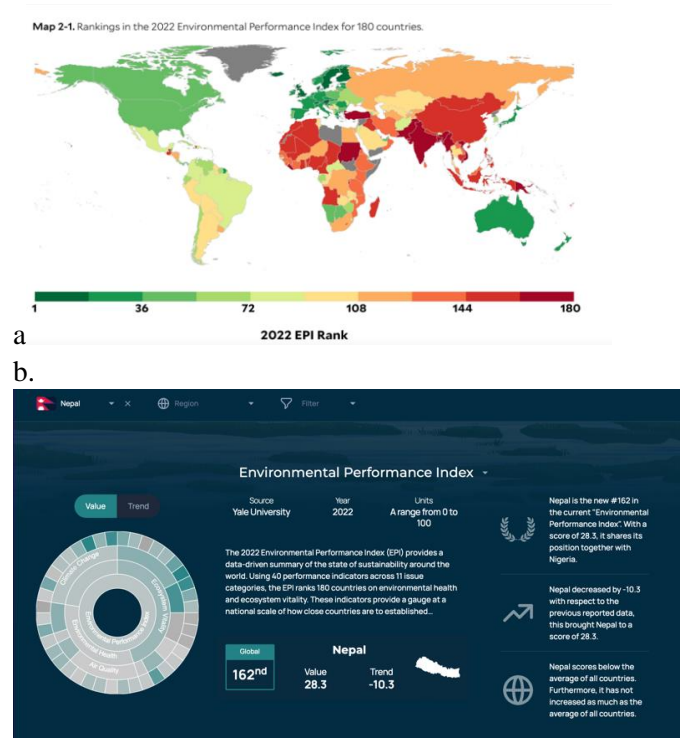


Figure 1: a. Global Environmental Performance Index (EPI) map for 2022. b. Nepal's Environmental Performance Index ranking.

Source: <https://global-reports.23degrees.eu/epi2022/root> (Retrieved on 09/07/2022)

Earlier studies have shown that transboundary and local aerosol particles affect the Pokhara valley [4]. Some of them are local in origin, while others are transboundary. Pollutants from the IGP region significantly affect it as well as Kathmandu valley. According to reports, biomass burning, industrial pollution, desert dust, and urban activities are significant sources of pollution in the IGP region [14], [15]. Based on images from the MODIS satellite and NOAA's HYSPLIT MODEL back trajectory, Regmi et al. (2020) report that an aerosol haze layer extends from the IGP to the Pokhara valley (Figure 2. a and b).

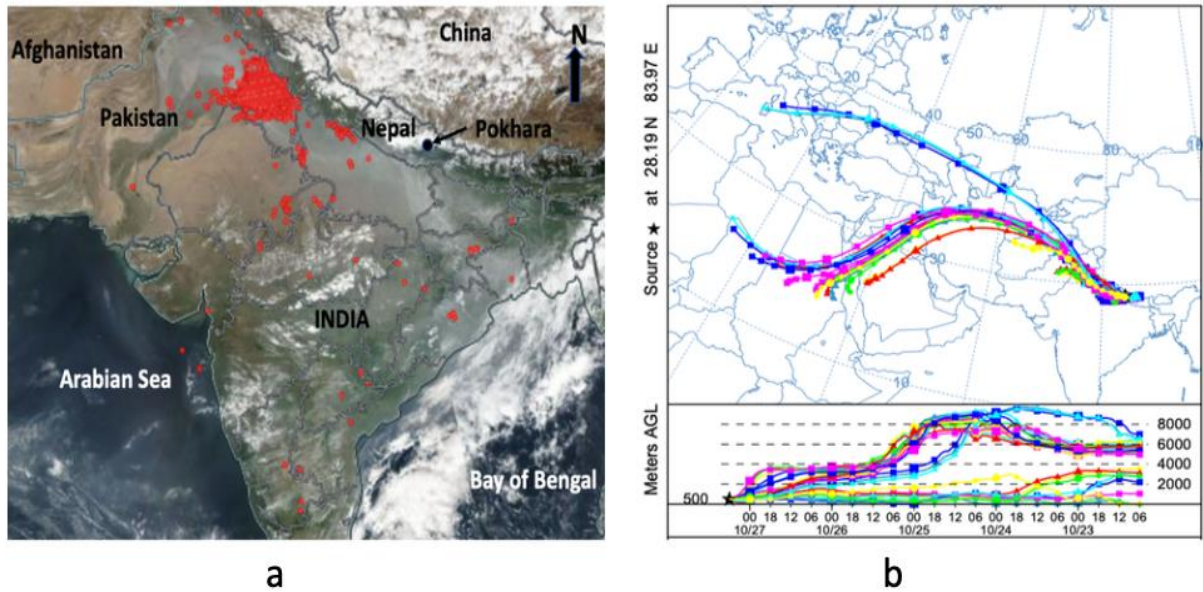


Figure 2: (a) The corrected reflectance true-color MODIS satellite image of 27 October 2017 shows intense air pollution plumes over the IGP. (b) NOAA HYSPLIT MODEL trajectories ended at 0600 UTC on 27 October 2017 (Regmi et al., 2020).

## 2. An overview of the materials and methods

### 2.1 The Purple air sensor's structure

A Purple-Air sensor was used to measure PM<sub>1.0</sub>, PM<sub>2.5</sub>, and PM<sub>10</sub>. This small and handy device can detect particles from 0.3 micrometers to 10.0 micrometers in six different sizes. This device has a six-sided shielding that provides high anti-interference performance and an option for air inlet/outlet direction. PMS5003 sensors are used to

detect and count suspended particles in the air. ESP 8226 microcontrollers and BME 280 environmental sensors are used (Fig. 3). BME 280 sensors measure pressure, temperature, and humidity within the units. Consequently, the ESP 8266 microcontroller communicates with the PMS5003 sensors and the Purple Air server via Wi-Fi, allowing the PM concentration data to be viewed and downloaded live on the Purple Air map (<https://www.purpleair.com/map>) via the application programming interface (API).

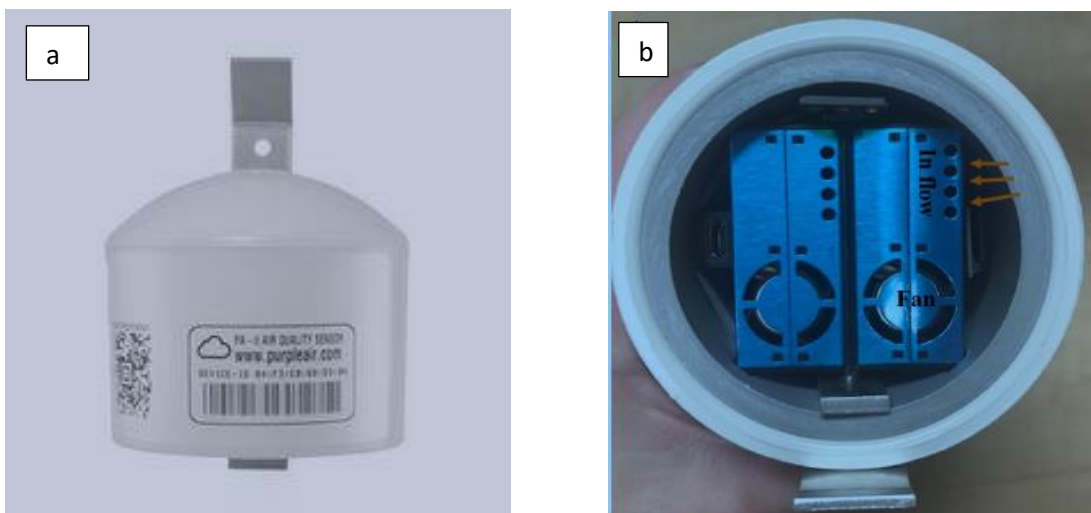


Figure 3: a. Photograph of Purple air. b. View of two blue sensors at the bottom of the PM-II unit.

## 2.2. Principles of operation

When the laser beam passes through an air passage, an air particle reflects some of the laser beams onto a detection plate using laser scattering. The detection plate measures the reflection as a pulse,

and the pulse's length determines the particle's size. The number of pulses counts particles. Based on MIE theory, the equivalent particle diameter of the microprocessor and the number of particles with different diameters per unit volume are calculated (<https://www.purpleair.com/map>).

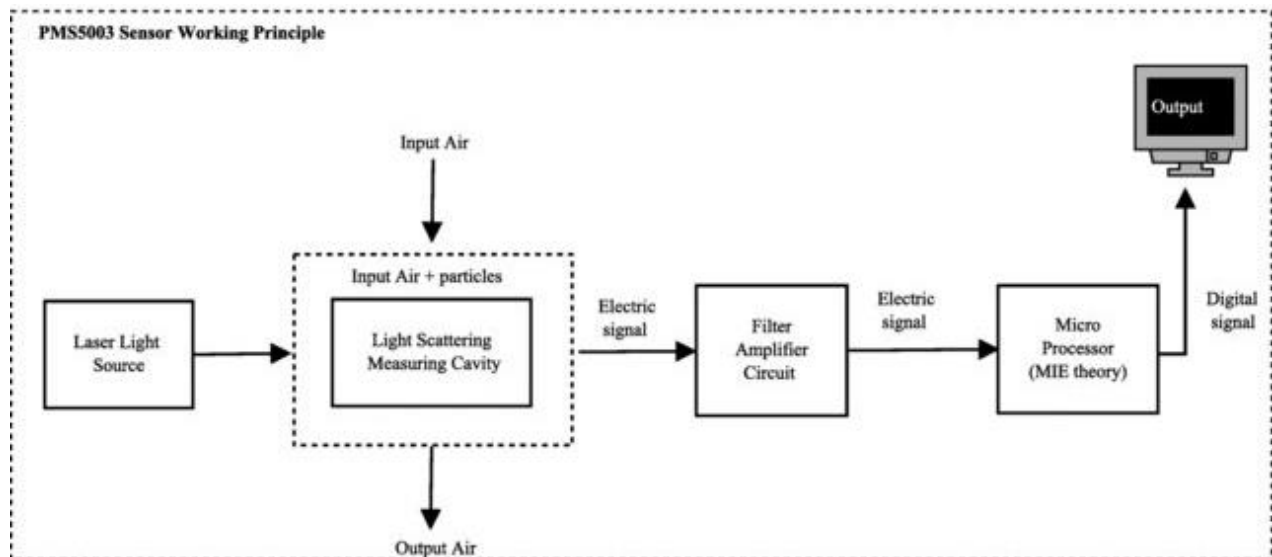


Figure 4: Purple Air II-AP/SD sensor and an overview of the PMS5003 working principle (Accessed on September 11, 2022 from [http://www.aqmd.gov/docs/default-source/aq-spec/resources-page/plantower-pms5003-manual\\_v2-3.pdf](http://www.aqmd.gov/docs/default-source/aq-spec/resources-page/plantower-pms5003-manual_v2-3.pdf))

## 2.3 Site Description:

Pokhara (28.23° N, 83.99° E) and Kathmandu (Pulchowk Engineering Campus 27.68° N, 85.31° E) are equipped with purple air monitors to measure the size of segregated PM in the air at the surface.

The Pokhara valley is the second-largest city in Nepal, located approximately 200 km west of Kathmandu at an altitude of 805 meters. The city is surrounded by hills, ranging in altitude from 1000 to 2000 meters. Approximately 35 km separates the north of IGP from the south side of Pokhara, while in the north, altitudes rise rapidly to over 7000

meters. During the summer, the mountains near Pokhara lift humid air masses, which leads to a lot of precipitation, which can significantly impact aerosol concentrations in the atmosphere [16].

Kathmandu valley, located 1325 meters above sea level, is the capital of Nepal. The city is located between the Indo-Gangetic Plain in the south, densely populated and a potential source of transboundary pollution, and the great Himalaya in the north [17]. It is surrounded by tall mountains with elevations ranging from 2000 m to 2800 m, creating a bowl-shaped structure that traps pollutants within the valley [18].



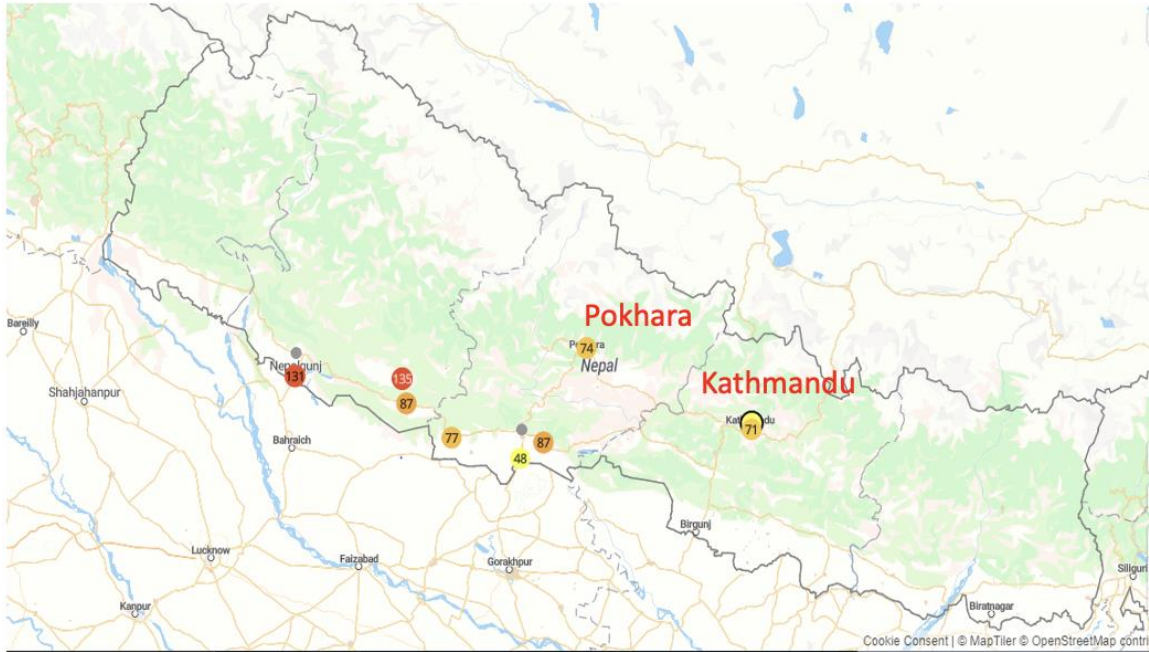


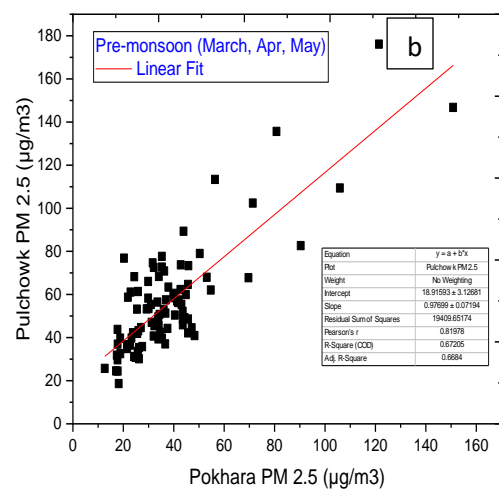
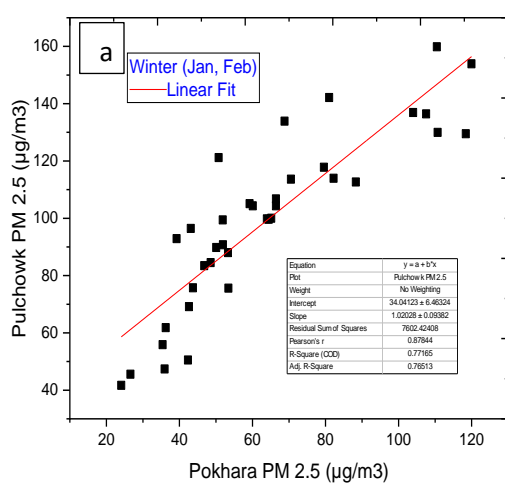
Figure 5: Map of Nepal showing the location of two cities, Kathmandu and Pokhara. Source: Purpleair.com/map © <https://www.openstreetmap.org/copyright>

### 3.Results and Discussions:

#### 3.1. Seasonal Variability of PM 2.5 and PM 10

Figure 6 (a to d) illustrate the seasonal scatterplot of simultaneously observed PM 2.5 data between Pulchowk and Pokhara. In Pulchowk and Pokhara, PM 2.5 correlates with 0.77 in winter, 0.67 in

premonsoon, 0.62 in monsoon, and 0.66 in postmonsoon. The seasonal variation was analyzed using a year of data due to data availability. PM 2.5 levels in these two cities are correlated significantly, suggesting similar air pollution embedded over the atmosphere, such as roadside dust, traffic pollution, and transboundary air pollution.



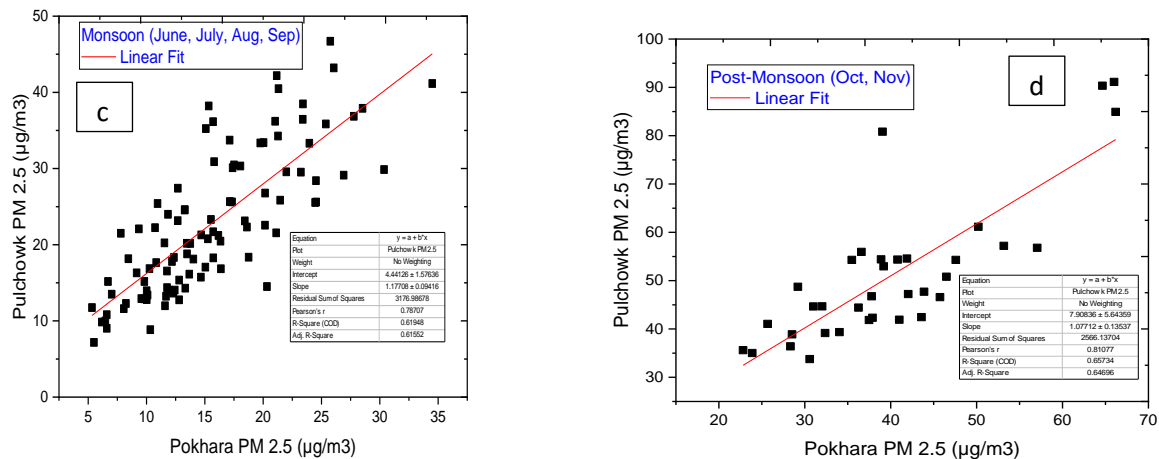


**Figure 6.** This figure shows the seasonal scatterplot for PM 2.5 in Pulchowk and Pokhara in 2020 a. winter b. pre-monsoon c. monsoon and d. post monsoon season.

Table 1 shows a seasonal variation of average PM<sub>2.5</sub> and PM<sub>10</sub> concentrations, along with standard deviations. Based on this data, Pokhara is relatively cleaner than Pulchowk. In Pokhara, fine and coarse mode particle concentrations are lower in all seasons than in Pulchowk. Pulchowk's PM<sub>2.5</sub> average is 1.63 times higher in winter, 1.46 times higher in premonsoon, 1.25 times higher in summer, and 1.32 times higher post-monsoon than Pokhara's. Similarly, Pulchowk leads Pokhara in PM 10 ratio by 1.71 in winter, 1.50 in premonsoon, 1.28 in monsoon, and 1.21 in post-monsoon compared to Pokhara. We notice that Pulchowk has significantly higher PM concentrations in winter and premonsoon. The remaining two seasons are also significantly polluted in Pulchowk. While

Pokhara shows a low PM 2.5 concentration except during winter (40µg/m<sup>3</sup> NAAQS, 2012), Pulchowk shows a high level all year but during monsoon. In Pokhara, PM 2.5 concentrations are lowest during monsoon (17.35 ± 3.51 µg/m<sup>3</sup>) and highest during winter (61.11 ± 15.67 µg/m<sup>3</sup>). Pulchowk also recorded the lowest value during monsoon (21.73± 5.53) µg/m<sup>3</sup> and maximum value during winter (99.72± 12.65) µg/m<sup>3</sup> significant seasonal variation in the concentration of PM 2.5. As shown in Table 1, PM 10 concentrations in both sites are lowest in monsoon and highest in winter. As shown in table 1, PM<sub>2.5</sub> / PM<sub>10</sub> measures fine particles in an area's atmosphere compared to coarse particles, which contribute similarly to total particulate matter in both cities.

Table 1: Seasonal average concentrations of PM 2.5 and PM 10 in Pokhara and Pulchowk along with the ratio of PM 2.5 to PM 10.

	PM <sub>2.5</sub> µg/m <sup>3</sup>		PM <sub>10</sub> µg/m <sup>3</sup>		PM <sub>2.5</sub> / PM <sub>10</sub>	
	Pokhara	Pulchowk	Pokhara	Pulchowk	Pokhara	Pulchowk
Winter	61.11±15.67	99.72± 12.65	68.05±13.03	116.39±12.87	0.89	0.86
Pre-Monsoon	38.03±20.59	55.72 ±19.95	43.57±10.91	65.49±23.86	0.87	0.85
Monsoon	17.35 ± 3.51	21.73± 5.53	18.38 ±7.77	23.56±7.67	0.94	0.92
Post-Monsoon	39.85± 9.66	52.78± 29.80	52.36± 6.60	63.54±31.72	0.76	0.83

### 3.2 An Overview of Meteorological Parameters and Variation of PM 2.5

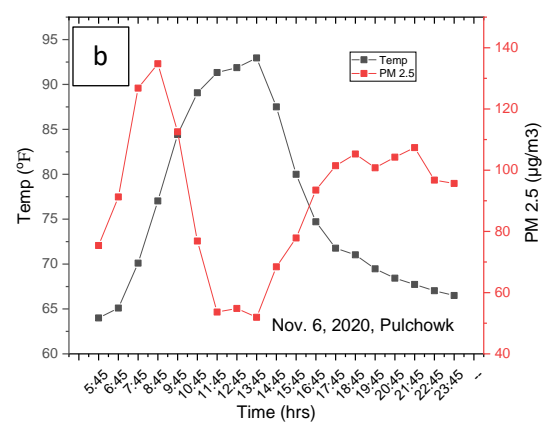
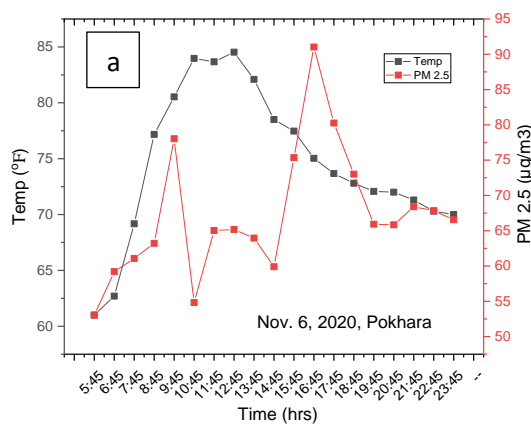
The table 2 presents the seasonal meteorological parameters for Pokhara and Pulchowk to illustrate the overall atmospheric dynamics. Both cities experience similar temperature variations, but

Pokhara's relative humidity and air pressure are significantly higher than Kathmandu's. As a result of Pokhara's higher relative humidity, the monsoon has had a more significant impact on overall aerosol concentration during summer than in Kathmandu, Pulchowk. According to a previous study, wind, temperature, humidity, rain, and solar radiation all influence air pollution levels [19]. Pokhara's higher rainfall may contribute to its lower PM 2.5 level, significantly lower than Pulchowk's. PM levels were examined at two stations on the same day based on temperature and relative humidity. The two days were selected based on the complete availability of data for all day hours at the two sites. Pokhara's PM 2.5 variation does not show any significant trend with temperature, as shown in figure 7 (a and b). However, it shows some inverse variation with temperature during the day, especially at noon and in the afternoon, which can be due to a reduction in traffic activities or the

diffusion of air pollution. In Pulchowk, however, PM concentrations show a change in PM variation opposite to temperature after around 8 am. Figures 7 (c and d) show the significant relationship between PM 2.5 concentrations and relative humidity (RH). In both sites, PM increased with an increase in RH on two specific days (Jan 28 and Nov 6, 2020); however, we cannot draw any specific conclusions about the results. It is likely that this variation results from anthropogenic pollution produced in the morning and evening at the same time as traffic, biomass burning, and lower temperatures that increase relative humidity. Few studies have found that PM concentrations increased relative humidity [20]. On the other hand, an industrial area with low precipitation had a negative correlation [21]. As far as PM production and dispersion are concerned, RH does not appear to have an effect [22].

Table 1: Seasonal climate parameters for Pokhara and Pulchowk from January 2020 through November 2020 in Pokhara and Pulchowk.

Season	Temperature (° C)		Relative Humidity (%)	
	Pokhara	Pulchowk	Pokhara	Pulchowk
Winter (Jan, Feb)	16.80	17.98	59.22	50.73
Pre-Monsoon (Mar, Apr, May)	24.22	24.01	55.80	48.76
Monsoon (June, July, Aug, Sep)	28.91	29.04	66.99	59.11
Post-Monsoon (Oct, Nov)	24.47	25.91	58.56	45.93



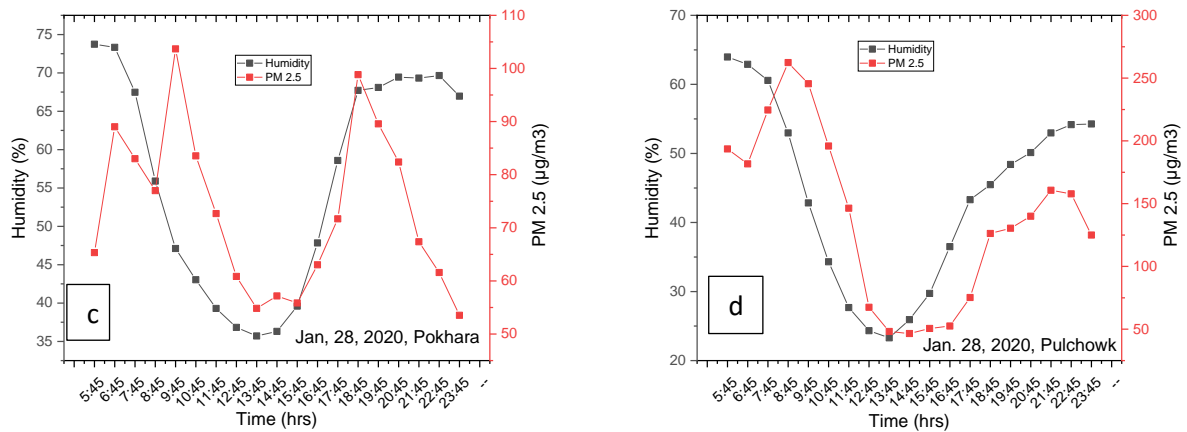


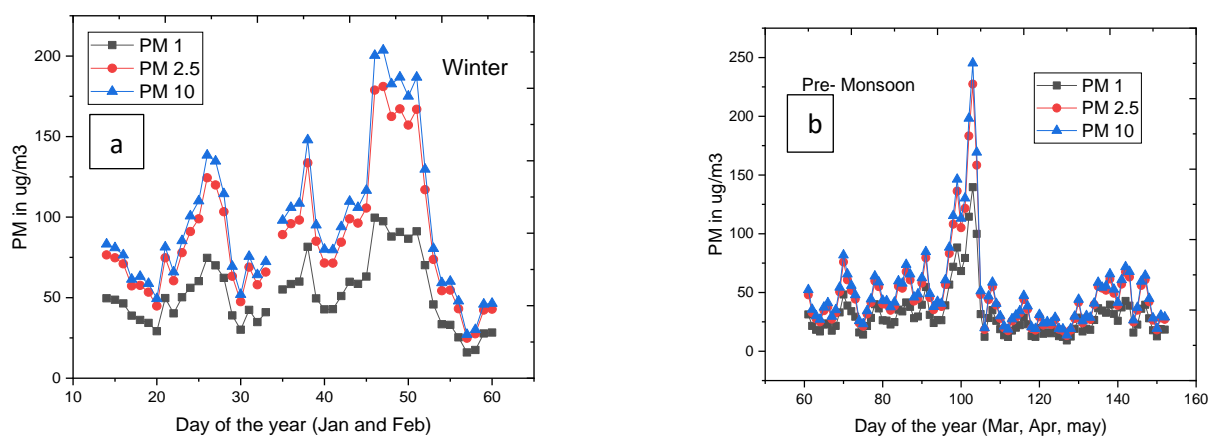
Figure 7: variation of PM 2.5 with relative humidity on two randomly selected days in Pokhara and Pulchowk. a. Variation of PM.25 and Temperature at Pokhara, b. Variation of PM.25 and Temperature at Pulchowk, c. Variation of PM.25 and Relative Humidity at Pokhara d. Variation of PM.25 and Relative Humidity at Pulchowk.

### 3.3 Daily Variation of PM 1, PM 2.5 and PM 10 in different Seasons

In figure 8 (a to d), the daily mean concentrations of PM 1, PM 2.5, and PM 10 in Pokhara are shown for different seasons, and in figure 9 (a to d), the daily mean concentrations of PM 1, PM 2.5, and PM 10 in Pulchowk are depicted for various seasons. According to the data, Pulchowk's PM 10 and PM 2.5 concentrations are higher than Pokhara's throughout the year. While observing the overall data each season, Pulchowk and Pokhara had maximum daily averages of 115.33  $\mu\text{g}/\text{m}^3$  and 159.86  $\mu\text{g}/\text{m}^3$  of PM 2.5, respectively, in winter. The pre-monsoon air quality in Pokhara was 155.24  $\mu\text{g}/\text{m}^3$ , and in Pulchowk, it was 176.14  $\mu\text{g}/\text{m}^3$ . As a result of the lockdown, followed by COVID-19,

the average concentration decreased in both cities. Nevertheless, it shows that the concentration is highest during the winter season, gradually decreases until the monsoon, then increases again during the post-monsoon.

Comparing the PM concentrations in Pokhara, mixed types of particles of all sizes contribute to the particulate matter during all seasons. Both PM 10 and PM 2.5 (coarse and fine modes) contribute nearly equally, with coarse mode dominating slightly. The ultrafine particles (PM 1) contribute significantly less, which may be due to the low effectiveness of the low-cost sensors, as previous studies have indicated that they are unreliable enough to track ultrafine particles [23].



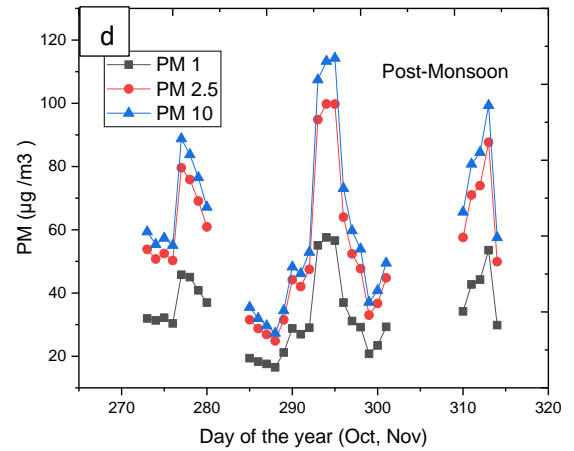
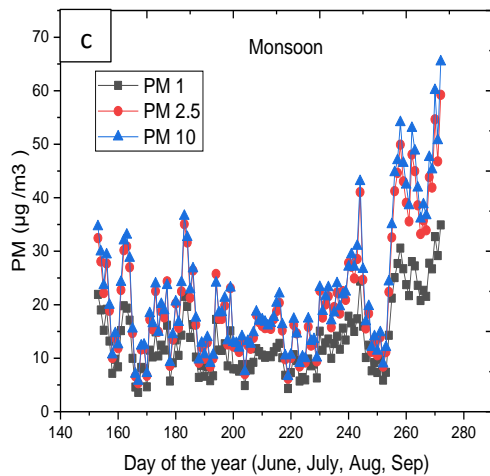


**Figure 8.** Comparison of Concentration of PM 1  $\mu\text{g}/\text{m}^3$ , PM 2.5  $\mu\text{g}/\text{m}^3$  and PM 10  $\mu\text{g}/\text{m}^3$  in Pokhara observation site during (a) winter, (b)pre-monsoon, (c) monsoon and (d) post monsoon season 2020.

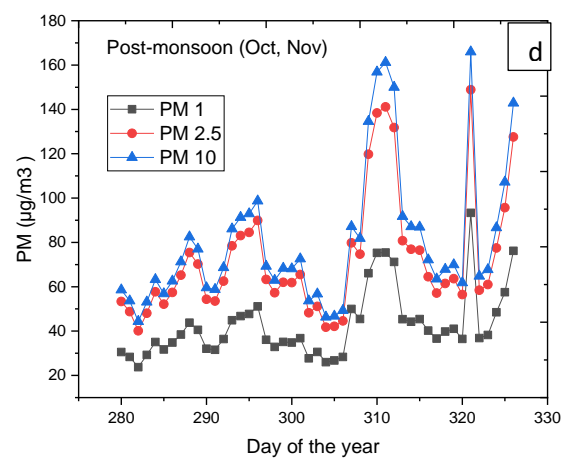
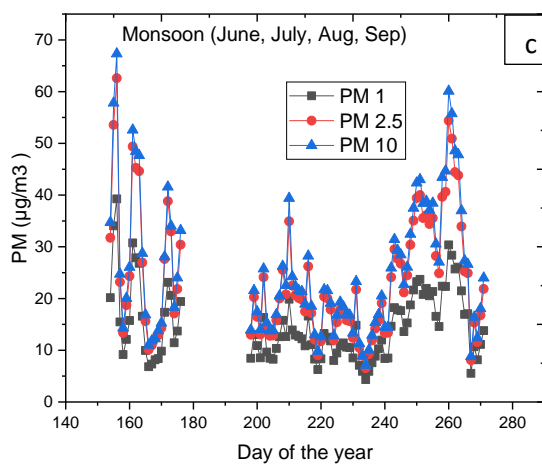
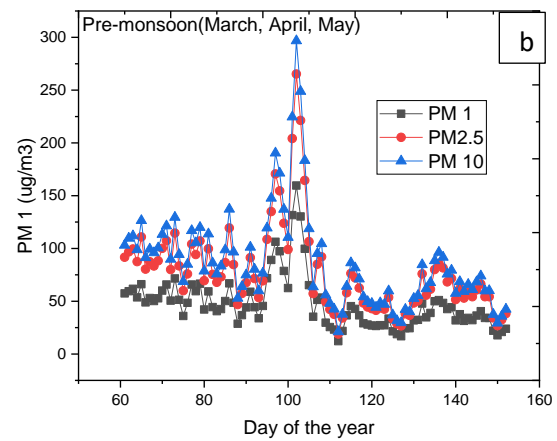
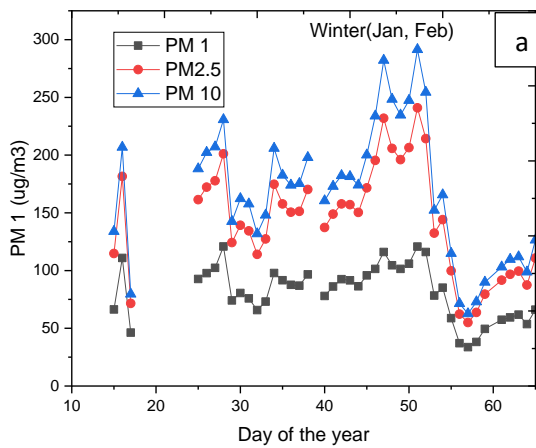


**Figure 9.** Comparison of Concentration of PM 1  $\mu\text{g}/\text{m}^3$ , PM 2.5  $\mu\text{g}/\text{m}^3$  and PM 10  $\mu\text{g}/\text{m}^3$  in Pokhara observation site during (a) winter, (b)pre-monsoon, (c) monsoon and (d) post monsoon season 2020.

## Conclusions:

This study used Purple-Air sensors to measure and analyze PM<sub>1.0</sub>, PM<sub>2.5</sub>, and PM<sub>10</sub> aerosol particles. The Purple-Air sensor data were also examined in ambient conditions to confirm air pollution trends observed in Kathmandu and Pokhara, Nepal's two major cities and climatically vulnerable regions between the Indo-Gangetic Plain (IGP) and the high mountains. The cities are also rapidly urbanizing, with many anthropogenic pollution sources locally. With such a low-cost sensor, we could also monitor the fluctuation in air pollution caused by traffic variations, such as the COVID-19 lockdown, and we noticed the decrease in pollution with the traffic reduction during this lockdown.

## References:

- [1] P. Gupta *et al.*, "Impact of California Fires on Local and Regional Air Quality: The Role of a Low-Cost Sensor Network and Satellite Observations," *Geohealth*, vol. 2, no. 6, pp. 172–181, 2018, doi: 10.1029/2018gh000136.
- [2] K. Ito *et al.*, "PM source apportionment and health effects: 2. An investigation of intermethod variability in associations between source-apportioned fine particle mass and daily mortality in Washington, DC," *J Expo Sci Environ Epidemiol*, vol. 16, no. 4, pp. 300–310, 2006, doi: 10.1038/sj.jea.7500464.
- [3] C. L. Weagle *et al.*, "Global Sources of Fine Particulate Matter: Interpretation of PM<sub>2.5</sub> Chemical Composition Observed by SPARTAN using a Global Chemical Transport Model," *Environ Sci Technol*, vol. 52, no. 20, pp. 11670–11681, 2018, doi: 10.1021/acs.est.8b01658.
- [4] J. Regmi *et al.*, "Investigation of Aerosol Climatology and Long-Range Transport of Aerosols over Pokhara, Nepal," *Atmosphere (Basel)*, vol. 11, no. 8, pp. 1–16, 2020, doi: doi:10.3390/atmos11080874.
- [5] H. Zhang, R. M. Hoff, and J. A. Engel-Cox, "The relation between moderate resolution imaging spectroradiometer (MODIS) aerosol optical depth and PM<sub>2.5</sub> over the United States: A geographical comparison by U.S. Environmental Protection Agency regions," *J Air Waste Manage Assoc*, vol. 59, no. 11, pp. 1358–1369, 2009, doi: 10.3155/1047-3289.59.11.1358.
- [6] A. van Donkelaar, R. v. Martin, C. Li, and R. T. Burnett, "Regional Estimates of Chemical Composition of Fine Particulate Matter Using a Combined Geoscience-Statistical Method with Information from Satellites, Models, and Monitors," *Environ Sci Technol*, vol. 53, no. 5, pp. 2595–2611, 2019, doi: 10.1021/acs.est.8b06392.
- [7] R. K. Aryal, B. Lee, R. Karki, A. Gurung, B. Baral, and S. Byeon, "Dynamics of PM<sub>2.5</sub> concentrations in Kathmandu Valley, Nepal," vol. 168, pp. 732–738, 2009, doi: 10.1016/j.jhazmat.2009.02.086.
- [8] T. Kitada and R. P. Regmi, "Dynamics of air pollution transport in late wintertime over Kathmandu Valley, Nepal: As revealed with numerical simulation," *Journal of Applied Meteorology*, vol. 42, no. 12, pp. 1770–1798, 2003, doi: 10.1175/1520-0450(2003)042<1770:DOAPTI>2.0.CO;2.
- [9] P. M. Shrestha, J. Regmi, U. Joshi, K. N. Poudyal, N. P. Chapagain, and I. B. Karki, "Study of Affecting Factors of Meteorological Parameters on Solar

- Radiation on Pokhara,” *Himalayan Physics*, vol. 9, pp. 45–52, 2020.
- [10] C. Sarkar, V. Sinha, B. Sinha, A. K. Panday, and M. Rupakheti, “Source apportionment of NMVOCs in the Kathmandu Valley during the SusKat-ABC international field campaign using positive matrix factorization,” pp. 8129–8156, 2017.
- [11] K. M. Shakya, M. Rupakheti, K. Aryal, and R. E. Peltier, “Respiratory effects of high levels of particulate exposure in a cohort of traffic police in Kathmandu, Nepal,” *J Occup Environ Med*, vol. 58, no. 6, 2016, doi: 10.1097/JOM.0000000000000753.
- [12] S. Shrestha, S. P. Puppala, B. Adhikary, and K. L. Shrestha, “Influence of semi-volatile aerosols on physical and optical properties of aerosols in the Kathmandu Valley,” no. April, pp. 1–33, 2017, doi: 10.5194/acp-2017-287.
- [13] B. M. Kim *et al.*, “Source apportionment of PM10 mass and particulate carbon in the Kathmandu Valley, Nepal,” *Atmos Environ*, vol. 123, pp. 190–199, 2015, doi: 10.1016/j.atmosenv.2015.10.082.
- [14] R. Gautam *et al.*, “Accumulation of aerosols over the Indo-Gangetic plains and southern slopes of the Himalayas: distribution, properties and radiative effects during the 2009 pre-monsoon season,” *Atmos Chem Phys*, vol. 11, no. 24, pp. 12841–12863, Dec. 2011, doi: 10.5194/acp-11-12841-2011.
- [15] M. Kumar *et al.*, “Long-term aerosol climatology over Indo-Gangetic Plain: Trend, prediction and potential source fields,” *Atmos Environ*, vol. 180, pp. 37–50, 2018, doi: 10.1016/j.atmosenv.2018.02.027.
- [16] K. N. Poudyal, B. K. Bhattarai, B. K. Sapkota, B. Kjeldstad, and N. R. Karki, “Estimation of Global Solar Radiation using Pyranometer and NILU-UV Irradiance Meter at Pokhara Valley in Nepal,” *Journal of the Institute of Engineering*, 2014, doi: 10.3126/jie.v9i1.10672.
- [17] A. K. Panday and R. G. Prinn, “Diurnal cycle of air pollution in the Kathmandu Valley, Nepal: Observations,” vol. 114, no. May, pp. 1–19, 2009, doi: 10.1029/2008JD009777.
- [18] R. P. Regmi, T. Kitada, and G. Kurata, “Numerical simulation of Late wintertime local flows in Kathmandu Valley, Nepal: Implication for air pollution transport,” *Journal of Applied Meteorology*, vol. 42, no. 3, pp. 404–416, 2003, doi: 10.1175/1520-0450(2003)042<0389:nsolwl>2.0.co;2.
- [19] R. Lapere, L. Menut, S. Mailler, and N. Huneus, “Seasonal variation in atmospheric pollutants transport in central Chile: Dynamics and consequences,” *Atmos Chem Phys*, vol. 21, no. 8, pp. 6431–6454, Apr. 2021, doi: 10.5194/acp-21-6431-2021.
- [20] Y. Cheng, K. bin He, Z. Y. Du, M. Zheng, F. K. Duan, and Y. L. Ma, “Humidity plays an important role in the PM2.5 pollution in Beijing,” *Environmental Pollution*, vol. 197, pp. 68–75, 2015, doi: 10.1016/j.envpol.2014.11.028.
- [21] R. Zalakeviciute, J. López-Villada, and Y. Rybarczyk, “Contrasted effects of relative humidity and precipitation on urban PM2.5 pollution in high elevation urban areas,” *Sustainability (Switzerland)*, vol. 10, no. 6, Jun. 2018, doi: 10.3390/su10062064.
- [22] C. Lou, H. Liu, Y. Li, Y. Peng, J. Wang, and L. Dai, “Relationships of relative humidity with PM2.5 and PM10 in the Yangtze River Delta, China,” *Environ Monit Assess*, vol. 189, no. 11, 2017, doi: 10.1007/s10661-017-6281-z.
- [23] F. M. J. Bulot *et al.*, “Long-term field comparison of multiple low-cost particulate matter sensors in an outdoor urban environment,” *Sci Rep*, vol. 9, no. 1, pp. 1–13, 2019, doi: 10.1038/s41598-019-43716-3.



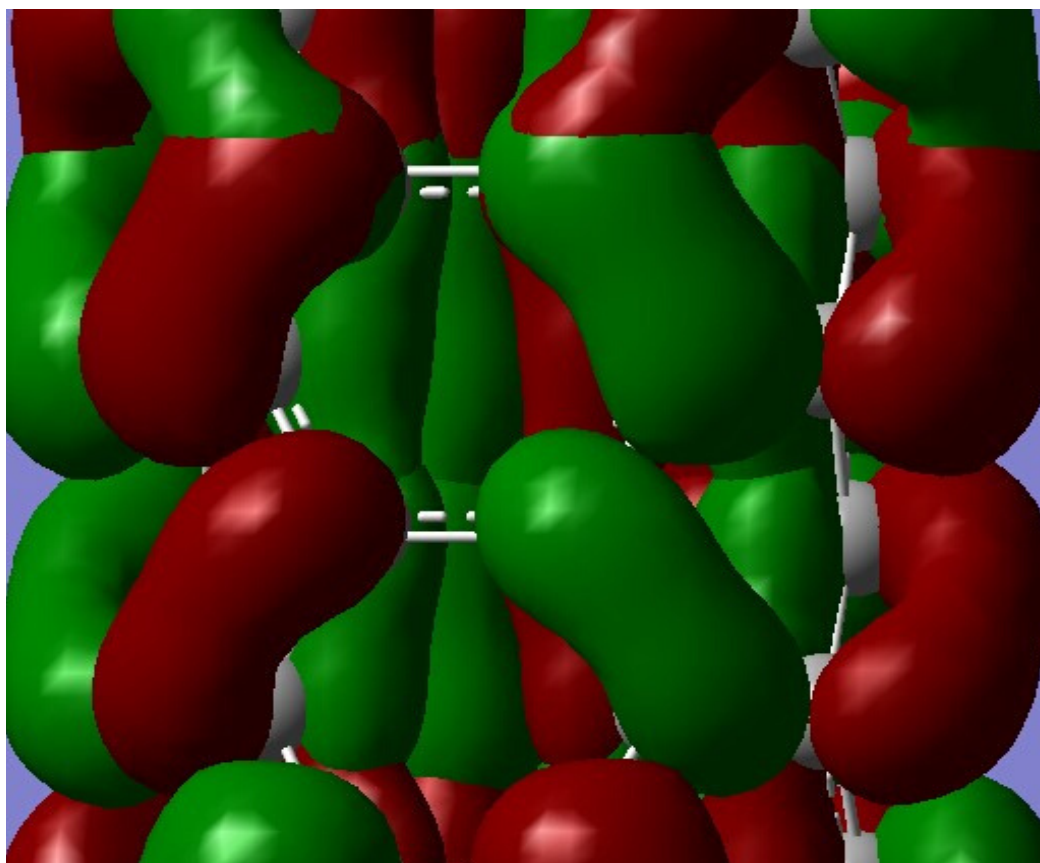


Volume 8, December 2019

ISSN 2542-2545

*The*  
**HIMALAYAN  
PHYSICS**

*A peer-reviewed Journal of Physics*



*Department of Physics, Prithvi Narayan Campus, Pokhara  
Nepal Physical Society, Western Chapter, Pokhara*

# Aerosol optical properties of size segregated aerosol particles and radiative forcing over Pokhara valley

Research Article

Jeevan Regmi<sup>1\*</sup>, Khem N Poudyal<sup>2</sup>, Amod Pokhrel<sup>3</sup>, Anthony Barinelli<sup>4</sup>, Rudra Aryal<sup>4</sup>

1 Central Department of Physics, Tribhuvan University, Kirtipur, Nepal

2 Dept. of Applied Sciences, Institute of Engineering, Tribhuvan University, Lalitpur, Nepal

3 University of California Berkeley, California, USA

4 Franklin Pierce University, 40 University Drive, Rindge, NH, USA

**Abstract:** The AERONET data from sun/sky radiometer over Pokhara (2017) was analyzed to observe aerosol optical depth (AOD) of size segregated particles and radiative forcing. Fine mode particles have over seventy percent of contribution to AOD in all months with the maximum, ninety-four percent, on November and February, and minimum on July, seventy-nine percent. The monthly mean top of atmosphere (TOA) forcing are negative  $-23.225 \pm 4.71 \text{ Wm}^{-2}$  in March,  $-28.958 \pm 4.71 \text{ Wm}^{-2}$  in April and  $-19.616 \pm 4.71 \text{ Wm}^{-2}$  in May. The negative value of TOA during all the months in pre-monsoon season indicates net cooling. Whereas surface forcing (BOA forcing) was found to be positive with a maximum value of  $111.18 \pm 27.63 \text{ Wm}^{-2}$  during April and a minimum of  $56.22 \pm 27.63 \text{ Wm}^{-2}$  during May. The resultant atmospheric forcing is the absorption due to aerosols within the atmosphere and found to be  $+267.57 \text{ Wm}^{-2}$  during April and  $+228.55 \text{ Wm}^{-2}$  during May; indicating significant heating of the atmosphere.

**Keywords:** Radiative Forcing • Aerosol Optical Depth • Coarse Mode/Fine Mode • Atmosphere (TOA and BOA)

## 1. Introduction

The radiation balance of the incoming and outgoing energy in the Earth-Atmosphere system is affected by external factors such as greenhouse gases and aerosols. Radiative forcing (RF), which is the change in the radiation budget received by the planet and energy radiated back to space, leads to either cooling or warming based on negative and positive RF [1]. Alternatively, the flux changes at the top of the atmosphere (TOA) is radiative forcing and is a better indicator of the global mean surface temperature [2]. Aerosol particles can influence climate directly by scattering and absorbing (in the case of black carbon) solar radiation [3]. Since a portion of the scattered radiation will be reflected back into space and leads to a cooling of the atmosphere. Fine particles of diameters less than one micron ( $\mu\text{m}$ ) are most effective for governing the strength of the aerosol optical properties [4].

\* Corresponding Author: [jsregmi28@gmail.com](mailto:jsregmi28@gmail.com)

The characteristic of chemical components of aerosols particles indicate for the strength of absorption and scattering of solar radiation by aerosol particles. Black carbon absorbs solar radiation, which leads to a warming of the atmosphere [5]. Black carbon deposition on snow and ice could decrease the surface albedo, leading to additional warming. Mineral dust also contributes for the absorption of radiation. Aerosol compounds such as sea salt, nitrate and sulfate scatter the light significantly than absorption resulting the cooling of the Earths atmosphere and therefore are also known as cooling agents. The indirect effect of aerosols is on the Cloud Microphysics that alters the cloud albedo by forming cloud condensation nuclei (CCN). The aerosols are responsible to reduce surface albedo upon deposition on snow, resulting in positive radiative forcing [6–8]. The aerosols can have both warming or cooling of the atmosphere called aerosol radiative forcing [9].

The deviation in radiation energy due to the interaction with atmospheric components is called attenuation. Absorption and Scattering of radiation are two processes included in attenuation. The radiation-matter interaction depends on wavelength of radiation, physical and chemical properties of the particle interacting with the radiation. It is known that more attenuation is possible in a region which has large numbers of such attenuators. The interaction and attenuation of radiation is determined by the optical depth ( $\tau$ ) and is given by,

$$\tau = \int \sigma \rho \, dx \quad (1)$$

where  $\rho$  is the density of the attenuator present in the path length  $dx$  in the direction of propagation and  $\sigma$  is the mass extinction cross section of the matter present within  $dx$ . In general, the intensity of radiation decreases exponentially with optical depth. If radiation with initial intensity  $I_0$  traverses a thickness  $dx$  with matter of optical depth  $\rho$  then the intensity after crossing this distance is given by;

$$I(\lambda) = I_0(\lambda) e^{-\tau} \quad (2)$$

This is called Beers law and sometimes it is referred to as Beer Lamberts law. The optical depth depends upon wavelength and number density of the attenuator. In order to get total attenuation of radiation, optical depth of all matters should be taken into account. Hence;

$$\tau(\lambda) = \tau_{Rayleigh}(\lambda) + \tau_{Ozone}(\lambda) + \tau_{Aerosol}(\lambda) + \tau_{Cloud}(\lambda) \quad (3)$$

where  $\tau_{Rayleigh}(\lambda)$ ,  $\tau_{Ozone}(\lambda)$ ,  $\tau_{Aerosol}(\lambda)$  and  $\tau_{Cloud}(\lambda)$  are optical depths caused by molecular, ozone, aerosols and clouds respectively [10].

The larger the optical thickness at a particular wavelength, the less light of that wavelength reaches Earths surface. Measurement of aerosol optical depth (AOD) provides important information of concentration, size distribution, and variability of aerosols in the atmosphere which are essential parameters for climate studies and to understand the overall effects of aerosols.

Aerosol optical depth (AOD,  $\tau(\lambda)$ ) is a quantitative measure of the extinction of solar radiation by aerosol scattering and absorption and is expressed in terms of Angstrom’s parameters,  $\alpha$  and  $\beta$  [11, 12] as;

$$\tau(\lambda) = \beta\lambda^{-\alpha} \tag{4}$$

where  $\alpha$  is the wavelength exponent that represents columnar aerosol size distribution in the atmosphere and used as a qualitative indicator of aerosol particle size and chemical components. The coefficient  $\beta$  is equal to  $\tau(\lambda)$  at a wavelength of  $1 \mu m$  and depends on the concentration of particles. Typical values of  $\beta$  vary from 0 to 0.5 indicating the higher the amount of aerosol present in the atmosphere with higher the values of  $\beta$  [13]. Size segregated monthly averaged AOD, which are automatically cloud cleared and manually inspected data, over an AERONET site of Nepal, Pokhara (28.18 N, 83.97 E) were received from AERONET webpage (<https://solrad-net.gsfc.nasa.gov/networks.html>) and analyzed. Comparing these data with RF gives a clear picture of aerosol characteristics. Coarse mode size distribution is being mechanically cut off at  $0.6 \mu m$  separating fine mode as smaller particles with radius smaller than  $0.6 \mu m$ . For air quality applications, this paper focuses on the analysis of total AOD, fine/coarse mode aerosol contributions in the AOD, comparison of RF with AOD [14]

The aerosol radiative forcing at the top of the atmosphere (TOA) or at the surface is defined as the difference in the net (down minus up) solar flux (solar plus long wave; in  $Wm^{-2}$ ) with and without aerosol, i.e..

$$\Delta F = (F_{a\downarrow} - F_{a\uparrow}) - (F_{0\downarrow} - F_{0\uparrow}) \tag{5}$$

where  $\Delta F$  denotes the irradiance (down-welling or upwelling,  $Wm^{-2}$ ) and  $(F \downarrow - F \uparrow)$  denotes the net irradiance (down-welling minus upwelling) computed with aerosol ( $F_a$ ) and without aerosol ( $F_0$ ) at either the TOA or the surface [15].

The aerosol radiative forcing efficiency is defined as the rate at which the atmosphere is forced per unit of aerosol optical depth at  $0.55 \mu m$  both at BOA and TOA:

$$\Delta F_{BOA/TOA}^{eff} = \Delta F_{TOA/BOA} / \tau(0.55) \tag{6}$$

It gives an evaluation of the direct radiative effect for each type of aerosol, characterized by absorption and size distribution [16]. Forcing efficiency depends upon nature of aerosol type. It is higher for absorbing aerosols like black carbon.

## 2. Methodology

### Aerosol Robotic Network (AERONET)

AERONET is a globally distributed network of automatic sun and sky scanning radiometers. Aerosol data from an AERONET site, Pokhara (28.187N, 83.975E), is retrieved for this study. AERONET uses CIMEL sun

and sky radiometer, which operates in two modes, direct sun measurements at 340 nm, 380 nm, 440 nm, 500 nm, 675 nm, 870 nm, 1020 nm, 1640 nm wavelengths and sky measurements at 440 nm, 675 nm, 870 nm and 1020 nm [17, 18]. These solar extinction measurements were used to compute aerosol optical depth (AOD), which were automatically computed by using a software and are available in the AERONET website. Holben et al. [17] presents the detailed estimation of uncertainty in computed AOD of approximately  $\pm 0.010$  to  $\pm 0.021$ , which is spectrally dependent with higher errors in the UV region.

## AERONET Data selection

In our analysis, we included fine-mode AOD, coarse mode and total AOD at 500 nm. First, we obtained daily means aerosol data from the website and were then used to calculate the monthly averages, by requiring at least 10 days per month. For the seasonal means it was required that all the months had sufficient amount of measurements. Eck et al. [19] included several example cases to show how the AERONET data have meaningful information for our study as well. These Level 2 size segregated daily averaged aerosol optical depth data also used to calculate the standard deviation while obtaining the monthly averaged data by using Microsoft excel math function. The percentage contribution of fine mode particles on total Aerosol optical depth is calculated and total AOD is compared with RF.

## RF data analysis

The sky radiance is measured along the solar principal plane (i.e., at constant azimuth angle, with varied scattering angles) up to nine times a day and along the solar almucantar (i.e., at constant elevation angle, with varied azimuth angles) up to six times a day. The approach is to acquire aureole and sky radiances observations through a large range of scattering angles from the sun through a constant aerosol profile to retrieve size distribution, phase function and aerosol optical depth. Sky radiance measurements are inverted with the Dubovik and Nakajima inversions to provide aerosol properties of size distribution and phase function over the particle size range of 0.1 to 5  $\mu m$ . We retrieved Version 3, Level 2.0 data of radiative forcing, from inversion products of AERONET site which assures high accuracy and quality-controlled data. Version 3 inversion description document describes the input data sets, scalar to vector computations, and additional retrieval products including sensitivity to input uncertainties.

## Radiative Forcing ( $\Delta F$ ) at the BOA (Bottom of Atmosphere) and at the TOA (Top of Atmosphere)

The study on the effect of atmospheric aerosols on the climate system is managed by AERONET by computing the direct radiative forcing at the BOA (Bottom of Atmosphere) and at the TOA (Top of Atmosphere). The aerosol radiative forcing strongly depends on the total aerosol extinction (AOD), the solar geometry and the surface type. Solar geometry is especially critical in estimating the  $\Delta F$  at the TOA, since a clear decrease of

the  $\Delta F$  absolute values has been documented as surface reflectivity increases, even changing the sign of the radiative forcing. It is found that over dark surfaces atmospheric aerosols always cool the Earth-atmosphere system, regardless of aerosol type [20, 21]. But, over the brightest surfaces, the total radiative effect depends on the aerosol absorption properties and on the SR values. It means a consistent comparison of the net aerosol effect requires the analysis for two ranges of surface reflectivity:  $SR \leq 30\%$  and  $SR \geq 30\%$ .

### 3. Results and Discussion

#### Contribution of Fine and coarse mode particles on AOD

The fractional contribution of Fine mode on AOD is shown in Figure 1. The fine mode particle contribution over all AOD is over seventy percentage in all months with the maximum, ninety-four percent, on November and February with minimum on July, seventy-nine percent. Particle size distribution is one of the most important parameters for characterizing the aerosol particles in the atmosphere. Seinfeld (1998) reports that the size distribution of particles in the atmosphere strongly indicates for the sources of aerosols. The coarse mode particles, diameters greater than 1 micrometer, are mainly produced by mechanical processes and injected into the atmosphere directly from anthropogenic and natural processes. On the other hand, fine mode particles, diameters smaller than 1 micrometer, are the particulate matters which are injected into the atmosphere through the process of combustion of wood, oil, coal, gasoline and other fuels. Because of the nature of their sources fine particles generally contain substantial amounts of organic material as well as soluble inorganics such as ammonium, nitrate and sulfate [22].

As a result, it is not surprising to see that the fine mode fractional AOD, percentage contribution of fine mode aerosols (Fig. 1) are strong in the months of pre-monsoon and post-monsoon seasons in comparison to months of summer monsoon. The post monsoon season (Oct-Nov) begins with a slow withdrawal of the monsoon. This retreat leads to an almost complete disappearance of moist air by October and resumes cool, clear, and dry weather. The summer monsoon, a strong flow of moist air from the southwest, follows the pre-monsoon period, which changes the particle composition and increases water contents in the atmosphere. Previous study shows that Pokhara has a significant Elemental Carbon contributed by biomass burning and fossil fuel combustion [3]. This shows that the concentration of fine mode particles stays abundantly in atmosphere for a long time and are significantly important for the attenuation of solar radiation over the Pokhara during the pre-monsoon and post-monsoon season in comparison to rainy season.

Fig. 2 shows that the aerosol impact on solar radiation elevated from post-monsoon season towards pre-monsoon seasons. This period must be impacted by anthropogenic aerosols and in the summer time the overall AOD decreases sharply and indicate for the impact of rainfall due to monsoon. The overall AOD in two months July and August is only about 12% of total average AOD of months February to April. This shows intense aerosol plumes in pre-monsoon period.

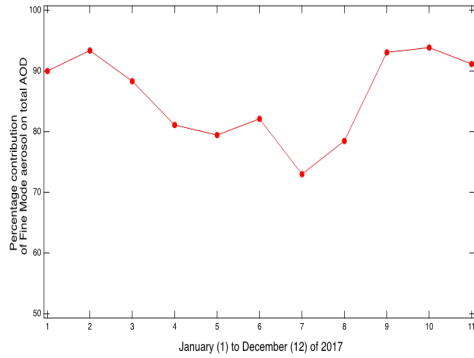


Figure 1. Percentage contribution of fine mode aerosol on total columnar AOD over Pokhara.

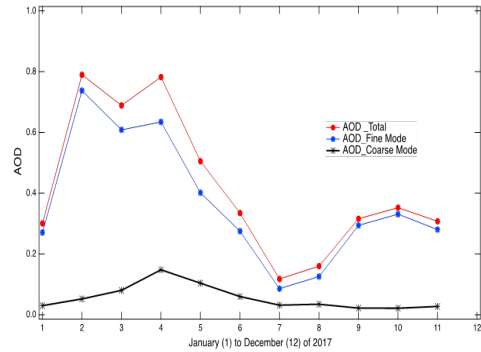


Figure 2. Monthly average total AOD and AODs due to fine and Coarse Mode particles.

### Variation of Radiative forcing

The Table 1 shows the radiative forcing in the season where the attenuation of solar radiation by aerosols are significantly high in comparison to other months. TOA forcing is found to be negative during all the months in pre-monsoon season which indicates net cooling as shown in figure 3 (c) and (d). The monthly mean TOA forcing was found to be  $-23.225 \pm 4.71 \text{ W m}^{-2}$  in March,  $-28.958 \pm 4.71 \text{ W m}^{-2}$  in April and  $-19.616 \pm 4.71 \text{ W m}^{-2}$  in May whereas surface forcing (BOA forcing) was found to positive with a maximum value of  $111.18 \pm 27.63 \text{ W m}^{-2}$  during April and a minimum of  $56.22 \pm 27.63 \text{ W m}^{-2}$  during May. The forcing efficiency was found to be maximum  $-65.619 \pm 6.504 \text{ W m}^{-2}$  in March indicating the abundant burning of biomass.

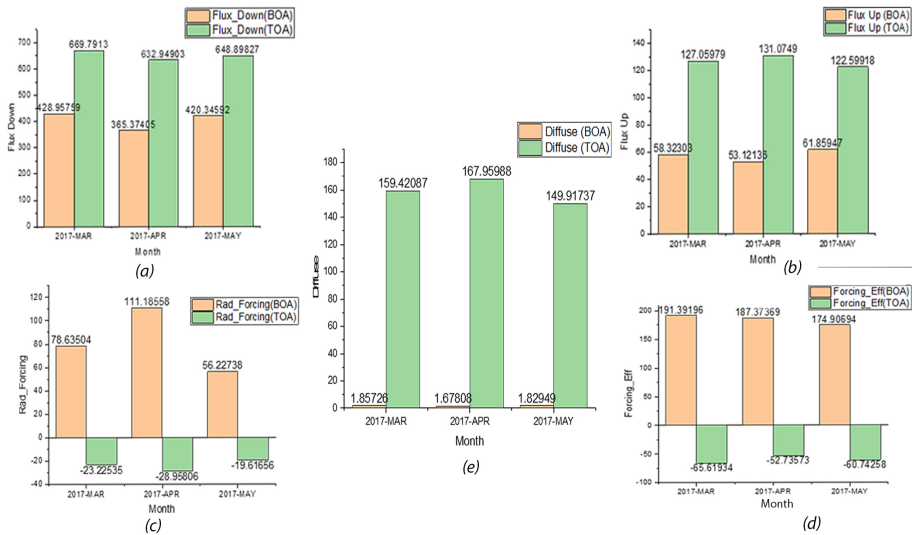


Figure 3. Variation of Radiative Forcing during Pre-Monsoon Period of 2017

Fig. 3(a) and Fig. 3(b) shows a net flux down and net flux up are positive in all the months of pre monsoon season. The resultant atmospheric forcing is the absorption due to aerosols within the atmosphere and found to be  $+267.57 \text{ Wm}^{-2}$  during April and  $+228.55 \text{ Wm}^{-2}$  during May indicating significant heating of the atmosphere. The forcing efficiency ( $\Delta F$ ) at the surface was found to be  $-65.6$ ,  $-52.7$  and  $-60.7 \text{ Wm}^{-2}$  during March, April and May respectively as seen in Fig. 3(d). Large aerosol induced negative surface forcing during pre-monsoon season is due to the mixing of anthropogenic aerosol pollution with transported natural dusts [23]. Figs. 4, 5 and 6 shows the daily variation of flux down, flux up and radiative forcing respectively at BOA and TOA. They reveal the significant variation of radiation pre and post monsoon days but it is almost washed out due to heavy precipitation during monsoon period.

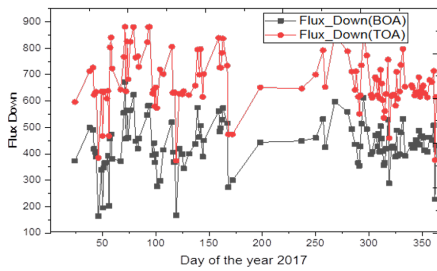


Figure 4. Daily variation of flux down at the top of atmosphere (TOA) and bottom of atmosphere (BOA).

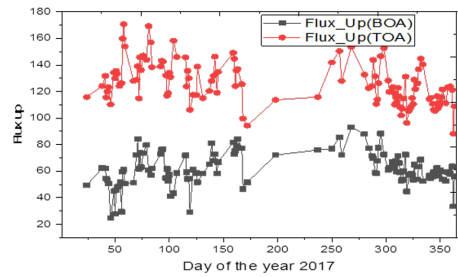


Figure 5. Daily variation of flux up at the top of atmosphere (TOA) and bottom of atmosphere (BOA).

The variety of components of solar radiation at the top of atmosphere and bottom of atmosphere are given in the Table 1 and graphs are presented in Figs. 3 to 7 [24]

Table 1. Variation of Radiative Forcing during Pre-Monsoon Period of 2017

Month of 2017	Flux_Down (BOA)	Flux_Down (TOA)	Flux_Up (BOA)	Flux_Up (TOA)	Rad.Forcing (BOA)	Rad.Forcing (TOA)	Forcing_Eff (BOA)	Forcing_Eff (TOA)	Diffuse (BOA)	Diffuse (TOA)
MARCH	428.96	669.79	58.32	127.06	78.63	-23.22	191.39	-65.62	1.86	159.42
APRIL	365.37	632.95	53.12	131.07	111.19	-28.96	187.37	-52.74	1.68	167.96
MAY	420.35	648.90	61.86	122.60	56.23	-19.62	174.91	-60.74	1.83	149.92
STDV	34.49	18.48	4.39	4.24	27.63	4.71	8.60	6.50	0.10	9.02

## Relationship between AOD and Radiative Forcing

The amount of cloud cover and duration of bright sunshine hour makes a difference in the amount of solar irradiance. Fig. 7 shows the monthly variation of diffuse radiation (BOA) and AOD<sub>500</sub>. It is seen that there is an increasing trend in AOD with decreasing value of diffuse solar radiation. Diffuse solar radiation is found to be more during winter than that of summer and consequently the value of AOD varied.



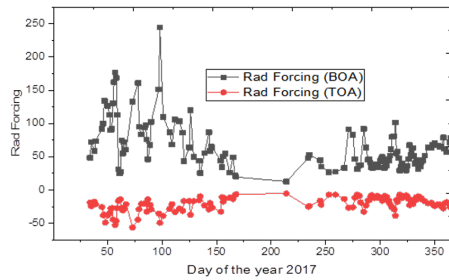


Figure 6. Variation of Radiative forcing and day of the year 2017.

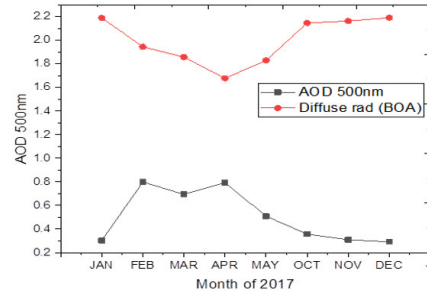


Figure 7. Monthly averaged Aerosol Optical Depth at 500 nm with the months of 2017.

## 4. Conclusions

Our finding based on the percentage contribution of fine mode aerosol particles on total AOD data suggests that using total AOD as a single predictor will not give a clear picture of aerosol components of the atmosphere. AOD weighs all types of aerosol components equally and does not consider the impact of size segregated particle composition. Presenting the contribution of different size of particles on overall AOD will indicate for the aerosol sources and origin of air particulate matter over the atmosphere. During the transition months (April-May and September-November) the aerosol patterns are dominated by fine particles, however in summer months the pattern is the hybrid mix of the two sizes of particles. Along with climatic and weather impacts, aerosol also leads to negative effects on public health and ecosystem. The study of contribution of aerosol on overall radiative forcing in this paper formulates the fundamental reasons for resulting the climate change from human induced changes in atmospheric composition. The results also suggest for the importance of further study by comparing aerosol chemical composition and size segregated aerosol particles for identifying the origin aerosol particles over Pokhara.

## 5. Acknowledgments

Authors are thankful to Dr. Arnico Kumar Panday, ICIMOD, Nepal, AERONET group of NASA, USA for sun/sky radiometers data <https://aeronet.gsfc.nasa.gov/> from Pokhara site.

## References

---

- [1] Verheggen B, Weijers E. Climate change and the impact of aerosol. Energy Research Centre of the Netherlands (ECN). 2010;.
- [2] Myhre G, Shindell D, Pongratz J. Anthropogenic and Natural Radiative Forcing. In: Climate change 2013 : the physical science basis; Working Group I contribution to the fifth assessment report of the Intergovernmental Panel on Climate Change. Cambridge: Cambridge University Press; 2014. p. 659–740.
- [3] Li C, Bosch C, Kang S, Andersson A, Chen P, Zhang Q, et al. Sources of black carbon to the Himalayan–Tibetan Plateau glaciers. *Nature communications*. 2016;7(1):1–7.
- [4] Che H, Zhao H, Wu Y, Xia X, Zhu J, Wang H, et al. Analyses of aerosol optical properties and direct radiative forcing over urban and industrial regions in Northeast China. *Meteorology and Atmospheric Physics*. 2015;127(3):345–354.
- [5] Konovalov IB, Lvova DA, Beekmann M, Jethva H, Mikhailov EF, Paris JD, et al. Estimation of black carbon emissions from Siberian fires using satellite observations of absorption and extinction optical depths. *Atmospheric Chemistry and Physics*. 2018;18:14889–14924.
- [6] Twomey S. The influence of pollution on the shortwave albedo of clouds. *Journal of the atmospheric sciences*. 1977;34(7):1149–1152.
- [7] Charlson RJ, Schwartz S, Hales J, Cess RD, Coakley JJ, Hansen J, et al. Climate forcing by anthropogenic aerosols. *Science*. 1992;255(5043):423–430.
- [8] Gul C, Puppala SP, Kang S, Adhikary B, Zhang Y, Ali S, et al. Concentrations and source regions of light-absorbing particles in snow/ice in northern Pakistan and their impact on snow albedo. *Atmospheric Chemistry and Physics*. 2018;18(7):4981.
- [9] Haywood J, Shine K. The effect of anthropogenic sulfate and soot aerosol on the clear sky planetary radiation budget. *Geophysical Research Letters*. 1995;22(5):603–606.
- [10] Bhattarai B. Factors affecting solar ultraviolet radiation, based on some case studies in Norway and Nepal. Norwegian University of Science and Technology; 2007.
- [11] Ångström A. On the atmospheric transmission of sun radiation. II. *Geografiska Annaler*. 1930;12(2-3):130–159.
- [12] Ångström A. Techniques of determining the turbidity of the atmosphere. *Tellus*. 1961;13(2):214–223.
- [13] McCartney EJ. Optics of the atmosphere: scattering by molecules and particles. New York, John Wiley and Sons, Inc. 1976;.
- [14] O’neill N, Eck T, Smirnov A, Holben B, Thulasiraman S. Spectral discrimination of coarse and fine mode optical depth. *Journal of Geophysical Research: Atmospheres*. 2003;108(D17).
- [15] Alam K, Trautmann T, Blaschke T, Majid H. Aerosol optical and radiative properties during summer and

- winter seasons over Lahore and Karachi. *Atmospheric Environment*. 2012;50:234–245.
- [16] García O, Díaz A, Expósito F, Díaz J, Dubovik O, Dubuisson P, et al. Validation of AERONET estimates of atmospheric solar fluxes and aerosol radiative forcing by ground-based broadband measurements. *Journal of Geophysical Research: Atmospheres*. 2008;113(D21).
- [17] Holben BN, Eck TF, Slutsker Ia, Tanre D, Buis J, Setzer A, et al. AERONETA federated instrument network and data archive for aerosol characterization. *Remote sensing of environment*. 1998;66(1):1–16.
- [18] Holben BN, Tanre D, Smirnov A, Eck T, Slutsker I, Abuhassan N, et al. An emerging ground-based aerosol climatology: Aerosol optical depth from AERONET. *Journal of Geophysical Research: Atmospheres*. 2001;106(D11):12067–12097.
- [19] Eck T, Holben B, Reid J, Arola A, Ferrare R, Hostetler C, et al. Observations of rapid aerosol optical depth enhancements in the vicinity of polluted cumulus clouds. *Atmospheric Chemistry & Physics Discussions*. 2014;14(13).
- [20] Garcia O, Díaz J, Expósito F, Díaz A, Dubovik O, Derimian Y, et al. Shortwave radiative forcing and efficiency of key aerosol types using AERONET data. *Atmospheric Chemistry & Physics Discussions*. 2011;11(12).
- [21] García O, Díaz J, Expósito F, Díaz A, Dubovik O, Derimian Y. Aerosol radiative forcing: AERONET-Based estimates. InTech; 2012.
- [22] Moody JL, Keene WC, Cooper OR, Voss KJ, Aryal R, Eckhardt S, et al. Flow climatology for physicochemical properties of dichotomous aerosol over the western North Atlantic Ocean at Bermuda. *Atmos Chem Phys*. 2014;14:691–717.
- [23] Dey S, Tripathi S. Aerosol direct radiative effects over Kanpur in the Indo-Gangetic basin, northern India: Long-term (2001–2005) observations and implications to regional climate. *Journal of Geophysical Research: Atmospheres*. 2008;113(D4).
- [24] Li Z, Xia X, Cribb M, Mi W, Holben B, Wang P, et al. Aerosol optical properties and their radiative effects in northern China. *Journal of Geophysical Research: Atmospheres*. 2007;112(D22).
- [25] Chung CE. Aerosol direct radiative forcing: a review. *Atmospheric Aerosols Regional Characteristics Chemistry and Physics*; Abdul-Razzak, H, Ed. 2012;p. 379–394.
- [26] Garcia O, Expósito F, Diaz J, Diaz A. Radiative forcing under aerosol mixed conditions. *Journal of Geophysical Research: Atmospheres*. 2011;116:D01201.
- [27] Iqbal M. An introduction to solar radiation. Elsevier; 2012.

## CERTIFICATES OF PARTICIPATION





Non-Resident Nepali Association International Coordination Council (NRNA-ICC) North-South Americas Regional Expert Conference 2020

### Certificate of Attendance, Presentation, and Recognition

The certificate is awarded to Mr. Jeevan Regmi in recognition of his oral presentation on, "**Scientific Evaluation of Air Pollution Over Two Big Cities in Nepal,**" given at the 2nd International Knowledge Conference for the Americas, held on 5-7 September 2020. This virtual conference's organizing committee highly appreciates his contribution to science communication on a national and international scale.

Dr. Iaxmi Pathak  
Conference Coordinator  
North-South American Regional Knowledge Conference, NRNA-ICC  
Date: September 8, 2020



**The 8<sup>th</sup> Asian Conference on Colloid & Interface Science (ACCIS 2019)**  
Sept. 24-27, Kathmandu, Nepal



### Certificate of Participation

This is to certify that  
**Jeevan Regmi**  
has participated and contributed **Poster Presentation** in  
**The 8<sup>th</sup> Asian Conference on Colloid & Interface Science (ACCIS 2019)** organized by the **Asian Society for Colloid and Surface Science (ASCASS)** held in Pulchowk Campus, Institute of Engineering, Tribhuvan University, Lalitpur, Kathmandu, Nepal.

  
Dr. Lok Kumar Shrestha  
Chairperson (ACCIS 2019)

September 27, 2019

  
Prof. Dr. Toyoko Imae  
President (ASCASS)





UNIVERSITY GRANTS COMMISSION  
विश्वविद्यालय अनुदान आयोग

Training for  
**Capacity Building on Geo-Information Technology for University  
Teaching and Research Human Resources**


Organized by the Department of Geography, Prithvi Narayan Campus, Pokhara with the financial support of University Grants Commission, Nepal from Ashadh 01 to 05, 2079 B.S. (June 15 to 19, 2022) in Pokhara

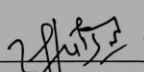
*Certificate of Participation*

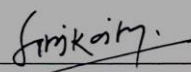
**JEEVAN REGMI**

Department of Physics, P.N. Campus, Pokhara

Successfully completed the courses Spatial Thinking, Introduction to GI Technologies, Data Capture and Vectorization, Geo-referencing, Projection and Transformation, Database Management, Introduction to Spatial Analysis and Output Design in ArcGIS 10x Software.

  
Dr. Krishna Prasad Poudel  
Professor of Geography  
Resource Person

  
Mr. Narajsh Paudel  
Head  
Geography Department, P.N. Campus

  
Prof. Dr. Saroj Koirala  
Campus Chief  
P.N. Campus



**Nepal Physical Society**

Ghantaghar, Kathmandu, Nepal

*International Conference on Frontiers of Physics-2022  
(ICFP-2022)*

This Certificate of appreciation is awarded to

**Mr. Jeevan Regmi**

from Prithvi Narayan Campus, TU, Nepal for his oral presentation on the title  
“Relative Humidity as a Correcting Factor on Comparing Surface Level Particle  
Concentration and Column Integrated Aerosol Optical Properties” in the

*International Conference on Frontiers of Physics - 2022*

held on January 22-24, 2022 via virtual platform.



Prof. Dr. Narayan P. Chapagain  
Conference Chair, ICFP-2022  
President, Nepal Physical Society


February 1, 2022

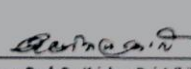


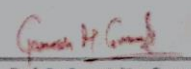
**National Conference on Recent Trends in Science, Technology and Innovation**  
RTSTI-2022 | Pokhara, Nepal

*Certificate of Participation*

This is to certify that Mr./Mrs. **JEEVAN REGMI** has participated as an **ORAL PRESENTER** entitled **Evaluation of Aerosol Extinction Efficiency Factors Using Lorentz-Mie Theory (PHO-06)** in the **National Conference on Recent Trends in Science, Technology and Innovation, RTSTI-2022** organized by Research Management Unit, Pashchimanchal Campus, Pokhara on 29<sup>th</sup> - 30<sup>th</sup> May, 2022.

  
**Asst. Prof. Nirmal Prasad Baral**  
Chairman, Organizing Committee, RTSTI  
Pashchimanchal Campus, Pokhara

  
**Assoc. Prof. Dr. Krishna Raj Adhikari**  
Chairman, Technical Committee, RTSTI  
Pashchimanchal Campus, Pokhara

  
**Prof. Dr. Ganesh Man Gurung**  
Chief Guest  
Chancellor, Gandaki University

**Organizer**  
Research Management Unit, RMU  
Pashchimanchal Campus  
Pokhara-16, Lamachaur

**Co-organizer**  
Gandaki Province Academy of  
Science and Technology (GPAST),  
Pokhara, Nepal

In association with

